School of Electrical and Computer Engineering

Combined Coding and Modulation in Frequency-Selective Mobile Communications

Manora Kumudinie Caldera

This thesis is presented as part of the requirement for the award of the Degree of Doctor of Philosophy of the Curtin University of Technology

March, 2000

ABSTRACT

Due to constraints on spectrum availability and transmitter power, both bandwidth and power efficient communication techniques are desirable for mobile radio. Continuous phase modulated (CPM) signals have gained attention because of their attractive power spectra (Steele, 1992). It has been shown that the trellis coded modulation (TCM) schemes could provide better bit error rate performances compared to the uncoded schemes (Ungerboeck, 1982). Therefore, the combination of TCM which improves error probability and CPM signals which yield low spectral occupancy is expected to provide good coding and modulation over bandwidth and power limited channels such as the one encountered in mobile radio communications.

In this research, a Trellis Coded Modulation (TCM) scheme, which combines convolutional coding and partial response Continuous Phase Modulation (CPM) such as Gaussian Minimum Shift Keying (GMSK), is investigated. Also, this study concentrates on the use of rate-½ convolutional codes, and GMSK (B_0T=0.3). The latter has been adopted in the Global System for Mobile Communications (GSM) system.

Appropriate codes are selected assuming Maximum Likelihood Sequence Detection (MLSD) based on the Viterbi algorithm using an extensive computer search. The bit-error-rate (BER) performances of the selected trellis coded GMSK schemes are theoretically evaluated in the presence of additive white Gaussian noise (AWGN) and frequency-flat fading. In the case of fading, the analysis is simplified to assume only amplitude-fading, and without considering the effect of fading on the phase of the received signal.

Computer simulations are used to evaluate the BER performances of the proposed trellis coded GMSK schemes in the presence of AWGN and practical impairments, such as sample timing offset and carrier phase errors.

Coding gains of up to 2.2dB at a BER of 10^{-3} are obtained under ideal sample timing and carrier recovery conditions. This has been achieved without increasing the receiver complexity based on the number of states in the Viterbi decoder, compared to the uncoded GMSK scheme. Furthermore, these coded schemes are more tolerant to sample timing and carrier phase impairments.

Also, the BER performances of the proposed trellis coded GMSK schemes have been extensively investigated by computer simulations for frequency-flat and frequency-selective fading channels. In the case of frequency-selective fading, the Viterbi decoding is made adaptive to cater for the channel impulse response variations with time. With this adaptive receiver, the irreducible BERs of the coded scheme is found to be lower than that of the uncoded. Performance improvements are obtained with a trellis coded GMSK scheme using a constraint length 2 code with a Viterbi decoder of 16 states compared to the 128 states required for the uncoded scheme. Further, the coded scheme has shown less sensitivity to carrier phase errors, compared to the uncoded.

ACKNOWLEDGMENTS

I would like to express my sincere gratitude to my supervisor Professor Kah Seng Chung for his constant guidance and encouragement throughout my PhD program. The invaluable contribution of his time and the useful suggestions based on his wide experience in Communications have helped me immensely.

In addition I owe a great debt of gratitude to the late Dr. Hashem Razavi, my co-supervisor, whose encouragement and unreserved support helped to make this thesis possible. I am also grateful to Dr. Hans-Jurgen Zepernick for providing me with valuable technical comments in the last stages of the work.

This thesis would not have been possible without financial assistance from Curtin University of Technology and the Australian Federation of University Women and I thank both institutions for that.

The thesis was written within the Communications Technology Research Group, and I wish to thank all its members: Nabil Afifi, Frank Chen, Jian Wei He, Keith Rainbow, Bijan Rohani and Jackson Yin, for their help and encouragement.

Especially I would like to thank Dr. Bijan Rohani for his valuable advice and encouragement while the thesis was in preparation.

Thanks are due to my friends Keith Rainbow, Bijan Rohani and Alex Lowe for proofreading the thesis. I would also like to acknowledge the administrative staff of the School of Electrical and Computer Engineering for their support.

In addition, I am deeply in debt to the many other unnamed individuals who have helped me in numerous ways and so made this thesis possible.

Above all, my husband, Havindra, son, Kavindu and daughter, Dinithi deserve my deepest gratitude for their remarkable patience and loving encouragement during the difficult times which inevitably occurred while doing this work.

TABLE OF CONTENTS

1. INTRODUCTION 1

1.1 Land Mobile Radio Communications 1

1.2 Scope of the Thesis 3

1.3 Organisation of the Thesis 3

1.4 A Summary of Original Contributions 6

2. BACKGROUND 7

2.1 Introduction 7

2.2 Signal Propagation in Land Mobile Radio Channels 7

2.3 Propagation Model of the Multipath Channel 9

2.3.1 Time spreading 10

2.3.2 Coherence bandwidth 11

2.3.3 Coherence time 13

2.3.4 The Doppler effect 14

2.4 Digital Modulation Schemes 15

2.4.1 CPM signals 16

2.4.1.1 GMSK modulation 18

2.4.1.2 GTFM modulation 21

2.5 Error Control Coding in Mobile Radio 23

2.6 Maximum Likelihood Sequence Decoding (MLSD) 27

2.6.1 Viterbi decoding algorithm 27

2.7 Trellis Coded Modulation 30

2.7.1 Ungerboeck codes 31

2.7.2 TCM with CPM signals 36

3. LITERATURE REVIEW 38

3.1 Introduction 38

3.2 TCM Schemes for AWGN Channels 38

3.2.1 Improved BER without sacrificing bandwidth 38

3.2.2 Sensitivity to carrier phase offset 39
3.3 Ungerboeck Codes over Fading Channels 40
3.4 Trellis Coded CPM Schemes over AWGN 46
3.5 Trellis Coded CPM over Fading Channels 51
3.5.1 Trellis coded CPM in flat fading channels 51
3.5.2 Trellis coded CPM in frequency-selective fading channels 53
4. SELECTION OF TRELLIS CODED GMSK SCHEMES 54
4.1 Introduction 54
4.2 Trellis Representation of GMSK Signal 55
4.3 Trellis Coded GMSK Signal 60
4.4 Trellis Diagrams for Trellis Coded GMSK Signals 64
4.5 Free Distances of Trellis Coded GMSK Signals 70
4.6 A Computer Search Method for Selecting the Appropriate Convolutional Codes 73
4.7 Selection of Appropriate Convolutional Codes 78
4.8 Trellis Diagrams of the Selected Coded GMSK Schemes 83
5. PERFORMANCE ANALYSIS OF THE SELECTED TRELLIS CODED GMSK SCHEMES 91
5.1 Introduction 91
5.2 Decoding Metric for Viterbi Decoding 92
5.2.1 Distance metric for AWGN channels 94
5.2.2 Distance metric for amplitude-fading channels 98
5.2.3 A summary on the upperbound of the probability of event error 102
5.3 Bounds of the Bit Error Probability 103
5.3.1 The transfer function of the error state diagram of the trellis Coded Scheme having Constraint Length 2 over AWGN Channels 109
5.3.2 The transfer function of the error state diagram of the trellis coded scheme having constraint length 2 over amplitude-fading channel 115

5.3.3 The bounds on the bit error probability of trellis coded GMSK scheme having constraint length 2 115
5.3.4 The transfer function of the error state diagram of the trellis coded scheme having constraint length 3 over AWGN channels 118
5.3.5 The transfer function of the error state diagram of the trellis coded scheme having constraint length 3 over amplitude-fading channel 123
5.3.6 The bounds on the bit error probability of trellis coded GMSK scheme having constraint length 3 123
5.4 Comments on the Analyses 125

6. PERFORMANCE OF SELECTED TRELLIS CODED GMSK SIGNALS IN THE PRESENCE OF AWGN 127

6.1 Introduction 127
6.2 Computer Simulation Model 127
6.3 Simulated BERs under Ideal Timing and Carrier Phase 130
6.4 The Effect of Timing Clock and Carrier Phase Errors 133
6.4.1 Simulation results in the presence of timing errors 135
6.4.2 Simulation results in the presence of carrier phase errors .. 141
6.4.3 Simulated BER performance in the presence of both timing and carrier phase errors 146
6.5 Summary 147

7. PERFORMANCE OF SELECTED TRELLIS CODED GMSK SIGNALS OVER FADING CHANNELS 149

7.1 Introduction 149
7.2 Simulation Model 149
7.2.1 Transmitter 149
7.2.2 Fading channel 150
7.2.2.1 Frequency non-selective (flat) fading 150
7.2.2.2 Frequency -selective fading 151
7.2.3 Receiver 152

7.3 Differential Phase Detection over Fading Channels 153
7.3.1 Simulation results over flat fading channels.....154
7.3.2 Simulated BER results over two-ray fading channels..... 155
7.4 An Improved Receiver with Adaptive Viterbi Detection Scheme ... 157
7.4.1 Simulation results over two-ray fading channels 158
7.4.4.1 Irreducible BERs over two-ray fading channel.....159
7.4.1.2 BER performances for different relative delays.....162
7.4.1.3 Influence of Doppler frequency on BER performance.....165
7.4.2 Simulated BERs over six-ray fading channels..... 166
7.5 Effect of Phase Errors at the Receiver 169
7.6 Summary 171

8. CONCLUSIONS AND RECOMMENDATIONS.....173

8.1 Summary of Results and Conclusions..... 173
8.2 Recommendations 178
8.2.1 Adaptive sampling 179
8.2.2 Adaptive channel estimation 179
8.2.3 Practical implementation 179

REFERENCES.....180

APPENDIX A-
THE UPPERBOUND OF P_E IN TERMS OF X_L AND X'_L.....A-1

APPENDIX B
SIMPLIFICATION OF $\exp[-\Delta_\lambda(x_k, x'_k)]$ FOR AN AWGN CHANNEL.....B-1

APPENDIX C
SIMPLIFICATION OF $\exp[-\Delta_\lambda(x_k, x'_k)]_{fading}$ FOR AN AMPLITUDE-FADING CHANNEL.....C-1

APPENDIX D
MATRIX TRANSFER FUNCTION OF THE ERROR STATE DIAGRAM OF THE TRELLIS CODED SCHEME HAVING CONSTRAINT LENGTH 2.....D-1

APPENDIX E
MATRIX TRANSFER FUNCTION OF THE ERROR STATE DIAGRAM OF THE TRELLIS CODED SCHEME HAVING CONSTRAINT LENGTH 3.....E-1

APPENDIX F
THE GSM PROPAGATION MODELS.....F-1

APPENDIX G
PUBLICATIONS.....G-1

APPENDIX H
COMPUTER PROGRAMS.....H-1

LIST OF FIGURES

Figure 2. 1 The various propagation paths followed by a transmitted signal before arriving at a mobile station obstructed by buildings from a base station.....8

Figure 2. 2 The examples showing (a) frequency-selective channel and (b) flat channel 12

Figure 2. 3 Pulse shapes $g(t)$ and the corresponding phase responses $q(t)$ for (a) CPFSK (b) duobinary FSK and (c) 3RC, CPM schemes (after Sundberg, 1986) 17

Figure 2. 4 Power spectra of GMSK signals (After Murota and Hirade, 1981) 19

Figure 2. 5 Frequency pulse shape of the GMSK signal when the normalised -3-dB bandwidth of the premodulation Gaussian filter B_0T= 0.3 20

Figure 2. 6 The eye-diagrams corresponding to $\sin[\phi(t)]$ and $\cos[\phi(t)]$ of the GMSK (B_0T= 0.3) signal.....20

Figure 2. 7 Schematic diagram of a GTFM modulator.....21

Figure 2. 8 Possible phase transitions of a GTFM signal within a bit period.....22

Figure 2. 9 The (n,k,ν) convolutional encoder 24

Figure 2. 10 A $(2,1,3)$ convolutional encoder 25

Figure 2. 11 Trellis diagram of the $(2,1,3)$ convolutional code.....26

Figure 2.12 Set-partitioning of the 8-PSK constellation. Here the free distance of each subsequent subset has a larger free distance. i.e., $d_0<d_1<d_2$ 32

Figure 2.13 A general structure of the encoder/modulator of TCM (After Ungerboeck ,1982).....32

Figure 2.14 Four-state Ungerboeck code for 8-PSK.....33

Figure 2.15 Trellis diagram of the rate-½ convolutional code used in the Ungerboeck code in Fig. 2.14.....33

Figure 2.16 Trellis of the Ungerboeck code for 4-state 8-PSK signal. Note that the signal phase state numbers are the same as given in Fig. 2.12.....34

Figure 2.17 Signal constellation of 4-PSK signal.....36

Figure 2.18 A block diagram of generating a trellis coded CPM signal.....36

Figure 3.1 (a) Symmetric and (b) asymmetric QPSK signal constellations 43

Figure 3.2 BER performance of rate-½ trellis coded symmetric and asymmetric QPSK in the presence of Rayleigh fading (After Divsalar and Simon, 1987).....43

Figure 4.1 The 16-state trellis diagram of the GMSK signal.....57

Figure 4.2 The 8-state trellis diagram of the GMSK signal.....59

Figure 4.3 The finite state diagram describing the phase changes over one bit period of GMSK signal.....60

Figure 4.4 A model of the trellis coded GMSK signal transmitted over an AWGN channel.....61

Figure 4.5 Detection of trellis coded GMSK signal using quadrature demodulation followed by Viterbi decoding.....61

Figure 4.6 A model of the trellis coded GMSK signal employing differential encoding.....62

Figure 4.7 The finite state diagram describing the phase changes over one bit period of differentially encoded GMSK signal 62

Figure 4.8 The trellis diagram of the differentially encoded GMSK signal.....63

Figure 4.9 (a) Encoder (b)Trellis diagram, of the code [3,1].....64

Figure 4.10 Construction of the combined trellis diagram of the code [3,1] with GMSK signal 66

Figure 4.11 Combined trellis diagram of the code [3,1] with GMSK signal.....67

Figure 4.12 Combined trellis diagram of the code [3,1] with differentially encoded GMSK signal.....68

Figure 4.13 (a) Encoder (b) Trellis diagram of the code, [1,3].....69

Figure 4.13c Combined trellis diagram of the code [1,3] with differentially encoded GMSK signal.....69

Figure 4. 14a The basic flow chart of the computer search.....75

Figure 4.14b The flow chart for the search for normalised squared FED...76

Figure 4.15 Combined trellis diagram of the code [3,1] with differentially encoded GMSK showing split and merge paths.....77

Figure 4.16 (a) Encoder (b)Trellis diagram, of the code [7,3].....84

Figure 4.16c Combined trellis diagram of the code [7,3] with differentially encoded GMSK signal.....84

Figure 4.17 (a) Encoder (b)Trellis diagram, of the code [6,3].....85

Figure 4.17c Combined trellis diagram of the code [6,3] with differentially encoded GMSK signal.....86

Figure 4.18 (a) Encoder (b) Trellis diagram, of the code [13,7].....87

Figure 4.18c Combined trellis diagram of the code [13,7] with differentially encoded GMSK signal.....88

Figure 4.19 (a) Encoder (b)Trellis diagram, of the code [15,7].....89

Figure 4.19c Combined trellis diagram of the code [15,7] with differentially encoded GMSK signal.....90

Figure 5.1 (a) Trellis diagram (b) Trellis diagram showing the error event (c) Error state diagram for a two-state trellis coded scheme.....106

Figure 5.2 (a) Trellis diagram of the code [3,1] combined with differentially encoded GMSK (b) Trellis diagram of the code [3,1].....110

Figure 5.3 Error state diagram of the code [3,1] in combination with differentially encoded GMSK.....111

Figure 5.4 The finite state diagram of the differentially encoded GMSK signal.....111

Figure 5.5 The bounds of the bit error probabilities for the trellis coded GMSK scheme in conjunction with the code [3,1] having constraint length 2 for AWGN and amplitude-fading channels.....118

Figure 5.6 (a) Trellis diagram of the code [7,3] (b) Trellis diagram of the code [7,3] combined with differentially encoded GMSK 119

Figure 5.7 Error state diagram of the code [7,3] in combination with differentially encoded GMSK..... 120

Figure 5.8 The bounds of the bit error probabilities for the trellis coded GMSK scheme in conjunction with the code [7,3] having constraint length 3 for AWGN and amplitude-fading channels..... 125

Figure 6.1 Simulation system model..... 127

Figure 6.2 Influence of the bandwidth of the receive filter on the BERs of uncoded and trellis coded GMSK signals..... 132

Figure 6.3 BERs of the uncoded and trellis coded GMSK signals..... 132

Figure 6.4 BER curves of uncoded and coded GMSK schemes, (1-4) with ideal carrier and timing recoveries, and (5-8) with ideal carrier recovery and fixed sampling time error of $\pm 25\%$ of T..... 138

Figure 6.5 BER curves of uncoded and coded GMSK schemes, (1-4) with ideal carrier and timing recoveries, and (5-8) with ideal carrier recovery and fixed sampling time error of $\pm 37.5\%$ of T..... 139

Figure 6.6 BER curves of uncoded and coded GMSK schemes, (1-4) with ideal carrier and timing recoveries, and (5-8) with ideal carrier recovery and random timing error of $\pm 25\%$ of T rms (bandwidth is 0.1% of the input bit rate)..... 140

Figure 6.7 BER curves of uncoded and coded GMSK schemes, (1-4) with ideal carrier and timing recoveries, and (5-8) with ideal carrier recovery and random timing error of $\pm 25\%$ of T rms (bandwidth is 0.5% of the input bit rate)..... 141

Figure 6.8 BER curves of uncoded and coded GMSK schemes, (1-4) with ideal timing and carrier recoveries, and (5-8) with ideal timing recovery and fixed carrier phase error of $\pm 15°$ 143

Figure 6.9 BER curves of uncoded and coded GMSK schemes, (1-4) with ideal timing and carrier recoveries, and (5-8) with ideal timing recovery and fixed carrier phase error of $\pm 18°$ 144

Figure 6.10 BER curves of uncoded and coded GMSK schemes, (1-4) with ideal timing and carrier recoveries, and (5-8) with ideal timing recovery and random carrier phase error of $\pm 18°$ rms (bandwidth is 1% of the input bit rate)..... 145

Figure 6.11 BER curves of uncoded and coded GMSK schemes, (1-4) with ideal timing and carrier recoveries, and (5-8) with fixed timing error of $\pm 25\%$ of T and fixed carrier phase error of $\pm 18°$ 146

Figure 7.1 Block diagram of a frequency non-selective Rayleigh fading simulator 151

Figure 7.2 Block diagram of a frequency-selective two-ray model..... 152

Figure 7.3 The BERs of the uncoded and trellis coded GMSK, using differential phase detection over flat fading channel..... 155

Figure 7.4 The irreducible BERs of the uncoded and trellis coded GMSK using differential phase detection over a two-ray fading channel..... 156

Figure 7.5 The irreducible BERs of the uncoded and trellis coded GMSK, for different relative delays. Signal blocks of 128 bits and 256 bits are assumed. 160

Figure 7.6 The irreducible BERs of the uncoded and trellis coded GMSK achieved using the decoder which is designed to accommodate relative delay of $3T$ 161

Figure 7.7 The irreducible BERs of the uncoded and trellis coded GMSK for two different lengths of training sequence..... 162

Figure 7.8 The BERs of the uncoded and trellis coded GMSK when the relative delay is $1T$..... 163

Figure 7.9 The BERs of the uncoded and trellis coded GMSK when the relative delay is $2T$ 163

Figure 7.10 The BERs of the uncoded and trellis coded GMSK when the relative delay is $3T$ 164

Figure 7.11 The BERs of the uncoded and trellis coded GMSK when the relative delay is $4T$ 164

Figure 7.12 The BERs of the uncoded and trellis coded GMSK at different vehicular speeds. A relative delay of $4T$ is assumed..... 166

Figure 7.13 The BERs of the uncoded and trellis coded GMSK for different vehicular speeds based on the rural area (RA) model.....167

Figure 7.14 The BERs of the uncoded and trellis coded GMSK for different vehicular speeds based on the hilly terrain (HT) model.....168

Figure 7.15 The BERs of the uncoded and trellis coded GMSK for different vehicular speeds based on the typical urban area (TU) model.....169

Figure 7.16 The BERs of the uncoded and trellis coded GMSK in the presence of phase errors, when the relative delay between the two paths of the two-ray frequency-selective fading model is $4T$.....170

Figure 7.17 The BERs of the uncoded and trellis coded GMSKin the presence of phase errors, when the relative delay between the two paths of the two-ray frequency-selective fading model is $1T$.....171

Figure F.1 The six-ray propagation channel models defined by the GSM for (a) the rural area, (b) the hilly terrain, and (c) the typical urban environment.....F-3

LIST OF TABLES

Table 2.1 Occupied bandwidth of GMSK schemes having various values of B_0T (After Murota and Hirade, 1981).....20

Table 4.1 The allowable phase transitions over one bit period of GMSK signal with respect to three consecutive input data bits.....56

Table 4.2 The modified phase transitions of GMSK with respect to three consecutive input data bits.....58

Table 4.3 The values of normalised squared FED of rate-1/2 convolutional codes having constraint length 2 when combined with differentially encoded GMSK. The corresponding numbers of states for Viterbi decoding are also shown.....80

Table 4.4 The values of normalised squared FED of rate-1/2 convolutional codes having constraint length 3 when combined with differentially encoded GMSK. The numbers of states required for Viterbi decoding are also shown.....81

Table 4.5 The values of normalised squared FED of rate-1/2 convolutional codes having constraint length 4 when combined with differentially encoded GMSK (only codes with 16 states in the Viterbi decoder are shown).....82

Table 4.6 The coding gains associated with the selected coded schemes.....83

Table 6.1 The required E_b/N_0 in dB to achieve a BER of 10^{-3}.....137

Table 6.2 The performance gain/loss in dB at a BER of 10^{-3} 147

Table 7.1 Throughput efficiencies of the uncoded and trellis coded schemes for signal block sizes of 128 bits and 256 bits.....159

Table F.1 Tap settings for the 6-tap typical rural area (RA) model.....F-2

Table F.2 Tap settings for the 6-tap hilly terrain (HT) model F-2

Table F.3 Tap settings for the 6-tap urban area (TU) model.....F-2

ABBREVIATIONS

AM	Amplitude modulation
ARQ	Automatic repeat request
AWGN	Additive white Gaussian noise
BCH	Bose Ray-Chaudhuri and Hocquenghem
BER	Bit error rate
CLASS	Classical
CPFSK	Continuous phase frequency shift keying
CPM	Continuous phase modulation
dB	Deci-Bell
DECT	Digital Enhanced cordless telecommunications
ED	Euclidean distance
EX-OR	Exclusive OR logical operation
FEC	Forward error correction
FED	Normalised free Euclidean distance
FM	Frequency modulation
FSK	Frequency shift keying
GMSK	Gaussian minimum shift keying
GSM	Global system for mobile communications
GTFM	Generalised tamed frequency modulation
HT	Hilly terrain
ISI	Inter-symbol interference
kb/s	Kilo bits per second
km/h	Kilo meters per hour

MHz	Mega hertz
MLSD	Maximum likelihood sequence decoding
MLSE	Maximum likelihood sequence estimator
MPSK	Multiple phase shift keying
MSK	Minimum shift keying
PCS	Personal communication system
PDC	Personal digital cellular system
pdf	Probability density function
PHPS	Personal handy phone system
PSK	Phase shift keying
QAM	Quadrature amplitude modulation
QPSK	Quadrature phase shift keying
RA	Rural area
RC	Raised cosine
REC	Rectangular
Rice	Rician
rms	Root mean square
SED	Normalised squared Euclidean distance
SNR	Signal-to-noise ratio
TCM	Trellis coded modulation
TFM	Tamed frequency modulation
TU	Typical urban area
UHF	Ultra high frequency
WSSUS	Wide-sense stationary uncorrelated scattering

LIST OF PRINCIPAL SYMBOLS AND NOTATIONS

$\oplus$	Exclusive-OR logic operation
τ	Relative path delay
$\tau(t)$	The propagation delay caused by the transmission medium
$\tau_n(t)$	Time varying propagation delay of the n^{th} multipath
$\delta(\tau)$	Impulse function
ν	Constraint length of the code
σ^2	Variance of Gaussian noise
σ_K^2	The variance of real and imaginary parts of sampled noise n_k
ρ	The random fading amplitude
ρ_k	The time varying random amplitude at time k
λ	Chernoff bound parameter
λ'_{opt}	The optimum value of the Chernoff bound parameter for AWGN channels
$(\lambda'_{opt})_{fading}$	The optimum value of the Chernoff bound parameter for amplitude-fading channels
ξ_i	The matrix transfer function at node **(i)**
ω_c	The carrier angular frequency
ω_m	The maximum Doppler frequency
$(.)^*$	Complex conjugate of an argument
$[.]^T$	Matrix transpose
ϕ_0	Initial phase
ϕ_k	the information carrying phase angles corresponding to the transmitted signal x_k

ϕ'_k	the information carrying phase angles corresponding to the incorrectly detected signal x'_k
$\phi_i(t)$	Phase angle of the signal $s_i(t)$
$\phi_r(t)$	Phase angle of the received signal
$\phi(t,\alpha)$	Information carrying phase
$\Delta\phi$	Carrier phase error
$\Delta\phi_j(t)$	The phase difference of the j^{th} signal at sampling intervals over one bit period
$\Delta\phi(mT)$	The allowable phase shift of the modulated carrier during the m^{th} bit period
$\Delta\theta_k$	The time varying phase introduced by fading at time k.
$\Delta\theta(mT)$	The allowable phase shift of the modulated carrier during the m^{th} bit added with 90°
$\Delta\Phi[(k+1)T]$	The phase difference at the sampling instant $(k+1)T$ between the two signals $s_i(t)$ and $s_j(t)$
Δf	Frequency offset
Δf_c	Coherence bandwidth
Δt	Timing error
$(\Delta t)_c$	Coherence time
a	Amplitude of the direct signal
b_m	The binary data at time $t=mT$
B_θ	The -3-dB bandwidth
c_j	Output of the j^{th} modulo-2 adder
$c_n(t)$	Attenuation factor for the signal received on the n^{th} path
d_{free}	The free distance of the coded signal
d_{ref}	The free distance of an uncoded signal operating with the same energy per bit as the coded signal

$d^2_n(i,j)$	The Squared Euclidean distance between the i^{th} and the j^{th} signal over an interval nT
$d^2_{min,N}$	The minimum normalised Squared Euclidean distance up to N symbol intervals.
$D^2_{min}(N)$	The minimum SED between all the pairs of paths which split at t=0 and remerge at t=NT
e	Error vector
$\bar{e}$	The complement of e
$\mathbf{e}_k$	k^{th} element of $\boldsymbol{E}_L$
E	Energy of the transmitted signal
E_b	Bit energy of the input bits to the encoder
$\boldsymbol{E}_L$	An L-sequence of error vectors
$E[.]$	The statistical expectation operation
f_b	Input bit rate
f_c	Carrier frequency
f_D	Doppler frequency shift
$g(t)$	Frequency pulse
$\mathbf{G}$	The matrix transfer function of the error state diagram
G_j	The connection between the j^{th} modulo-2 adder and each stage of the shift register.
$G(e)$	Error weight matrix corresponding to an error vector e
h	Modulation index
$\boldsymbol{h}(t,\tau)$	Impulse response of the channel
$\boldsymbol{H}(t,f)$	The time varying transfer function of the channel
Im{.}	Imaginary part of the complex signal
$I_0(.)$	The modified zeroth order Bessel function

$I_r(nT+t_0)$	The inphase component of the received signal at the sampling instant of $t=nT+t_0$
k	Number of information bits in a code
k_0	The number of samples giving an offset corresponding to the maximum eye opening
$m(Y_L, X_L)$	The maximum likelihood decoding metric used by the trellis decoder for the correct sequence X_L
$m(Y_L, X'_L)$	The maximum likelihood decoding metric used by the trellis decoder for the incorrect sequence X'_L
n	Number of coded bits from the encoder
n_k	The k^{th} sample of complex Gaussian noise
N_0	Power spectral density of AWGN
$n(t)$	Additive white Gaussian noise
$p(.)$	Probability density function
$P[X_L]$	The probability of transmitting X_L.
$[P_b]_{l.b.}$	The lowerbound on the bit error probability
$[P_b]_{u.b.}$	The upperbound on the bit error probability
$P_e(\Delta\phi, \Delta t)$	The error probability corresponding to the joint effect of phase and timing error
P_{Error}	The probability of error of the received signal
P_E	The error probability of an error event
$P(X'_L \mid X_L)$	The probability of selecting the coded sequence X'_L when X_L has been transmitted
$P_E(L, X'_L, X_L)$	The probability of occurrence of an error event X'_L of length L, when the sequence X_L has been transmitted
$q(t)$	Phase shaping pulse
$Q_r(nT+t_0)$	The quadrature component of the received signal at the sampling instant of $t=nT+t_0$
r	Roll-off factor of the Nyquist-3 filter

$r(t)$	Received signal
R_c	Code rate
Re{.}	Real part of the complex signal
$R_h(\tau)$	The multipath intensity profile
$\boldsymbol{R}_h(t_0, \tau_0, \tau_1)$	The autocorrelation function of the channel impulse response, $\boldsymbol{h}(t_0, \tau)$, at $\tau=\tau_0$ and $\tau=\tau_1$
$\boldsymbol{R}_H(t_0, f_0, f_1)$	The autocorrelation function of $\boldsymbol{H}(t_0,f)$, at $f=f_0$ and $f=f_1$
$\boldsymbol{R}_H(t_0, t_1, f_0)$	The autocorrelation function of $\boldsymbol{H}(t,f_0)$, at $t=t_0$ and $t=t_1$
$r_{LP}(t)$	The low-pass equivalent of the received signal $r(t)$
$s_0(t)$	Transmitted signal
$s_{flat}(t)$	Signal output of the frequency non-selective Rayleigh fading simulator
t_i	The matrix label of the i^{th} branch
t_0	The sampling offset
T	Transmitted bit duration
T_b	Bit duration of the input bits to the encoder
$T(D)$	The scalar transfer function of the error state diagram
$u_0(t)$	Complex envelope of the modulated wave
x_k	k^{th} element of $\boldsymbol{X_L}$
$\boldsymbol{X_L}$	Coded sequence of length L
$\boldsymbol{X'_L}$	The incorrectly detected sequence instead of $\boldsymbol{X_L}$
y_k	k^{th} element of $\boldsymbol{Y_L}$
$\boldsymbol{Y_L}$	The received sequence corresponding to the coded sequence $\boldsymbol{X_L}$

CHAPTER 1

INTRODUCTION

1.1 Land Mobile Radio Communications

Due to the increasing demand for more capacity and better quality mobile radio services, digital mobile communication technology providing highly reliable voice and/or high-speed data transmission continues to evolve. For example, advanced digital modulation and demodulation techniques play a crucial role in improving the capacity of a mobile communication system. For this reason, it continues to attract research efforts aiming at achieving digital modulation schemes with better spectral and power efficiencies. The primary objective of spectrally efficient modulation is to maximise the channel bandwidth utilisation, normally expressed in units of bits/s/Hz. Preferably, this will be achieved in conjunction with good power efficiency, i.e., a prescribed average bit error rate (BER) would be achieved with minimum expenditure of signal power. Furthermore, the prefered modulation scheme will have a constant envelope, so that efficient non-linear power amplifiers may be used without causing undesirable spectral splashing.

Continuous Phase Modulation (CPM) signals have gained attention in mobile radio applications because of their compact power spectra (Steele, 1992). Furthermore, the inherent constant envelope property of the CPM signals permits the use of non-linear power amplifiers in the transmitter. Therefore, CPM signals are good candidates for mobile radio communications, which often demand the use of a modulation-demodulation scheme having compact spectrum and good power efficiency. An example of CPM signals is the Gaussian Minimum Shift Keying (GMSK) (Murota and Hirade, 1981) as used in the GSM (Global System for Mobile Communications) mobile telephony system.

In mobile radio communications, the received signal is subject to multipath fading caused by reflection, diffraction, and scattering of the transmitted signal by the surrounding obstacles. Multipath fading can give rise to variations in the received signal level and signal distortions. This will lead to degradation of the BER performance of the transmission link. In these multipath propagation environments, error control coding techniques are often used to achieve the required BER performance (Pieper *et al*, 1978; Ali Adel *et al,* 1989; Schlegel *et al,* 1989; Soliman *et al,* 1992). Moreover, with error control coding techniques, sufficient redundant bits are added to the transmitted information bits to allow the receiver to detect and possibly correct the erroneous bits. However, such additional redundant bits will lead to a higher transmission rate, thus increasing the transmission bandwidth as compared to an uncoded scheme. One way of avoiding this bandwidth expansion would be for the coded scheme to adopt a multi-level signalling format instead of using simple binary signalling. Since most multi-level signalling schemes suffer from lower noise margins, a larger transmitted signal power is therefore needed to maintain the same bit error rate as binary signalling. Alternatively, a more effective scheme called trellis coded modulation (TCM), which combines coding and modulation together, as proposed by Ungerboeck (1982) may be adopted.

Often with TCM, a convolutional code is used in combination with a higher order modulation scheme. The received signal is then processed by a receiver that combines both the demodulation and decoding in a single step, as opposed to first demodulating and then decoding the data in more conventional coding and modulation schemes. The key to improving the BER performance of TCM is to map the coded bits to appropriate signal space states of the modulated signal, such that the free distance (minimum Euclidean distance) between the different coded signal sequences is maximised. It has been shown by Ungerboeck (1982) that the BER performance of a TCM scheme can be improved without sacrificing bandwidth and power efficiency. As a result, TCM schemes, which have been originally developed for use in additive white Gaussian noise (AWGN)

channels, have received attention for applications in bandwidth and power limited mobile radio systems (Ungerboeck, 1982; Divsalar and Simon, 1987).

1.2 Scope of the Thesis

This research aims at studying a spectrally efficient communication scheme, which is also tolerant to frequency-selective fading often encountered in mobile radio environments. In this study, a trellis coded modulation scheme, which combines convolutional coding, and partial response CPM, such as GMSK, is investigated. Also, this study concentrates on the use of rate-½ convolutional codes, and GMSK (B_0T=0.3), the modulation scheme adopted in the GSM system (Mouly and Pautet, 1995). Extensive computer simulations have been used to evaluate the performance of the proposed scheme in the presence of AWGN, as well as frequency non-selective and frequency-selective fading conditions. Furthermore, theoretical analyses have been carried out assuming AWGN and frequency non-selective amplitude-fading channels.

1.3 Organisation of the Thesis

This thesis is organised into eight chapters. Chapter 2 presents a background introduction to mobile radio communications. This begins by outlining the various channel parameters, which may influence the performance of digital mobile transmission. The principles of CPM signals are then explained. This is followed by a description of trellis coding, which is often also referred to as convolutional coding. The most widely used trellis decoding method based on the Viterbi algorithm (Viterbi, 1967) is then described. Finally, the theory behind the trellis coded modulation (TCM) scheme, which is the main theme of this research, is explained.

Chapter 3 presents an extensive literature survey showing the results under AWGN and various fading conditions of published research on TCM schemes, which use set partitioning or Ungerboeck codes (Ungerboeck,

1982; Divsalar and Simon, 1987). Also, various criteria for selecting the appropriate convolutional codes for use with CPM signals in the presence of AWGN are discussed. Finally, published results of research on trellis coded CPM signals over fading channels are reviewed.

Chapter 4 presents the selection of appropriate trellis coded signals to be evaluated in this study. The modulation method to be used in these TCM schemes is the GMSK as adopted in the GSM system (Steele, 1992). Furthermore, it is assumed that the TCM signal will be decoded by Maximum Likelihood Sequence Decoding (MLSD) based on the Viterbi algorithm. A computer search technique is used for determining the free distances associated with different trellis coded CPM signals. Here, the free distance is defined as the minimum Euclidean distance between two signal paths leaving a common state in the combined trellis and merging into another common state at a later time. Also, the receiver complexity, as indicated by the number of states in the Viterbi decoder, is considered. It will be shown that a reduction of the number of states in the Viterbi decoder could be obtained by introducing differential encoding before the modulation as suggested by Morales-Moreno *et al* (Morales-Moreno *et al*, 1994). The final choice of an appropriate TCM scheme is based on one with the largest free distance in conjunction with the minimum number of states in the combined trellis. The free distances of the selected trellis coded schemes together with their achievable coding gains, as compared to the uncoded scheme, are tabulated in Table 4.6.

In Chapter 5, the error rate performances for the selected trellis coded CPM schemes in the presence of AWGN as well as frequency non-selective fading are evaluated analytically. In the case involving fading, the analysis is simplified to include only amplitude fading and assuming that the effect of fading on the phase of the received signal is fully tracked at the receiver. In these analyses, upper and lower bounds of the BERs are obtained for the selected trellis coded schemes in the presence of AWGN and amplitude-fading. However, the BER performances obtained in the case of amplitude-

fading will be better than what could be achieved in practice as the analyses ignore the influence of fading on the phase of the received signal.

The BER performances of the selected TCM schemes in the presence of AWGN have been studied by computer simulations and presented in Chapter 6. The influence of practical system impairments such as sample timing offset and carrier phase error on the BER performances has also been considered in the study. In the simulations, the trellis coded signal is assumed to be coherently detected and decoded using the Viterbi algorithm to select the most likely transmitted sequence.

Chapter 7 presents the bit error rates evaluated by computer simulations of the selected TCM schemes under fading conditions, including both frequency-flat and frequency-selective fading. The effect of frequency-selective fading on the BER has first been investigated using a two-ray propagation channel model. This is then followed by adopting the six-ray empirical propagation models proposed in the GSM standards (ETSI, 1993). In the simulations, coherent demodulation is assumed. However, in the case of frequency-selective fading, the Viterbi decoding process is made adaptive to cater for changes of the channel impulse response with time. Since the focus of this study is not on the adaptive estimation of impulse response, which is a research area in itself, it is assumed that the impulse response of the channel is already available for computing the actual states of the Viterbi decoder. In this study, the Viterbi decoder is designed to accommodate a channel delay spread of up to 4 symbol periods as specified for the GSM system. The resulting BER curves for the coded and the uncoded schemes are presented and discussed.

Finally, Chapter 8 concludes the thesis by stating the main contributions of this research. Also, recommendations are made for future studies.

1.4 A Summary of Original Contributions

To the best knowledge of the author, the following contributions have not been previously published by other researchers:

- A spectrally efficient communication scheme, which combines rate-½ convolutional coding and GMSK (B_0T=0.3), for applications over frequency-selective fading has been proposed. The appropriate codes have been selected using an extensive computer search technique based on the largest free Euclidean distance achievable with the minimum number of states required in the Viterbi decoder. Distance gains of up to 5.06 dB have been obtained with the selected coded schemes as compared to the uncoded scheme in the presence of AWGN.

- The influence of timing and phase deviations on the BER performance of the proposed receiver, which employs MLSD based on the Viterbi algorithm, in the presence of AWGN has been studied. Extensive computer simulations on the BER performances of the selected trellis coded schemes show that the proposed receiver is more tolerant to phase and timing errors as compared to the uncoded scheme, (refer to Table 6.2).

- An adaptive Viterbi decoder has been proposed for the detection of the coded scheme in the presence of frequency-selective fading. The proposed receiver has been designed to accommodate channel delay spreads of up to four symbol periods. A large reduction in the receiver complexity, in terms of the number of states in the adaptive Viterbi decoder, has been achieved for the coded scheme as compared to the uncoded scheme. Extensive computer simulations of the coded scheme using the proposed receiver show that BER performance of better than 10^{-2} is achievable even for a delay spread of four symbol periods. As specified by the GSM system, a BER performance of 10^{-2} is required for voice communication. Furthermore, the proposed coded scheme shows less sensitivity to carrier phase errors.

CHAPTER 2

BACKGROUND

2.1 Introduction

This chapter provides a background introduction to mobile radio transmission. It begins with a description of multipath fading which influences the performance of modern mobile communication systems, such as the cellular and personal communication systems (PCS), operating in the ultra-high frequency (UHF) band. Digital modulation schemes, which are suitable for mobile radio transmission, are then discussed. In this description, emphasis is placed upon CPM signals due to their excellent spectral characteristics. In view of the variations in received signal level caused by multipath propagation, error control technique is often used to improve the BER performance in mobile communication systems. One such forward error control technique is the use of convolutional codes. A detailed description of the trellis structure of convolutional codes will also be presented here. This is followed by a discussion of the Viterbi algorithm, which is widely used for decoding convolutional codes. Finally, the theory behind trellis coded modulation (TCM) is discussed.

2.2 Signal Propagation in Land Mobile Radio Channels

In a land mobile radio system, the propagation path between the mobile and the base station is generally obscured by buildings, hills and other objects surrounding the mobile station. This is illustrated in Fig. 2.1. As a result, the signal arriving at the receiver is considered to be the vector sum of the various signal components following different propagation paths. This phenomenon, often referred to as multipath fading, can cause fluctuations in the amplitude, phase and angle of arrival of the signal received at the receiver. Furthermore, a multipath channel may exhibit time-varying

characteristics because of movement of the mobile units. Due to the uncertainty in the propagation environment, the time varying mobile radio signal is usually characterised in terms of statistical parameters.

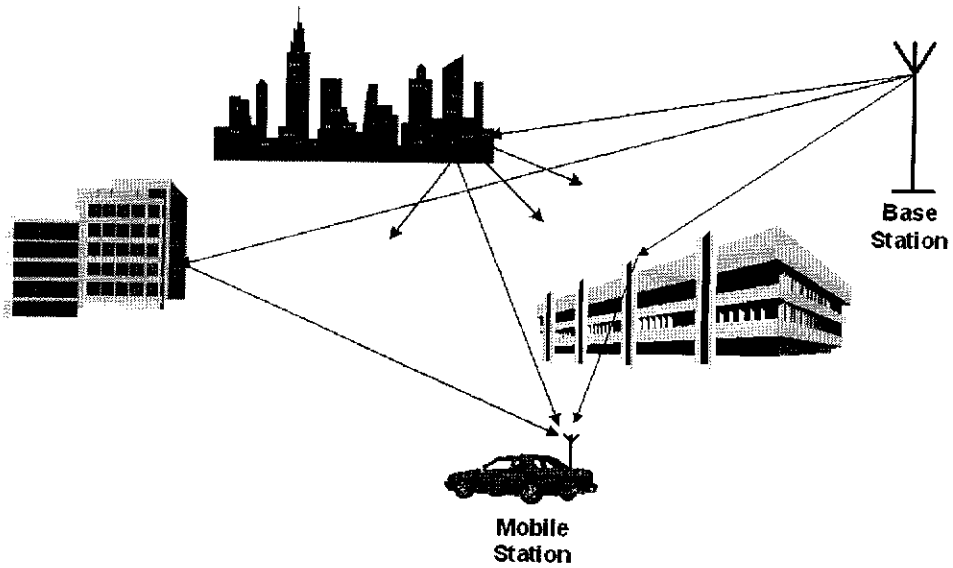

Figure 2. 1 The various propagation paths followed by a transmitted signal before arriving at a mobile station obstructed by buildings from a base station.

For example, the envelope variation of the received signal in the absence of a direct line-of-sight component has been shown to have a Rayleigh distribution (Jakes, 1974). The probability density function (pdf), $p(r)$, of the Rayleigh distributed envelope of amplitude r, having a variance σ_r^2 is given by

$$p(r) = \begin{cases} (r/\sigma_r^2)\exp(-r^2/2\sigma_r^2) & r \geq 0 \\ 0 & \text{otherwise}. \end{cases} \tag{2.1}$$

However, when a line-of-sight path is present, the received signal due to this direct path normally predominates over the indirect paths. In this case, the envelope of the received signal is found to follow the Rician distribution (Jakes, 1974). When the amplitude of the direct signal component is a, the pdf, $p(r)$, of the Rician distributed envelope of amplitude r of the received signal, is expressed as

$$p(r) = \begin{cases} (r/\sigma_r^2)\exp\left(-\dfrac{r^2+a^2}{2\sigma_r^2}\right) I_0\left(\dfrac{ar}{\sigma_r^2}\right) & r \geq 0 \\ 0 & \text{otherwise}. \end{cases} \tag{2.2a}$$

Here $I_0(.)$ is the modified zeroth order Bessel function which can be mathematically expressed as

$$I_0(z) = \sum_{i=0}^{\infty} \left(\frac{z^i}{i!2^i} \right). \tag{2.2b}$$

When a becomes zero in Eq. (2.2a), i.e., when no line-of-sight signal component is present, Eq. (2.2a) reduces to Eq. (2.1) representing the Rayleigh distribution.

It has been found that the received signal encountered in urban mobile radio communication tends to follow the Rayleigh distribution. However, in satellite mobile radio transmission, a line-of-sight component is likely to be present, so that the received signal envelope can be assumed to be Rician distributed. In both of these cases, the phases of the received signal components are normally assumed uniformly distributed from 0 to 2π.

2.3 Propagation Model of the Multipath Channel

A multipath fading channel can be modelled by considering the multipath effects on a transmitted signal $s_0(t)$ represented by

$$s_0(t) = \mathrm{Re}\left[u_0(t)\exp(j2\pi f_c t)\right], \tag{2.3}$$

where $u_0(t)$ is the complex envelope of the modulated signal and f_c is the carrier frequency. The received signal $r(t)$ arriving through N different propagation paths can be expressed as

$$r(t) = \sum_{n=1}^{N} c_n(t) s_0[t - \tau_n(t)], \tag{2.4}$$

where $c_n(t)$ is the attenuation factor for the signal received via the n^{th} path and $\tau_n(t)$ is the associated propagation delay. The channel parameters $c_n(t)$ and $\tau_n(t)$ are specified as time-dependent functions in order to indicate the time-varying nature of the channel. Substituting Eq. (2.3) in Eq. (2.4) yields

$$r(t) = \mathrm{Re}\left\{\left[\sum_{n=1}^{N} c_n(t)\exp[-j2\pi f_c \tau_n(t)] u_0(t-\tau_n(t))\right]\exp(j2\pi f_c t)\right\}. \tag{2.5}$$

Thus, the low-pass equivalent of the received signal $r(t)$ becomes

$$r_{LP}(t) = \sum_{n=1}^{N} c_n(t)\exp[-j2\pi f_c \tau_n(t)]\boldsymbol{u}_0(t-\tau_n(t)). \quad (2.6)$$

Now, if the transmitted signal $\boldsymbol{u}_0(t)$, is replaced by an impulse function $\delta(t)$, then the equivalent low-pass impulse response of the channel may be expressed as

$$\boldsymbol{h}(t) = \sum_{n=1}^{N} c_n(t)\exp[-j2\pi f_c \tau_n(t)]\delta(t-\tau_n(t)). \quad (2.7a)$$

Also, the received signal may be assumed to be a continuum of multipath components (Jakes, 1974). As a result, the continuous impulse response of the channel at time t, due to an impulse applied at time $(t-\tau)$, becomes

$$\boldsymbol{h}(t,\tau) = c(t)\exp(-j2\pi f_c \tau)\delta(t-\tau). \quad (2.7b)$$

2.3.1 Time spreading

Using the time-varying representation of the impulse response of the channel, $\boldsymbol{h}(t,\tau)$, a number of useful correlation functions and power spectral density functions can be developed to characterise a fading multipath channel. For the derivations of these functions, a wide-sense stationary uncorrelated scattering (WSSUS) model is assumed (Bello, 1963). Accordingly, the attenuations and phase shifts of the individual multipath components are uncorrelated.

The signal propagation through the multipath medium will cause time spreading of the transmitted signal due to the individual propagation delay associated with each path. The time spreading of the multipath channel may be investigated by considering the autocorrelation function, $\boldsymbol{R}_h(t_0,\tau_0,\tau_1)$, of the channel impulse response, $\boldsymbol{h}(t,\tau)$, at $t=t_0$, defined as (Bello, 1963)

$$\boldsymbol{R}_h(t_0,\tau_0,\tau_1) = \tfrac{1}{2} E[\boldsymbol{h}^*(t_0,\tau_0)\,\boldsymbol{h}(t_0,\tau_1)]. \quad (2.8)$$

Here, * denotes the complex conjugate. Now, assuming that the individual received signal components associated with paths having delays τ_0 and τ_1 are uncorrelated, Eq. (2.8) can be simplified to (Bello, 1963)

$$\boldsymbol{R}_h(t_0,\tau_0,\tau_1) = R_h(t_0,\tau_0)\,\delta(\tau_0-\tau_1). \quad (2.9)$$

Moreover, since the channel statistics are considered to be wide-sense stationary, the resulting autocorrelation function becomes independent of t_0 and τ_0. As a result, $R_h(t_0, \tau)$ may be re-written as $R_h(\tau)$. In this case, the autocorrelation function simply becomes the average power of the received signal at the output of the channel, as a function of the relative time delay τ. Accordingly, the autocorrelation function, $R_h(\tau)$, is called the multipath intensity profile or the delay power spectrum of the channel. The range of values of τ over which $R_h(\tau)$ is essentially nonzero (typically of a value 10-20 dB below the strongest component) is referred to as the multipath delay spread or the maximum excess delay of the channel.

2.3.2 Coherence bandwidth

Characterisation of the effect of multipath delay spread can also be carried out in the frequency domain. This is based on the time-varying Fourier transform, $\boldsymbol{H}(t,f)$, of the impulse response, $\boldsymbol{h}(t,\tau)$. In this case, the autocorrelation function, $\boldsymbol{R}_H(t_0, f_0, f_1)$, of the transfer function, $\boldsymbol{H}(t,f)$, at $t=t_0$, can be defined as (Bello, 1963)

$$\boldsymbol{R}_H(t_0, f_0, f_1) = \tfrac{1}{2}\, E\,[\boldsymbol{H}^*(t_0, f_0)\, \boldsymbol{H}(t_0, f_1)]. \tag{2.10}$$

Due to the assumption of the channel being WSSUS, the autocorrelation function, $\boldsymbol{R}_H(t_0, f_0, f_1)$ is dependent only on the frequency difference $\Delta f = f_1 - f_0$ rather than the individual frequencies f_0 and f_1. Furthermore, the autocorrelation function is independent of t_0. Consequently, $\boldsymbol{R}_H(t_0, f_0, f_1)$ may be written as $\boldsymbol{R}_H(\Delta f)$.

Since $\boldsymbol{R}_H(\Delta f)$ is an autocorrelation function expressed in the frequency domain, it provides a measure of the frequency coherence of the channel. Thus, when two sinusoids with frequency separation greater than Δf are transmitted through the channel, they may be affected differently by the channel. The maximum frequency separation for which the fading

characteristics of these sinusoids are strongly correlated (typically $|R_H(\Delta f)| > 0.5$), is called the coherence bandwidth, (Δf_c), of the channel (Proakis, 1989).

The effect of the frequency coherence on the frequency spectrum of a received signal is illustrated in Fig. 2.2. When the bandwidth W of the transmitted signal, is wider than the coherence bandwidth of the channel, (Δf_c), the channel is said to be frequency-selective. In this case, the spectrum of the received signal is affected in differing degrees across the signal bandwidth. On the other hand, if the coherence bandwidth of the channel is larger than the bandwidth of the transmitted signal, the channel is said to be frequency non-selective or flat for the transmitted signal. In such a channel, the spectrum of the received signal is affected more uniformly across its bandwidth as illustrated in Fig. 2.2.

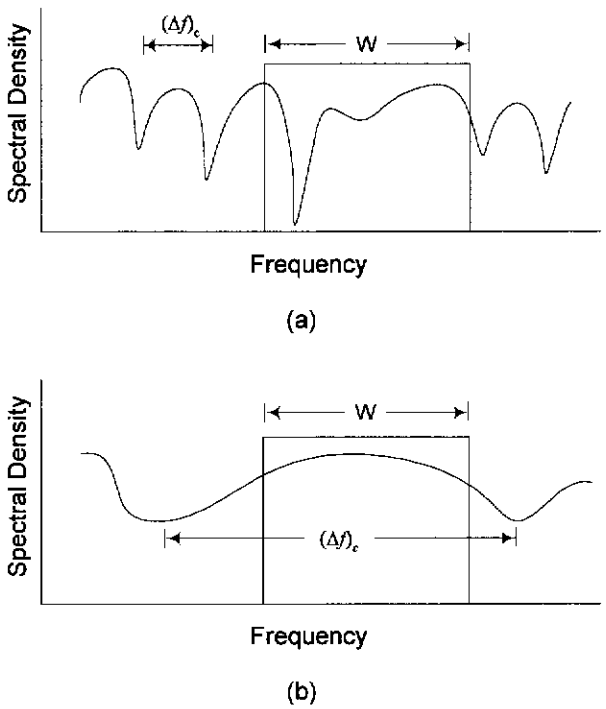

Figure 2.2 The examples showing (a) frequency-selective channel and (b) flat channel.

2.3.3 Coherence time

The influence of the time variations of the channel on the transmitted signal can be determined from the autocorrelation function of $H(t,f)$ in terms of the time variable t. In this case, the corresponding autocorrelation function, $R_H(t_0, t_1, f_0)$, of the transfer function, $H(t,f)$, at an arbitrary frequency $f=f_0$, is given by (Bello, 1963)

$$R_H(t_0, t_1, f_0) = \tfrac{1}{2} E\,[H^*(t_0, f_0)\, H(t_1, f_0)]. \tag{2.11}$$

Since the channel is WSSUS, the autocorrelation function, $R_H(t_0,t_1,f_0)$, depends only on the time difference $\Delta t=t_1-t_0$ rather than the individual times of t_0 and t_1. Furthermore, the autocorrelation function is independent of the choice of frequency f_0. Consequently, $R_H(t_0, t_1, f_0)$ may be expressed as $R_H(\Delta t)$, which is only a function of the time difference.

The time separation $(\Delta t)_c$ over which the autocorrelation function $R_H(\Delta t)$, is greater than 0.5 is referred to as the coherence time of the channel (Proakis, 1989). In this case, when an unmodulated carrier of a given frequency is transmitted through the channel, the fading characteristics of the received signal observed at time instants separated by more than the coherence time, are practically uncorrelated. In other words, if the symbol duration of the transmitted signal is larger than the coherence time, the channel characteristics can change significantly during a time interval of one symbol period. As a result, the received baseband pulse shape will be affected by the channel. Such a channel is usually referred to as a fast fading channel. Conversely, if the symbol interval is small in comparison to the coherence time, the channel characteristics can be expected to remain largely unchanged during the symbol interval. As a result, no significant changes in the received pulse shape are expected, and the channel is said to be a slow fading channel. Hence, the rate of channel variations increases with a decrease in the coherence time and vice versa.

2.3.4 The Doppler effect

When an unmodulated carrier of frequency f_0 is transmitted over a channel, the resultant power spectral density, $S_H(\upsilon)$, of the received signal can be given by the Fourier transform of the autocorrelation function of the received signal $R_H(\Delta t)$ as

$$S_H(\upsilon) = \int_{-\infty}^{\infty} R_H(\Delta t)\, e^{-j2\pi\upsilon\Delta t}\, d(\Delta t). \tag{2.12}$$

In Eq. (2.12), $\upsilon = f - f_0$ represents the frequency with respect to the carrier frequency f_0. If the channel is time-invariant, i.e., $R_H(\Delta t)=1$, it follows from Eq. (2.12) that $S_H(\upsilon)$ becomes equal to the delta function, $\delta(\upsilon)$, at $\upsilon=0$. Conversely, in the presence of channel time variations, i.e., $R_H(\Delta t)\neq 1$, $S_H(\upsilon)$ will have nonzero values for spectral components of $\upsilon\neq 0$. That is, the spectrum of the transmitted carrier spreads as a direct consequence of the changes in the channel. This effect is commonly referred to as the Doppler effect.

The range of values of υ over which $S_H(\upsilon)$ is essentially nonzero is called the Doppler spread of the channel. Often, the Doppler spread, f_D is also referred to as the fading rate of the channel, since it is directly proportional to the rate of change of the channel. In a mobile environment, where the channel time variations are determined by the relative speed, v, of the transmitter and receiver, f_D is given by (Jakes, 1974)

$$f_D = \frac{v}{c} f_0, \tag{2.13}$$

where, c denotes the speed of light in free-space, and f_0 is the carrier frequency. Since $S_H(\upsilon)$ is related to $R_H(\Delta t)$ by the Fourier transform, the reciprocal of Doppler spread is a measure of the coherence time of the channel. That is,

$$(\Delta t)_c \approx \frac{1}{f_D}. \tag{2.14}$$

Eq. (2.14) indicates that the coherence time of the channel decreases with an increase of the Doppler spread, which is a measure of the rate of variations of the channel.

2.4 Digital Modulation Schemes

Due to the limited spectrum available, it is desirable that any digital modulation technique employed in mobile radio transmission has a high bandwidth efficiency, i.e., the bit rate per channel bandwidth is high for a given power expenditure and at a specific bit error rate. Furthermore, due to the use of nonlinear (class C) power amplifiers to minimise battery drain in portable and mobile applications, the modulated signal must have a relatively constant envelope to prevent any regrowth of spectral sidelobes caused by the use of nonlinear amplifiers. The filtering of such sidelobes may lead to distortions in the demodulated signal.

A variety of digital modulation techniques are currently being used in mobile radio communication systems. Two of the most widely used modulation schemes for current digital mobile cellular and personal communication systems (PCS), are continuous phase modulation (CPM) and $\pi/4$ phase shifted quadrature phase shift keying ($\pi/4$-QPSK). The former is used in the Pan-European digital mobile cellular radio system known as Global System for Mobile communications (GSM) and the Digital Enhanced Cordless Telecommunications (DECT) standard (Gibson, 1996). The latter is used in the North American IS-54 digital cellular system, Japanese Personal Digital Cellular system (PDC), and Japanese Personal Handy Phone System (PHPS) (Gibson, 1996). As the present research focuses on the application of CPM with trellis coding, a detailed description of CPM is given in the following section.

2.4.1 CPM signals

Continuous Phase Modulation (CPM) can be viewed as both frequency modulation and phase modulation technique having a constant envelope (Anderson *et al,* 1986). The CPM signal can have a compact spectrum with good bit-error-rate performance, and this makes it attractive for applications in mobile radio communications. In CPM, the carrier phase varies in a continuous manner as a change in the input data symbol occurs. A comprehensive treatment of CPM is provided in (Anderson *et al,* 1986). The mathematical representation of a CPM signal has the form (Anderson *et al,* 1986)

$$s(t,\alpha) = \sqrt{2E/T}\ \cos\left(2\pi f_c t + \phi(t,\alpha) + \phi_0\right) \tag{2.15}$$

where E is the symbol energy of the signal, T is the symbol duration, and f_c is the carrier frequency. The arbitrary constant ϕ_0, represents the initial phase and can be set to zero with no loss of generality. The information carrying phase $\phi(t,\alpha)$ is given by

$$\phi(t,\alpha) = \pi h \sum_{i=-\infty}^{\infty} \alpha_i\, q(t - iT) \tag{2.16}$$

where

$$q(t) = \int_{-\infty}^{t} g(\tau)\, d\tau \tag{2.17}$$

and $\alpha_i = \pm 1, \pm 3, \pm 5, \ldots, \pm(M\text{-}1)$ for M-ary even data. For binary data, $\alpha_i = \pm 1$. The frequency pulse $g(t)$ in Eq. (2.17) determines the way the phase of the modulated signal changes in response to an input data symbol. Normally, $g(t)$ has a normalised area of unity and a smooth pulse shape with finite duration, i.e., $g(t) \neq 0$ for $0 \leq t \leq LT$, where L is the pulse length measured in symbol intervals. The rate of change of the phase or the instantaneous frequency is proportional to the parameter h, which is normally referred to as the modulation index, and is defined by

$$h = \frac{\text{peak - to - peak frequency deviation}}{\text{bit rate}}.$$

From Equations (2.16) and (2.17), it may be noted that a large class of CPM schemes can be realised by choosing different frequency pulses $g(t)$ and varying the parameters h and M. Now, if a frequency pulse $g(t)$ extends over

more than one symbol interval, the resulting signal is normally referred to as partial response CPM. On the other hand, if the duration of the frequency pulse is less than or equal to one symbol interval, it is referred to as full response CPM. In general, a narrower spectrum is obtained with partial response CPM compared to full response signals (Aulin *et al*, 1981).

Some of the more popular frequency pulse shapes, $g(t)$, and their corresponding phase responses, $q(t)$, for CPM schemes such as, Continuous Phase Frequency Shift Keying (CPFSK), duobinary FSK and 3RC (3 Raised cosine) are shown in Fig. 2.3. The CPFSK and duobinary FSK signals are generated using rectangular pulses of durations T and $2T$, respectively, whereas 3RC is generated using a raised cosine pulse of length $3T$.

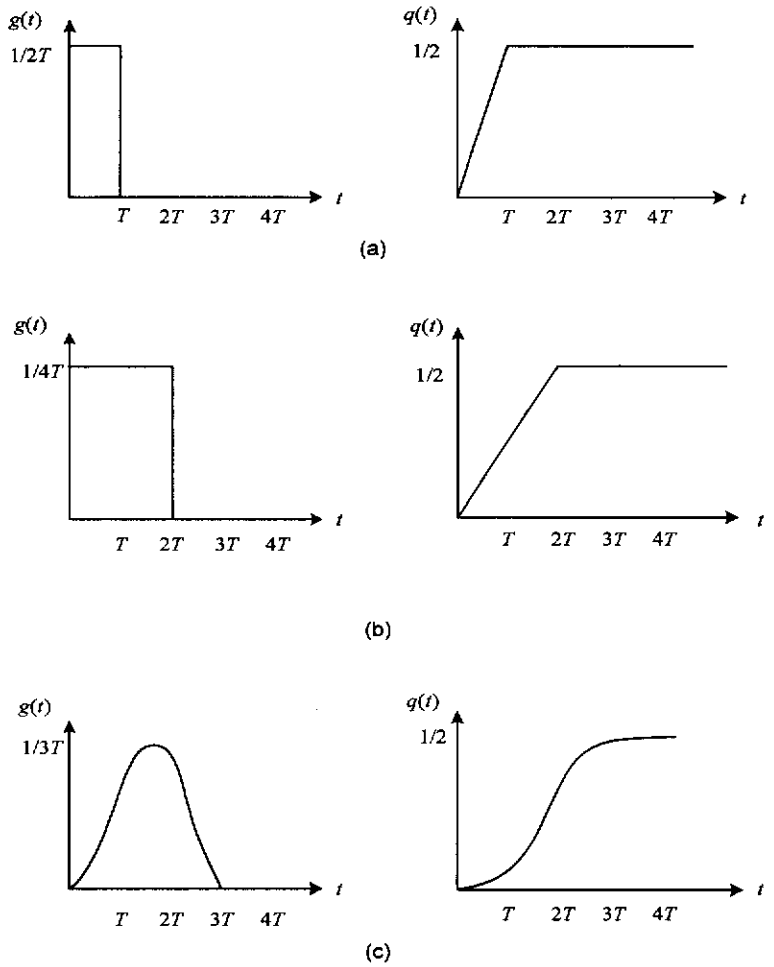

Figure 2.3 Pulse shapes $g(t)$ and the corresponding phase responses $q(t)$ for (a) CPFSK (b) duobinary FSK and (c) 3RC, CPM schemes (after Sundberg, 1986).

Other partial response CPM schemes of particular interest for mobile radio communications are GMSK (Murota and Hirade, 1981) and GTFM (Chung, 1984). For example, GMSK with a Gaussian pre-modulation filter having a normalised bandwidth of B_oT=0.3 is the modulation scheme adopted in the GSM system (Gibson, 1996).

2.4.1.1 GMSK modulation

GMSK is a modified form of Minimum Shift Keying (MSK), and is a special case of binary CPFSK in which the modulation index is set at 0.5. In this case, the 1REC (1 rectangular) premodulation pulse used in the conventional MSK is replaced by a Gaussian pulse with a smoother pulse shape. It has been shown that GMSK can achieve a narrower spectrum than the MSK (Murota and Hirade, 1981).

With GMSK, the impulse response of the Gaussian premodulation filter is given by

$$g(t) = A\sqrt{\frac{2\pi}{\ln 2}}\ B_0 \exp\left\{\frac{-2\pi^2 B_0^2 t^2}{\ln 2}\right\} \tag{2.18}$$

where B_0 is the -3-dB bandwidth and A is a constant. By varying the -3-dB bandwidth of the Gaussian premodulation filter, a set of different GMSK signals each having different power spectra can be obtained. The power spectra of the GMSK signals plotted against the normalised frequency difference from the carrier frequency f_c, with the variation of the normalised -3-dB bandwidth of the Gaussian premodulation filter are shown in Fig. 2.4 (Murota and Hirade, 1981). It may be seen from Fig. 2.4, that when B_oT of the GMSK signal tends to infinity, the power spectrum of GMSK coincides with that of MSK.

The spectral occupancy of a signal may be expressed by its bandwidth which is defined as the frequency band around the carrier frequency containing 99% of the total signal power (Pasupathy, 1979; Sundberg, 1986). Table 2.1 presents the approximate bandwidths containing 99% of total

power of GMSK schemes with several values of B_oT. It may be observed from Fig. 2.4 and Table 2.1, that the spectral occupancy of the GMSK signal is mainly controlled by the parameter B_oT. Therefore, for a given mobile application, this parameter must be carefully selected, so that out of band radiation requirements are met. For example, GMSK modulation with B_oT=0.3 is adopted in the GSM system, whereas GMSK having B_oT=0.5 is used in the DECT system (Gibson, 1996).

When B_oT=0.3, the GMSK pulse is extended just over 3 bit periods as shown in Fig. 2.5. In this case, the phase change of GMSK (B_0T=0.3) during the m^{th} bit period depends mainly on the three consecutive bits at t=$(m$-1$)T$, mT and $(m$+1$)T$ giving rise to a considerable amount of controlled ISI in the transmitted signal. The effect of ISI on the phase of the GMSK signal may also be observed from the eye diagrams corresponding to $\sin[\phi(t)]$ and $\cos[\phi(t)]$, as shown in Fig. 2.6.

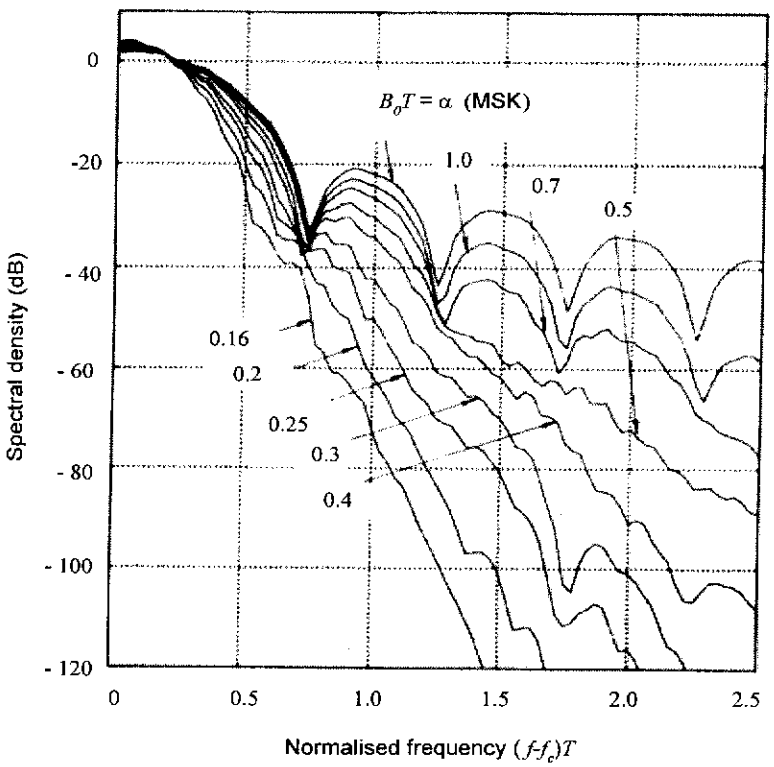

Figure 2.4 Power spectra of GMSK signals (After Murota and Hirade, 1981).

Modulation Type	Bandwidth containing 99% of power
GMSK (B_0T=0.2)	$0.79/T$
GMSK (B_0T=0.25)	$0.86/T$
GMSK (B_0T=0.30)	$0.90/T$
GMSK (B_0T=0.50)	$1.04/T$
GMSK (B_0T=∞) (MSK)	$1.20/T$

Table 2.1 Occupied bandwidth of GMSK schemes having various values of B_0T (After Murota and Hirade, 1981).

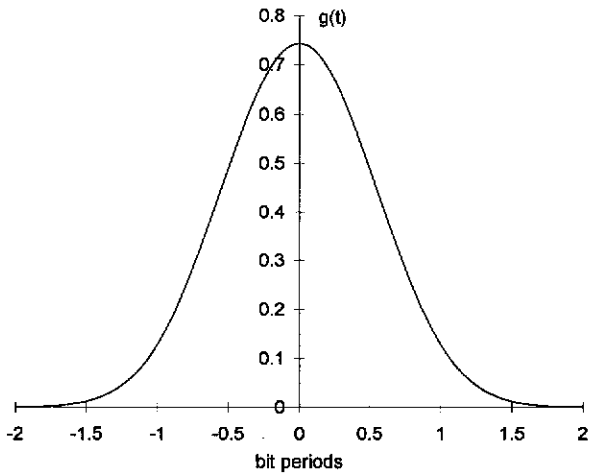

Figure 2.5 Frequency pulse shape of the GMSK signal when the normalised -3-dB bandwidth of the premodulation Gaussian filter B_0T= 0.3.

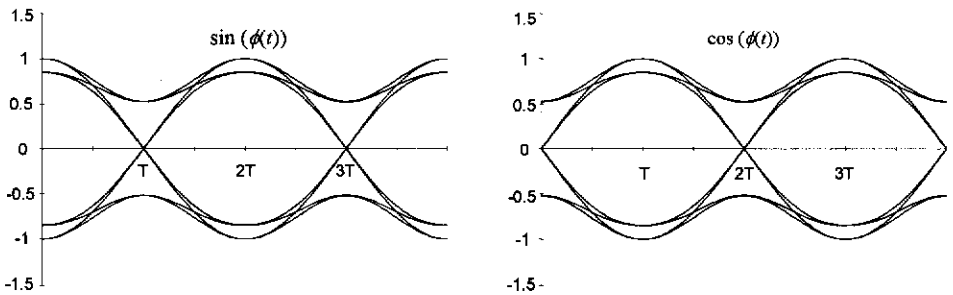

Figure 2.6 The eye-diagrams corresponding to $\sin[\phi(t)]$ and $\cos[\phi(t)]$ of the GMSK (B_0T=0.3) signal.

2.4.1.2 GTFM modulation

Generalised Tamed Frequency Modulation (GTFM) is another class of spectrally efficient constant envelope partial response CPM schemes. In GTFM, the incoming binary data is processed in a specific pre-modulation filter, which consists of a 3-tap transversal filter followed by a Nyquist-3 low pass filter, as shown in Fig. 2.7. The Nyquist-3 filter in conjunction with the frequency modulator serves to ensure that the phase, $\phi(t)$, after a smooth transition, settles at one of the prescribed values at the end of a bit period. The 3-tap transversal filter introduces correlative encoding, influencing input data over three bit periods for the phase function $\phi(t,\alpha)$ (Chung, 1984).

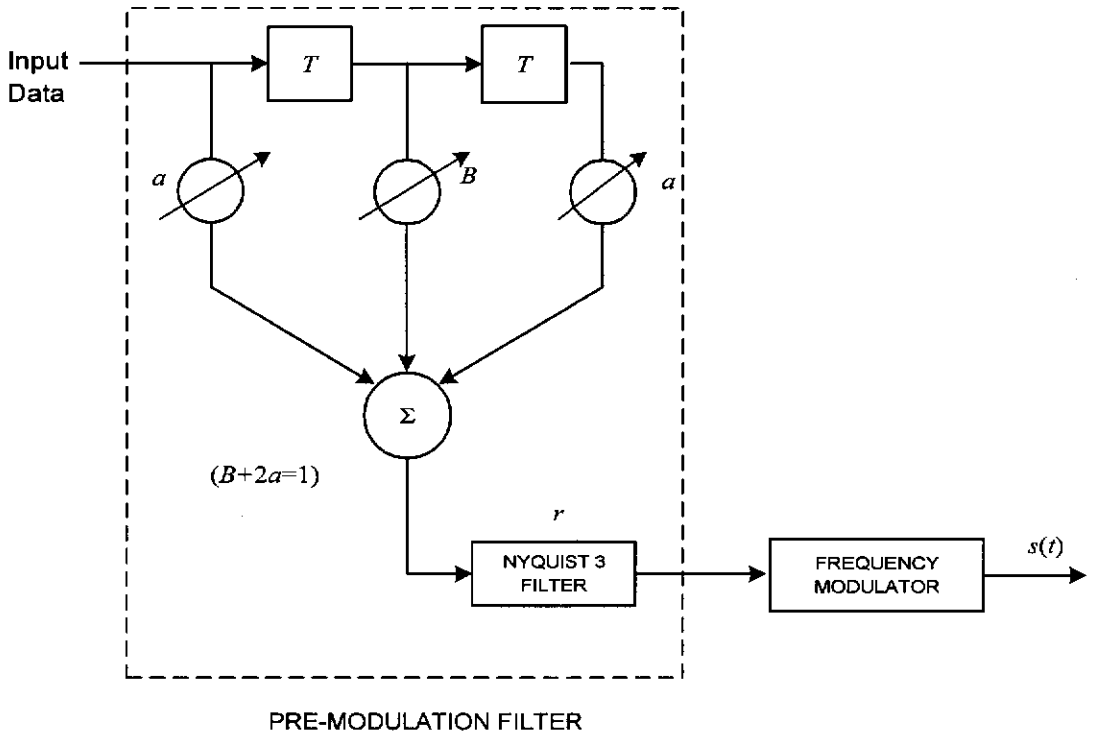

Figure 2.7 Schematic diagram of a GTFM modulator.

With this pre-modulation filter, the allowable phase shifts of the modulated carrier during the m^{th} bit period can be expressed as

$$\Delta\phi(mT) = \pi/2\,(ab_{m-1} + Bb_m + ab_{m+1}) \qquad (2.19)$$

where, b_{m-1}, b_m, and b_{m+1} represent the binary data at time $t = (m\text{-}1)T$, mT and $(m+1)T$, respectively and T represents the bit period. The binary data b_m are either +1 or -1. The constants a and B satisfy the condition $(2a+B)=1$, so that the maximum change in phase over one bit period is restricted to $\pm\pi/2$

radians. Fig. 2.8 shows the eight possible phase transitions over one bit period for a GTFM signal. By varying the tap coefficients, a and B, of the transversal filter and the roll-off factor, r, of the Nyquist-3 filter, a whole class of signals, each with a given set of allowable phase shifts, can be obtained.

When B=0.5 and r=0.00, a special case of GTFM, called Tamed Frequency Modulation (TFM), is obtained. For TFM,

$$\Delta\phi(mT) = \pi/2\ (1/4\ b_{m-1} + 1/2\ b_m + 1/4\ b_{m+1}). \tag{2.20}$$

Here, the phase changes of $\pi/2$ radians are obtained if the three successive bits have the same polarity, whereas the phase remains constant for three bits of alternating polarity. Phase changes of $\pm\pi/4$ are related with the bit configurations $+++$, $+--$, $--+$, and $---$. Consequently, $\Delta\phi(m) \in \{0, \pm\pi/4, \pm\pi/2\}$, where, $\Delta\phi(m) = \Delta\phi(mT)$ modulo - 2π to remove ambiguity.

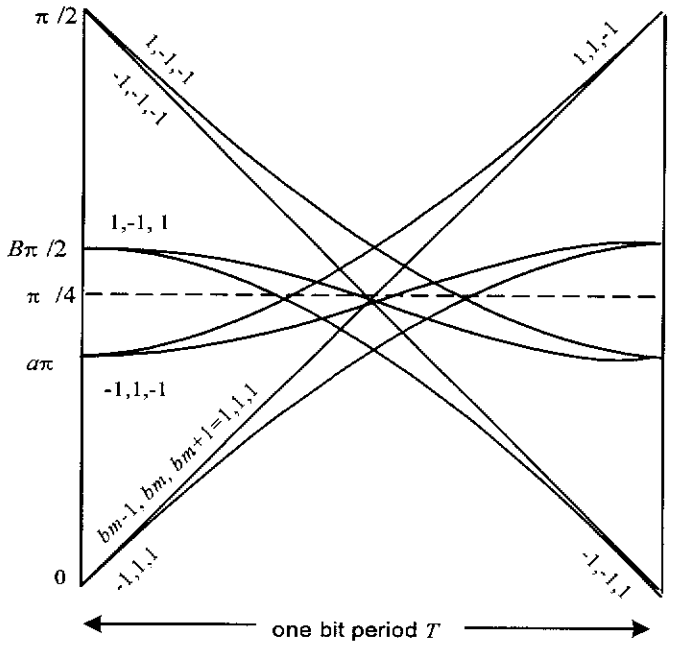

Figure 2.8 Possible phase transitions of a GTFM signal within a bit period.

Eq. (2.19) may be used to determine the values of $\Delta\phi(mT)$ for GMSK (B_0T=0.3) which are required for the decoding process.

2.5 Error Control Coding in Mobile Radio

Multipath fading, which could give rise to large signal level variations, or intersymbol interference, or both, often introduces degradation in the BER performance of a mobile radio link. In practice, this BER degradation may be compensated through diversity and/or error control techniques (Jakes,1974; Ventura-Travest *et al*, 1997; Diaz *et al*, 1998). A detailed explanation of common diversity methods can be found in (Shwartz *et al*, 1974; Jakes, 1974; Proakis, 1989).

Error control schemes that are commonly used in digital communication systems are automatic repeat request (ARQ) and forward error correction (FEC). With ARQ, if an error is detected at the receiving end, then retransmission of the same data is requested over the return channel. However, if a return channel is not available, then FEC is the only error control scheme that can be used. In general, if a return channel is available and the bit error rate needed is not particularly low, then a simpler ARQ scheme may be preferred over a more complicated FEC scheme (Sklar, 1988). With FEC techniques, redundant bits are added to the transmitted data. At the receiver, these redundant bits are then used for detecting and correcting the erroneous bits. The addition of redundant bits however increases the actual transmission rate, leading to a larger bandwidth requirement.

FEC codes are often divided into two broad categories, namely, block codes and convolutional codes. In block codes, blocks of k information bits are encoded into blocks of n bits with $n > k$. Such a code is usually described as an (n,k) block code. The code rate R_c is defined as the ratio k/n, and is a measure of the amount of redundancy introduced by the encoder. Several common types of block codes for error correction are Hamming, Golay, Reed-Muller, Bose Ray-Chaudhuri and Hocquenghem (BCH) and Reed-Solomon (Clark and Cain, 1981).

Convolutional codes are also often known as trellis codes. They are particularly suitable in applications where the information symbols to be transmitted arrive serially in long sequences rather than in blocks. That is, in convolutional codes, long sequences of information symbols are encoded continuously in a serial form. Convolutional encoding is usually denoted by (n,k,ν) and implemented using shift registers as shown in Fig. 2.9. Here, k input bits to the encoder, are sequentially shifted through a ν- stage shift register yielding n output bits, with $n > k$. Consequently, the code rate is defined as $R_c = k/n$, as in block codes. Note that the same code (n,k,ν) may be generated using encoders of different structures. The length of the shift register in the encoder is usually referred to as the constraint length of the code.

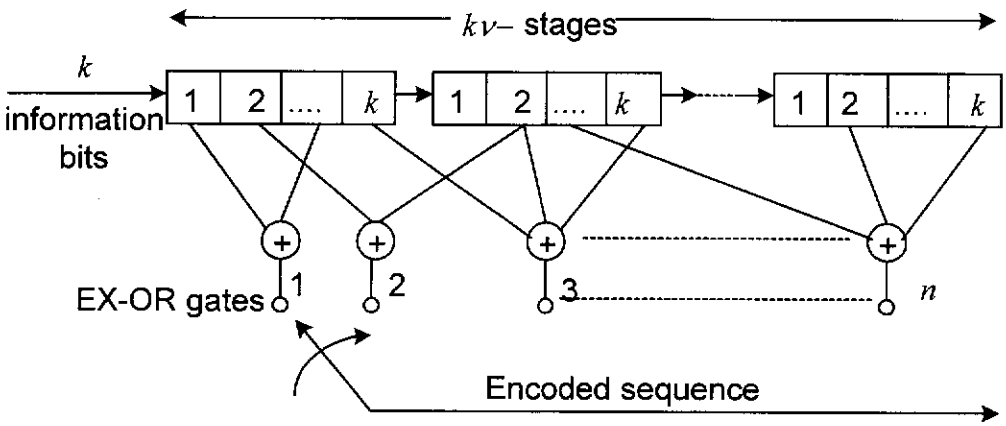

Figure 2.9 The (n,k,ν) convolutional encoder

We now consider an example of a $(2,1,3)$ convolutional encoder, as shown in Fig. 2.10. Here the length of the shift register is 3. The message digits are applied serially at the input of the shift register. With this convolutional encoder, there are two output bits, c_1 and c_2 for every input bit. These two encoder outputs c_1 and c_2 are formed by modulo-2 additions of the shift register outputs, such that, $c_1 = D_1 \oplus D_2 \oplus D_3$ and $c_2 = D_1 \oplus D_3$, where operator $\oplus$ denotes the modulo-2 addition.

Often, a convolutional code is described by a row vector called the connection vector,

$$G_j = (g_{j1}, g_{j2}, \ldots, g_{j\nu}), \qquad j=1,2,\ldots,n. \tag{2.21}$$

This connection vector, G_j, specifies the connection between the j^{th} modulo-2 adder and each stage of the shift register. The component g_{ji} is equal to 1 if the j^{th} modulo-2 adder is connected to stage i of the shift register; otherwise it is equal to zero. Therefore, the encoder shown in Fig. 2.10, has the connection vectors G_1 = [1 1 1] and G_2 = [1 0 1]. These connection vectors can also be represented by the generator polynomials $[1+D+D^2, 1+D^2]$ or in octal form as [7,5].

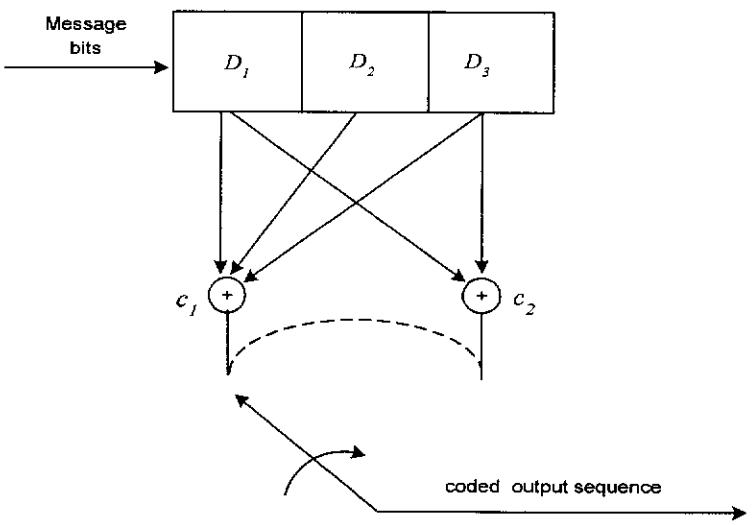

Figure 2.10 A (2,1,3) convolutional encoder.

The coding operation of the convolutional encoder, shown in Fig. 2.10, may be explained with reference to an input digit pattern ***11010***. Initially, the shift registers have been initialised to zero, so that their outputs are all in the ***0*** state. When the first input data bit ***1*** is entered into D_1, with the other two later stages D_2 and D_3 remaining in the ***0*** state, the two modulo-2 adders show the two output bits as c_1=***1*** and c_2=***1***. Next, with the second message bit ***1*** entering the shift register stage D_1, the previous data bit ***1*** in D_1 is now shifted to D_2 while D_3 is still unchanged and in the ***0*** state. In this case, the modulo-2 adder outputs become c_1=***0*** and c_2=***1***, so that the decoder output is ***01***. This process repeats for every input data bit, and as such, the convolutional encoder operates on a continuous basis.

The trellis diagram of the (2,1,3) convolutional encoder of Fig. 2.10 is shown in Fig. 2.11. The states of the trellis diagram are represented by the contents of the shift registers D_3 and D_2. The trellis starts when all the shift registers are in state *0*. The transitions corresponding to each bit of input data are denoted by a solid line if the input is *0*, and by a dotted line for an input *1*. Thus, when the input data is *0* the encoder output is *00* (the solid line), and when the input digit is *1*, the encoder output is *11* (the dotted line). The encoder will then be in one of the two states corresponding to nodes *a* or *b*. Similarly, after the first two input digits, the encoder will be in one of the four states corresponding to nodes *a*, *b*, *c* or *d* as shown in Fig. 2.11. It can be seen from this trellis diagram that the structure is repetitive after two input digits.

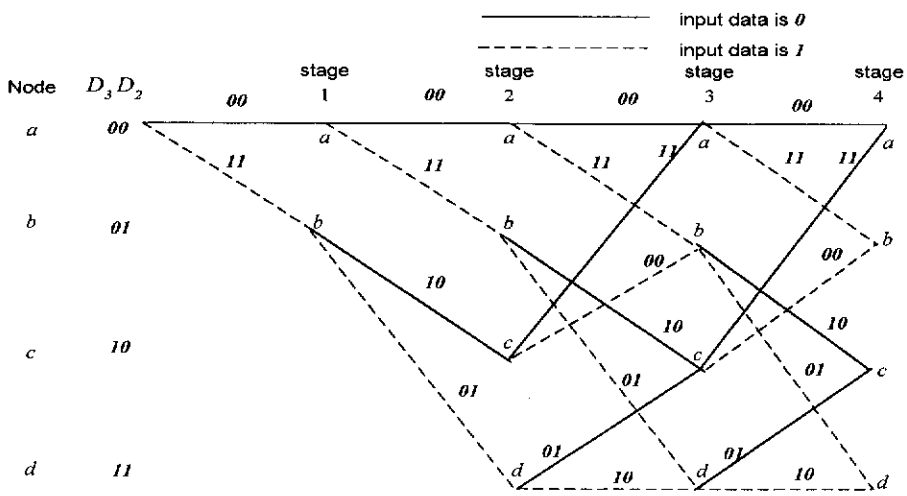

Figure 2.11 Trellis diagram of the (2,1,3) convolutional code.

There are a number of schemes for decoding convolutional codes, such as the sequential decoding algorithm originally proposed by Wozencraft (Wozencraft, 1957) and subsequently modified by Fano (Fano, 1963), and the syndrome decoding and threshold decoding (Clark and Cain, 1981). However, the most widely used algorithm for decoding convolutional codes is the maximum likelihood sequence decoding (MLSD) based on the Viterbi algorithm (Viterbi, 1967).

2.6 Maximum Likelihood Sequence Decoding (MLSD)

Assume that a codeword $X^{(m)}$ is transmitted corresponding to a message m which entered the encoder, and on the basis of the corresponding received sequence Y, the decoder produces a decoded message m'. If all the input data sequences are equally likely, then the probability of erroneously decoding the sequence is minimised for (Proakis, 1989)

$$P(Y|X^{(m')}) \geq P(Y|X^{(m)}) \qquad \text{for all } m \neq m'. \tag{2.22}$$

Here, the conditional probabilities $P(Y|X^{(.)})$, are called the likelihood functions. Accordingly, the maximum likelihood decoder compares the likelihood functions corresponding to each possible transmitted data sequence and chooses the sequence corresponding to the largest value of these likelihood functions as the most likely transmitted sequence. It can be shown that the maximisation of the likelihood function in the presence of AWGN is equivalent to minimising the signal space distance between the transmitted data sequences (Haykin, 1988). Hence, the MLSD simply selects a codeword closest in distance in the signal space to the received word. For an L-bit long binary data sequence, the maximum likelihood decision requires the storage of the 2^L possible transmitted codewords and the computation of the likelihood functions associated with these 2^L sequences. As a result, the complexity of MLSD increases exponentially with the length L of the transmitted sequence. However, both the computational and storage requirements of MLSD can be significantly reduced through the use of the Viterbi algorithm (Viterbi, 1967).

2.6.1 Viterbi decoding algorithm

The Viterbi algorithm is an efficient and practical technique for decoding convolutional codes. This algorithm makes use of the trellis structure of the code. A brief description of it will be presented here. For a more detailed treatment of the Viterbi algorithm, consult (Wozencraft and Jacobs, 1965; Viterbi and Omura, 1979).

The Viterbi algorithm operates by computing and comparing the distances in the signal space between the received word and all the possible transmitted codewords. For example, the signal space distance between two transmitted codewords v_i and v_j represented by the signals $s_i(t)$ and $s_j(t)$ respectively, over an interval $0 \leq t \leq nT$ can be computed based on the squared Euclidean distance defined as (Anderson *et al*, 1986)

$$d^2_n(i,j) = \int_0^{nT} (s_i(t) - s_j(t))^2 \, dt. \tag{2.23}$$

Alternatively, for some signal sets, the signal space distance between two codewords can also be obtained based on the Hamming distance, which is defined as the number of locations in which the bits in the two codewords differ. For example, if codeword 1 is a vector denoted by v_1=(*1 1 0 1 0 1*) and codeword 2 is a vector denoted by v_2=(*1 1 1 0 0 0*), then the Hamming distance between the two codewords v_1 and v_2 is found by the operation $\| v_1 \oplus v_2 \|$ to be equal to 3.

The operation of the Viterbi algorithm can be explained using the trellis of the (2,1,3) convolutional code shown in Fig. 2.11. Note that starting from node *a* at the initial stage, there are two branches, *00* and *11*, leading to node *a* and node *b*, respectively. The signal space distances between the received signal up to stage 1 and the possible transmitted signals represented by these two branches, are first obtained. These metrics, defined as the branch metrics, may be based on either the Euclidean distance or for some signal sets the Hamming distance. The above two branches are then extended to four branches leading to nodes *a*, *b*, *c* and *d*, respectively at stage 2. Next, the branch metrics, corresponding to the signal space distances between the received signal from stage 1 to stage 2, and each of these 4 branches originating from *a* and *b*, are obtained. The path metric at each node at stage 2 is then obtained by adding up the corresponding branch metrics. It may be observed from Fig. 2.11, that after stage 2 of the binary trellis, two paths will lead to a given node at every stage. For example, the two paths corresponding to the branches labelled by *00-00-11* and *11-10-00* initiated from node *a*, merge at node *b* after three transitions. Note that any particular

path through the trellis that stems from node *b* will add identical terms to the path metrics $d^{(0)}$ and $d^{(1)}$ of these two paths. Consequently, if $d^{(0)}>d^{(1)}$ at the merged node *b* after the three transitions, the metric of the path having $d^{(0)}$ will continue to be larger than the metric of the path having $d^{(1)}$ for any path that stems from node *b* at stage 3. This means that the path corresponding to $d^{(0)}$ can be discarded from further consideration. With the Viterbi decoding algorithm, the path metrics corresponding to the two paths leading to each node are obtained. Then the path at each node having the smallest path metric (known as the survivor) is retained as the most likely path. This procedure is repeated for all the nodes at each trellis stage. As a result, there will be four surviving paths at each stage, one terminating at each node, and a corresponding metric for each survivor. These surviving paths at each stage are always the surviving paths at their preceding stages. Therefore, as the decoding progresses through the trellis, a unique surviving path may exist at the initial stages of the trellis. This unique surviving path at the initial stages may be accepted as the decoded path. The corresponding decoded bits may be delivered to the user without waiting for the last trellis level to be reached. With this, the decoding delay associated with the Viterbi decoding of a long sequence may be reduced.

As explained in the above example, it may be observed that with a binary convolutional code having a constraint length of ν, there are $2^{\nu-1}$ surviving paths at each stage of the trellis diagram and there are $2^{\nu-1}$ corresponding metrics, one for each surviving path. Consequently, the complexity of a Viterbi decoder grows exponentially with the constraint length of the code. As a result, the use of the Viterbi algorithm is limited to codes with relatively small values of ν (Bhargava *et al*, 1981). However, with the Viterbi algorithm, the total number of operations required to decode an L-bit long binary sequence becomes $L2^{\nu-1}$ compared to 2^L with MLSD as discussed in Section 2.6. Therefore, for sequences with $L>\nu$, the total number of operations required by the Viterbi algorithm to decode a sequence becomes far smaller than the total number of operations that would otherwise be required for other MLSD algorithms.

2.7 Trellis Coded Modulation

The desired BER performance of a communication scheme, which is constrained by its transmit power level, may be obtained by incorporating error control techniques. This is achieved at the expense of a larger transmission bandwidth to accommodate redundancy of the error control coding. On the other hand, in a bandwidth limited environment, a spectrally more efficient scheme such as a higher order modulation scheme may be used to reduce the bandwidth requirement. However, such modulation schemes have smaller noise margins. These seemingly contradictory requirements of spectral and power efficiencies, may be accommodated in an approach called Trellis Coded Modulation (TCM), which combines coding and modulation together. TCM was originally developed for AWGN channels (Ungerboeck, 1982). It was shown by Ungerboeck (Ungerboeck, 1982) that the BER performance of a digital transmission scheme could be improved without an increase in power and bandwidth through the use of TCM.

In a TCM receiver, the demodulation and decoding are performed as a single process. Usually, the performance measures of these schemes are based on the Euclidean distance between the coded signal sequences in signal space, rather than the Hamming distance of the convolutional code. That is, the selection of the code and of the signal constellation are not separately performed. One way to enhance the error performance of these schemes is to design the trellis encoder so as to achieve the largest free distance. The free distance is the minimum non-zero Euclidean distance between the coded signals (Biglieri *et al*, 1991).

There are two broad classes of TCM schemes for band-limited channels. The first type combines convolutional coding with multi-level signalling. As this type of TCM was first proposed by Ungerboeck (1982), they are often referred to as Ungerboeck codes. The second type involves the use of convolutional coding with CPM signals.

2.7.1 Ungerboeck codes

With the Ungerboeck codes, the TCM encoder consists of a convolutional encoder and a signal mapper. The signal constellation of an Ungerboeck code contains more signal phase states than are required for an uncoded scheme with the same data rate. The key to improving the BER performance of these TCM schemes is to map the coded bits to corresponding phase states in the signal space, such that the free Euclidean distance between the different coded signal sequences is maximised. Ungerboeck invented a heuristic mapping rule called "mapping by set partitioning" for maximising the free distance of these TCM schemes. This approach involves partitioning of a signal set successively into subsets, with increasing free distances between the signal phase states of these subsets. Moreover, each of these subsets usually contains equally spaced signal points. In the following sections, the distances will be referred to as the Euclidean distances in the signal space. The concept of set-partitioning is illustrated in Fig. 2.12 for a circular constellation corresponding to the 8-PSK signal set. Such a mapping approach is also applicable to QPSK and QAM. In Fig. 2.12, the free distance, d_0, of the signal phase states of the subset **A** becomes $2\sin(\pi/8)=0.7654$. Similarly, the corresponding free distances d_1 and d_2 of the subsets **B** and **C** become 1.4142 and 2, respectively. Each of the eight phase states of the 8-PSK signal set in Fig. 2.12 is numbered for convenience in assigning them to the trellis diagram at a later stage.

A general structure of an encoder/modulator for TCM, demonstrating the idea of set partitioning, is shown in Fig. 2.13 (Ungerboeck ,1982). Here, out of the n input bits, n' bits are coded by a rate $(n'/(n'+1))$ binary convolutional encoder, producing $(n'+1)$ coded bits. These bits are then used to select one of the $2^{(n'+1)}$ subsets. The remaining $(n-n')$ uncoded bits determine which one of the $2^{(n-n')}$ signal phase states in the particular subset is to be transmitted. The distance properties of a TCM scheme can be studied using its trellis diagram as explained in the following example.

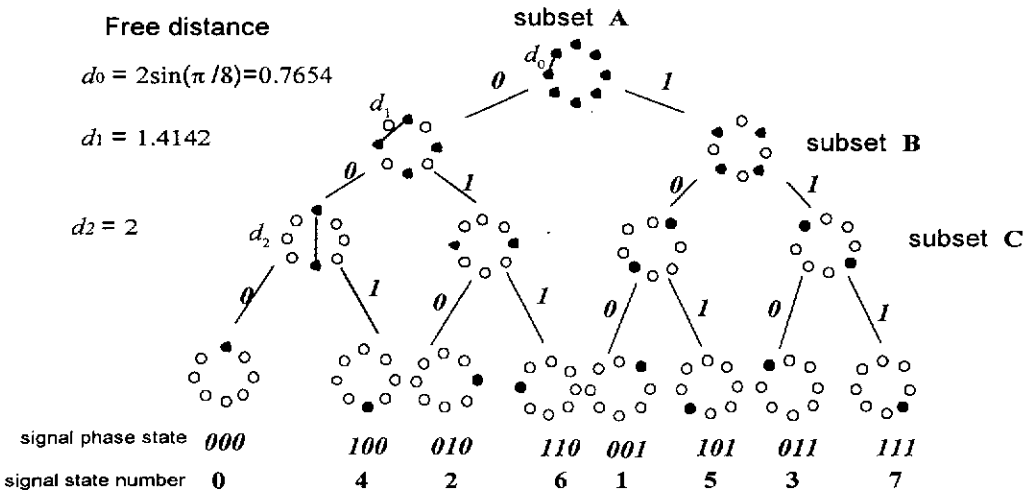

Figure 2.12 Set-partitioning of the 8-PSK constellation. Here the free distance of each subsequent subset has a larger free distance. i.e., $d_0 < d_1 < d_2$

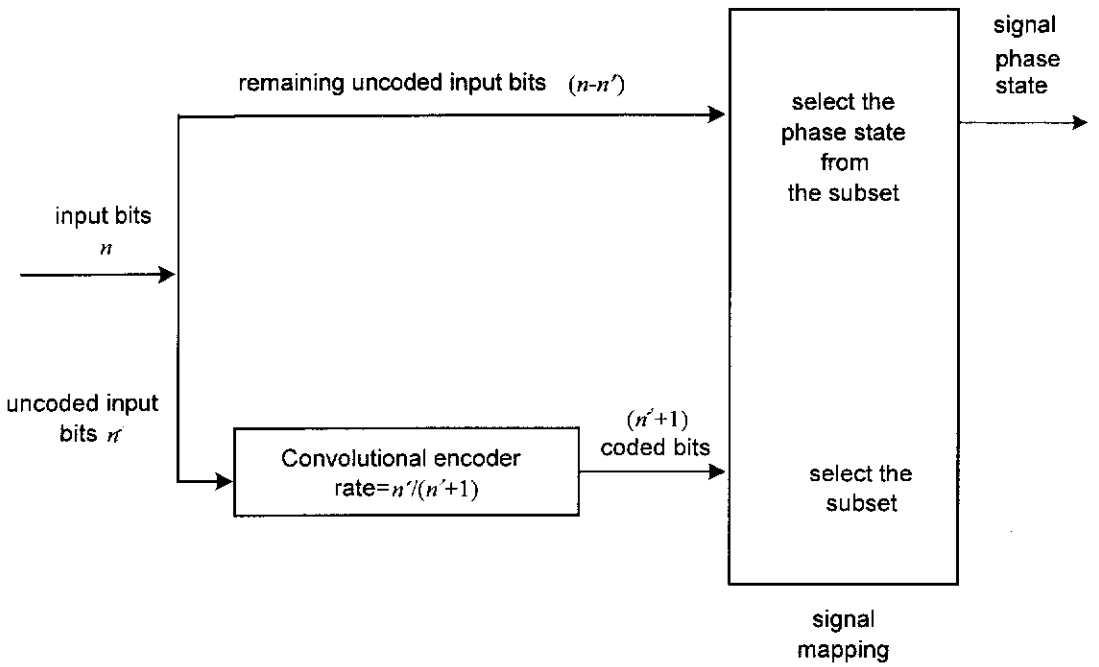

Figure 2.13 A general structure of the encoder/modulator of TCM (After Ungerboeck ,1982).

Consider the Ungerboeck code as shown in Fig. 2.14. Here one of the two input bits is encoded using a rate-½ convolutional encoder having constraint length 3. i.e., in this example, n=2 and n'=1. The corresponding trellis diagram of the convolutional encoder is represented in Fig. 2.15. In the trellis diagram, each transition A/YZ represents the two coded bits YZ corresponding to the input bit A. The number of states in the Ungerboeck code is determined by the constraint length ν, of the convolutional code.

Therefore, the Ungerboeck code shown in Fig. 2.14 can be represented by $2^{\nu-1}=4$ states. The two coded bits in this example select one out of the $2^{(n'+1)}=4$ subsets and the uncoded bit selects which one of the $2^{(n-n')}=2$ signal phase states of the selected subset is to be transmitted. Since the most significant bit of the incoming binary data to the modulator is left uncoded, each branch of the trellis of the convolutional code shown in Fig. 2.15 corresponds to two different signal phase states in the 8-PSK modulator. This leads to parallel transitions, which take place when two or more branches are connected to the same nodes of the trellis. The corresponding trellis diagram of the 4-state Ungerboeck code for 8-PSK is shown in Fig. 2.16.

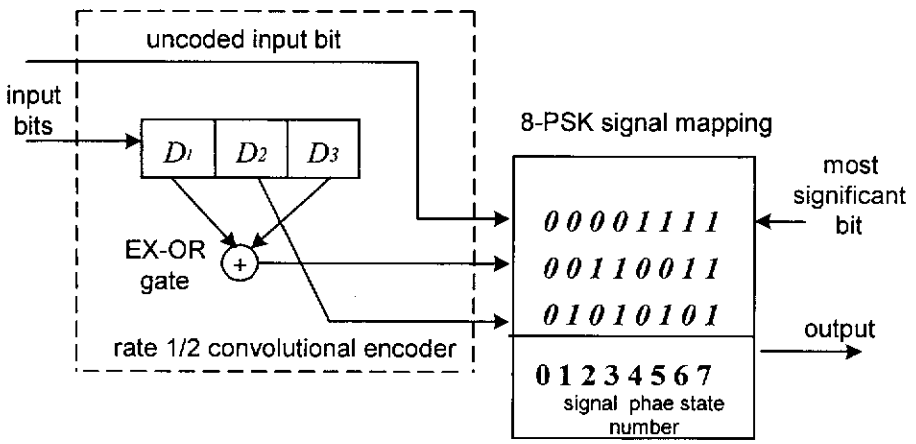

Figure 2.14 Four-state Ungerboeck code for 8-PSK.

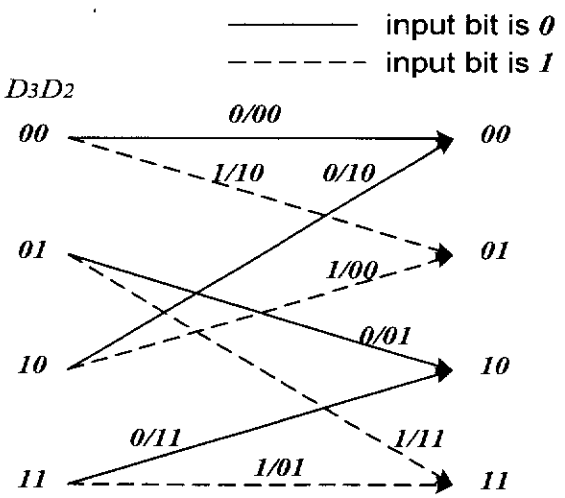

Figure 2.15 Trellis diagram of the rate-½ convolutional code used in the Ungerboeck code in Fig. 2.14.

The numbering of the 8-PSK signal phase states used in this example is the same as that shown in Fig. 2.12. Similarly, the free distances d_0, d_1 and d_2 between these signal phase states are shown in Fig. 2.12. For this example, the phase states of the 8-PSK signal set are assigned to the 4-state trellis shown in Fig. 2.16 according to the following rules (Ungerboeck, 1987):

- parallel transitions are associated with signal phase states having maximum distance, which is d_2 in this example, between them. Therefore, signal phase states corresponding to the subsets (**0**,**4**), (**2**,**6**), (**1**,**5**) or (**3**,**7**) are associated with parallel transitions.
- transitions originating from, or joining in, the same phase state are associated with the signal phase states having at least distance d_1 (the next largest distance) between them. This includes the phase states in the subsets (**0**,**4**,**2**,**6**) or (**1**,**3**,**5**,**7**).
- all the phase states of the 8-PSK signal are used in the trellis diagram with equal frequency and symmetry.

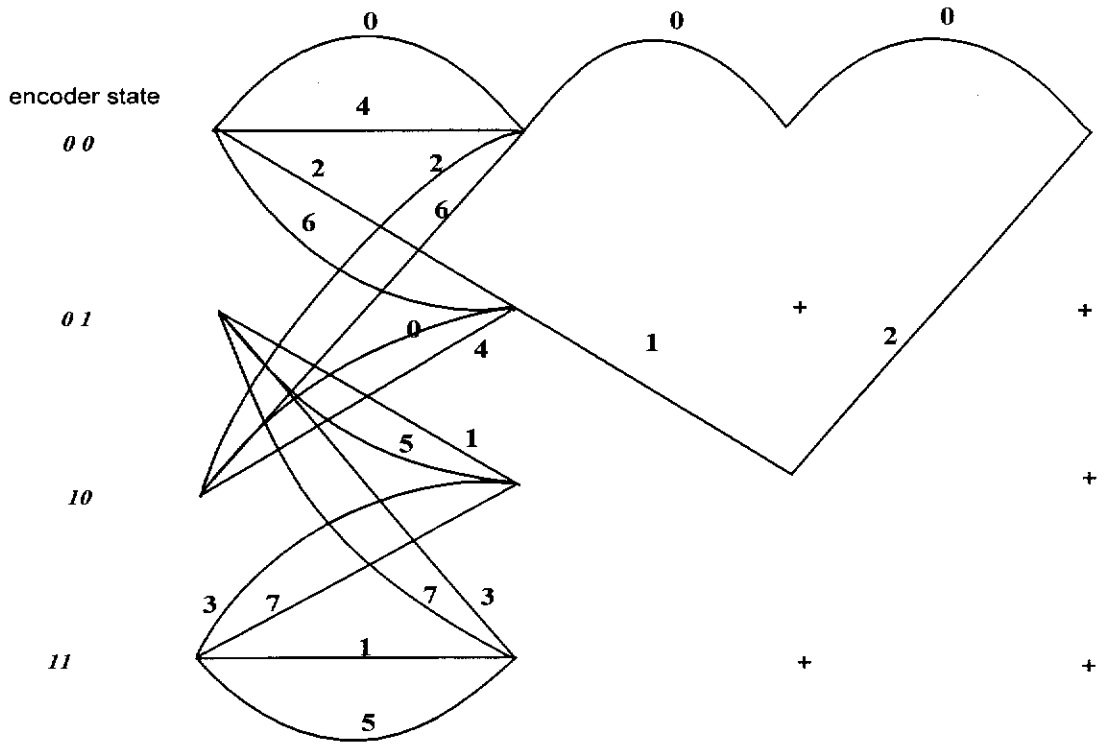

Figure 2.16 Trellis of the Ungerboeck code for 4-state 8-PSK signal. Note that the signal phase state numbers are the same as given in Fig. 2.12.

The free distance of a TCM code may be obtained using the minimum Euclidean distance associated with parallel transitions and the pair of paths that diverge at one state and re-merge at another after more than one transition. As shown in Fig. 2.16, the Euclidean distance between the 8-PSK signal phase states assigned to parallel transitions becomes the distance between the signal phase states corresponding to the subsets (0,4), (2,6), (1,5) or (3,7). As a result, this distance equals to $d_2 = 2$. It may be observed from Fig. 2.16 that the paths corresponding to the signal phase states 0-0-0 and 2-1-2 diverge at one state and re-merge at another after more than one transition. The squared Euclidean distance between these two paths becomes the sum of the squared distances d_1^2, d_0^2 and d_1^2, which equals 4.586. Thus, the Euclidean distance between these two paths becomes 2.1415. As a result, the free distance, d_{free}, which is given by the minimum value between the above two distances of this TCM signal, becomes 2.

As the number of information bits in each signalling interval in the above TCM scheme is 2, the uncoded 4-PSK signal set may be considered as the modulation scheme of interest for performance comparison. The signal constellation of 4-PSK is shown in Fig. 2.17. Thus, the free distance associated with uncoded 4-PSK signal set becomes $\sqrt{2}$ =1.4142. When coded and uncoded signals have the same average power, the asymptotic coding gain that can be achieved from these Ungerboeck codes is given by (Haykin, 1988)

$$\text{Asymptotic coding gain} = 10\log_{10}\left(\frac{d_{free}^2}{d_{ref}^2}\right) \tag{2.24}$$

where d_{free} is the free distance of the TCM code and d_{ref} is the free distance of an uncoded signal operating with the same energy per bit. The d_{ref} of this example is $\sqrt{2}$. Therefore, from Eq. (2.24), the coding gain achieved for this 8-PSK TCM code over uncoded 4-PSK is $10\log_{10}(2)$ = 3 dB.

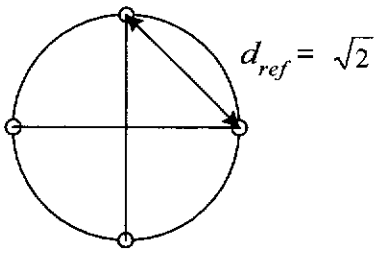

Figure 2.17 Signal constellation of 4-PSK signal.

However, this improvement in performance of TCM schemes is only achieved through additional signal processing, leading to a higher receiver complexity. With the advancement of microelectronics, the additional complexity may be overcome by employing high speed integrated signal processors. As a result, the application of trellis coded signals has now been made practical (Viterbi 1991).

2.7.2 TCM with CPM signals

The second type of trellis coded modulation scheme involves the use of trellis codes combined with spectral efficient CPM signals.

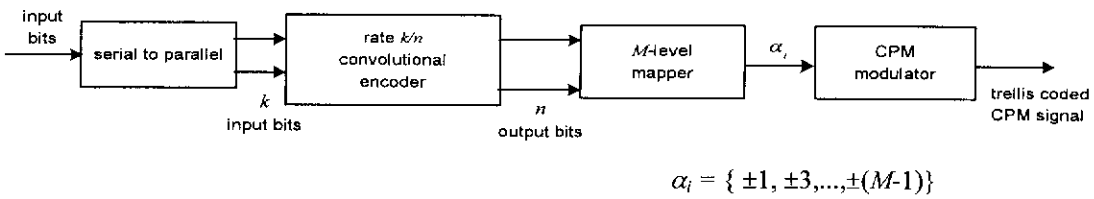

Figure 2.18 A Block diagram of generating a trellis coded CPM signal.

A trellis coded CPM signal can be realised as shown in Fig. 2.18. Here, the rate k/n convolutional encoder produces n output bits to every k input bits. These n output bits are then mapped to the M-ary real number input α_i=±1, ±3, ±5,..., ±(M-1), before sending through the CPM modulator. The most popular mapper used in coded CPM is the natural mapper. For example, it maps the n=2 convolutional outputs ***00, 01, 10*** and ***11*** to the CPM inputs α_i uniformly as -3, -1, +1 and +3. However, a non-uniform mapping between the coded bits and the phase increments of the CPM signal may also be used

(Luise and Reggiannini, 1993). In trellis coded CPM, the input bits to the CPM signal are correlated due to the convolutional coding. This correlation between the input bits to the CPM signal cuts out some transitions in the CPM trellis. As a result, this decreases the connectivity of the CPM trellis, resulting in an increase in the minimum merge length (Rimoldi, 1989). Generally, larger merge lengths involve larger free distances, and the coded CPM schemes having larger free distances will have better bit error rate performances (Anderson *et al*, 1986). Consequently, in designing a good trellis coded CPM signal, it is essential that the convolutional encoder, the mapper and the CPM scheme be jointly optimised to provide a power and spectrally efficient code. The "set-partitioning" method involved in optimising multi-level signalling is not explicitly applied to CPM signals. Instead, the optimisation is carried out by considering the largest free distance of the convolutional code combined with the CPM signal. In this case, it is assumed that the observation interval over which the minimum distance is calculated is large enough so that the maximum obtainable free distance is reached (Anderson *et al*, 1986). This assumption has been made in the present study in obtaining the largest free distances of the coded CPM signals.

The distance properties for the optimum combinations of different convolutional codes having different code rates and constraint lengths, and various CPM schemes such as M-ary CPFSK with different modulation indices, are given in (Anderson *et al*, 1986). A detailed explanation of the optimisation of convolutional codes combined with CPM signals, such as GMSK, based on the largest free distance is given in Chapter 4 of this thesis.

CHAPTER 3

LITERATURE REVIEW

3.1 Introduction

A considerable number of research papers have been published on ways of improving BER performance and spectral efficiency in mobile radio communications. Amongst these, Forward Error Control (FEC) coding techniques are often proposed for improving the BER performance. However, with these traditional FEC techniques, BER improvement is achieved at the expense of increased transmission bandwidth. This is due to the inclusion of redundant bits necessary for detection and subsequent correction of the bits in error. This bandwidth expansion associated with FEC may be avoided by adopting the trellis coded modulation (TCM) techniques, which involve high-level modulation schemes, such as, multi-level phase and multi-level amplitude schemes. Moreover, these conventional TCM schemes have been found to yield good coding gains in the presence of AWGN (Ungerboeck, 1982; 1987). In view of the narrow spectral characteristics of CPM signals, an additional gain in spectral efficiency may be achieved with the use of CPM signals in TCM schemes (Abrishamkar and Biglieri, 1991).

3.2 TCM Schemes for AWGN Channels

3.2.1 Improved BER without sacrificing bandwidth

As discussed in Section 2.7, TCM signals were originally developed by Ungerboeck (1982) for AWGN channels. In his study, the selection of TCM schemes involving multi-level PSK and multi-level AM is discussed. The selection criterion aims at maximising the free distances of the TCM schemes. This is achieved by mapping the coded bits into multi-level signals

based on a heuristic mapping rule called "mapping by set partitioning". A detailed explanation of this heuristic rule has been given in Section 2.7.1.

Computer simulations have been used to show the BER performances of the selected TCM schemes. The BER performances in Ungerboeck's study were based on the error-event probability, which will be discussed in detail in Chapter 5. The signal detection is achieved by coherent demodulation assuming ideal carrier recovery, followed by MLSD based on the Viterbi algorithm. The simulation results obtained show that up to 4 dB coding gain could be obtained with the selected TCM schemes, designed using codes having 4 and 8 states, compared to the uncoded schemes having the same number of information bits per symbol. It was also observed that improvements in the order of 6 dB or more could be obtained with more complex codes having a greater number of states. Moreover, these gains were obtained without expanding the transmission bandwidth or reducing the effective information rate as would be required by traditional FEC schemes.

3.2.2 Sensitivity to carrier phase offset

Ungerboeck and several other authors (Fugino *et al*, 1985; Leib *et al*, 1986; 1987) have shown that the TCM schemes are more sensitive to carrier phase offset as compared to uncoded schemes in the presence of AWGN. The effect of carrier phase offset on the performance of TCM schemes in the presence of AWGN is discussed in (Ungerboeck, 1987). In his study, TCM schemes, which combine codes having 4 or 8 states with 8-PSK, are considered. The investigations in his study were also based on the error event probability as in his previous study (Ungerboeck, 1982). The required SNRs for achieving an error event probability of 10^{-5} for the uncoded and the trellis coded schemes as a function of carrier phase offset have been reported.

The reported results indicate that the TCM schemes are more sensitive to carrier phase errors compared to the uncoded QPSK scheme. However, the

uncoded scheme requires a higher SNR to achieve the required error event probability compared to the coded schemes for smaller values of phase offset.

It has also been shown in (Fugino, *et al*, 1985), that a constant carrier phase offset of 5° may degrade the performance of coded 8-PSK scheme by up to 1 dB. A similar study of the BER performance of trellis coded MPSK schemes in the presence of carrier phase errors has been carried out by (Leib *et al*, 1987). The carrier phase noise in their study is modelled as an integrated white noise process. The numerical results obtained using uncoded QPSK and rate-2/3 coded 8-PSK schemes show that the coded schemes are more sensitive to carrier phase error compared to the uncoded scheme. From the above published results, it may also be observed that TCM schemes involving coherent detection may require good carrier tracking systems to obtain good BER performances.

3.3 Ungerboeck codes over Fading Channels

As the frequency spectrum is at premium in mobile telephony, TCM schemes with superior bandwidth utilisation appear to be attractive candidates for mobile applications compared to the traditional FEC schemes. Application of TCM in fading environments has been studied by several authors (Divsalar and Simon ,1987; Huang and Campbell, 1991; Cavers and Ho, 1992). Most of the studies reported on the performance analysis of Ungerboeck codes over fading channels (Cavers and Ho, 1992; Huang and Campbell, 1991). The performance analysis of the proposed trellis coded CPM scheme in the present study closely follow the work by Divsalar and Simon (1987). Therefore, the research carried out by Divsalar and Simon (1987) is reviewed in detail.

Divsalar and Simon (1987) have studied the performance of trellis coded multi-level PSK schemes over a frequency non-selective fading channel using a combination of theoretical analysis and computer simulation. They

assume that the received signal is detected using coherent detection with perfect carrier recovery. In addition, only the effect of fading on the amplitude is considered in the analysis. The effect of fading on the phase of the received signal is assumed to be fully compensated by either tracking the phase in a phase locked loop, or utilising a pilot tone calibration technique (McGeehan and Bateman, 1984; Cavers and Liao, 1992). However, the addition of a pilot tone, or pilot tones to the transmitted signal for the purpose of recovering the faded carrier at the receiver may need a larger bandwidth.

The analysis is further simplified by assuming block interleaving with an infinite interleaving depth, so that the fading channel can be considered memoryless giving rise to independent errors. The subsequent performance analysis of the TCM schemes is then carried out based on the techniques designed for memoryless channels in obtaining the upper and lower bounds of the BERs. The assumption of infinite interleaving depth however, leads to an infinite transmission delay. In practice, the depth of interleaving is chosen in relation to the maximum fade duration anticipated and the maximum delay allowed. For example, for the case of speech transmission, the total delay must be kept under 60 ms (Biglieri *et al*, 1991).

As discussed in section 2.7.1, the signal points in the MPSK constellation in conventional trellis coded MPSK are uniformly (symmetrically) spaced. However, Divsalar *et al* studied a trellis coded QPSK with an asymmetric constellation in an attempt to further improve the BER performance. The asymmetric QPSK signal constellation is designed by introducing non uniformity into the spacing between the signal points in the constellation as shown in Fig 3.1. This non uniformity ϕ introduced is referred to as "asymmetry" (Divsalar *et al*, 1987). The asymmetry in the signal constellation, which provides the best BER performance in the presence of AWGN and signal fading, has also been obtained.

In addition, the theoretical upperbounds on BER have been obtained for both the symmetric and the optimum asymmetric rate-½ trellis coded QPSK signals. This has been carried out based on the transfer function of the error state diagram of the coded scheme (Proakis, 1989; Clarke and Cain, 1981) assuming Rayleigh and Rician statistical fading models. A detailed explanation of this technique is given in Chapter 5. The analytical results for uncoded BPSK having the same number of information bits per symbol as rate-½ trellis coded QPSK have also been obtained for comparison.

The above analytical results have then been verified by computer simulations assuming ideal carrier recovery. In this computer simulation study, an interleaving depth of 512 bits for a data rate of 4800 bits/s and a fixed Doppler frequency of 100 Hz have been assumed. In this case, the fading statistics could be considered to be independent from one symbol to the next. Therefore, the channel may be approximated to be memoryless, as assumed in the analytical study.

The analytical and the simulated results obtained in the presence of Rayleigh fading are shown in Fig. 3.2. The results show that a significant improvement in the BER performance may be obtained with the use of trellis coded schemes compared to the uncoded QPSK, in the presence of Rayleigh fading. Moreover, the signal with the optimum asymmetric constellation shows improved bit error rate performance over the conventional symmetric signal sets. In this case, the asymmetric TCM scheme achieves a gain of approximately 1.5 dB at a BER of 10^{-3} over a Rayleigh fading channel compared to the symmetric scheme.

Similar BER improvements for the symmetric and optimum asymmetric TCM schemes over Rician channels have also been reported.

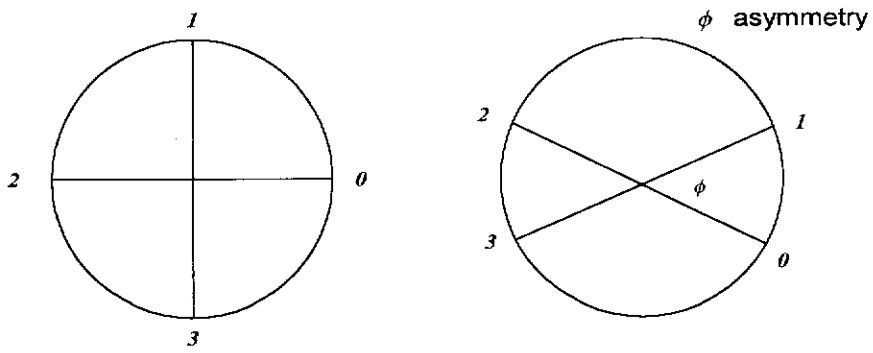

Figure 3.1 (a) Symmetric and (b) asymmetric QPSK signal constellations.

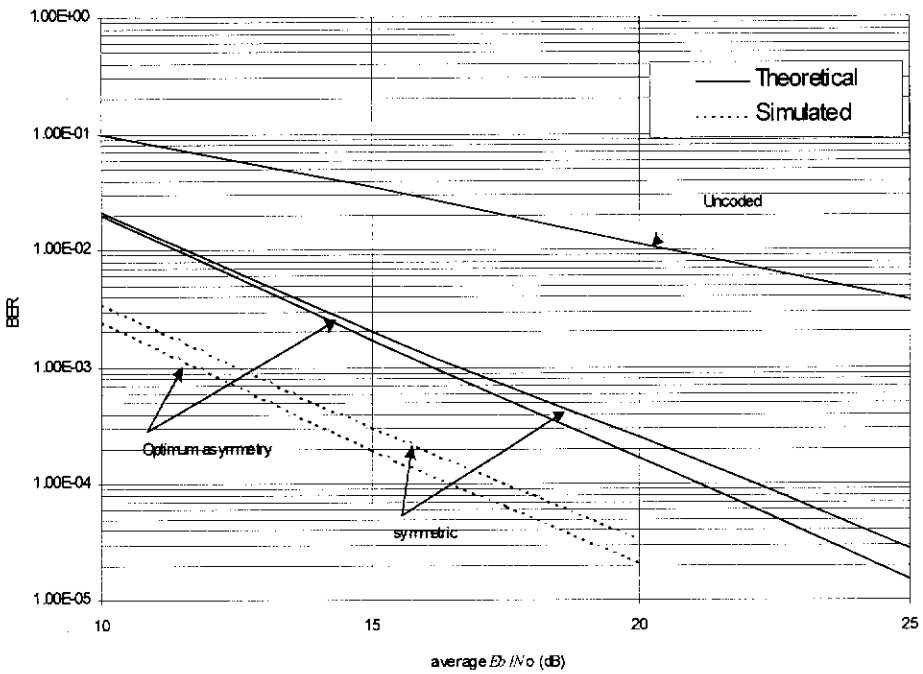

Figure 3.2 BER performance of rate-½ trellis coded symmetric and asymmetric QPSK in the presence of Rayleigh fading (after Divsalar and Simon, 1987).

When pilot tones are used for aiding coherent demodulation, as suggested in the above study (Divsalar and Simon, 1987), narrowband bandpass filter(s) are used in the pilot tone extractor to isolate the pilot tone(s) from the modulation. In this case, these bandpass filters must have bandwidths sufficiently wide to account for the Doppler shift (Biglieri *et al*, 1991). As such,

wider filter bandwidths are required for larger Doppler shifts. This results in more noise in the extracted carrier reference. The effect of such noisy carrier references on the BER performance of TCM schemes has also been examined (Divsalar and Simon, 1987). This has been done by modifying their earlier simulations, which assume ideal carrier recovery, to include a technique referred to as dual pilot tone calibration (Simon, 1986). With this technique, two tones of equal power are inserted symmetrically at the edges of the data spectrum for the purpose of coherent demodulation. It has been observed from their study, that the performance of the reference-based coherent detection scheme in Rician fading is degraded by 2-3 dB compared to ideal coherent detection schemes assuming perfect carrier recovery.

To avoid the complicated carrier recovery circuits needed at the receiver in coherent detection schemes, Simon and Divsalar (1988) have extended their previous study (Divsalar and Simon, 1987) to obtain the performance of a simpler receiver based on differential detection. In their later study (Simon and Divsalar, 1988), the performance of trellis coded multi-level differential shift keying (M-DPSK) has been considered for flat fading channels. Again, an asymmetric signal set has been chosen and the upperbound on the bit error probability has been obtained for rate-½ trellis coded QPSK using differential detection. The resulting BER upperbounds have been compared with those reported for coherent detection assuming perfect carrier recovery (Divsalar and Simon, 1987). A performance degradation of around 1.5 dB over the range of BERs considered (10^{-2} to 10^{-5}) has been reported with differential detection, compared to ideal coherent detection, over both Rician and Rayleigh channels. Moreover, it had been shown in their earlier study (Divsalar and Simon, 1987) that the performance gain of the ideal coherent detection scheme, compared to the reference based coherent detection scheme, is around 2-3 dB. Thus, Simon and Divsalar (1988) have concluded that 0.5 to 1.5 dB performance gain may be achieved by using a simpler receiver based on differential detection, compared to the reference-based coherent detection.

A similar study has been carried out by Cavers and Ho (1992) on BER performance analysis of TCM in flat Rayleigh fading channels, assuming again that the fading affects only the amplitude. However, their study is not restricted to MPSK signals as in the previous studies (Divsalar and Simon, 1987; Simon and Divsalar, 1988), but includes multi-level QAM (Quadrature amplitude modulation) schemes using coherent and differential detection schemes. In this case, unlike the upperbounds in the previous studies, an exact expression for the pairwise error event probability has been obtained. The reported results show that the theoretical results fall within 2 dB of the simulated results for BER of less than or equal to 10^{-2} and normalised fading rates of 0.01 and 0.03.

There are a number of other publications in the literature that deal with the performance of trellis coded multilevel PSK and multilevel DPSK over different fading conditions. Schlegel *et al* (1989) have performed work similar to the above studies by examining the performance of TCM over flat fading channels using Chernoff bounding techniques. Also in their work, design criteria for constructing trellis codes suitable for transmission over fading channels are considered. McLane *et al* (1988) have examined the performance of rate 2/3 trellis coded, 8-PSK and differential 8-PSK (8-DPSK) over a shadowed Rician fading channel using computer simulations. Lee and McLane (1990) have shown that the BER of the proposed scheme by McLane et al (1988) can be improved by using a convolutional interleaver. The design of a new 4-state rate 2/3 trellis coded 8-PSK has been introduced by Jamali and Le-Ngoc (1991). The simulations performed assuming light shadowed Rician fading channels show that this proposed TCM scheme achieves an additional coding gain of around 0.4 dB at a BER of 10^{-3}, compared to the Ungerboeck's 4-state 8PSK scheme.

3.4 Trellis Coded CPM Schemes over AWGN

Trellis coded CPM signals operating in the presence of AWGN have been studied by many researchers (Lindell *et al*, 1984; Pizzi and Wilson, 1985; Anderson *et al*, 1986; Ho and McLane, 1988). As discussed in Section 2.7.2, the "set-partitioning" method involved in maximising the free distance of trellis coded multi-level signals is not explicitly applied to trellis coded CPM signals. Instead, the code selection in these studies is carried out by simply considering the largest free distance of the coded CPM scheme.

Lindell *et al* (1984), have studied the selection of rate-½ convolutional (trellis) codes of various constraint lengths, combined with binary and 4-level CPFSK modulation having various modulation indices. Lindell *et al* assume that the received signal corrupted by AWGN is detected using coherent detection based on MLSD. The selection of the coded CPFSK scheme is carried out by considering the minimum normalised squared Euclidean distance of the combined code defined by,

$$d^2_{\min,N} = \min_{u_\alpha, u_\beta} \frac{1}{2E} \int_0^{NT} [s(t,\alpha)-s(t,\beta)]^2 \, dt \qquad (3.1)$$

where E and T are the transmitted energy per bit and the transmitted bit duration, respectively. The coded CPM signals, corresponding to the input data sequences, u_α and u_β, to the convolutional encoder, are $s(t,\alpha)$ and $s(t,\beta)$, respectively. Here, the integral in Eq. (3.1) extends over the time, NT, that the two signals $s(t,\alpha)$ and $s(t,\beta)$ differ. Thus, $d^2_{\min,N}$ is the minimum normalised squared Euclidean distance between coded signals, defined up to N symbol intervals. It is assumed in their study (Lindell *et al*, 1984) that the observation interval (NT), over which the minimum distance is calculated, is large enough to ensure that the maximum obtainable minimum distance (maximum free distance) is reached. As the selection of appropriate coded CPM signals in the present study is also based on the largest free distance, a detailed explanation for obtaining the free distance of coded CPM signals will be given in Chapter 4.

The results obtained in their study (Lindell *et al*, 1984) showed that rate-½ trellis coded, binary and 4-CPFSK signals are optimal, i.e., providing the largest minimum normalised squared Euclidean distance, when the modulation index is approximately around 0.5. Further, it has been observed that the minimum normalised squared Euclidean distance for a given modulation index h, $d^2_{\min}(h)$, increases with the constraint length of the convolutional code. For example, with rate-½ convolutionally encoded binary CPFSK, when h=0.5, $d^2_{\min}(0.5)$ is increased from 4 to 6 when the constraint length is increased from 2 to 3. The corresponding value of $d^2_{\min}(0.5)$ for uncoded MSK, which equals 2, is used for performance comparisons. Hence, by comparing the free distances of the coded and uncoded schemes, they have concluded in their study that the coded CPFSK schemes achieve a considerable distance gain compared to the uncoded MSK.

Lindell *et al* (1984) have also observed that the minimum value of N for which $d^2_{\min,N}(h)=d^2_{\min}(h)$, increases with the constraint length. For example, with rate-½ convolutionally encoded 4-level CPFSK, when h=0.5, the corresponding values of N were 3, 7, 9 and 13 for constraint lengths of 2, 3, 4 and 5, respectively. The value of N at which the free distance is achieved is an important parameter as it directly relates to the path memory of the MLSE detector at large E_b/N_o (Aulin *et al*, 1981). Therefore, it may also be concluded that the computational complexity of the receiver grows rapidly with the constraint length due to the increase in the value of N.

The bandwidth of a trellis coded CPM scheme is expanded by a factor corresponding to the reciprocal of the coding rate. Since the code rate is less than 1, any coding gain of the trellis coded CPM schemes is achieved at the expense of an increase in the transmission bandwidth. For this reason, it is preferable to adopt a convolutional code with a high rate so as to keep the bandwidth expansion small. Convolutional codes of rates 1/2, 2/3, 3/4,... are normally considered (Anderson *et al*, 1991).

The power-bandwidth trade-off of trellis coded CPFSK using rate-½ convolutional codes has been studied in (Lindell *et al*, 1984; Anderson *et al*, 1986). Here, the power is considered as the distance gain in dB relative to the uncoded MSK which has a squared free distance of 2. i.e., the distance gain in dB=$10\log(d^2_{\min}(h)/2)$. The bandwidth is defined as the frequency band containing 99% of the total signal power, as given in Section 2.4.1.1. Here, the spectral measurements of the coded CPFSK schemes are only estimated by using the uncoded CPFSK spectra at a given h and expanding them by the code rate, ½. Comparison of the obtained results shows that coded 4-CPFSK schemes having the same spectral efficiency as uncoded MSK may achieve a power efficiency corresponding to a distance gain of approximately 2 dB. An additional gain in power efficiency may be achieved using a larger constraint length. However, this may only be achieved with an increase in the computational complexity of the receiver requiring a larger observation interval N.

The spectral efficiency of a coded CPM may be increased by using partial response signals which have a more attractive power spectrum than the full response signals (Aulin *et al*, 1981). Also, the partial response signals provide a more attractive power-bandwidth trade-off than the full response signals (Aulin *et al*, 1981). The distance properties of convolutionally coded partial response CPM signals such as 2RC and 3RC using coherent MLSD over AWGN channels have been studied in Pizzi and Wilson (1985). The optimisation of rate-½ convolutional codes combined with partial response CPM signals is obtained based on the maximum free distance, as in the previous study (Lindell *et al*, 1984). The optimum codes having the largest free distances have been obtained using the trellis based algorithm described by Mulligan and Wilson (1984).

Coded partial response 4-level 2RC and 4-level 3RC CPM signals with modulation indices of less than or equal to 0.5, and convolutional codes with constraint lengths 2, 3 or 4 have been considered in their study (Pizzi and Wilson, 1985). An improvement in the free distance has been obtained with

coded partial response CPM schemes having modulation index 0.5 compared to that of coded 4-CPFSK schemes. For example, the free distance of the coded 4-CPFSK with constraint length 2 codes obtained under these conditions was found to be equal to 3.0, whereas the corresponding free distances of the coded partial response schemes employing 4-level 2RC and 4-level 3RC were 3.04 and 3.83, respectively. However, this improvement in distance with partial response schemes may only be obtained with an increase in the complexity of the MLSD, requiring a larger value of N to reach the free distance. For example, the coded 4-CPFSK reaches the free distance after 3 symbol intervals, whereas the coded partial response CPM schemes 4-2RC and 4-3RC reach it after 4 and 8 symbol intervals, respectively. Also, Pizzi and Wilson (1985) have observed that the free distance of coded partial response schemes may be improved using codes having higher constraint length. However, this is achieved at the expense of the complexity of the MLSD.

A comparison of the power-bandwidth performance of coded 4-CPFSK and coded 4-level partial response signals has also been carried out in their study (Pizzi and Wilson, 1985) using a method similar to those used in (Lindell *et al*, 1984; Anderson *et al*, 1986). It is observed that the coded partial response 4-RC scheme having a modulation index of 0.5 combined with a convolutional code with constraint length 2, achieves a distance gain as well as a bandwidth gain compared to the corresponding coded 4-CPFSK schemes. Therefore, it may be concluded from their results, that trellis coded partial response CPM signals will yield better energy-bandwidth performances compared to coded full response schemes. Nevertheless, this improvement may only be achieved at the expense of more complex MLSD receivers, as the effective constraint length of the encoder is dictated by the memory of the partial response signal, as well as the memory of the convolutional code. This observation suggests that further research is needed to derive power and bandwidth efficient trellis coded partial response CPM schemes with less complex receivers.

The complexity of a MLSD receiver involving Viterbi decoding depends on the number of states in the Viterbi decoder. It has been shown in (Morales-Moreno *et al*, 1994), that the number of states in the combined Viterbi receiver of trellis coded partial response signal, such as TFM, may be reduced by adopting differential encoding prior to modulation. In their study, rate 1/2 and 2/3 convolutional codes combined with differentially encoded TFM schemes were studied assuming coherent detection over AWGN channels. The selection of these coded schemes has been carried out based on the maximum free distance as discussed in (Lindell *et al*, 1984: Pizzi and Wilson, 1985) for a given code rate and a fixed number of states in the combined Viterbi receiver.

The coding gains of the selected codes and their receiver complexities based on the number of states in the combined Viterbi decoder, were compared with the uncoded schemes. It is observed from their study, that with rate-½ convolutional codes combined with differentially encoded TFM, coding gains of more than 3 dB may be achieved with simpler receivers having a lesser number of states compared to the uncoded one. Furthermore, coding gains of more than 7 dB could be achieved with rate-½ codes, having more complex receivers with 128 or 256 states. From these observations, it may be concluded that receiver complexity, based on the number of states in the Viterbi decoder of trellis coded schemes using partial response CPM such as TFM, may be reduced through the use of differential encoding prior to modulation.

Ho and McLane (1988), have also analysed various trellis coded CPM schemes using MLSD over AWGN channels based on the energy-bandwidth performances and the receiver complexity in terms of the number of states in the Viterbi decoder. Their results also confirmed that the coded partial response schemes perform better than the coded full response schemes. However, the partial response schemes need more complex receivers than the full response schemes.

3.5 Trellis Coded CPM over Fading Channels

3.5.1 Trellis coded CPM in flat fading channels

The use of Trellis coded CPM, such as CPFSK, on shadowed mobile satellite channels with coherent detection has been proposed in (Kerr and McLane, 1992). The BER performance of the proposed system has been obtained using simulations and analysis. Perfect carrier recovery has been assumed in the analysis. However, as in (Divsalar and Simon, 1987), only the effect of fading on the received signal amplitude has been considered. The effect of bit interleaving on the BER performance has been studied by introducing convolutional interleaving to compensate for burst errors due to slow fading (Lee and McLane, 1988). The branch metric computations required for the optimal Viterbi decoder have been obtained before de-interleaving. The decoding metrics were calculated using the phase trellis of the modulator observed over more than one symbol interval. These metrics were then sent through the de-interleaver to the Viterbi decoder, which works with the code trellis. In this manner, even though both the modulator and the code trellises were considered in the decoding process, the combined property of the trellis coded CPM signal is not used. Therefore, the detection scheme in this case can be considered to be sub-optimal.

In the simulations, the non-interleaved system comprising of a rate-½, 4-state convolutional code combined with a h=1/4 CPFSK modulator is used for performance comparison over various shadowing fading conditions. The simulation results show that sub-optimal coherent detection with interleaving, achieves a significant bit error performance advantage over the non-interleaved coded CPFSK systems having the same number of states in the decoder trellis. For example, the 16-state coded scheme with interleaving (with an interleaving degree of 18) achieves a 4.2 dB gain at a BER of 10^{-3} in a light shadowed fading environment when the normalised fading bandwidth is set at 0.01. However, such interleaving depths may produce time delays that are more than the limit that could be used in digital speech transmission (Kerr and McLane, 1992). Therefore, such a system may not be suitable for

digital speech applications, as the required interleaving depths lead to an unacceptable real-time delay. However, the proposed scheme may be suitable for data transmission which requires low BERs but is less sensitive to delay than speech transmission.

The above study of Kerr and McLane (Kerr and McLane, 1992), based on sub-optimal coherent detection, has been extended to trellis coded partial response CPM schemes in Rician fading channels (Yiin and Stuber, May 1996). The upperbound on the bit error probability has been derived for interleaved partial response CPM in flat fading channels using the transfer function bound technique (Proakis, 1989, Clarke and Cain, 1981), which is similar to the technique used in Divsalar and Simon (1987). The analytical upperbounds are compared with the simulated results using rate-½ convolutionally coded 2RC (h=1/4), over Rician and Rayleigh fading conditions. A comparison of the simulated results with the analytical upperbound shows that the analytical upperbound is tight to within 1.5-2 dB. Furthermore, the effect of the observation interval over which the decoding metrics are calculated on the BER performance has also been studied. They have observed around 1 dB performance gain when the observation interval is increased from two-symbols to three-symbols. However, a longer observation interval may require more complex receivers.

The essential phase tracking required in coherent detection may be difficult to achieve in a narrowband system, which suffers from rapid amplitude and phase variations (Hirono *et al*, 1984). In this case, it may be beneficial to consider a non-coherent detection scheme. Yiin and Stuber (August, 1996) have extended their previous study (Yiin and Stuber, May 1996) to obtain the BER performances of trellis coded partial response CPM on interleaved flat Rician fading channels using non-coherent detection. The results obtained show that the proposed non-coherent receiver is less than 0.5 dB inferior to that of the coherent receiver, which requires complex carrier recovery circuits, but having the same observation interval.

Abrishamkar and Biglieri (1991) have studied two detection schemes based on coherent and non-coherent detection of trellis coded CPM over a channel affected by Gaussian noise and frequency non-selective fading. In these two detection schemes, simpler sub-optimal receivers are proposed. The performances of these two schemes have been evaluated by computing the computational cut-off rate (R_0) of the discrete channel generated by CPM over AWGN, Rician and Rayleigh fading channels.

Also, in their study (Abrishamkar and Biglieri, 1991), the Rayleigh fading channel has been modelled as in (Divsalar and Simon, 1987), i.e., assuming fading affects only the amplitude of the received signal. The results obtained for coded CPFSK using coherent and non-coherent sub-optimal detection are compared with the optimum coherent detection of trellis coded PSK. They observe a substantial degradation in the performance (6-7 dB to achieve an R_0 of 2) over the Rayleigh fading channel for the sub-optimal non-coherent symbol-by-symbol detection scheme using a considerably simpler receiver, compared to the optimum coherent receiver.

3.5.2 Trellis coded CPM in frequency-selective fading channels

The BER performances of the trellis coded schemes discussed in the previous section, have been obtained assuming frequency non-selective fading conditions. The effect of ISI in a frequency-selective fading channel on the performances of trellis coded CPM schemes has been studied in (Yiin and Stuber, 1997). In their study, two equaliser structures, MLSE and soft-output, have been proposed. Since the focus of the present study is not on the equalisation methods, only the results obtained are summarised. Both analytical and simulation results show that large coding gains can be achieved with the trellis coded CPM schemes compared to the uncoded, when MLSE decoding is combined with equalisation. For example, the simulation results of the trellis coded 1RC and 2RC schemes obtained using the MLSE equaliser, assuming the six-ray typical urban channel model as recommended by the GSM standard, have shown coding gains of about 6 dB at a BER of 10^{-4}.

CHAPTER 4

SELECTION OF TRELLIS CODED GMSK SCHEMES

4.1 Introduction

As discussed in Section 2.7.2, it is essential to have a proper trellis code in combination with an appropriate modulation scheme, so that the resultant TCM signal is able to achieve the desired power and spectral efficiencies. The code selection in trellis coded CPM schemes is often carried out based on the criterion of achieving the largest free Euclidean distance in the combined coded signal (Anderson *et al*, 1986). This chapter presents the selection of appropriate trellis codes to be used in combination with GMSK (Murota and Hirade, 1981). In the present study, the criteria for the selection of the trellis codes have been based on two considerations; namely the achievable Euclidean distance, and the complexity of the receiver in terms of the number of phase states involved in the Viterbi decoder. A reduction in the receiver complexity has been obtained through the use of differential encoding prior to modulation (Morales-Moreno, *et al*, 1988; 1994).

To aid in the selection of appropriate trellis codes, a computer search program has been developed for determining the free Euclidean distance associated with a specific trellis coded GMSK scheme. The selection process involves two steps. First, the rate-½ convolutional codes of different constraint lengths, which yield the largest free distances when combined with differentially encoded GMSK (B_0T=0.3), are identified. Then, the complexity of the associated Viterbi decoder is determined for each of these candidate schemes. Eventually, the trellis coded and differentially encoded GMSK schemes, which possess the largest free distances, as well as the minimum number of phase states associated with Viterbi decoding, are selected for further in-depth study.

4.2 Trellis Representation of GMSK Signal

As described in Section 2.4.1, the information carrying phase $\phi(t)$ of a GMSK signal, can be expressed as

$$\phi(t) = \pi h \int_{-\infty}^{t} \sum_{i=-\infty}^{\infty} \alpha_i \, g(\tau - iT) \, d\tau \tag{4.1}$$

where α_i = ± 1 for binary data. Here, the frequency pulse shape $g(t)$ is Gaussian as presented in Section 2.4.1.1. In this study, $g(t)$ corresponds to the impulse response of a Gaussian lowpass filter with a normalised –3dB bandwidth B_0T=0.3. This GMSK signal has been adopted in the GSM standard.

As observed in Fig. 2.5, the GMSK pulse with B_0T=0.3 extends just over three bit periods. In this case, the phase change, $\Delta\phi(mT)$ of GMSK (B_0T=0.3) signal[1] at the end of the m^{th} bit period will be governed by three consecutive input data bits, as in the case with GTFM. Consequently, the phase changes $\Delta\phi(mT)$ at the end of the m^{th} bit period for the GMSK signal may be derived from Eq. (2.19), which is repeated here for convenience,

$$\Delta\phi(mT) = \pi/2 \, (a \, b_{m-1} + B \, b_m + a \, b_{m+1})$$

where $(2a+B)=1$. Here, b_{m-1}, b_m and b_{m+1} represent the binary data at $t=(m-1)T$, mT and $(m+1)T$, respectively.

Using Eq. (4.1), the value of B for the GMSK signal, is found to be approximately equal to 0.644. Accordingly, the possible phase transitions of the GMSK signal over one bit period are shown in the Table (4.1). Here, a binary *0* is represented by -1, and a binary *1* is represented by +1.

[1] From here onwards, the GMSK signal referred to will be that with $B_0T = 0.3$.

Input data			Allowable phase transitions
b_{m-1}	b_m	b_{m+1}	$\Delta\phi(mT)$
-1	-1	-1	-90°
-1	-1	+1	-58°
-1	+1	-1	26°
-1	+1	+1	58°
+1	-1	-1	-58°
+1	-1	+1	-26°
+1	+1	-1	58°
+1	+1	+1	90°

Table 4.1 The allowable phase transitions over one bit period of GMSK signal with respect to three consecutive input data bits.

Based on the above phase changes, the trellis diagram and the finite state diagram representing the phase states for this GMSK signal can be obtained as described below. Assume the phase value of the state at the beginning of the m^{th} bit period to be 0°, with the two previous data bits, $b_{m-1}=b_m$= -1. In this case, if the next data bit b_{m+1}= -1, the phase value for the new state at the end of the m^{th} bit period, becomes (0°)+(–90°)=–90°. On the other hand, if b_{m-1}= +1, this phase value becomes (0°)+(–58°)=–58°. Now, if the phase of the current state is –90°, and a +1 arrives, the phase for the new state becomes (–90°)+(–58°)=–148°. On the other hand, the state moves to a new phase value of (–90°)+(–90°)=–180°, if the new data bit is –1. Similarly, if the phase of the current state is –58°, a +1 causes the transition to the state (–58°)+(+58°)=0°, and a -1 produces a new state (–58°)+(26°)=–32°. Following the same procedure for all the possible data bit combinations, the corresponding phase changes over one bit period can be represented by the 16-state trellis representing the GMSK modulator, as shown in Fig. 4.1. Here, each of the allowable phase states at the end of the m^{th} bit period is governed by the two previous input data bits b_{m-1} and b_m. For clarity, the trellis corresponding to an incoming data bit b_{m+1}= -1 is represented by a solid line, while the trellis for b_{m+1}= +1 is represented by a dashed line. It can be

observed from the trellis in Fig. 4.1, that different phase states associated with different combinations of b_{m-1} and b_m, may have identical phase values. For example, the same phase value of -90 is associated with the phase state having b_{m-1}= -1 and b_m= -1, as well as the phase state having b_{m-1}= +1 and b_m= +1. In order to distinguish these phase states, they are represented in the trellis by having a prime or not. e.g., $\pm 90°$ or $\pm 90°'$.

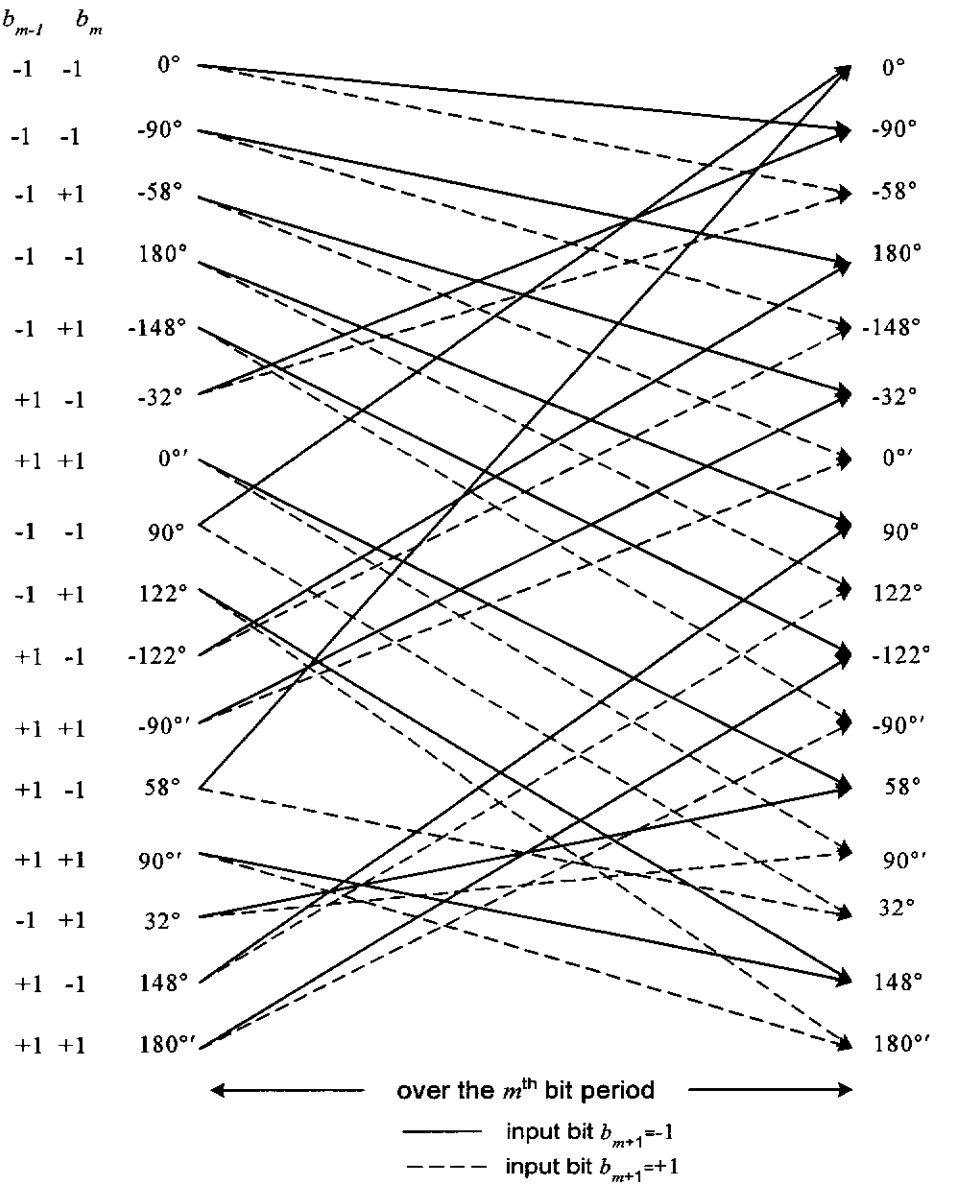

Figure 4.1 The 16-state trellis diagram of the GMSK signal.

It has been shown in (Morales-Moreno *et al*, 1988; 1994) that the 16-state representation of the GTFM signal (B=0.5, r=0.00) may be simplified by adding an extra +90° phase change to $\Delta\phi(mT)$. As a result, the new phase change over one bit period, $\Delta\theta(mT)$, is given by,

$$\Delta\theta(mT) = \Delta\phi(mT) + 90. \tag{4.2}$$

It is obviously of interest to try applying the same technique to GMSK to see if a similar simplification is possible. Applying this modification to $\Delta\phi(mT)$ of GMSK signal, the new values of phase change $\Delta\theta(mT)$ associated with the different combinations of three consecutive input data bits are shown in Table 4.2.

Input data			Modified phase transitions $\Delta\theta(mT)$
b_{m-1}	b_m	b_{m+1}	
-1	-1	-1	0°
-1	-1	+1	32°
-1	+1	-1	116°
-1	+1	+1	148°
+1	-1	-1	32°
+1	-1	+1	64°
+1	+1	-1	148°
+1	+1	+1	180°

Table 4.2 The modified phase transitions of GMSK with respect to three consecutive input data bits.

Replacing $\Delta\phi(mT)$ with the new phase transitions $\Delta\theta(mT)$ in constructing the trellis, a simpler 8-state trellis, as shown in Fig. 4.2, can be derived for the GMSK signal. The corresponding 8-state finite state representation of the GMSK signal is shown in Fig. 4.3. As before, when two different phase states associated with two different combinations of data bits b_{m-1} and b_m, share the same phase value, these phase states are denoted by a phase value with and without a prime. This simplification technique for the GMSK trellis, by adding an extra +90° phase change to $\Delta\phi(mT)$, leads to a simpler decoder.

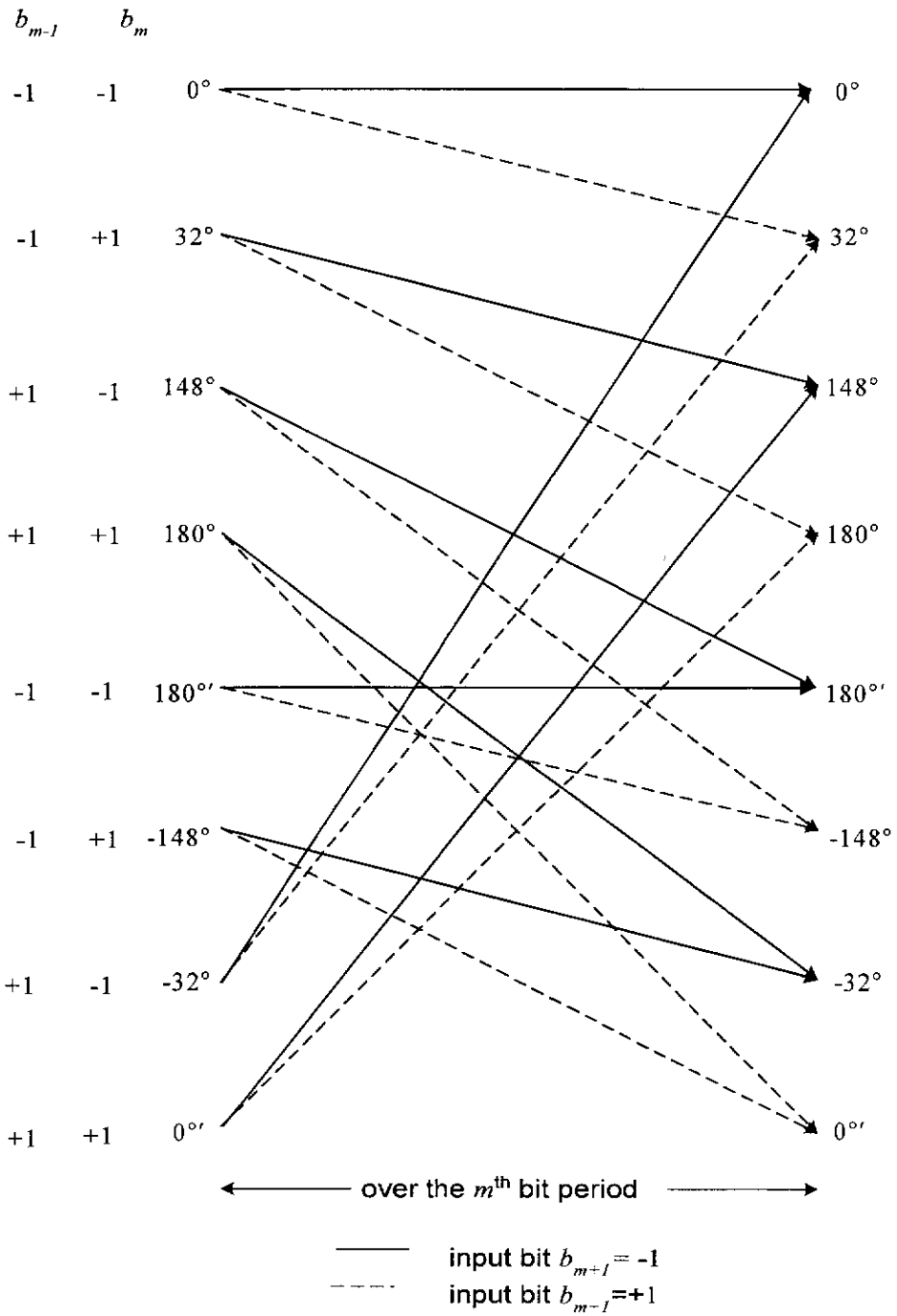

Figure 4.2 The 8-state trellis diagram of the GMSK signal.

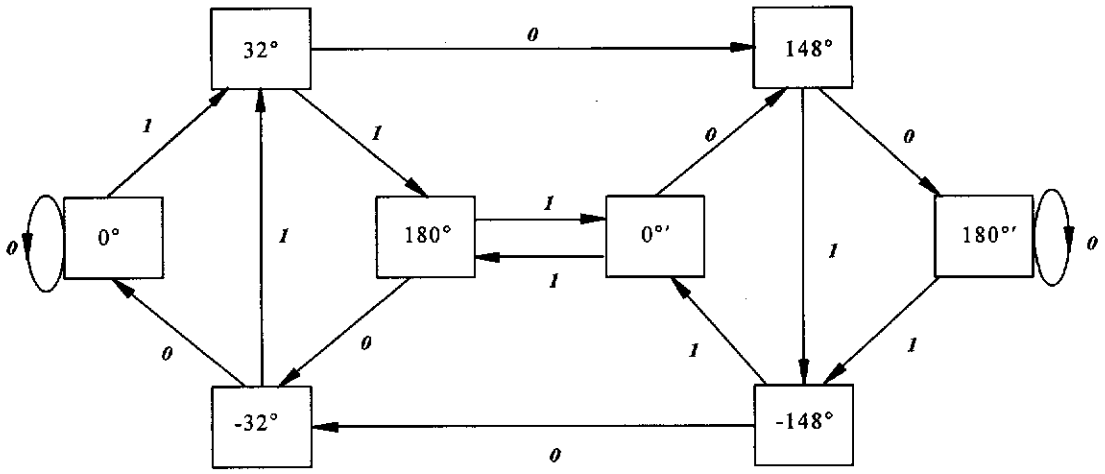

Figure 4.3 The finite state diagram describing the phase changes over one bit period of GMSK signal.

4.3 Trellis Coded GMSK Signal

In this study, various trellis coded GMSK schemes, which are formed by combining rate-½ convolutional codes having different constraint lengths with GMSK signal, have been considered. These trellis coded GMSK signals have been evaluated based on an AWGN model as shown in Fig. 4.4. A binary convolutional encoder **G**, expressed in (n,k,ν), accepts k serial input bits to yield n output bits using a ν-stage shift register. The resulting code has a rate of k/n and a constraint length of ν. Note that for a rate-½ code, the actual transmission rate of $1/T$ is twice the input bit rate of $1/T_b$. As a result, the transmitted bit energy, E, associated with a coded bit becomes $E_b/2$, where E_b is the energy of an input data bit.

The output of the convolutional encoder **G** is serially fed to the GMSK modulator **M**, which generates the trellis coded GMSK signal $s(t,\alpha)$, where α=±1 for binary data. The received signal $r(t)$ is assumed to be the sum of the transmitted signal $s(t,\alpha)$ and zero mean additive white Gaussian noise, $n(t)$, having double sided power spectral density $N_0/2$. A coherent quadrature demodulator in conjunction with soft decision Viterbi decoding, as shown in Fig. 4.5, is then used to recover the input data from $r(t)$. Here the recovered phase values, $\phi_r(t)$, obtained using the in-phase and the quadrature

components, $I_r(t)$ and $Q_r(t)$, of the received signal, are used in the Viterbi decoder to estimate the most likely transmitted data sequence.

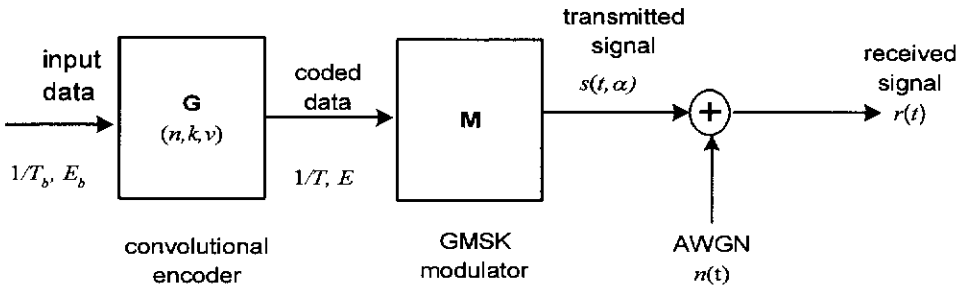

Figure 4.4 A model of the trellis coded GMSK signal transmitted over an AWGN channel.

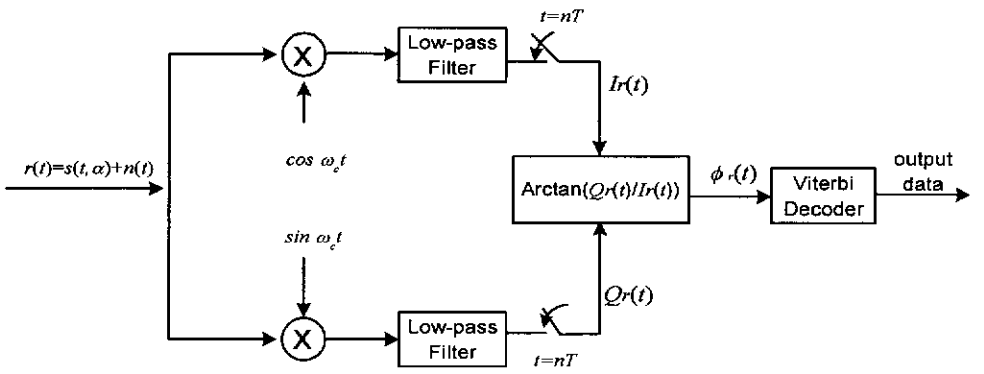

Figure 4.5 Detection of trellis coded GMSK signal using quadrature demodulation followed by Viterbi decoding.

With Viterbi decoding, the complexity of the receiver is largely governed by the number of phase states in the trellis representing the coded signal, i.e., the complexity is upperbounded by the product of the number of states for the convolutional code, and the number of states associated with the modulated signal. It has been observed that the complexity of the Viterbi decoder for the trellis coded schemes involving GTFM (B=0.5, r=0.00) may be reduced through the use of differential encoding (Morales-Moreno *et al*, 1988; 1984). Based on this observation, differential encoding has been applied prior to the GMSK modulation as shown in Fig. 4.6, anticipating a similar reduction in the complexity of the receiver. The relationship between

the output a_n, and the input b_n, of a differential encoder is given by $a_n=b_n \oplus b_{n-1}$ where $\oplus$ denotes modulo-2 addition (or EX-OR logical operation). Taking this differential encoding process into account, the finite state diagram for the differentially encoded GMSK signal is shown in Fig. 4.7. The corresponding trellis diagram of this differentially encoded GMSK signal is shown in Fig. 4.8. In Fig. 4.7 and Fig. 4.8, each transition is associated with coded bits, b_n, at the input of the differential encoder.

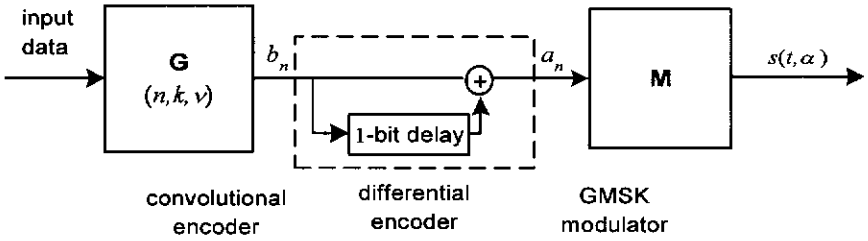

Figure 4.6 A model of the trellis coded GMSK signal employing differential encoding.

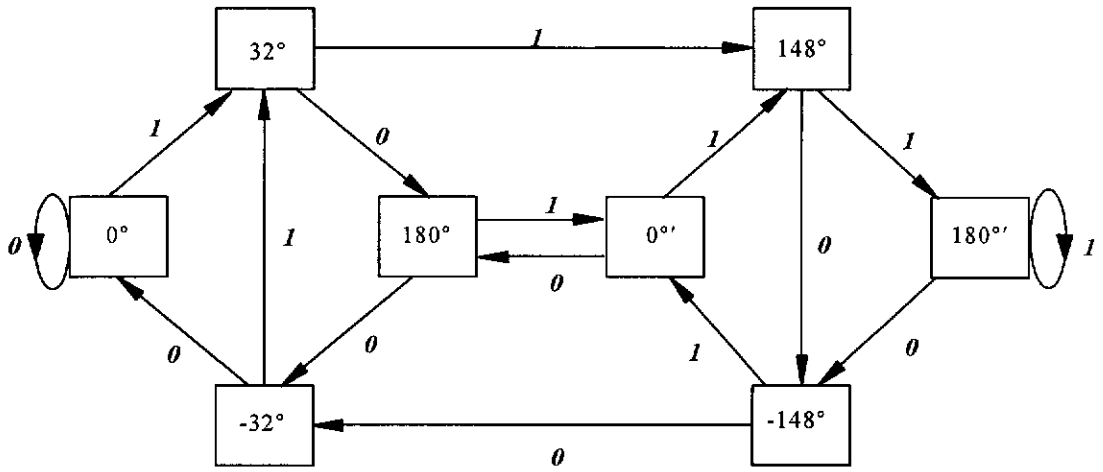

Figure 4.7 The finite state diagram describing the phase changes over one bit period of differentially encoded GMSK signal.

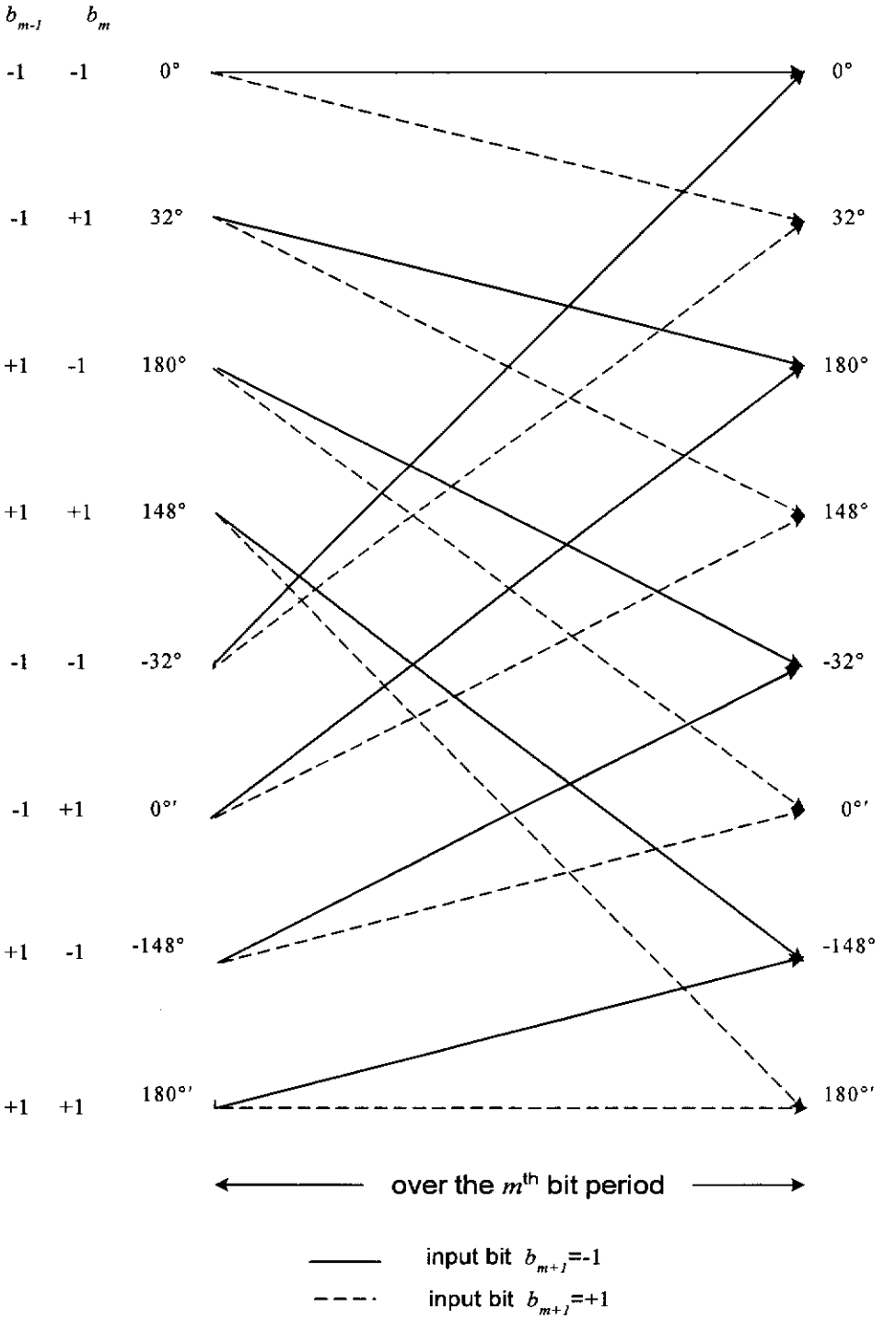

Figure 4.8 The trellis diagram of the differentially encoded GMSK signal.

4.4 Trellis Diagrams for Trellis Coded GMSK Signals

The construction of the trellis diagram for a trellis coded GMSK signal is illustrated using the following example, which combines the trellis of a rate-½ convolutional code with that of GMSK.

Consider a (2,1,2) rate-½ convolutional code having constraint length 2. Suppose the encoder of this code, as shown in Fig. 4.9a, has the connection vectors G_1=[1 1] and G_2=[0 1]. As explained in Section 2.5, these connection vectors can also be represented as generator polynomials [1+D, 1] or in octal form as [3,1]. In the rest of this thesis, the octal form representation will be adopted for specifying a convolutional code. The operation of the encoder, as shown in Fig. 4.9a, is described by the trellis representation of Fig. 4.9b. A detailed description of the coding operation and the construction of the trellis diagram of a convolutional encoder has been given in Section 2.5.

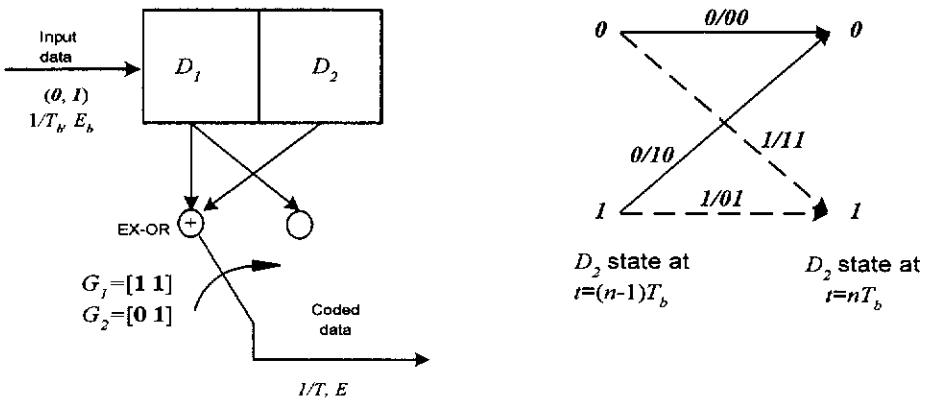

(a) (b)

Figure 4.9 (a) Encoder **(b)** Trellis diagram, of the code [3,1].

The states of the trellis diagram representing the trellis coded GMSK signal are dictated by both the binary state of the encoder and the phase state of the GMSK signal. For example, if the shift registers of the encoder shown in Fig. 4.9a are initialised to zero, and the initial phase state of the GMSK modulator is at 0°, then the initial state of the combined state machine will be at the state, (*0*,0°). When an input data bit *1* enters into D_1, it will give rise to two coded bits *11*, as shown in Fig. 4.9a. When the next data bit enters the shift register D_1, the previous data bit *1* is now shifted to D_2, resulting in the

encoder state D_2, at the end of the first data bit period, becoming *1*, as shown in Fig. 4.9b. Consequently, the binary state of the trellis coded GMSK signal after the first data bit period will be *1*. The coded bits *11* are then serially sent to the GMSK modulator as shown in Fig. 4.4. The resulting phase state of the combined state machine will be the phase state of the modulator at the end of the two coded bit periods *11*. From Fig. 4.2, the phase state of the modulator will reach 180° at the end of the input bit period T_b, after going through an intermediate phase state of 32°. The intermediate phase state corresponds to the phase value after the first coded bit period T. Thus, when an input data bit *1* enters D_1, the combined state machine will reach the state (*1*,180°) through the intermediate phase value of 32°, as shown in Fig. 4.10a. Here, the intermediate phase values after one coded bit period T, when going from one state to the other, are shown at the middle of each line. Similarly, when the initial state of the combined state machine is at (*0*,0°), a data bit *0* input to D_1, will transfer the combined state machine to the state (*0*,0°) through the intermediate phase value of 0° as shown in Fig. 4.10a.

Now, starting from these two new states, the next possible states of the combined state machine corresponding to the data bits *0* and *1* input to the encoder stage D_1, can be obtained in a similar manner. For example, when the current state of the combined state machine is (*1*,180°), the encoder state D_2, is also *1*. When an input data bit *0* enters into D_1, the two corresponding coded bits will now be *10*, as shown in Fig. 4.9a. When the next data bit enters the shift register D_1, the previous data bit *0* is now shifted to D_2, moving the next binary state of the trellis coded GMSK signal to *0*. As shown in Fig. 4.2, the two coded bits *10* will move the initial phase state of the trellis coded signal, 180°, to 148° through the intermediate phase state of 0°'. Thus, the next state of the trellis coded signal when an input data bit *0* enters the encoder stage D_1, will be (*0*,148°). This is illustrated in Fig. 4.10b. Similarly, when the input data bit to the encoder stage D_1 is *1* and the current state of the combined state machine is (*1*,180°), the corresponding coded bits *01* will move the trellis coded signal to the state (*1*,32°) through the intermediate phase state of -32°.

Repeating this procedure for all the new states in the combined state machine, the combined trellis diagram as shown in Fig. 4.10c is obtained. It can be observed from Fig. 4.10c, that the initial state (θ,0°) of the combined state machine may only reach one of the 8 states. Consequently, the 8-state trellis representing the rate-½ convolutional code [3,1], when combined with the GMSK signal used by the Viterbi decoder, can be presented as shown in Fig. 4.11.

The above technique will be used in this study to construct the combined trellis diagrams required for obtaining the free Euclidean distances of the proposed trellis coded GMSK schemes.

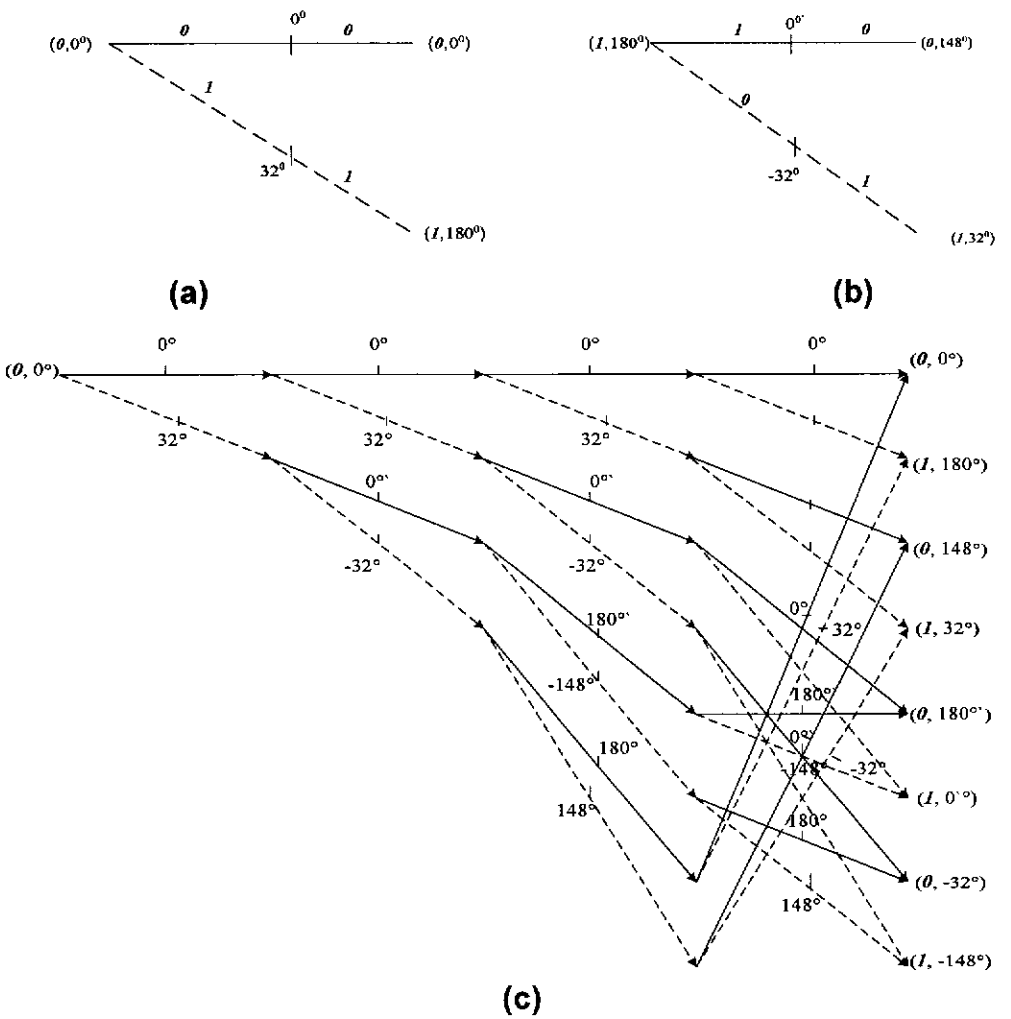

Figure 4.10 Construction of the combined trellis diagram of the code [3,1] with GMSK signal.

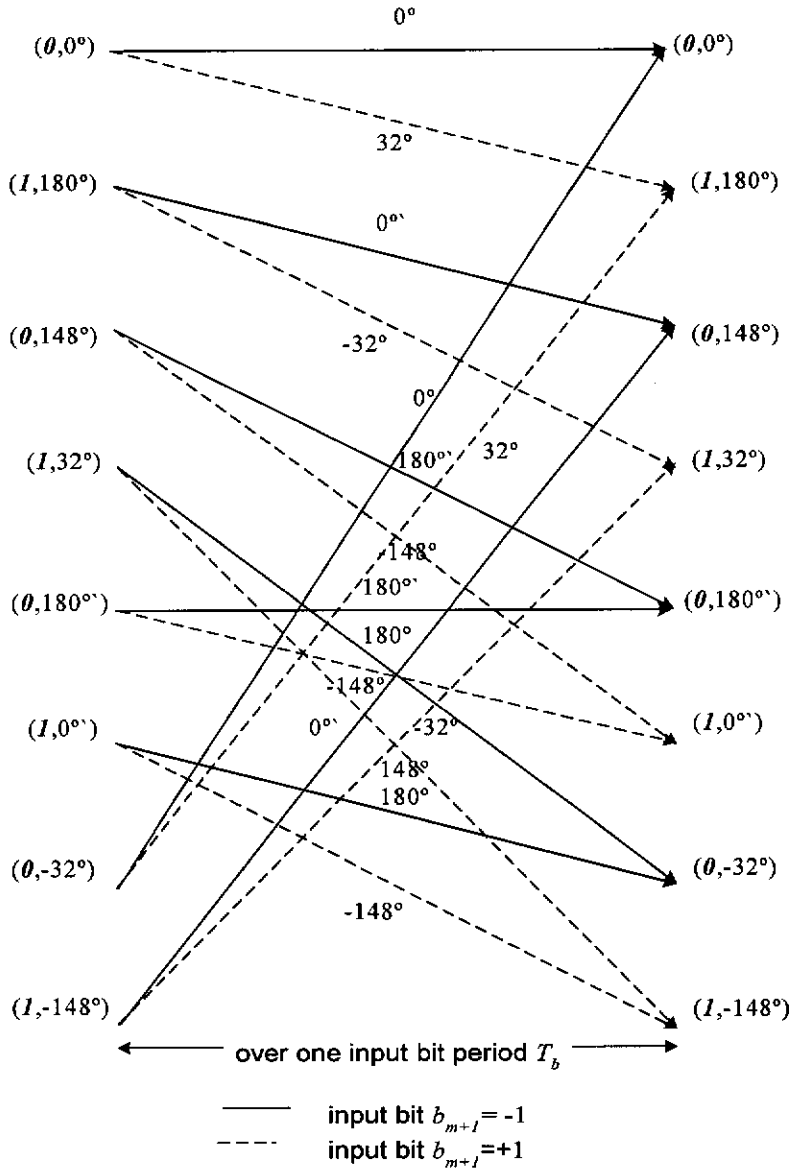

Figure 4.11 Combined trellis diagram of the code [3,1] with GMSK signal.

Next, the effect of differential encoding prior to modulation, on the receiver complexity, based on the number of states in the combined trellis, is studied. In this case, the same rate-½ convolutional code, [3,1], used in the previous example, is combined with the differentially encoded GMSK signal. In this case, the coded bits are differentially encoded before sending them to the GMSK modulator, as shown in Fig. 4.6. The combined trellis diagram of the code [3,1] with the differentially encoded GMSK signal, as shown in Fig. 4.12, has been obtained by combining the trellis of the code [3,1], given in Fig. 4.9a, with the trellis of the differentially encoded GMSK signal given in Fig. 4.8. From the trellis diagrams shown in figures 4.11 and 4.12, it is observed

that differential encoding prior to modulation leads to a reduction in the number of states in the combined trellis, reducing the receiver complexity. It has also been observed from Fig. 4.2, that the number of states in the trellis representing the uncoded GMSK is 8. Therefore, it can be seen that the coded scheme using the code [3,1] in combination with differentially encoded GMSK modulation has a less complex receiver, compared to that of the uncoded.

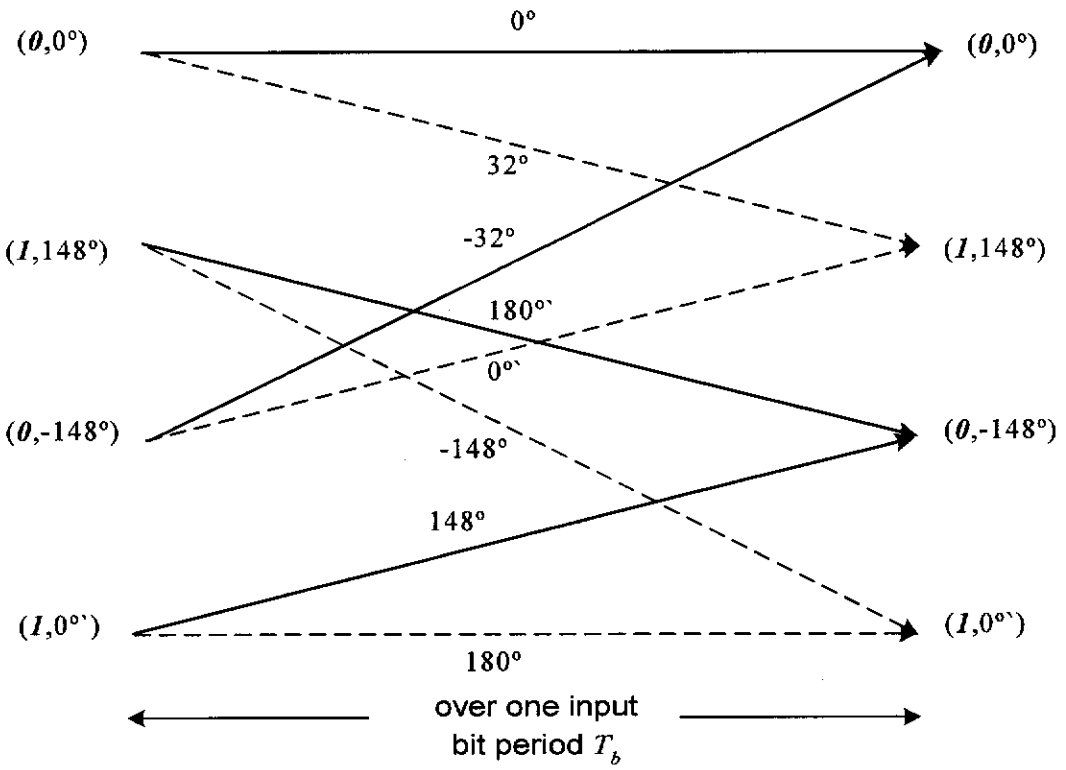

Figure 4.12 Combined trellis diagram of the code [3,1] with differentially encoded GMSK signal.

Now, the effect of the connection vectors of a particular code on the number of states in the combined receiver is demonstrated using a code having the same constraint length, 2 as before. Here, the generator matrix of the previous code [3,1] is exchanged to give the code [1,3] and produce the connection vectors G_1=[0 1] and G_2=[1 1]. The encoder, and the trellis diagram of the code [1,3] are shown in Figures 4.13a and 4.13b, respectively. As shown in Fig. 4.13b, the number of states in the trellis of this code is 2, as in the code [3,1]. However, when the code [1,3] is combined with differentially encoded GMSK, the total number of states in the combined trellis becomes 8 as shown in Fig. 4.13c. Thus, it may be observed from Figures 4.12 and

4.13c, that the receiver complexity of the trellis coded and differentially encoded GMSK, with code having the generator polynomial [1,3], is doubled compared to that of the code with [3,1]. Moreover, the number of states in the resultant trellis with the code [1,3] is the same as that of the uncoded GMSK. From this example, it may be concluded that the receiver complexity of a combined coded scheme using a code with the same constraint length may also depend on the connection vectors of the code.

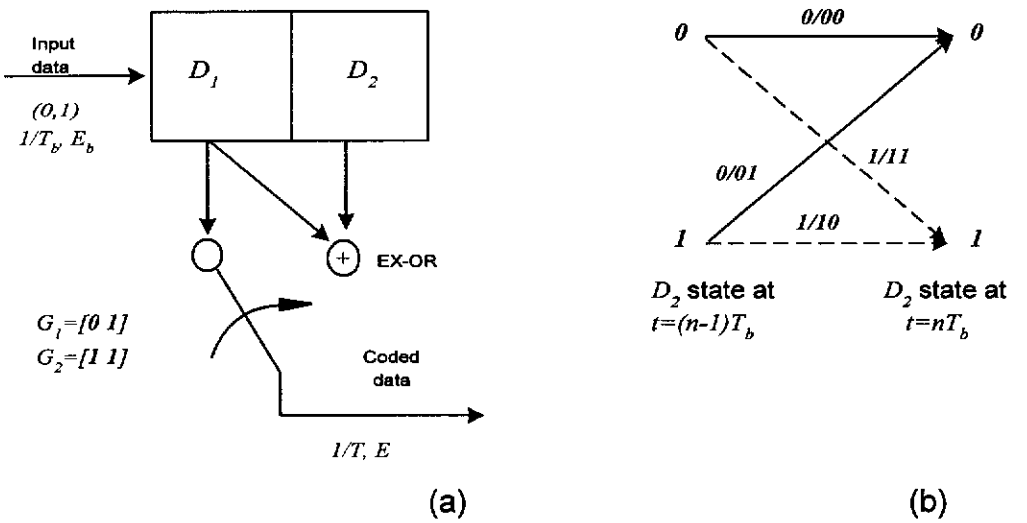

Figure 4.13 (a) Encoder **(b)** Trellis diagram, of the code [1,3].

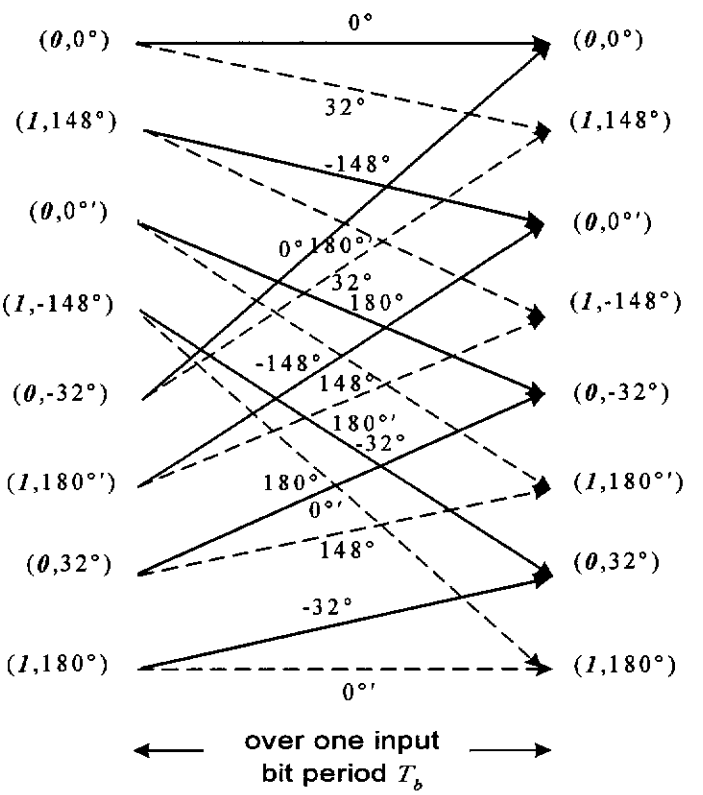

Figure 4.13c Combined trellis diagram of the code [1,3] with differentially encoded GMSK signal.

4.5 Free Distances of Trellis Coded GMSK Signals

As discussed in Section 4.3, in this study the detection of various trellis coded GMSK signals, corrupted by AWGN, is carried out assuming coherent quadrature demodulation, followed by soft decision Viterbi decoding. A detailed description of the Viterbi decoding has been given in Section 2.6.1. The distance measure normally used in Viterbi decoding for selecting the conventional convolutional codes, is the free Hamming distance (Viterbi and Omura, 1979; Clark and Cain, 1981). However, in this study the selection of the appropriate trellis coded GMSK signals is based on the largest free distance of the coded scheme (Lindell *et al*, 1984, Anderson *et al*, 1986), so that the code and the GMSK signal are considered as a single entity. Also, note that the distances discussed in the rest of the study are referred to as the signal-space distances.

The squared free distance of a coded scheme is defined as the minimum Squared Euclidean Distance (SED) in signal space between any two signal paths which originate from a common node and merge into a single node at a later time in the combined trellis (Anderson *et al*, 1991). Therefore, to determine the value of the free squared distance or the minimum SED of a combined coded scheme, the SEDs of all possible pairs of paths, which split and remerge at a later time in the trellis, have to be considered. If $D^2_{min}(N)$ is the minimum SED between all the pairs of paths which split at t=0 and remerge at t=NT, then the squared free distance becomes the global minimum of such minimum SEDs for all the values of N. That is (Anderson *et al*, 1986),

$$D^2_{free} = \min_{N} [D^2_{min}(N)], \tag{4.3}$$

where N ideally extends to infinity. The SED in signal-space between any two given signals $s_i(t)$ and $s_j(t)$, over an interval $kT \leq t < (k+1)T$ can be expressed as (Anderson and Sundberg, 1991)

$$D^2_k(i,j) = \int_{kT}^{(k+1)T} [s_i(t) - s_j(t)]^2 \, dt. \tag{4.4}$$

This results in

$$D^2_{min}(N) = \min_{s_i(t) \neq s_j(t)} \left\{ \sum_{k=0}^{N-1} \int_{kT}^{(k+1)T} \left[s_i(t) - s_j(t) \right]^2 dt \right\}. \quad (4.5)$$

The integral in Eq. (4.5) can be expanded as

$$\int_{kT}^{(k+1)T} \left[s_i(t) - s_j(t) \right]^2 dt = \int_{kT}^{(k+1)T} s^2_i(t)\, dt + \int_{kT}^{(k+1)T} s^2_j(t)\, dt - 2 \int_{kT}^{(k+1)T} s_i(t) s_j(t)\, dt. \quad (4.6)$$

The signals $s_i(t)$ and $s_j(t)$ considered in this study are constant envelope GMSK signals, represented by

$$s_i(t) = \sqrt{2E/T}\, \cos\left(2\pi f_c t + \phi_i(t) + \phi_0\right) \quad (4.7a)$$

and

$$s_j(t) = \sqrt{2E/T}\, \cos\left(2\pi f_c t + \phi_j(t) + \phi_0\right). \quad (4.7b)$$

Here ϕ_0 is an arbitrary constant, which represents the initial phase of the signal. This can be set to zero with no loss of generality. The phases $\phi_i(t)$ and $\phi_j(t)$ are the phase angles in modulo-2π at time t, of the two signals $s_i(t)$ and $s_j(t)$, respectively, and E is the transmitted signal energy per bit over one bit interval T. As presented in Section 4.3, note that with the coded schemes using rate-½ codes, each input bit having a period T_b and energy E_b, provides two coded bits, each with a period $T=T_b/2$ and energy $E=E_b/2$. Using the expressions in Eq. (4.7a) and Eq. (4.7b) for $s_i(t)$ and $s_j(t)$, Eq. (4.6) can be re-written as

$$\int_{kT}^{(k+1)T} \left[s_i(t) - s_j(t) \right]^2 dt = 2E - 2 \int_{kT}^{(k+1)T} s_i(t) s_j(t)\, dt,$$

$$= 2E - 2 \int_{kT}^{(k+1)T} \frac{2E}{T} \cos\left[2\pi f_c t + \phi_i(t)\right] \cos\left[2\pi f_c t + \phi_j(t)\right] dt,$$

$$= 2E - \int_{kT}^{(k+1)T} \frac{2E}{T} \cos\left[\phi_i(t) - \phi_j(t)\right] dt$$

$$- \int_{kT}^{(k+1)T} \frac{2E}{T} \cos\left[4\pi f_c t + \phi_i(t) + \phi_j(t)\right] dt.$$

As $f_c >> \frac{1}{T}$, the second integral averages out to zero over one bit period T. Hence,

$$\int_{kT}^{(k+1)T} \left[s_i(t) - s_j(t)\right]^2 dt \approx 2E - \int_{kT}^{(k+1)T} \frac{2E}{T} \cos\left[\phi_i(t) - \phi_j(t)\right] dt.$$

$$\approx \frac{2E}{T} \int_{kT}^{(k+1)T} \left\{1 - \cos[\Delta\Phi(t)]\right\} \, dt, \tag{4.8}$$

where, $\Delta\Phi(t)=[\phi_i(t)-\phi_j(t)]$. Assuming that the signal shape consisted of instantaneous phase changes, i,e., $\Delta\Phi(t)= \Delta\Phi[(k+1)T]$ for $kT< t \leq (k+1)T$, Eq. (4.8) can be approximated as

$$\int_{kT}^{(k+1)T} \left[s_i(t) - s_j(t)\right]^2 \, dt \approx 2E \left\{1 - \cos\left[\Delta\Phi\left[(k+1)T\right]\right]\right\}. \tag{4.9}$$

Here, $\Delta\Phi[(k+1)T]$ is the phase difference at the sampling instant $(k+1)T$ between the two signals $s_i(t)$ and $s_j(t)$. With this, Eq. (4.5) can be written as

$$D^2_{min}(N) = \min_{s_i(t)\neq s_j(t)} \left[\sum_{k=0}^{N-1} 2E \left\{1 - \cos\left[\Delta\Phi\left[(k+1)T\right]\right]\right\}\right]. \tag{4.10}$$

Here, $s_i(t)\neq s_j(t)$ is equivalent to $\Delta\Phi(t)\neq 0$.

Eq. (4.10) is often normalised with respect to the bit energy in order to obtain a measure of distance that depends only on the code structure and not the coded bit energy (Anderson *et al*, 1991). This may be achieved by forming the normalised minimum SED, $d^2_{min}(N)$, defined by (Lindell *et al*, 1984)

$$d^2_{min}(N) = \min_{s_i(t)\neq s_j(t)} \left[\frac{1}{2E} \sum_{k=0}^{N-1} \int_{kT}^{(k+1)T} \left[s_i(t) - s_j(t)\right]^2 dt\right]. \tag{4.11}$$

From Eq. (4.10) and (4.11), the normalised minimum SED between all the pairs of paths which split at $t=0$ and remerge at $t=NT$ can be obtained as

$$d^2_{min}(N) = \min_{s_i(t)\neq s_j(t)} \left[\sum_{k=0}^{N-1} \left\{1 - \cos\left[\Delta\Phi\left[(k+1)T\right]\right]\right\}\right]. \tag{4.12}$$

Based on Eq. (4.12), the normalised minimum SEDs of any level N, at $t=NT$, can be obtained. Then, by considering a very long observation interval NT (i.e., ideally $N\rightarrow\infty$), the normalised squared free distance of a coded scheme can be obtained.

4.6 A Computer Search Method for Selecting the Appropriate Convolutional Codes

The appropriate convolutional codes, which when combined with differentially encoded GMSK to produce the largest free distance, are first selected using a computer search method. Those coded schemes having the largest free distances are then examined for their complexity in terms of the number of phase states involved in Viterbi decoding.

The computer search procedure used in this study can be explained using the flow charts shown in Fig. 4.14a and Fig. 4.14b. With this procedure, the search for the minimum distances associated with convolutional codes of different constraint lengths can be independently carried out. The search for the code is initiated with a given constraint length. The phase angles representing the states of the combined trellis of a coded scheme having that defined constraint length are then input. The normalised squared free Euclidean distance, Max[FED], is set to zero at the start of the search. Then, the search proceeds with the normalised minimum SED of the specified coded scheme obtained according to the steps in Fig. 4.14b.

Initially, the normalised minimum SED is set to a large value. Starting from a state at time t=0, the paths that remerge at level N, i.e., after N input bit periods, NT_b, are found. The normalised SED of these paths are then computed as explained in the following example for the trellis shown in Fig. 4.15. Here, the rate-½ code having the generator polynomial [3,1] is combined with differentially encoded GMSK. In this case of coded transmission, if the sampling is carried out at the actual transmission rate $1/T$, which equals to $2/T_b$, there will be twice as many samples involved in calculating the distance compared to the uncoded scheme. From Fig. 4.15, it can be seen that the first remerge of the paths initiated from the state at t=0 occurs after 3 input bit periods $3T_b$, corresponding to 6 coded bit periods $6T$. The SED of the pair of paths which split and remerge in Fig. 4.15, starting at t=0 from the state $(\theta,0^\circ)$ and remerging at state $(\theta,0^\circ)$ after $6T$ can be obtained according to Eq. (4.9) as

$$d^2(6) = \sum_{k=0}^{5} 2E\left\{1-\cos\left[\Delta\Phi\left[(k+1)T\right]\right]\right\}. \tag{4.13}$$

Here, $\Delta\Phi[(k+1)T]$ is the phase difference at the sampling instants $(k+1)T$ between the signals representing the two merged paths. Using the phase values of these paths at the sampling instants as shown in Fig. 4.15, Eq. (4.13) can be expanded as

$$\begin{aligned} d^2(6) &= 2E\ \{\ [1-\cos(0^\circ-32^\circ)] + [1-\cos(0^\circ-148^\circ)] + [1-\cos(0^\circ-180^\circ)] \\ &\quad + [1-\cos(0^\circ-(-148^\circ))] + [1-\cos(0^\circ-(-32^\circ))] + [1-\cos(0^\circ-0^\circ)]\ \} \\ &= 12E. \end{aligned} \tag{4.14}$$

According to Eq. (4.11), this SED is equivalent to a normalised SED of 6. At this stage, if the corresponding value of normalised SED obtained for these two paths is smaller than the current normalised minimum SED, the new one is updated as the minimum at that particular level, i.e., N=3. Similarly, the normalised SED values of all the paths which split from each state at t=0, and remerge at a common state at $t=NT_b$ (N=3,4, ...N`) are calculated, and the corresponding normalised minimum SED at each level N, is updated. By comparing the values of minimum normalised SEDs obtained at each level, the global minimum of the normalised SED or the normalised FED of the particular coded scheme is obtained. Theoretically, the observation interval NT_b should be extended to infinity in order to obtain the free distance of a coded scheme (Anderson *et al*, 1986). However, in practice, the values of minimum SEDs tend to converge to the FED over a sufficiently large value of N. In this study, it has been observed that the global minimum of the normalised SED of all the coded schemes considered was reached within $16T_b$.

Once the value of normalised squared FED of each individual coded scheme is calculated, it is compared against the current value of the largest normalised squared FED, as shown in the blocks between **M** and **P** of Fig. 4.14a. If the value of the newly determined normalised squared FED is greater than that of the previous value, it will then be updated as the new maximum FED. This search procedure is repeated for all the available codes of the same specified constraint length in combination with differentially

encoded GMSK, until a code having the largest normalised FED is found. The same search procedures are then repeated, for selecting the appropriate codes of different constraint lengths when combined with differentially encoded GMSK.

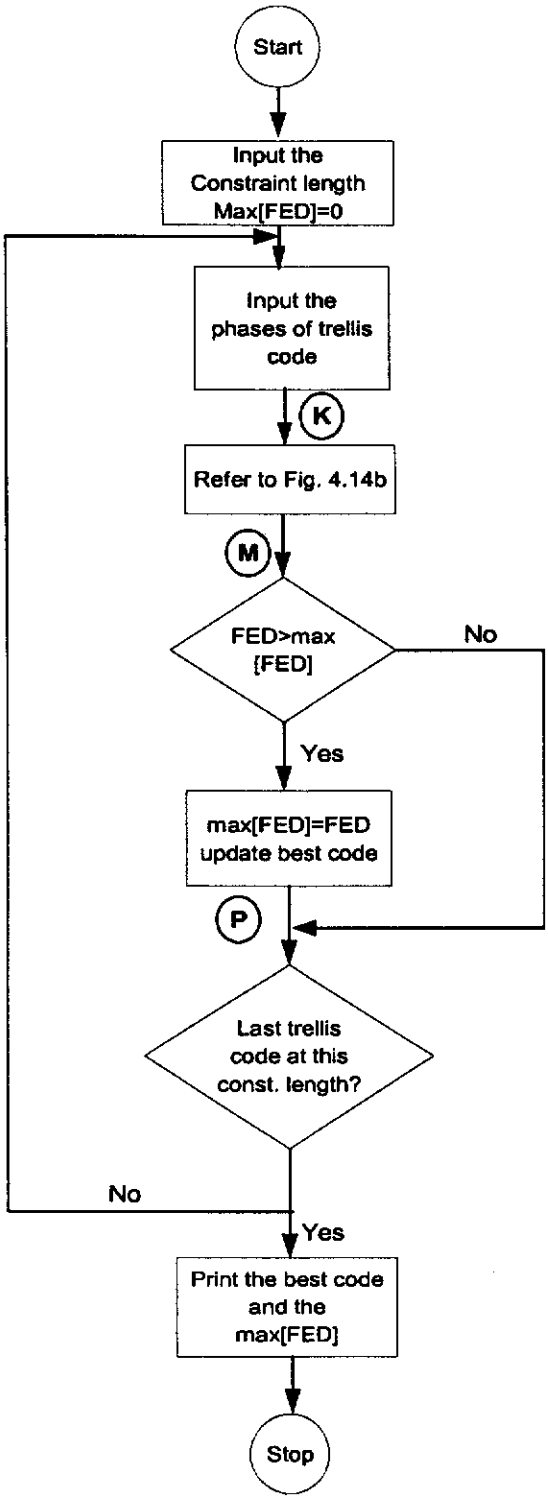

Note : FED – normalised squared free Euclidean distance
: Refer to Fig. 4.14b for the operations of the blocks between **K** and **M**

Figure 4.14a The basic flow chart of the computer search.

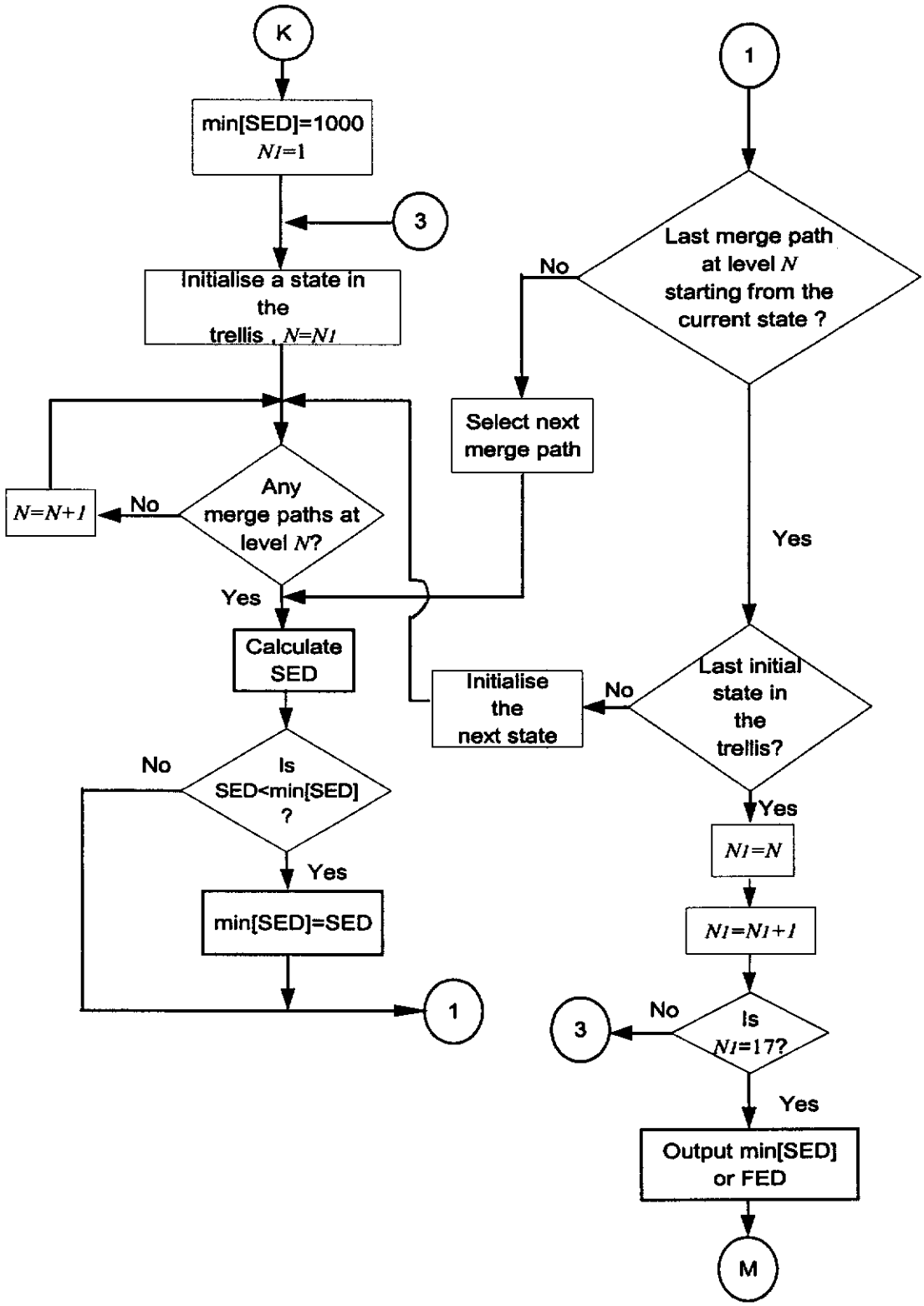

Note : SED – normalised squared Euclidean distance

Figure 4.14b The flow chart for the search for normalised squared FED.

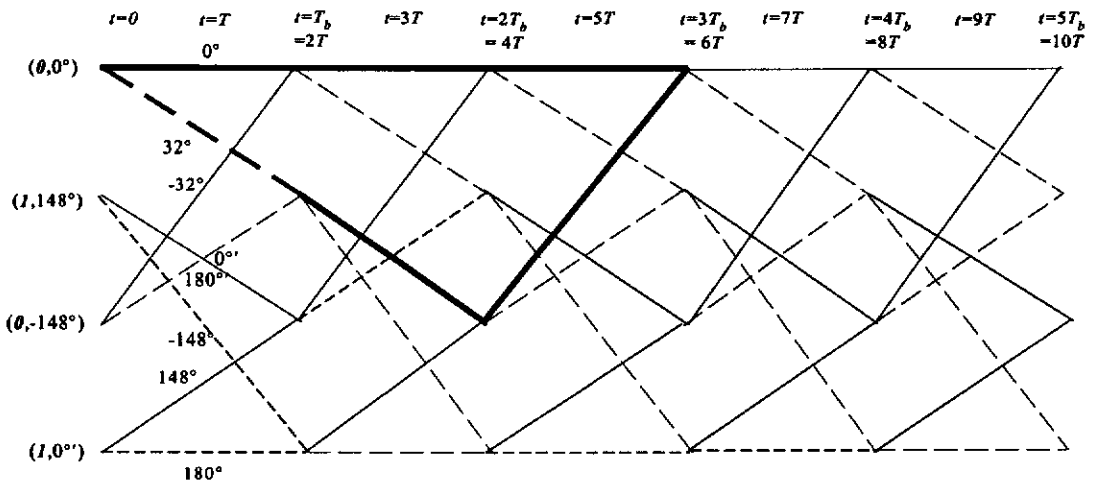

Figure 4.15 Combined trellis diagram of the code [3,1] with differentially encoded GMSK showing split and merge paths.

The computational complexity of the search increases exponentially with the number of states in the combined trellis. Furthermore, a larger number of states gives rise to an increased receiver complexity based on the Viterbi decoding. Consequently, only the codes with a maximum of 16 states in their combined trellises have been considered in this research.

It has been observed from this study that codes having different combinations of generator polynomials with constraint length 4, when combined with differentially encoded GMSK, may provide either 16 or 32 states in their combined trellises. In view of the increased computational efforts and decoder complexity, only codes which yield 16 states in the combined trellis, have been considered. As a result, the total number of such codes with constraint lengths 2, 3, and 4 considered in this study are 8, 40, and 56, respectively.

4.7 Selection of Appropriate Convolutional Codes

The values of normalised squared FEDs of rate-½ convolutional codes having constraint length 2 when combined with differentially encoded GMSK signals obtained by computer search are presented in Table 4.3. The corresponding numbers of states involved in Viterbi decoding are also given in Table 4.3. Results obtained for codes having constraint lengths 3 and 4 are tabulated in Tables 4.4 and 4.5, respectively. In these tables, those codes having the largest values of normalised squared FEDs with different complexities are signified in bold face. From Tables 4.3 to 4.5, codes of constraint lengths 2, 3, and 4 associated with the largest FED as well as requiring the minimum number of states in the combined trellis are selected for further detailed study. A summary of these selected codes is tabulated in Table 4.6.

For a particular selected coded GMSK scheme, the asymptotic coding gain, based on its free distance, with respect to the uncoded GMSK signal can be defined as (Haykin, 1988)

$$\text{asymptotic coding gain} = 10\log_{10}\left[\frac{\text{normalised squared FED of the coded signal}}{\text{normalised squared FED of the uncoded signal}}\right] \tag{4.15}$$

The normalised squared FED of the uncoded GMSK signal has been obtained using the phase states of the trellis of the GMSK signal as given in Fig. 4.2. Accordingly, the squared FED of the uncoded GMSK signal normalised with respect to the input bit energy E_b over an input bit interval T_b is found to be 1.74227. Thus, the asymptotic coding gains of the selected codes are obtained using Eq. (4.15). These coding gains are presented in Table 4.6. It should be noted that the calculation of coding gains is carried out based on the input bit energy E_b over input bit interval T_b. The computed squared FEDs of the coded schemes are also normalised to the input bit energy E_b. In the case of rate-½ codes, the transmitted coded bit energy E=E_b/2 as discussed in Section 4.3.

From the results presented in Table 4.6, it may be observed that combining the selected constraint length 2 code [3,1], with differentially encoded GMSK, a coding gain of 2.36 dB can be obtained. Moreover, it can be seen that this coding gain is achieved with a decoder having half the number of states compared to the uncoded GMSK signal. Thus, when the code [3,1] is combined with differentially encoded GMSK, this leads to a decrease in receiver complexity compared to the uncoded GMSK, while yielding a coding gain of 2.36 dB.

For codes with constraint length 3, two codes [6,3] and [7,3] have been selected as the appropriate codes. It may also be observed from Table 4.6, that these two selected codes when combined with differentially encoded GMSK produce a coding gain of 3.61 dB. Moreover, these two codes require the same number of states in the Viterbi decoder as the uncoded GMSK. These results show that for codes of constraint length 2 and 3, which have been appropriately chosen, when combined with differentially encoded GMSK could achieve coding gains compared to the uncoded scheme without increasing the decoder complexity. On the other hand, for the selected codes having constraint length 4, [13,7] and [15,7], the decoder complexity based on the number of states in the receiver is doubled compared to the uncoded scheme. However, a larger coding gain of 5.06 dB is achieved when compared to codes of constraint length 2 and 3. This means that codes with constraint length 4 may be suitable for applications in which a larger coding gain is required for a slight increase in receiver complexity.

Generator polynomial of the code in octal form	Normalised squared FED of the coded signal	Number of states in the Viterbi decoder
[1,2]	3.48455	8
[1,3]	5.43837	8
[2,1]	4.00000	4
[2,2]	4.00000	8
[2,3]	6.00000	8
[3,1]	**6.00000**	**4**
[3,2]	5.43837	8
[3,3]	**8.00000**	**8**

Note : The above codes have been tested based on only the normalised FED and the complexity of the Viterbi decoder. They have not been tested for catastrophy.

Table 4.3 The values of normalised squared FED of rate-½ convolutional codes having constraint length 2 when combined with differentially encoded GMSK. The corresponding numbers of states for Viterbi decoding are also shown.

Generator polynomial of the code in octal form	Normalised squared FED of the coded signal	Number of states in the Viterbi decoder	Generator polynomial of the code in octal form	Normalised squared FED of the coded signal	Number of states in the Viterbi decoder
[1,4]	3.48455	16	[6,4]	5.43837	16
[1,5]	5.74227	16	[6,5]	7.69610	16
[1,6]	4.92292	16	[6,6]	8.00000	16
[1,7]	6.87674	16	[6,7]	8.00000	16
[2,4]	3.48455	16	[7,4]	6.87674	16
[2,5]	5.74227	16	**[7,5]**	**9.69610**	**16**
[2,6]	5.43837	16	[7,6]	7.48455	16
[2,7]	7.18065	16	[7,7]	8.00000	16
[3,4]	4.92292	16	[4,1]	3.48455	8
[3,5]	7.74227	16	[4,2]	4.00000	8
[3,6]	6.87674	16	[4,3]	5.43837	8
[3,7]	7.48455	16	[5,1]	5.74227	8
[4,4]	4.00000	16	[5,2]	5.74227	8
[4,5]	5.74227	16	[5,3]	7.69610	8
[4,6]	6.00000	16	[6,1]	5.43837	8
[4,7]	7.18065	16	[6,2]	6.00000	8
[5,4]	5.74227	16	**[6,3]**	**8.00000**	**8**
[5,5]	8.00000	16	[7,1]	7.18065	8
[5,6]	7.74227	16	[7,2]	7.18065	8
[5,7]	**9.69610**	**16**	**[7,3]**	**8.00000**	**8**

Note : The above codes have been tested based on only the normalised FED and the complexity of the Viterbi decoder. They have not been tested for catastrophy.

Table 4.4 The values of normalised squared FED of rate-½ convolutional codes having constraint length 3 when combined with differentially encoded GMSK. The numbers of states required for Viterbi decoding are also shown.

Generator polynomial of the code in octal form	Normalised squared FED of the coded signal	Generator polynomial of the code in octal form	Normalised squared FED of the coded signal
[10,1]	3.48455	[14,1]	4.92292
[10,2]	3.48455	[14,2]	5.43837
[10,3]	4.92292	[14,3]	6.87674
[10,4]	4.00000	[14,4]	6.00000
[10,5]	5.74227	[14,5]	7.74227
[10,6]	5.43837	[14,6]	8.00000
[10,7]	6.87674	[14,7]	7.48455
[11,1]	5.74227	[15,1]	7.18065
[11,2]	5.78845	[15,2]	7.18065
[11,3]	5.48455	[15,3]	9.13447
[11,4]	5.74227	[15,4]	7.74227
[11,5]	8.00000	[15,5]	10.0000
[11,6]	7.18065	[15,6]	9.43837
[11,7]	9.69610	**[15,7]**	**11.18065**
[12,1]	5.74227	[16,1]	6.87674
[12,2]	5.74227	[16,2]	7.18065
[12,3]	7.74227	[16,3]	7.48455
[12,4]	5.74227	[16,4]	7.18065
[12,5]	8.00000	[16,5]	9.69610
[12,6]	7.69610	[16,6]	8.00000
[12,7]	4.60781	[16,7]	8.00000
[13,1]	7.74227	[17,1]	7.18065
[13,2]	7.18065	[17,2]	6.66520
[13,3]	9.43837	[17,3]	7.78455
[13,4]	7.18065	[17,4]	7.18065
[13,5]	10.0000	[17,5]	11.13447
[13,6]	9.13447	[17,6]	7.48455
[13,7]	**11.18065**	[17,7]	8.00000

Note : The above codes have been tested based on only the normalised FED and the complexity of the Viterbi decoder. They have not been tested for catastrophy.

Table 4.5 The values of normalised squared FED of rate-½ convolutional codes having constraint length 4 when combined with differentially encoded GMSK (only codes with 16 states in the Viterbi decoder are shown).

Constraint length	Generator polynomial of the selected code in octal form	Normalised squared free distance of the coded signal	Number of states in the Viterbi decoder	Asymptotic coding gain compared to uncoded GMSK* (dB)
2	[3,1]	6.00000	4	2.360
3	[6,3]**	8.00000	8	3.609
	[7,3]	8.00000	8	3.609
4	[13,7]	11.18065	16	5.063
	[15,7]	11.18065	16	5.063

Note : *The normalised squared FED of uncoded GMSK is 1.74227
** As explained in page 84, code [6,3] is catastrophic

Table 4.6 The asymptotic coding gains associated with the selected coded schemes.

4.8 Trellis Diagrams of the Selected Coded GMSK Schemes

In this section, the trellis diagrams used in Viterbi decoding corresponding to the selected codes with constraint lengths 2, 3 and 4 combined with differentially encoded GMSK are presented.

The code [3,1] has been selected as the appropriate code with constraint length 2. The combined trellis of the selected code [3,1] with differentially encoded GMSK is shown in Figure 4.12. The selected codes, [7,3] and [6,3] having constraint length 3, can be expressed by their connection vectors G_1=[1 1 1], G_2=[0 1 1], and G_1=[1 1 0], G_2=[0 1 1], respectively. The corresponding encoder and the trellis diagram associated with the code [7,3] are shown in Figures 4.16a and 4.16b, respectively. The combined trellis diagram used in calculating the FED of the code [7,3] when combined with differentially encoded GMSK is shown in Figure 4.16c. The corresponding

diagrams of the encoder, the trellis and the combined trellis diagram of the code [6,3] are presented in Figures 4.17a, 4.17b, and 4.17c, respectively.

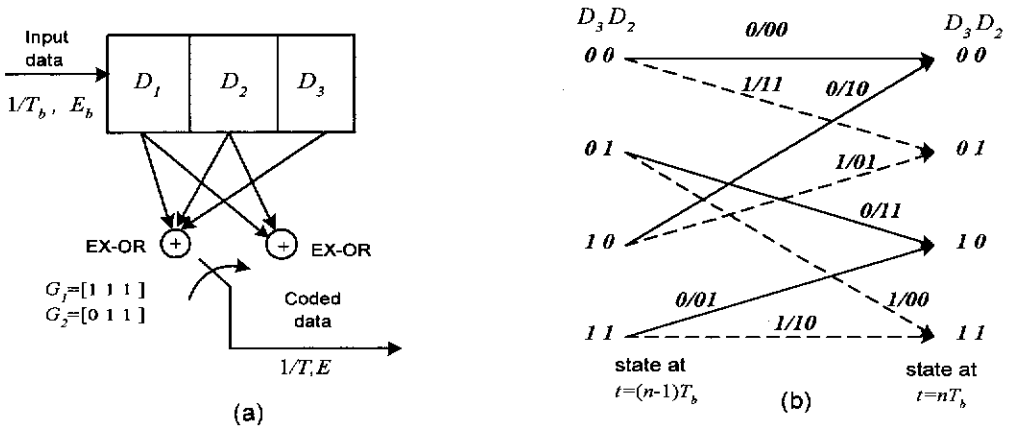

Figure 4.16 (a) Encoder **(b)** Trellis diagram, of the code [7,3].

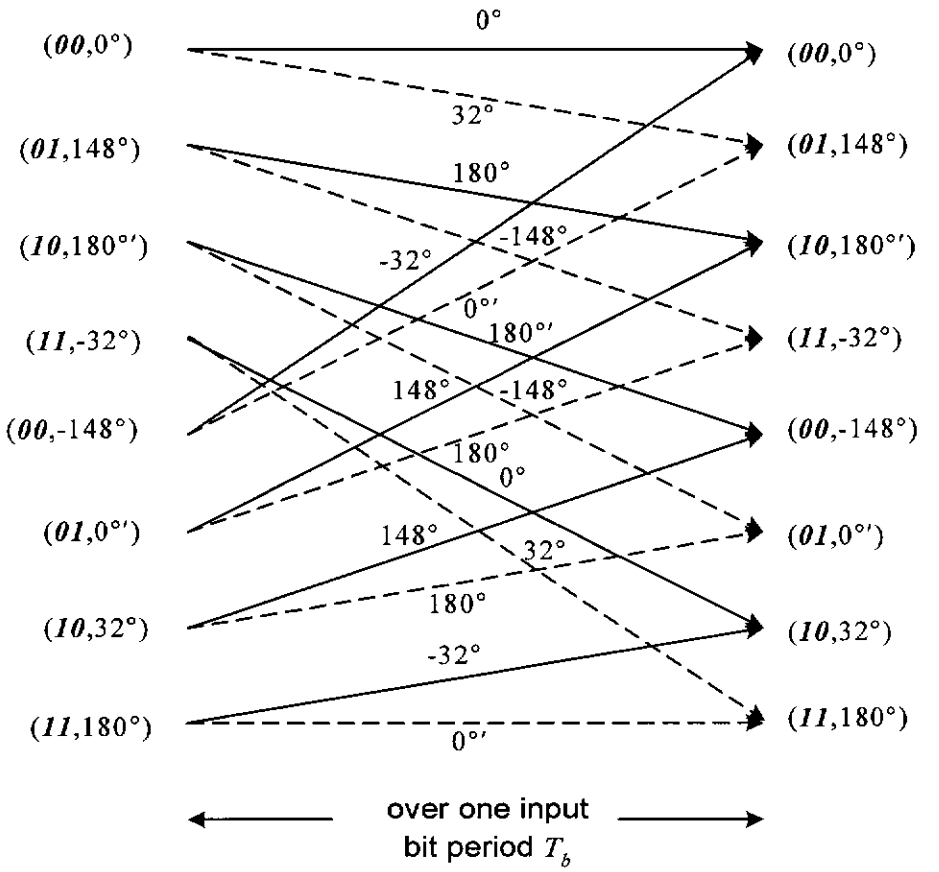

Figure 4.16c Combined trellis diagram of the code [7,3] with differentially encoded GMSK signal.

The code [6,3] is a catastrophic code and can be eliminated in the study. With catastrophic codes, a finite number of channel errors can cause an infinite number of information errors. Moreover, it can be observed from the combined trellis diagram for the code [6,3], as shown in Fig. 4.17c, that there

is symmetry between the states having the same phase values with different encoder states. For example, consider the two states (*01*, 32°) and (*10*,32°) having the same phase value 32°. Here, when the input bit to the encoder is *0*, the state (*01*,32°) will reach the state (*10*,180`°) through the intermediate phase state 148°. On the otherhand, the other state (*10*,32°) reaches a state having the same phase value 180`° through the same intermediate phase state 148° when the input bit to the encoder is *1*. The Viterbi decoding in this study is based on the Euclidean distances between the received signal and all the possible transmitted signals. Such Euclidean distances are calculated using the phase differences at the sampling instants as expressed in Eq. (4.9). Therefore, when the combined state is initially at (*01*, 32°), the distance between a received signal and the transmitted signal corresponding to input bit *0* becomes the same as that of the distance initiating from the state (*10*, 32°) corresponding to input bit *1*. This produces an ambiguity in the decoder, giving the same distances corresponding to bits having opposite polarity. Because of this ambiguity, the code [6,3] has not been considered for detailed study. Therefore, only the code [7,3] having constraint length 3 when combined with differentially encoded GMSK has been considered in this study.

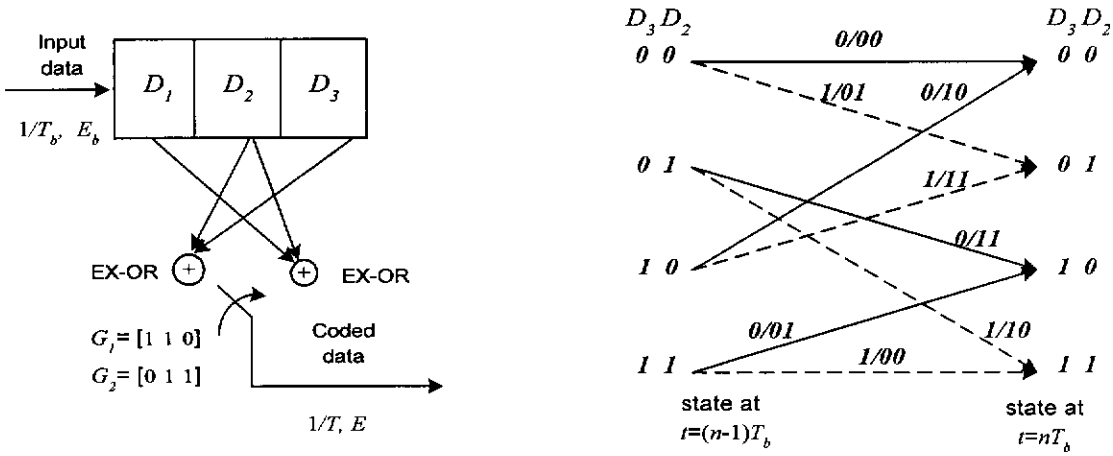

(a) (b)

Figure 4.17 (a) Encoder **(b)** Trellis diagram, of the code [6,3].

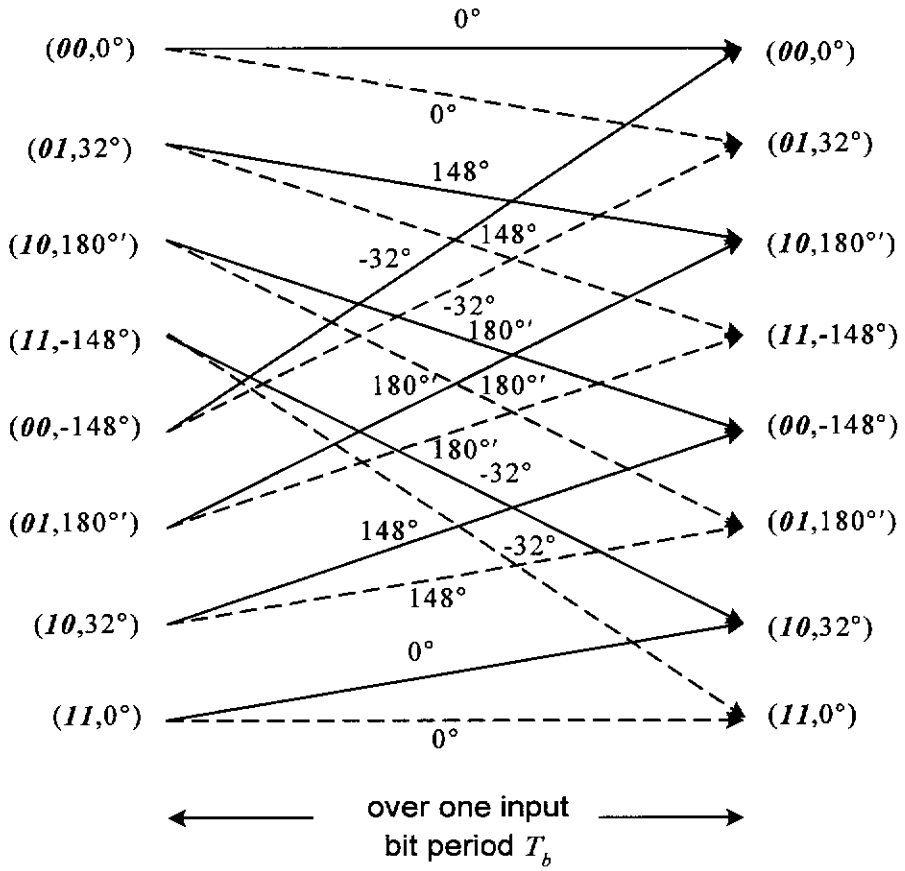

Figure 4.17c Combined trellis diagram of the code [6,3] with differentially encoded GMSK signal.

The selected codes having constraint length 4, [13,7] and [15,7], can be expressed by their connection vectors G_1=[1 0 1 1], G_2=[0 1 1 1], and G_1=[1 1 0 1], G_2=[0 1 1 1], respectively. The encoder, the trellis diagram, and the combined trellis diagram of the code [13,7] are shown in Figures 4.18a, 4.18b and 4.18c, respectively. The corresponding diagrams for the code [15,7] are presented in Figures 4.19a, 4.19b, and 4.19c, respectively.

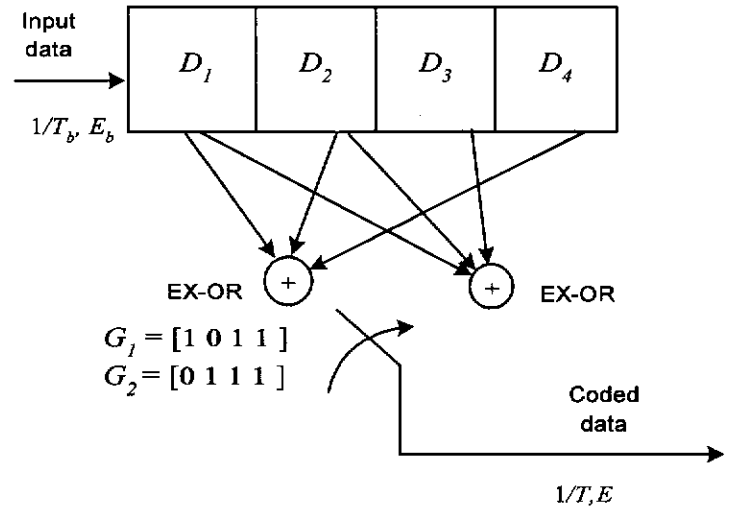

(a)

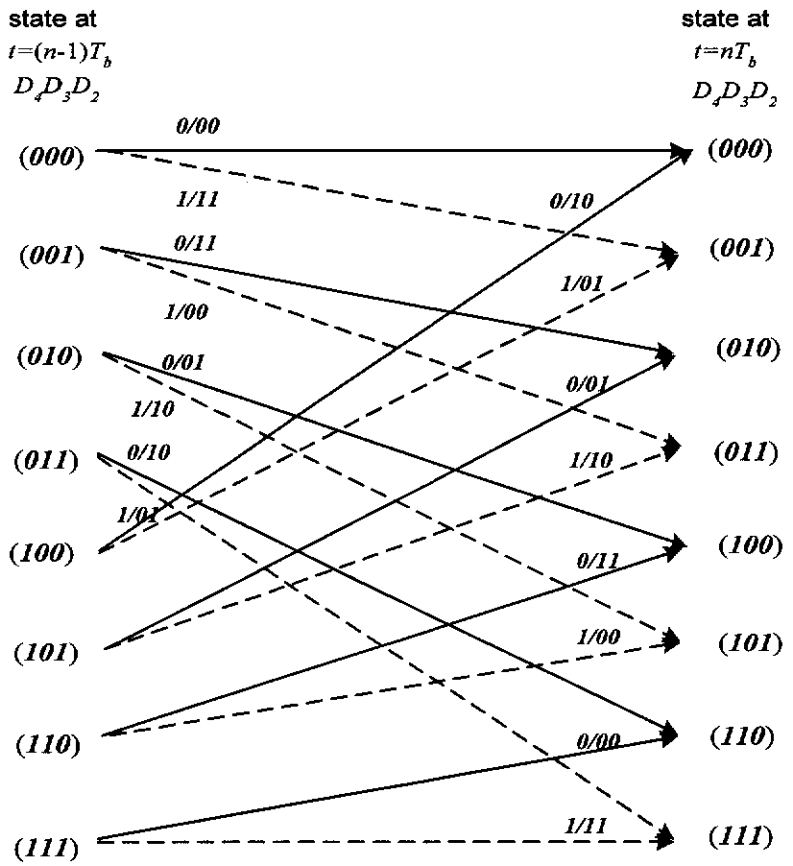

(b)

Figure 4.18 (a) Encoder **(b)** Trellis diagram, of the code [13,7].

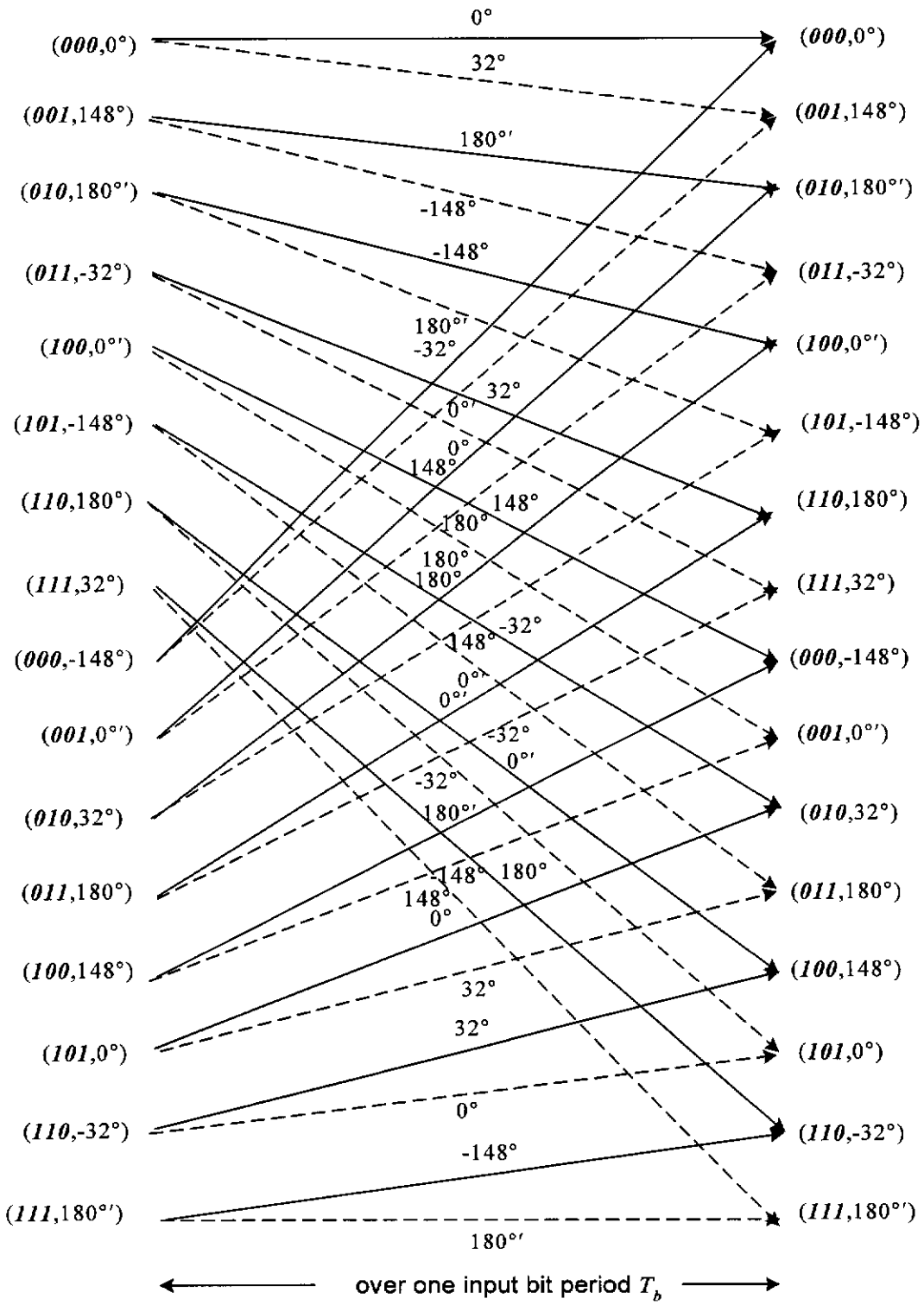

Figure 4.18c Combined trellis diagram of the code [13,7] with differentially encoded GMSK signal.

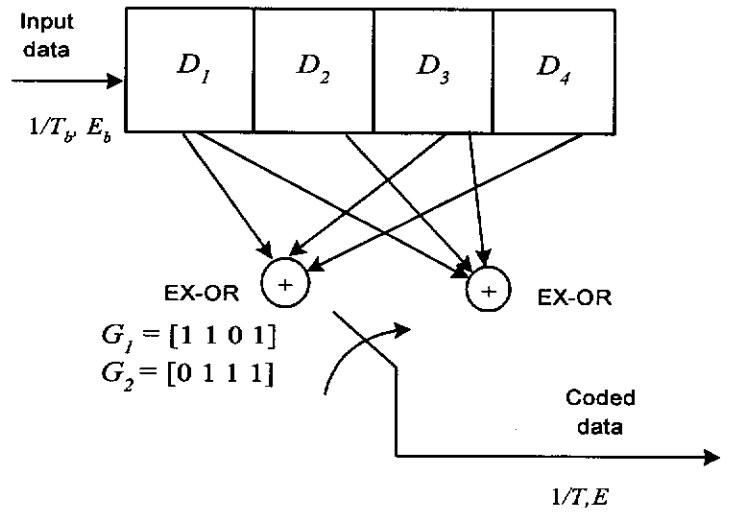

(a)

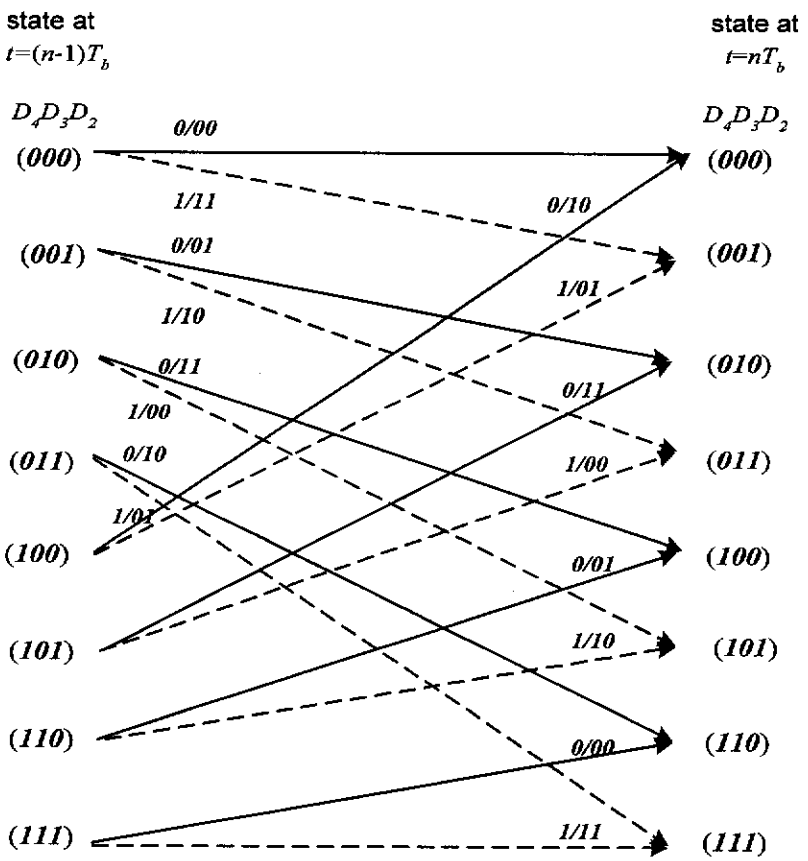

(b)

Figure 4.19 (a) Encoder **(b)** Trellis diagram, of the code [15,7].

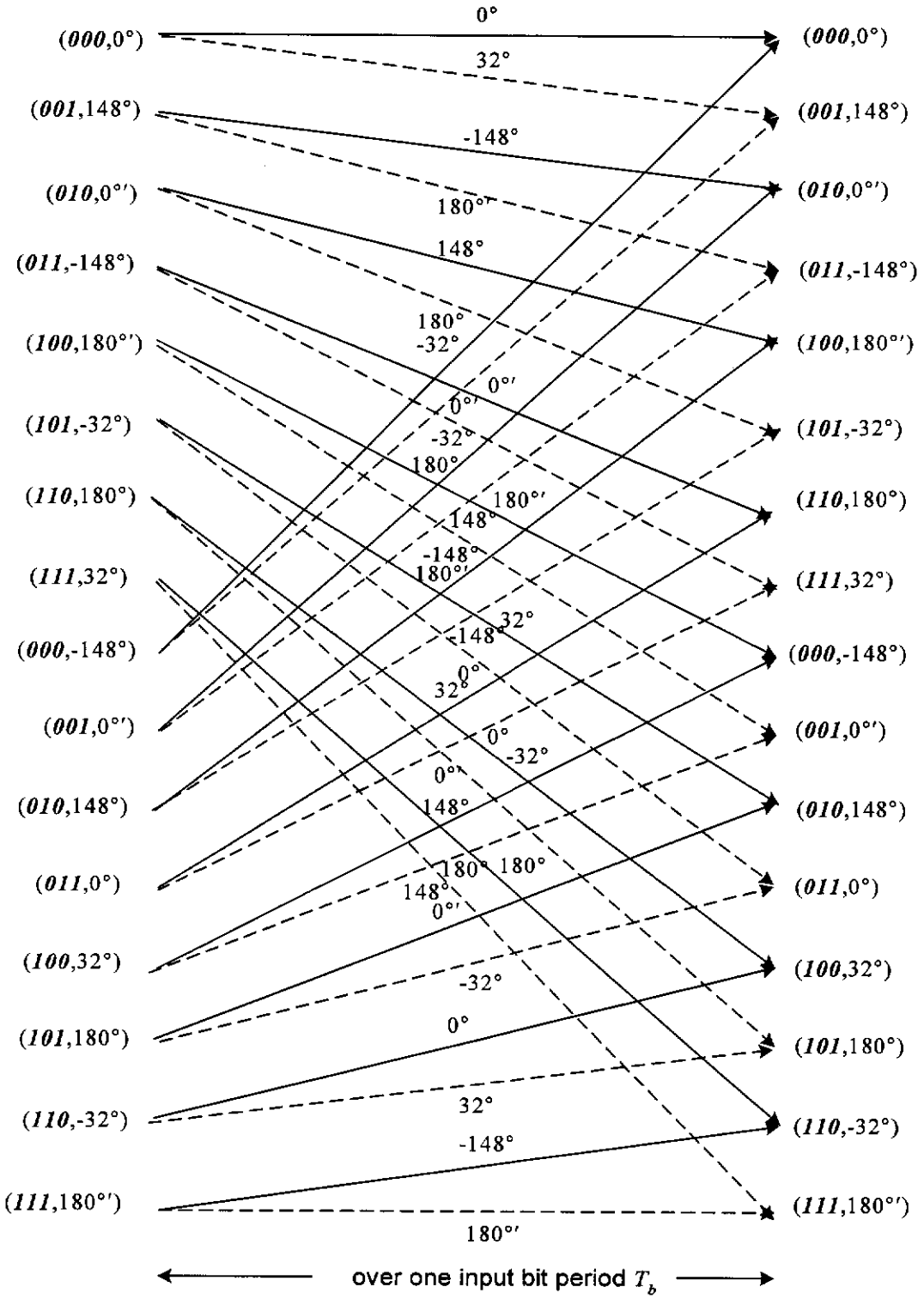

Figure 4.19c Combined trellis diagram of the code [15,7] with differentially encoded GMSK signal.

CHAPTER 5

PERFORMANCE ANALYSIS OF THE SELECTED TRELLIS CODED GMSK SCHEMES

5.1 Introduction

The bit error rate performances of the selected trellis coded GMSK schemes as described in Chapter 4 are analytically evaluated in this chapter. The upper and lower bounds on the probability of bit errors for these selected trellis coded GMSK schemes have been derived for an AWGN channel, as well as for a channel encountering amplitude fading. These bounds have been obtained based on the union bound techniques, assuming that the channel is memoryless, and maximum likelihood decoding is used (Clarke and Cain, 1981; Viterbi and Omura, 1979; Wozencraft and Jacobs, 1965).

In the case of a fading channel, the signal samples are correlated. For the union bound techniques to be applicable for a fading channel, bit interleaving of sufficient depth is assumed. Bit interleaving is often applied in practice to disperse error bursts associated with transmission over a fading channel, so that the channel approximates a memoryless channel. Furthermore, the effect of fading on the phase of the received signal is assumed to be fully compensated by tracking the phase variations with some form of phase-locked-loop or by means of pilot tone calibration techniques (McGeehan *et al*, 1984; Davarian, 1987). Consequently, in this study, only the amplitude of the received signal is considered to be affected by fading. This assumption has also been made in previous studies (Divsalar *et al*, 1987; Schlegel and Costello, 1989; Yiin and Stuber, 1996). With these assumptions, the upper and the lower bounds on the bit error probabilities over AWGN and amplitude-fading channels have been obtained for the selected TCM signals

described in Chapter 4. The analysis adopted here follows closely the work by Divsalar and Simon (1987) and Biglieri, *et al* (1991).

5.2 Decoding Metric for Viterbi Decoding

In this analysis, the received signal is assumed to be detected using coherent demodulation followed by MLSD based on the Viterbi algorithm. As discussed in Section 2.6, the MLSD compares the values of the signal space distance of the received data sequence with those for all the possible transmitted sequences. The transmitted sequence having the signal space distance closest to the received sequence is selected as the most likely transmitted sequence.

Assume that when a coded sequence $X_L=(x_1, x_2,.., x_k,... x_L)$ of length L is transmitted, the corresponding received sequence is $Y_L=(y_1, y_2,.., y_k,... y_L)$ where x_k and y_k are the k^{th} elements of the transmitted and the received signals at time k, respectively. The decoder may wrongly select $X'_L=(x'_1, x'_2,.., x'_k,... x'_L)$ instead of X_L whenever the log-likelihood decoding metrics $m(Y_L, X'_L)$ and $m(Y_L, X_L)$ used by the decoder corresponding to these two sequences satisfy the condition (Proakis, 1989)

$$m(Y_L, X'_L) \geq m(Y_L, X_L). \tag{5.1}$$

In this case, the selected sequence X'_L corresponds to a path in the trellis, which split from the correct path X_L at a given time and remerges after L discrete time intervals, creating an error event of length L.

As the log-likelihood function is used as the decoding metric, and if the channel is memoryless, then the corresponding metric of a sequence can be expressed by the sum of the metrics for each transmitted and received pair in the sequence over the length of the error event (Biglieri *et al*, 1991). Thus, the decoding metrics corresponding to the incorrectly decoded sequence, X'_L and the transmitted sequence, X_L, may be expressed as

$$m(Y_L, X'_L) = \sum_{k=1}^{L} m(y_k, x'_k) \tag{5.2a}$$

and $$m(Y_L, X_L) = \sum_{k=1}^{L} m(y_k, x_k). \quad (5.2b)$$

As a result, Eq. (5.1), which corresponds to the condition for making an erroneous decision, can be expressed as

$$\sum_{k=1}^{L} m(y_k, x'_k) \geq \sum_{k=1}^{L} m(y_k, x_k). \quad (5.3)$$

Consequently, the probability $P(X'_L| X_L)$, which represents the probability of selecting the coded sequence $X'_L=(x'_1, x'_2,.., x'_k,... x'_L)$ when $X_L=(x_1, x_2,.., x_k,... x_L)$ has been transmitted is given by (Biglieri *et al*, 1991)

$$P(X'_L|X_L) = P\left\{\left(\sum_{k=1}^{L} m(y_k, x'_k) \geq \sum_{k=1}^{L} m(y_k, x_k)\right)\middle| X_L\right\}. \quad (5.4)$$

Assuming that X'_L and X_L are random variables, the probability of occurrence of an error event X'_L of length L, when the sequence X_L has been transmitted may be expressed as

$$P_E(L, X'_L, X_L) = P[X_L]\, P(X'_L| X_L) \quad (5.5)$$

where, $P[X_L]$ is the probability of transmitting X_L.

Then, the upperbound of the error probability of an error event of any length may be obtained as shown in Eq. (A.7) of Appendix A as

$$P_E \leq \sum_{L=1}^{\infty} \sum_{X_L} \sum_{X'_L \neq X_L} P[X_L]\, P(X'_L| X_L). \quad (5.6)$$

Substituting Eq. (5.4) in Eq. (5.6), we obtain

$$P_E \leq \sum_{L=1}^{\infty} \sum_{X_L} \sum_{X'_L \neq X_L} P[X_L] P\left\{\left(\sum_{k=1}^{L} m(y_k, x'_k) \geq \sum_{k=1}^{L} m(y_k, x_k)\right)\middle| X_L\right\}. \quad (5.7)$$

It has been shown that a tighter upperbound for P_E of Eq. (5.7), is often obtained by applying the Chernoff bound (Divsalar and Simon, 1987; Yiin and Stuber, 1996). According to Chernoff bound, if r is a continuous random variable, then (Wozencraft and Jacobs 1965),

$$P(r \geq 0) \leq E[\exp(\lambda r)] \quad \text{for any } \lambda \geq 0. \quad (5.8)$$

Here, $E[.]$ denotes the statistical expectation operation. The tightest upperbound in this case may be obtained by selecting the value of λ which

minimises the value of $E[\exp(\lambda r)]$. When r is the sum of L independent continuous random variables $r_1, r_2, \ldots, r_k, \ldots, r_L$, then Eq. (5.8) becomes

$$P\left\{\sum_{k=1}^{L} r_k \geq 0\right\} \leq \prod_{k=1}^{L} E[\exp(\lambda r_k)]. \tag{5.9}$$

It follows that the probability $P(X'_L|X_L)$ given in Eq. (5.4) may be upperbounded by applying the Chernoff bound, so that

$$P(X'_L|X_L) = P\left\{\left(\sum_{k=1}^{L} m(y_k, x'_k) - \sum_{k=1}^{L} m(y_k, x_k)\right) \geq 0 | X_L\right\}$$

$$\leq \prod_{k=1}^{L} E\left\{\exp[\lambda(m(y_k, x'_k) - m(y_k, x_k))] | X_L\right\}. \tag{5.10}$$

Thus, the upperbound of P_E given in Eq. (5.7) may be expressed as

$$P_E \leq \sum_{L=1}^{\infty} \sum_{X_L} \sum_{X'_L \neq X_L} P[X_L] \prod_{k=1}^{L} E\left\{\exp[\lambda(m(y_k, x'_k) - m(y_k, x_k))] | X_L\right\}$$

$$\leq \sum_{L=1}^{\infty} \sum_{X_L} \sum_{X'_L \neq X_L} P[X_L] \prod_{k=1}^{L} \exp[-\Delta_\lambda(x_k, x'_k)] \tag{5.11}$$

where,

$$\exp[-\Delta_\lambda(x_k, x'_k)] = E\left\{\exp[\lambda(m(y_k, x'_k) - m(y_k, x_k))] | X_L\right\}. \tag{5.12}$$

It is observed from Eq. (5.11), that the upperbound of the probability of event error P_E, depends on the decoding metrics used by the decoder. The derivations of the decoding metrics for both the AWGN and fading channels will now be presented.

5.2.1 Distance metric for AWGN channels

Consider a signal transmitted in the presence of AWGN. The received signal, y_k, at a given time k corresponding to a transmitted signal, x_k, is given by

$$y_k = x_k + n_k. \tag{5.13}$$

Here, n_k is the k^{th} sample of zero mean Gaussian noise with variance σ^2. In general, x_k, y_k and n_k are complex variables (Biglieri *et al*, 1991). The complex noise n_k can be represented in terms of its real and imaginary parts, which are uncorrelated zero mean Gaussian random variables, each with variance $\sigma_K^2 = \sigma^2/2$.

In the presence of AWGN, the maximum likelihood decoding metric $m(y_k, x_k)$ becomes (Proakis 1989, Divsalar and Simon 1987)

$$m(y_k, x_k) = \ln\left[p(n_k)\right]. \tag{5.14a}$$

Here, $p(n_k)$ is the probability density function (pdf) of Gaussian noise n_k, given by

$$p(n_k) = \frac{1}{\sqrt{2\pi\sigma^2}} \exp\left(-\frac{n_k^2}{2\sigma^2}\right). \tag{5.14b}$$

Applying Eq. (5.13) and Eq. (5.14b) in Eq. (5.14a), we obtain

$$m(y_k, x_k) = \ln\left\{\frac{1}{\sqrt{2\pi\sigma^2}} \exp\left(-\frac{|y_k - x_k|^2}{2\sigma^2}\right)\right\},$$

$$= \ln\left(\frac{1}{\sqrt{2\pi\sigma^2}}\right) - \frac{|y_k - x_k|^2}{2\sigma^2}. \tag{5.15a}$$

Similarly, the decoding metric $m(y_k, x'_k)$, corresponding to the incorrectly decoded sequence can be expressed as

$$m(y_k, x'_k) = \ln\left(\frac{1}{\sqrt{2\pi\sigma^2}}\right) - \frac{|y_k - x'_k|^2}{2\sigma^2}. \tag{5.15b}$$

Using the decoding metrics given in Eq. (5.15a) and Eq. (5.15b), the exponent function, $\exp[-\Delta_\lambda(x_k, x'_k)]$, given in Eq. (5.12) can be expressed as

$$\exp[-\Delta_\lambda(x_k, x'_k)] = E\left\{\exp\left[\frac{\lambda}{2\sigma^2}\left(-|y_k - x'_k|^2 + |y_k - x_k|^2\right)\right] \middle| \boldsymbol{X}_L\right\}$$

$$= E\left\{\exp\left[\lambda'\left(-|y_k - x'_k|^2 + |y_k - x_k|^2\right)\right] \middle| \boldsymbol{X}_L\right\}, \tag{5.16}$$

where $\lambda' = \frac{\lambda}{2\sigma^2}$.

The statistical expectation operation of Eq. (5.16) can be further simplified for AWGN channels as shown in Eq. (B.12) of Appendix B as

$$\exp\left[-\Delta_\lambda(x_k, x'_k)\right] = \exp\left(-\lambda'|x_k - x'_k|^2\right)\exp\left(2\sigma_K^2\lambda'^2|x_k - x'_k|^2\right). \tag{5.17}$$

The complex random variables x_k and x'_k can be represented in the quadrature forms as shown in Eq. (B.3a) and Eq. (B.3b) as

$$x_k = \exp(\mathrm{j}\phi_k) = (\cos\phi_k + \mathrm{j}\sin\phi_k) \tag{5.18a}$$

and $$x'_k = \exp(\mathrm{j}\phi'_k) = (\cos\phi'_k + \mathrm{j}\sin\phi'_k) \tag{5.18b}$$

where ϕ_k and ϕ'_k are the information carrying phase angles corresponding to the transmitted signal x_k and the incorrectly detected signal x'_k, at time k, respectively. From Eq. (5.18a) and Eq. (5.18b),

$$\begin{aligned} |x_k - x'_k|^2 &= [\cos(\phi_k) - \cos(\phi'_k)]^2 + [\sin(\phi_k) - \sin(\phi'_k)]^2 \\ &= 2[1 - \cos(\phi_k - \phi'_k)]. \end{aligned} \tag{5.19}$$

Substituting Eq. (5.17) and Eq. (5.19) into Eq. (5.11), the upperbound of the probability of event error P_E becomes

$$P_E \le \sum_{L=1}^{\infty} \sum_{X_L} \sum_{X'_L \neq X_L} P[X_L] \prod_{k=1}^{L} \exp\{-\lambda'[2(1-\cos(\phi_k - \phi'_k))]\} \exp\{2\sigma_K^2 \lambda'^2 [2(1-\cos(\phi_k - \phi'_k))]\}. \tag{5.20}$$

As presented in Section 5.2, the tightest upperbound of P_E can be obtained by selecting the Chernoff bound parameter λ', which minimises the exponent function, $\exp[-\Delta_\lambda(x_k, x'_k)]$ (Wozencraft and Jacobs, 1965). Consequently, the optimum value of the Chernoff bound parameter, λ'_{opt}, will be the one, which yields

$$\frac{\partial}{\partial \lambda'} \{\exp[-\Delta_\lambda(x_k, x'_k)]\} = 0 \tag{5.21a}$$

and

$$\frac{\partial^2}{\partial \lambda'^2} \{\exp[-\Delta_\lambda(x_k, x'_k)]\} > 0 \quad \text{for } \lambda' > 0. \tag{5.21b}$$

By applying the condition given in Eq. (5.21a) to Eq. (5.17), we obtain,

$$|x_k - x'_k|^2 [4\sigma_K^2 \lambda' - 1] = 0.$$

This results in either,

$$|x_k - x'_k|^2 = 0$$

or

$$\lambda' = \frac{1}{4\sigma_K^2}.$$

Using the relationship of Eq. (5.21b), we obtain that

$$\frac{\partial^2}{\partial \lambda'^2} \{\exp[-\Delta_\lambda(x_k, x'_k)]\} = 0 \text{ when } |x_k - x'_k|^2 = 0,$$

and $\frac{\partial^2}{\partial \lambda'^2} \{\exp[-\Delta_\lambda(x_k, x'_k)]\} > 0$ when $\lambda' = \frac{1}{4\sigma_K^2}$ and $|x_k - x'_k|^2 \neq 0$.

There will always be some values of k in which $|x_k - x'_k|^2 \neq 0$. Thus, the only realistic value of the Chernoff bound parameter λ', which yields the

minimum $\exp[-\Delta_\lambda(x_k, x'_k)]$, satisfying the conditions given in Eq. (5.21a) and Eq. (5.21b) can be obtained as

$$\lambda'_{opt} = \frac{1}{4\sigma_K^2}. \tag{5.22}$$

Applying this value of λ'_{opt}, in Eq. (5.20), the tightest upperbound of P_E can be expressed as

$$P_E \le \sum_{L=1}^{\infty} \sum_{X_L} \sum_{X'_L \neq X_L} P[X_L] \prod_{k=1}^{L} \exp\left\{\left(\frac{-1}{4\sigma_K^2}\right)\left[1-\cos(\phi_k - \phi'_k)\right]\right\}. \tag{5.23}$$

Assuming that the signal power of the transmitted sequence is normalised to unity, the ratio of the transmitted signal energy E to noise spectral density N_0, can be expressed as

$$\frac{E}{N_0} = \frac{1}{\sigma^2}. \tag{5.24}$$

As discussed in Section 4.3, the energy of the transmitted coded bits E for rate-½ codes is half the energy of the individual input bits E_b, i.e., $E=E_b/2$. Moreover, as discussed in Section 5.2.1, $\sigma_K^2 = \sigma^2/2$, so that, Eq. (5.24) becomes

$$\frac{E}{N_0} = \frac{E_b}{2N_0} = \frac{1}{\sigma^2} = \frac{1}{2\sigma_K^2}$$

Consequently,

$$\frac{E_b}{N_0} = \frac{1}{\sigma_K^2}. \tag{5.25}$$

Substituting Eq. (5.25) in Eq. (5.23), the upperbound of P_E in the presence of AWGN becomes

$$P_E \le \sum_{L=1}^{\infty} \sum_{X_L} \sum_{X'_L \neq X_L} P[X_L] \prod_{k=1}^{L} \exp\left\{\left(\frac{-E_b}{4N_0}\right)\left[1-\cos(\phi_k - \phi'_k)\right]\right\}. \tag{5.26}$$

Eq. (5.26) may also be expressed as

$$P_E \le \sum_{L=1}^{\infty} \sum_{X_L} \sum_{X'_L \neq X_L} P[X_L] \prod_{k=1}^{L} \exp\left[\left(\frac{-E_b}{4N_0}\right) d^2(x_k, x'_k)\right]$$

with the incremental decoding metric

$$d^2(x_k, x'_k) = \left[1-\cos(\phi_k - \phi'_k)\right]. \tag{5.27}$$

5.2.2 Distance metric for amplitude-fading channels

The upperbound of probability of error P_E, as given by Eq. (5.26) for an AWGN channel has been obtained assuming that the received signal samples are independent random variables. However, in a fading channel, this assumption may not be valid as the signal samples are usually correlated. Moreover, bit interleaving may be applied to make the signal samples uncorrelated, so that the same bit error probability bounding techniques for an AWGN channel may be adopted for the fading channel. In practice, the depth of interleaving is finite, but for the purpose of analysis in this study, bit interleaving of infinite depth is assumed. As the ideal interleaving is assumed for this analysis, the actual bounds obtained may be somewhat worse than the bounds obtained in this study.

In a mobile environment, where there is no line-of-sight propagation, the amplitude of the received signal follows the Rayleigh distribution given by

$$\begin{aligned} p(\rho) &= 2\,\rho\,\exp(-\rho^2) && \rho \geq 0 \\ &= 0 && \rho < 0 \end{aligned} \qquad (5.28)$$

where $p(\rho)$ is the pdf of the normalised amplitude fading ρ, of the received signal.

If x_k=exp(jϕ_k) is the signal transmitted over a fading channel at a given time k, then the received signal y_k can be expressed as

$$y_k = \rho_k \exp\,[\mathrm{j}(\phi_k + \Delta\theta_k)] + n_k. \qquad (5.29a)$$

Here, ρ_k is the time varying random amplitude and $\Delta\theta_k$ is the time varying phase introduced by fading at time k. In view of the assumption of a memoryless channel, the ρ_ks are independent random variables. It is assumed in this analysis, that the phase variations caused by fading of the received signal is zero, i.e., $\Delta\theta_k$= 0. Consequently, only the effect of fading on the amplitude of the received signal is considered. As a result, the received signal y_k at a given time k may be expressed as

$$\begin{aligned} y_k &= \rho_k \exp(\phi_k) + n_k. \\ &= \rho_k\, x_k + n_k. \end{aligned} \qquad (5.29b)$$

As the Gaussian noise n_k, can now be expressed as

$$n_k = y_k - \rho_k x_k.$$

The pdf of n_k, becomes

$$p(n_k) = \frac{1}{\sqrt{2\pi\sigma^2}} \exp\left(-\frac{|n_k|^2}{2\sigma^2} \right)$$

$$= \frac{1}{\sqrt{2\pi\sigma^2}} \exp\left(-\frac{|y_k - \rho_k x_k|^2}{2\sigma^2} \right). \quad (5.30)$$

As discussed in Section 5.2.1, the maximum likelihood decoding metric corresponding to the correct sequence, $m(y_k,x_k)$, for the amplitude-fading channel can be written as

$$m(y_k, x_k) = \ln [p(n_k)].$$

From Eq. (5.30),

$$m(y_k, x_k) = \ln \frac{1}{\sqrt{2\pi\sigma^2}} \exp\left(-\frac{|y_k - \rho_k x_k|^2}{2\sigma^2} \right)$$

$$= \ln \left(\frac{1}{\sqrt{2\pi\sigma^2}} \right) - \frac{|y_k - \rho_k x_k|^2}{2\sigma^2}. \quad (5.31a)$$

Similarly, the decoding metric corresponding to the incorrectly decoded sequence, $m(y_k,x'_k)$, can be expressed as

$$m(y_k, x'_k) = \ln \left(\frac{1}{\sqrt{2\pi\sigma^2}} \right) - \frac{|y_k - \rho_k x'_k|^2}{2\sigma^2}. \quad (5.31b)$$

Now, using Eq. (5.6), the upperbound of the conditional probability of event error, $(P_E|\rho)$, over an amplitude-fading channel can be expressed as

$$(P_E|\rho) \le \sum_{L=1}^{\infty} \sum_{X_L} \sum_{X'_L \neq X_L} P[X_L]\, P(X'_L|\, X_L). \quad (5.32)$$

As given in Eq. (5.10) and Eq. (5.11), the conditional probability $P(X'_L|\, X_L)$, over amplitude-fading channel can be expressed as

$$P(X'_L|X_L) = P\left\{ \left(\sum_{k=1}^{L} m(y_k, x'_k) - \sum_{k=1}^{L} m(y_k, x_k) \right) \ge 0 \middle| X_L \right\}$$

$$\le \prod_{k=1}^{L} \exp[-\Delta_\lambda (x_k, x'_k)]_{fading} \quad (5.33)$$

where

$$\exp[-\Delta_\lambda(x_k, x'_k)]_{fading} = E\left\{\exp\left[\lambda\left(m(y_k, x'_k) - m(y_k, x_k)\right)\right] \middle| X_L\right\}.$$

The resulting upperbound of the conditional probability of event error, $(P_E|\rho)$, for an amplitude-fading channel can then be expressed as

$$(P_E|\rho) \le \sum_{L=1}^{\infty} \sum_{X_L} \sum_{X'_L \neq X_L} P[X_L] \prod_{k=1}^{L} \exp[-\Delta_\lambda(x_k, x'_k)]_{fading} \qquad (5.34)$$

Using the corresponding decoding metrics given in Eq. (5.31a) and Eq. (5.31b), the exponent function, $\exp[-\Delta_\lambda(x_k, x'_k)]_{fading}$, for an amplitude-fading channel can be obtained as

$$\begin{aligned}\exp[-\Delta_\lambda(x_k, x'_k)]_{fading} &= E\left\{\exp\left[\frac{\lambda}{2\sigma^2}\left(-|y_k - \rho_k x'_k|^2 + |y_k - \rho_k x_k|^2\right)\right] \middle| X_L\right\} \\ &= E\left\{\exp\left[\lambda'\left(-|y_k - \rho_k x'_k|^2 + |y_k - \rho_k x_k|^2\right)\right] \middle| X_L\right\}, \qquad (5.35)\end{aligned}$$

where $\lambda' = \dfrac{\lambda}{2\sigma^2}$.

Evaluating the statistical expectation operation, Eq. (5.35) can be simplified as shown in Eq. (C.8) of Appendix C as

$$\exp[-\Delta_\lambda(x_k, x'_k)]_{fading} = \exp\left(-\lambda'\rho_k^2|x_k - x'_k|^2\right)\exp\left(2\sigma_K^2\lambda'^2\rho_k^2|x_k - x'_k|^2\right). \qquad (5.36)$$

From Eq. (5.19), $|x_k - x'_k|^2 = 2[1 - \cos(\phi_k - \phi'_k)]$, so that Eq. (5.36) becomes

$$\exp[-\Delta_\lambda(x_k, x'_k)]_{fading} = \exp\left\{-\lambda'\rho_k^2\left[2\left(1 - \cos(\phi_k - \phi'_k)\right)\right]\right\}\exp\left\{2\sigma_K^2\lambda'^2\rho_k^2\left[2\left(1 - \cos(\phi_k - \phi'_k)\right)\right]\right\}. \qquad (5.37)$$

As discussed in Section 5.2, the tightest upperbound of the conditional probability of event error, $(P_E|\rho)$, over an amplitude-fading channel can be obtained by selecting the Chernoff bound parameter, λ', which minimises the exponent function, $\exp[-\Delta_\lambda(x_k, x'_k)]_{fading}$. Using the first and the second partial derivatives of $\exp[-\Delta_\lambda(x_k, x'_k)]_{fading}$, the optimum value of λ', which produces the minimum value of $\exp[-\Delta_\lambda(x_k, x'_k)]_{fading}$ can be obtained as shown in Eq. (5.21a) and Eq. (5.21b) as

$$(\lambda'_{\text{opt}})_{fading} = \frac{1}{4\sigma_K^2}. \qquad (5.38)$$

Applying this value of $(\lambda'_{\text{opt}})_{fading}$ in Eq. (5.37), the resulting upperbound of the conditional probability of event error, $(P_E|\rho)$ for an amplitude-fading channel given in Eq. (5.34) can be expressed as

$$(P_E|\rho) \le \sum_{L=1}^{\infty} \sum_{X_L} \sum_{X'_L \neq X_L} P[X_L] \prod_{k=1}^{L} \exp\left\{\left(\frac{-1}{4\sigma_K^2}\right)\rho_k^2[1-\cos(\phi_k - \phi'_k)]\right\}. \quad (5.39)$$

Recall from Eq. (5.25), $\frac{E_b}{N_0} = \frac{1}{\sigma_K^2}$, so that

$$(P_E|\rho) \le \sum_{L=1}^{\infty} \sum_{X_L} \sum_{X'_L \neq X_L} P[X_L] \prod_{k=1}^{L} \exp\left\{\left(\frac{-E_b}{4N_0}\right)\rho_k^2[1-\cos(\phi_k - \phi'_k)]\right\}. \quad (5.40)$$

Now, the probability of event error, P_E, can be expressed as

$$P_E = \int_{-\infty}^{+\infty} (P_E|\rho) p(\rho) \mathrm{d}\rho.$$

This results in

$$P_E \le \sum_{L=1}^{\infty} \sum_{X_L} \sum_{X'_L \neq X_L} P[X_L] \prod_{k=1}^{L} \int_{-\infty}^{+\infty} \exp\left\{\left(\frac{-E_b}{4N_0}\right)\rho_k^2[1-\cos(\phi_k - \phi'_k)]\right\} p(\rho_k)\mathrm{d}\rho_k. \quad (5.41)$$

Using the pdf of the amplitude fading, $p(\rho)$ given in Eq. (5.28), Eq. (5.41) can be expressed as

$$P_E \le \sum_{L=1}^{\infty} \sum_{X_L} \sum_{X'_L \neq X_L} P[X_L] \prod_{k=1}^{L} \int_{0}^{+\infty} \exp\left\{\left(\frac{-E_b}{4N_0}\right)\rho_k^2[1-\cos(\phi_k - \phi'_k)]\right\} 2\rho_k \exp(-\rho_k^2) d\rho_k. \quad (5.42)$$

The integral in Eq. (5.42) can be simplified, so that

$$\int_{0}^{+\infty} \exp\left\{\left(\frac{-E_b}{4N_0}\right)\rho_k^2[1-\cos(\phi_k - \phi'_k)]\right\} 2\rho_k \exp(-\rho_k^2) d\rho_k =$$

$$\int_{0}^{+\infty} 2\rho_k \exp\left\{-\left[1+\frac{E_b}{4N_0}[1-\cos(\phi_k - \phi'_k)]\right]\rho_k^2\right\} d\rho_k \quad (5.43)$$

The integral on the right hand side of Eq. (5.43) can be represented in the form, $\int_0^{\infty} 2\rho \exp(-\rho^2 u)\mathrm{d}\rho$, where $u = \left[1+\frac{E_b}{4N_0}[1-\cos(\phi_k - \phi'_k)]\right]$.

Since the above integral can be expressed in the form of the pdf of Rayleigh distribution, it can be shown that (Lathi, 1995), $\int_0^{\infty} 2u\rho \exp(-\rho^2 u)\mathrm{d}\rho = 1$, which leads to $\int_0^{\infty} 2\rho \exp(-\rho^2 u)\mathrm{d}\rho = 1/u$. With this simplification, Eq. (5.43) can be expressed as

$$\int_0^{+\infty} \exp\left\{\left(\frac{-E_b}{4N_0}\right)\rho_k^2\left[1-\cos(\phi_k-\phi_k')\right]\right\} 2\rho_k \exp(-\rho_k^2)d\rho_k = \left[1+\frac{E_b}{4N_0}\left[1-\cos(\phi_k-\phi_k')\right]\right]^{-1}. \tag{5.44}$$

Substituting Eq. (5.44) in Eq. (5.42), the probability of event error, P_E, for an amplitude fading channel can be expressed as

$$P_E \le \sum_{L=1}^{\infty}\sum_{X_L}\sum_{X_L'\neq X_L} P[X_L]\prod_{k=1}^{L}\left[1+\frac{E_b}{4N_0}\left[1-\cos(\phi_k-\phi_k')\right]\right]^{-1}. \tag{5.45}$$

5.2.3 A summary on the upperbound of the probability of event error

From Eq. (5.26) and Eq. (5.45), the upperbounds of the probabilities of event error P_E, for an AWGN channel and an amplitude-fading channel are expressed as follows:

For an AWGN channel,

$$P_E \le \sum_{L=1}^{\infty}\sum_{X_L}\sum_{X_L'\neq X_L} P[X_L]\prod_{k=1}^{L}\exp\left[\left(\frac{-E_b}{4N_0}\right)d^2(x_k,x_k')\right], \tag{5.46a}$$

and for an amplitude-fading channel,

$$P_E \le \sum_{L=1}^{\infty}\sum_{X_L}\sum_{X_L'\neq X_L} P[X_L]\prod_{k=1}^{L}\left\{1+\frac{E_b}{4N_0}d^2(x_k,x_k')\right\}^{-1} \tag{5.46b}$$

where, $d^2(x_k,x_k') = [1-\cos(\phi_k - \phi'_k)]$.

5.3 Bounds of the Bit Error Probability

Now, if E_L is an L-sequence of error vectors ($\mathbf{e}_1$, $\mathbf{e}_2$,..., $\mathbf{e}_{L-1}$, $\mathbf{e}_L$), the incorrectly detected sequence $X'_L=(x'_1, x'_2,\ldots, x'_{L-1}, x'_L)$ may be expressed as

$$X'_L = X_L \oplus E_L.$$

where X_L is the transmitted sequence and the symbol $\oplus$ represents exclusive-OR logic operation. As such, E_L will be zero whenever $X'_L=X_L$. Then, the upperbound of the probability of event error P_E, for an AWGN channel as given in Eq. (5.46a) may be expressed as

$$P_E \le \sum_{L=1}^{\infty} \sum_{E_L \neq 0} \sum_{X_L} P[X_L] \prod_{k=1}^{L} \exp\left[\left(\frac{-E_b}{4N_0}\right) d^2(x_k, x'_k)\right]$$

$$\le \sum_{L=1}^{\infty} \sum_{E_L \neq 0} \sum_{X_L} P[X_L] \exp\left[\left(\frac{-E_b}{4N_0}\right) \sum_{k=1}^{L} d^2(x_k, x'_k)\right]$$

$$\le \sum_{L=1}^{\infty} \sum_{E_L \neq 0} W(E_L) \qquad (5.47a)$$

where

$$W(E_L) = \sum_{X_L} P[X_L] \exp\left[\left(\frac{-E_b}{4N_0}\right) \sum_{k=1}^{L} d^2(x_k, x'_k)\right]. \qquad (5.47b)$$

From Eq. (5.47a), it can be seen that the probability of event error P_E, is upperbounded by a sum, over the possible error events, of functions of the vectors E_L causing the error events (Biglieri *et al*, 1991). As shown in Biglieri *et al* (1991), these functions $W(E_L)$ may be obtained using the error state diagram representing the particular trellis coded scheme.

For linear codes, the error state diagram of a coded scheme may be obtained assuming that an all-zero coded sequence has been transmitted (Proakis, 1989). Then, a decoding error is said to occur whenever the all zero path is not the survivor. Consequently, in an error state diagram, each path connecting the initial state to the final state represents a non-zero

codeword. A detailed description of the error state diagrams can be found in (Bhargava *et al,* 1981; Viterbi and Omura, 1979).

As shown in Biglieri, *et al* (1991), each path representing a non-zero code word in the error state diagram may be represented by an $N \times N$ error weight matrix $G(\mathbf{e}_k)$ with N being the number of bits in the codeword. For example for rate-½ trellis coded schemes, N becomes 2 and the general form of the error weight matrix $G(\mathbf{e})$ corresponding to an error vector e=(e_1e_2) may be defined as (Biglieri *et al*, 1991)

$$G(e_1e_2)_{(\phi)} = \frac{1}{2}\begin{bmatrix} D^{\|f(00)-f(e_1e_2)\|^2} & D^{\|f(10)-f(\bar{e}_1e_2)\|^2} \\ D^{\|f(01)-f(e_1\bar{e}_2)\|^2} & D^{\|f(11)-f(\bar{e}_1\bar{e}_2)\|^2} \end{bmatrix} \tag{5.48}$$

where $D = \exp\left(-\frac{E_b}{4N_0}\right)$ and $\bar{e}$ denotes the complement of e. The sub script ϕ in the matrix in Eq. (5.48) represents the initial phase state of the path in the error state diagram corresponding to the error vector e=(e_1e_2). If the error vector e is (11), then $\|f(00)-f(e_1e_2)\|^2$ becomes the distance metric between the two coded signals (00) and (11) having a phase ϕ corresponding to the initial state of that path. These distance metrics may be evaluated using the decoding metrics given in Eq. (5.27).

As discussed in Biglieri *et al* (1991), the total error weight matrix representing all the error events becomes the product of the path error weight matrices along the path connecting the initial state to the final state of an error state diagram. As a result, $W(\boldsymbol{E}_L)$ in Eq. (5.47b) is shown by Biglieri *et al* (1991) to be

$$W(\boldsymbol{E}_L) = \frac{1}{N}\mathbf{1}^T \prod_{k=1}^{L} G(\mathbf{e}_k)\,\mathbf{1} \tag{5.49}$$

where $\mathbf{1}$ is a column N-vector with all the elements equal to 1.

Substituting Eq. (5.49) in Eq. (5.47a), the upperbound of event error probability P_E, may be expressed as

$$P_E \leq \sum_{L=1}^{\infty} \sum_{\mathbf{E}_L \neq 0} \frac{1}{N} \mathbf{1}^T \prod_{k=1}^{L} G(\mathbf{e}_k)\, \mathbf{1}. \tag{5.50}$$

The set of error weight matrices corresponding to all the non-zero codewords of the error state diagram may be represented by the matrix transfer function of the error state diagram $\mathbf{G}$ (Bhargava *et al,* 1981) as

$$\mathbf{G} = \sum_{L=1}^{\infty} \sum_{\mathbf{E}_L \neq 0} \prod_{k=1}^{L} G(\mathbf{e}_k). \tag{5.51}$$

For any $N \times N$ matrix $\mathbf{A}$, $\mathbf{1}^T\mathbf{A}\mathbf{1}$ becomes the sum of all the entries in $\mathbf{A}$. Therefore, the scalar transfer function of the error state diagram $T(D)$ may be expressed as (Bhargava *et al,* 1981)

$$T(D) = \frac{1}{N} \mathbf{1}^T \mathbf{G}\, \mathbf{1}. \tag{5.52}$$

Consequently, from Eq. (5.51) and Eq. (5.52), the upperbound of event error probability P_E, given in Eq. (5.50) may be expressed as

$$P_E \leq T(D) \qquad \text{where } D = \exp\left(-\frac{E_b}{4N_0}\right). \tag{5.53}$$

So far in this chapter, we have discussed the upperbound of the event error probability, P_E. However, from the user point of view, the number of information bits decoded in error, that is, the bit error probability is a more important and practical performance measure compared to the event error probability. Hence the upperbound on the bit error probability is next derived using the transfer function approach used in finding the bounds of event error probability. According to Biglieri *et al* (1991), this may be obtained by incorporating the number of information bits in error in the corresponding error weight matrices $G(\mathbf{e}_k)$ resulting from the incorrect path decision. Assuming that the all-zero code word has been transmitted, each error weight matrix is multiplied by a factor J^{ε}, where ε is the number of non-zero information bits associated with the corresponding error vector (Bhargava *et al*, 1981). Accordingly, each error weight matrix corresponding to a non-zero information bit is multiplied by a factor $J^1=J$ and else is multiplied by $J^0=1$. For

example, consider the trellis diagram of a code shown in Fig. 5.1a. The split and merge paths in the trellis diagram, creating an error event are shown in bold face in Fig. 5.1b. The error state diagram corresponding to the trellis diagrams shown in Fig. 5.1a and Fig. 5.1b is presented in Fig. 5.1c. In the error state diagram of Fig. 5.1c, each path connecting the initial state A to the final state C represents a non-zero codeword.

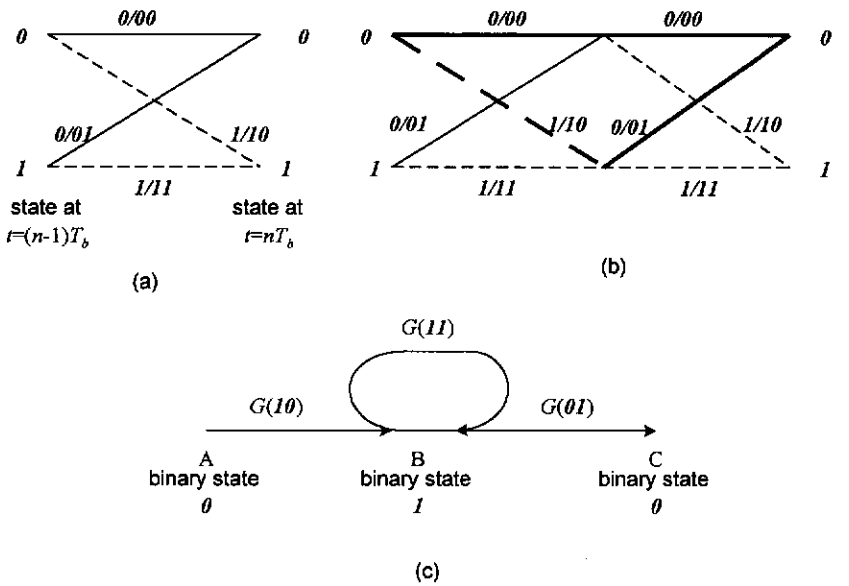

Figure 5.1 (a) Trellis diagram **(b)** Trellis diagram showing the error event **(c)** Error state diagram for a two-state trellis coded scheme.

It is observed from Fig. 5.1b and 5.1c that the transition from the initial binary state *0* (state A) to binary state *1* (state B) corresponds to the error vector *10* in the error state diagram. Furthermore, it can be seen that the number of non-zero information bits associated with this incorrect path decision is one. Consequently, this may be incorporated by multiplying the elements of the corresponding error weight matrix $G(10)$ by a factor J, as discussed in the previous paragraph. Using this method, the transfer function of the error state diagram $T(D,J)$ incorporating the number of information bits in error corresponding to transition from one state to the other in the error state diagram, may be obtained by multiplying each error weight matrix by J^{ε}, where ε is the corresponding number of non-zero information bits associated with those error vectors. Thus the exponent of J in each term of $T(D,J)$ gives the number of information bits in error for the paths corresponding to that term. Therefore, the number of bits in error for each path can be computed

by differentiating $T(D,J)$ with respect to J and then letting J=1 (Bhargava *et al*, 1981). As a result, Biglieri *et al* (1991), expressed the upper bound on the bit error probability as

$$P_b \leq \frac{\partial}{\partial J} T(D,J)\Big|_{J=1, D=\exp(-E_b/4N_0)} . \tag{5.54}$$

Furthermore, Biglieri *et al* (1991) have shown that an upperbound on the bit error probability, P_b, tighter than the one given in Eq. (5.54), may be obtained by expressing the conditional probability $P(X'_L|\, X_L)$ as (Viterbi and Omura, 1979)

$$P(X'_L|\, X_L) = \frac{1}{2}\operatorname{erfc}\left\{\left[\left(\frac{E_b}{4N_0}\right)\sum_{k=1}^{L} d^2(x_k, x'_k)\right]^{\frac{1}{2}}\right\}. \tag{5.55}$$

Using the inequality (Bhargava *et al*, 1981; Viterbi and Omura, 1979),

$$\operatorname{erfc}\left(\sqrt{\frac{x+y}{2}}\right) \leq \operatorname{erfc}\left(\sqrt{\frac{x}{2}}\right)\exp\left(\frac{-y}{2}\right), \qquad x \geq 0 \text{ and } y \geq 0 \tag{5.56}$$

and the free distance, d_{free} of the coded scheme, the error function in Eq. (5.55) may be expressed as

$$\operatorname{erfc}\left(\sqrt{\frac{E_b}{4N_0}d_{free}^2 + \frac{E_b}{4N_0}\sum_{k=1}^{L} d^2(x_k, x`_k) - \frac{E_b}{4N_0}d_{free}^2}\right) \leq \operatorname{erfc}\left(\sqrt{\frac{E_b}{4N_0}d_{free}^2}\right) \exp\left(\frac{E_b}{4N_0}d_{free}^2 - \frac{E_b}{4N_0}\sum_{k=1}^{L} d^2(x_k, x`_k)\right) \tag{5.57}$$

Substituting the inequality given by Eq. (5.57) in Eq. (5.55), the upperbound of P_E as given in Eq. (5.6) may be expressed as

$$P_E \leq \frac{1}{2}\operatorname{erfc}\left(\sqrt{\frac{E_b}{4N_0}d_{free}^2}\right)\exp\left(\frac{E_b}{4N_0}d_{free}^2\right)\sum_{L=1}^{\infty}\sum_{E_L\neq 0}\sum_{X_L} P[X_L]\exp\left[\left(\frac{-E_b}{4N_0}\right)\sum_{k=1}^{L} d^2(x_k, x'_k)\right]. \tag{5.58}$$

As shown in Eq. (5.47a) and Eq. (5.47b),

$$\sum_{L=1}^{\infty}\sum_{E_L\neq 0}\sum_{X_L} P[X_L]\exp\left[\left(\frac{-E_b}{4N_0}\right)\sum_{k=1}^{L} d^2(x_k, x'_k)\right] = \sum_{L=1}^{\infty}\sum_{E_L\neq 0} W(E_L).$$

From Eq. (5.49) and Eq. (5.51), we obtain

$$\sum_{L=1}^{\infty}\sum_{E_L\neq 0} W(E_L) = \frac{1}{N}\mathbf{1}^T \mathbf{G}\, \mathbf{1} \tag{5.59a}$$

By applying Eq. (5.52) in Eq. (5.59a)

$$\sum_{L=1}^{\infty}\sum_{E_L\neq 0} W(\boldsymbol{E}_L) = T(D) \tag{5.59b}$$

Substituting Eq. (5.59b) in Eq. (5.58), an upperbound on the event error probability, P_E, for an AWGN channel may be expressed as (Biglieri *et al*, 1991)

$$P_E \leq \frac{1}{2}\operatorname{erfc}\left(\sqrt{\frac{E_b}{4N_0}d_{free}^2}\right)\exp\left(\frac{E_b}{4N_0}d_{free}^2\right)\, T(D). \tag{5.60}$$

Similarly, using Eq. (5.54), Biglieri *et al* (1991) have obtained a tighter upper bound on the bit error probability, P_b, as

$$P_b \leq \frac{1}{2}\operatorname{erfc}\left(\sqrt{\frac{E_b}{4N_0}d_{free}^2}\right)\exp\left(\frac{E_b}{4N_0}d_{free}^2\right)\, \frac{\partial}{\partial J}T(D,J)\Big|_{J=1,D=exp(-E_b/4N_0)}. \tag{5.61}$$

Moreover, as the minimum value for $\left[\left(\frac{E_b}{4N_0}\right)\sum_{k=1}^{L} d^2(x_k,x_k')\right]^{\frac{1}{2}}$ in Eq. (5.55) corresponds to the free distance, it has also been shown in Biglieri *et al* (1991), that the lower bound on the bit error probability for an AWGN channel is given by

$$P_b \geq \frac{1}{2}\operatorname{erfc}\left(\sqrt{\frac{E_b d_{free}^2}{4N_0}}\right). \tag{5.62}$$

From Equations (5.61) and (5.62), it may be seen that the upper and lower bounds on the bit error probability of a trellis coded scheme over an AWGN channel may be obtained based on the free distance of a particular trellis coded scheme together with the transfer function $T(D,J)$ of the error state diagram representing the scheme. The free distances of the selected trellis coded schemes have been obtained in Chapter 4. The derivations of the transfer functions of the corresponding error state diagrams of these selected trellis coded schemes will be discussed in the following sections.

5.3.1 The transfer function of the error state diagram of the trellis coded scheme having constraint length 2 over AWGN channels

In this section, the error state diagram of the selected trellis coded scheme having constraint length 2 is first obtained using the combined trellis diagram. As shown in Table 4.6, code [3,1] has been selected as the appropriate code having constraint length 2. The trellis of the code [3,1] having constraint length 2 combined with differentially encoded GMSK, and the trellis diagram of the code [3,1] alone have been reproduced from Section 4.4 and shown in Fig. 5.2a and Fig. 5.2b, respectively. Assuming that an all-zero coded sequence has been transmitted, the error state diagram of this trellis coded scheme can be represented as shown in Fig. 5.3. It is observed from Fig. 5.3, each path connecting the initial state ($\boldsymbol{0}$,0°) at node (**0**), and the final state ($\boldsymbol{0}$,0°) at node (**4**) represents an error event. Let the matrix transfer function at any node (**i**) be denoted by ξ_i, and the branch matrix labels are denoted as t_1, t_2, t_3, ..., t_7. Thus, the matrix transfer function, **G** of the error state diagram shown in Fig. 5.3 may be expressed by ξ_4. It may be seen from Fig. 5.3, that node (**4**) can only be reached from node (**3**) through the branch having the matrix label t_7. Thus, the matrix transfer function **G** of the error state diagram may be expressed as (Biglieri *et al*, 1991)

$$\mathbf{G} = \xi_3 t_7 \tag{5.63a}$$

Furthermore, it may be observed that node (**3**) can be reached either from node (**2**) through the branch labelled as t_3, or from node (**1**) through the branch labelled as t_4. Thus, ξ_3 can be written as

$$\xi_3 = \xi_2 t_3 + \xi_1 t_4 \tag{5.63b}$$

Similarly,
$$\xi_2 = \xi_2 t_6 + \xi_1 t_2 \tag{5.63c}$$

and
$$\xi_1 = t_1 + \xi_3 t_5 \tag{5.63d}$$

According to Biglieri *et al* (1991), the branch matrix labels t_1, t_2, t_3, ..., t_7 of the error state diagram may be obtained using the error weight matrix $G(\mathbf{e})_{(\phi)}$ as given in Eq. (5.48). From Fig. 5.2a and Fig. 5.3, the branch matrix label t_1

representing the transition from the state (*0*,0°) to (*1*,148°) corresponds to the error vector **e**=(*11*). Similarly, it may be observed that the other branch matrix labels in the error state diagram t_2, t_3, ..., t_7 correspond to the following error vectors:

$t_2 \rightarrow$**e** = (*01*) initiating from the phase state of 148°,

$t_3 \rightarrow$**e** = (*10*) initiating from the phase state of 0°',

$t_4 \rightarrow$**e** = (*10*) initiating from the phase state of 148°,

$t_5 \rightarrow$**e** = (*11*) initiating from the phase state of -148°,

$t_6 \rightarrow$**e** = (*01*) initiating from the phase state of 0°' and

$t_7 \rightarrow$**e** = (*00*) initiating from the phase state of -148°.

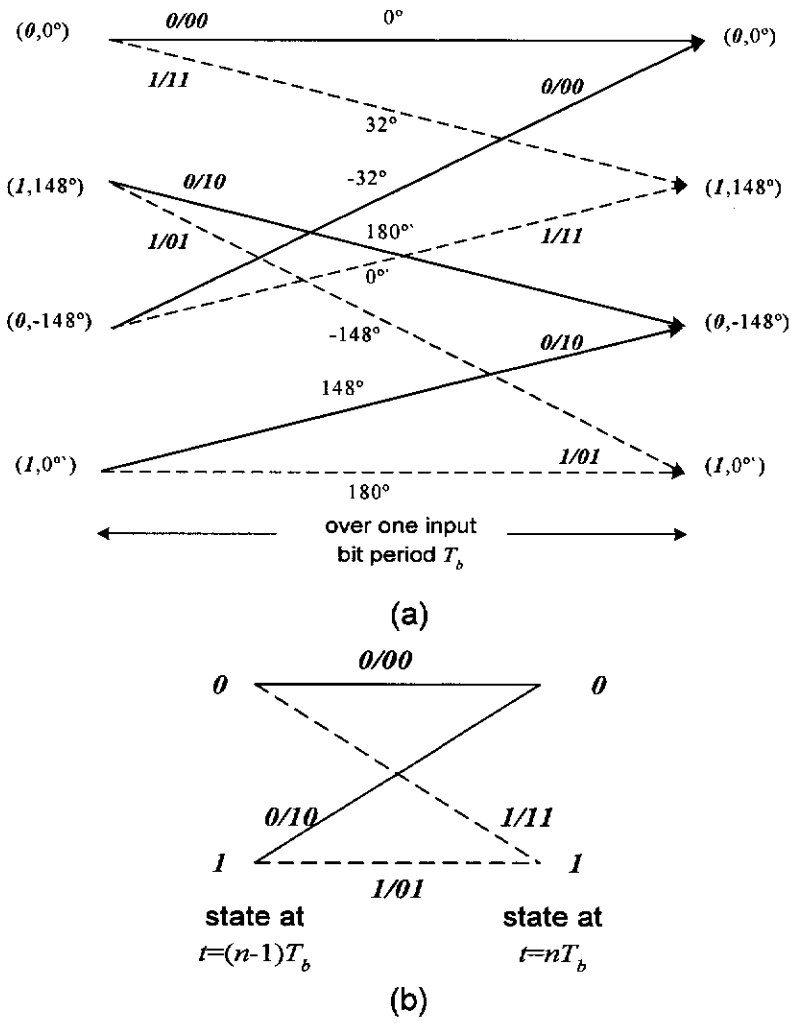

Figure 5.2 (a) Trellis diagram of the code [3,1] combined with differentially encoded GMSK (b) trellis diagram of the code [3,1].

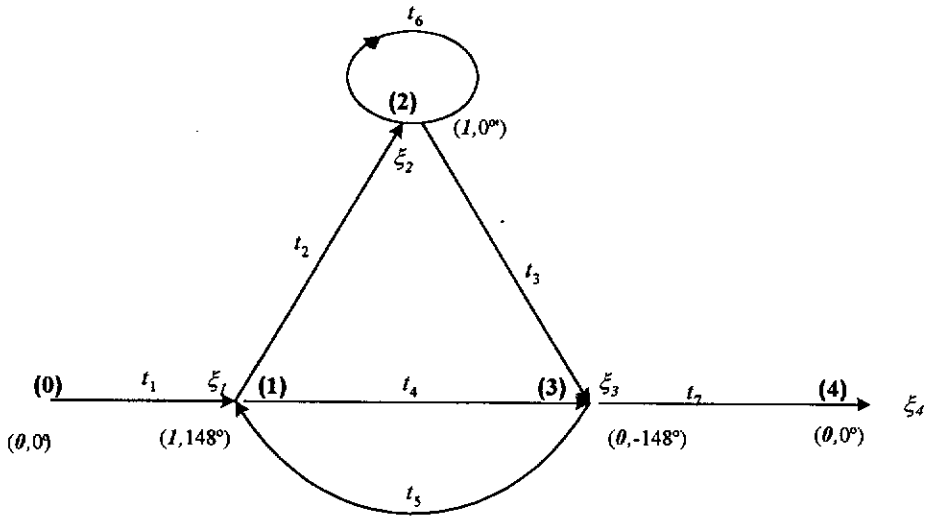

Figure 5.3 Error state diagram of the code [3,1] in combination with differentially encoded GMSK.

Now, from Eq. (5.48), the error weight matrix $G(\mathbf{e})_{(\phi)}$ representing t_1 may be expressed as

$$G(\mathbf{e})_{(\phi)} = \frac{1}{2}\begin{bmatrix} D^{\|f(00)-f(e_1e_2)\|^2} & D^{\|f(10)-f(\bar{e}_1e_2)\|^2} \\ D^{\|f(01)-f(e_1\bar{e}_2)\|^2} & D^{\|f(11)-f(\bar{e}_1\bar{e}_2)\|^2} \end{bmatrix} \tag{5.64}$$

where $\mathbf{e}=(11)$ and $\phi = 0°$. Then, $\|f(00)-f(e_1e_2)\|^2$ in the matrix $G(\mathbf{e})_{(\phi)}$ becomes the distance metric between the two coded sequences (00) and (11) having the initial phase state of 0°. The phases corresponding to these transmitted coded bits required in obtaining the distance metrics for AWGN channels, as given in Eq. (5.27) may be obtained using the finite state diagram of the differentially encoded GMSK signal as shown in Fig. 4.7. For the purpose of easy reference, this finite state diagram has been reproduced in Fig. 5.4.

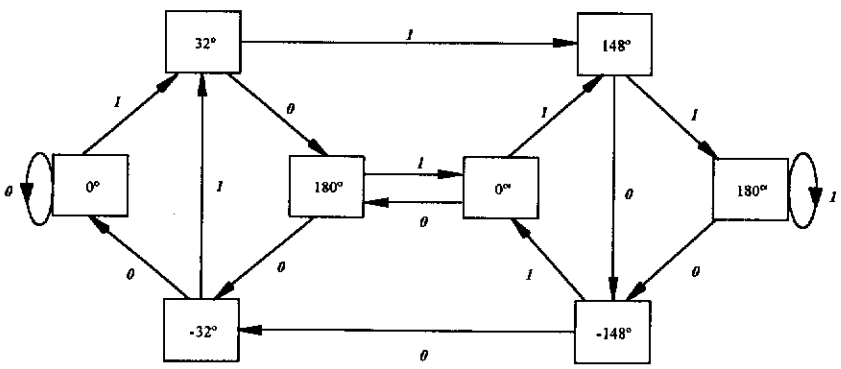

Figure 5.4 The finite state diagram of the differentially encoded GMSK signal.

As observed in Fig. 5.4, the phase state at the end of the two coded bits (*00*) initiating from phase state of 0° becomes 0° going through the intermediate phase state of 0°. Similarly, the phase state at the end of coded bits (*11*) initiating from the phase state of 0° becomes 148° going through the intermediate phase state of 32°. Then, the distance metric in the presence of AWGN, between the two coded signals (*00*) and (*11*) having the initial phase state of 0° may be obtained using Eq. (5.27), such that

$$\left\| f(00) - f(11) \right\|^2 = [1\text{-}\cos(0°\text{-}32°)]+[1\text{-}\cos(0°\text{-}148°)]$$

$$= 2. \qquad (5.65a)$$

Similarly, $\left\| f(10) - f(\bar{e}_1 e_2) \right\|^2$ in the matrix $G(\mathbf{e})_{(\phi)}$, as given in Eq. (5.64), represents the distance metric between the two coded signals (*10*) and (*01*) having the initial phase state of 0°. From Fig. 5.4, it may be observed that the intermediate phase states corresponding to these two coded signals become 32° and 0°, respectively. The corresponding phase states at the end of the two coded bits become 180° and 32°, respectively. Consequently, the corresponding distance metric over AWGN between the two coded signals (*10*) and (*01*) may be obtained as

$$\left\| f(10) - f(\bar{e}_1 e_2) \right\|^2 = [1\text{-}\cos(32°\text{-}0°)]+[1\text{-}\cos(180°\text{-}32°)]$$

$$= 2. \qquad (5.65b)$$

The remaining elements $\left\| f(01) - f(e_1 \bar{e}_2) \right\|^2$ and $\left\| f(11) - f(\bar{e}_1 \bar{e}_2) \right\|^2$ of the error weight matrix $G(\mathbf{e})_{(\phi)}$, as given in Eq. (5.64), represent the distance metrics corresponding to the coded signals [(*01*), (*10*)], and [(*11*), (*00*)], respectively. These elements may also be obtained using the phase values of the states corresponding to the respective coded signals. From Fig. 5.4, the phase states corresponding to the two coded signals (*01*) and (*10*) become (0°,32°) and (32°,180°), respectively. Moreover, the phase states corresponding to the two coded signals (*11*) and (*00*) become (32°,148°) and (0°,0°), respectively. Then the corresponding distance metrics over AWGN between these coded signals may be expressed as

$$\left\| f(\boldsymbol{01}) - f(e_1\overline{e_2}) \right\|^2 = [1\text{-}\cos(0°\text{-}32°)]+[1\text{-}\cos(32°\text{-}180°)] = 2 \qquad (5.65c)$$

and

$$\left\| f(\boldsymbol{11}) - f(\overline{e_1 e_2}) \right\|^2 = [1\text{-}\cos(32°\text{-}0°)]+[1\text{-}\cos(148°\text{-}0°)] = 2. \qquad (5.65d)$$

Now, the error weight matrix $G(\mathbf{e})_{(\phi)}$, as given in Eq. (5.64), representing the branch matrix label t_1 from node (**0**) to (**1**) of the error state diagram, may be obtained from the Equations (5.65a) to (5.65d) as

$$t_1 = G(\boldsymbol{11})_{(\phi)} = \frac{1}{2}\begin{bmatrix} D^2 & D^2 \\ D^2 & D^2 \end{bmatrix}. \qquad (5.66)$$

As shown in Fig. 5.2a and Fig. 5.2b, the input bit corresponding to the error vector $\mathbf{e}=(\boldsymbol{11})$ representing the transition from the state ($\boldsymbol{0}$,0°) to state ($\boldsymbol{1}$,148°), is $\boldsymbol{1}$. The number of non-zero input bits in error in this transition may be incorporated in the error weight matrix by multiplying the elements of the corresponding error weight matrix $G(\boldsymbol{11})$ by a factor J as discussed in Section 5.3. Accordingly, the branch matrix label t_1 may be expressed as

$$\begin{aligned} t_1 &= \frac{1}{2}J\begin{bmatrix} D^2 & D^2 \\ D^2 & D^2 \end{bmatrix} \\ &= \frac{1}{2}D^2J\begin{bmatrix} 1 & 1 \\ 1 & 1 \end{bmatrix} \end{aligned} \qquad (5.67a)$$

Similarly, the rest of the branch matrices labeled t_2, t_3,...., t_7 as indicated in the error state diagram of Fig. 5.3 may be obtained using the same procedure, such that

$$t_2 = G(\boldsymbol{01})_{(148°)}J \qquad (5.67b)$$

$$t_3 = G(\boldsymbol{10})_{(0°)} \qquad (5.67c)$$

$$t_4 = G(\boldsymbol{10})_{(148°)} \qquad (5.67d)$$

$$t_5 = G(\boldsymbol{11})_{(-148°)}J \qquad (5.67e)$$

$$t_6 = G(\boldsymbol{01})_{(0°)}J \qquad (5.67f)$$

and

$$t_7 = G(\boldsymbol{00})_{(-148°)} \qquad (5.67g)$$

With the corresponding error weight matrices given in Equations (5.67b) to (5.67g) obtained using Eq. (5.48), the branch matrices t_2, t_3, ..., t_7 may be expressed as

$$t_2 = \frac{1}{2} D^{0.152} J \begin{bmatrix} 1 & 1 \\ 1 & 1 \end{bmatrix} \quad (5.68a)$$

$$t_3 = \frac{1}{2} \begin{bmatrix} D^{1.59} & D^{1.59} \\ D^{2.152} & D^{2.152} \end{bmatrix} \quad (5.68b)$$

$$t_4 = \frac{1}{2} \begin{bmatrix} D^{1.59} & D^{1.59} \\ D^{2.152} & D^{2.152} \end{bmatrix} \quad (5.68c)$$

$$t_5 = \frac{1}{2} D^2 J \begin{bmatrix} 1 & 1 \\ 1 & 1 \end{bmatrix} \quad (5.68d)$$

$$t_6 = \frac{1}{2} D^{0.152} J \begin{bmatrix} 1 & 1 \\ 1 & 1 \end{bmatrix} \quad (5.68e)$$

and $$t_7 = \frac{1}{2} \begin{bmatrix} 1 & 1 \\ 1 & 1 \end{bmatrix} \quad (5.68f)$$

Substituting the branch matrices given in Eq. (5.67a) and Equations (5.68a) to (5.68f) in Equations (5.63a) to (5.63d), the matrix transfer function **G** of the error state diagram in the presence of AWGN can be derived as shown in Eq. (D.7a) of Appendix D, such that

$$\mathbf{G} = \frac{D^2 J(D^{1.59} + D^{2.152})}{2[2 - 2D^{0.152} J - D^2 J(D^{1.59} + D^{2.152})]} \begin{bmatrix} 1 & 1 \\ 1 & 1 \end{bmatrix} \quad (5.69)$$

According to Eq. (5.52), the transfer function of the error state diagram $T(D,J)$, is then given by

$$T(D,J) = \frac{1}{N} \mathbf{1}^T \mathbf{G}\, \mathbf{1}. \quad (5.70)$$

As discussed in Section 5.3.1, for rate-½ coded schemes, N=2 and **1** is a column N-vector with all of its elements equal to 1. As a result,

$$T(D,J) = \frac{1}{2} \frac{D^2 J(D^{1.59} + D^{2.152})}{2[2 - 2D^{0.152} J - D^2 J(D^{1.59} + D^{2.152})]} \begin{bmatrix} 1 & 1 \end{bmatrix} \begin{bmatrix} 1 & 1 \\ 1 & 1 \end{bmatrix} \begin{bmatrix} 1 \\ 1 \end{bmatrix}$$

$$= \frac{D^2 J(D^{1.59} + D^{2.152})}{[2 - 2D^{0.152} J - D^2 J(D^{1.59} + D^{2.152})]}. \quad (5.71)$$

5.3.2 The transfer function of the error state diagram of the trellis coded scheme having constraint length 2 over amplitude-fading channel

As shown in Eq. (5.46a) and (5.46b), the upperbound of the probability of event error P_E, for an amplitude-fading channel can be obtained by replacing the function $\exp\left[\left(\frac{-E_b}{4N_0}\right)d^2(x_k,x_k')\right]$ in the upperbound for an AWGN channel by the function $\left\{1+\frac{E_b}{4N_0}d^2(x_k,x_k')\right\}^{-1}$. As a result, the elements of the matrix $G(\mathbf{e})_{(\phi)}$ given in Eq. (5.48) over an amplitude-fading channel may be obtained by merely replacing D^{δ} by $\left\{1+\frac{E_b}{4N_0}\delta\right\}^{-1}$, where δ is the distance metric over an AWGN channel.

The transfer function of the error state diagram $T(Z,J)$ over an amplitude-fading channel is derived, as shown in Eq. (D.7b) of Appendix D, and is given by

$$T(Z,J) = \frac{(1+2Z)^{-1}J[(1+1.59Z)^{-1}+(1+2.152Z)^{-1}]}{\{2-2(1+0.152Z)^{-1}J-(1+2Z)^{-1}J[(1+1.59Z)^{-1}+(1+2.152Z)^{-1}]\}} \tag{5.72}$$

where $Z=\frac{E_b}{4N_0}$ denotes the average bit energy to noise spectral density ratio.

5.3.3 The bounds on the bit error probability of trellis coded GMSK scheme having constraint length 2

According to Eq. (5.61), the upperbound on the bit error probability P_b depends on the derivative of $T(D,J)$ with respect to J. Now, by taking the partial derivative with respect to J of $T(D,J)$ as given in Eq. (5.71), it is shown that

$$\frac{\partial}{\partial J}T(D,J)\Big|_{J=1,D=\exp(-E_b/4N_0)} = \frac{[2-2D^{0.152}J-D^2J(D^{1.59}+D^{2.152})]D^2(D^{1.59}+D^{2.152})}{[2-2D^{0.152}J-D^2J(D^{1.59}+D^{2.152})]^2}$$

$$-\frac{D^2J(D^{1.59}+D^{2.152})[-2D^{0.152}-D^2(D^{1.59}+D^{2.152})]}{[2-2D^{0.152}J-D^2J(D^{1.59}+D^{2.152})]^2}$$

$$= \frac{2D^2(D^{1.59}+D^{2.152})}{[2-2D^{0.152}-D^2(D^{1.59}+D^{2.152})]^2}. \qquad (5.73)$$

As given in Table 4.6, the free distance d^2_{free}, of the selected code [3,1] when combined with differentially encoded GMSK is equal to 6. Using this value of d^2_{free} and the derivative of $T(D,J)$ as given in Eq. (5.73), the upper bound on the bit error probability, $[P_b]_{u.b.}$, of the trellis coded scheme having constraint length 2 over an AWGN channel may be obtained from Eq. (5.61), such that

$$[P_b]_{u.b.} \le \frac{1}{2}\operatorname{erfc}\left(\sqrt{\frac{6E_b}{4N_0}}\right)\exp\left(\frac{6E_b}{4N_0}\right)\frac{2D^2(D^{1.59}+D^{2.152})}{[2-2D^{0.152}-D^2(D^{1.59}+D^{2.152})]^2}. \qquad (5.74)$$

where $D = \exp\left(-\frac{E_b}{4N_0}\right)$. However, note that this bound is only valid over the range of E_b/N_0 values for which the denominator in Eq. (5.74) is not equal to zero. Similarly, the lower bound on the bit error probability, $[P_b]_{l.b.}$, of the trellis coded scheme having constraint length 2 over an AWGN channel may be obtained using Eq. (5.62) as

$$[P_b]_{l.b.} \ge \frac{1}{2}\operatorname{erfc}\left(\sqrt{\frac{6E_b}{4N_0}}\right). \qquad (5.75)$$

Furthermore, the upperbound on the bit error probability of the trellis coded scheme over an amplitude-fading channel may be obtained using the transfer function of the error state diagram expressed in Eq. (5.72). By analogy with the upperbound on the bit error probability over an AWGN channel, as given in Eq. (5.54), the upper bound over an amplitude-fading channel may now be expressed as (Biglieri *et al*, 1991)

$$P_b \le \frac{\partial}{\partial J}T(Z,J)\Big|_{J=1,Z=E_b/4N_0} \qquad (5.76)$$

Now, by taking the partial derivative with respect to J of the transfer function of the error state diagram $T(Z,J)$ over an amplitude-fading channel as given in Eq. (5.72), it is shown that

$$\left.\frac{\partial}{\partial J}T(Z,J)\right|_{J=1,Z=E_b/4N_0} =$$

$$\frac{\{2-2(1+0.152Z)^{-1}J-(1+2Z)^{-1}J[(1+1.59Z)^{-1}+(1+2.152Z)^{-1}]\}(1+2Z)^{-1}[(1+1.59Z)^{-1}+(1+2.152Z)^{-1}]}{\{2-2(1+0.152Z)^{-1}J-(1+2Z)^{-1}J[(1+1.59Z)^{-1}+(1+2.152Z)^{-1}]\}^2}$$

$$-\frac{(1+2Z)^{-1}J[(1+1.59Z)^{-1}+(1+2.152Z)^{-1}][-2[1+0.152Z]^{-1}-[1+2Z]^{-1}([1+1.59Z]^{-1}+[1+2.152Z]^{-1})]}{\{2-2(1+0.152Z)^{-1}J-(1+2Z)^{-1}J[(1+1.59Z)^{-1}+(1+2.152Z)^{-1}]\}^2}$$

$$=\frac{2(1+2Z)^{-1}[(1+1.59Z)^{-1}+(1+2.152Z)^{-1}]}{\{2-2(1+0.152Z)^{-1}-(1+2Z)^{-1}[(1+1.59Z)^{-1}+(1+2.152Z)^{-1}\}^2} \qquad (5.77)$$

From Eq. (5.76), the upper bound on the bit error probability, $[P_b]_{u.b.}$, of the selected trellis coded scheme having constraint length 2 over an amplitude-fading channel may be expressed as

$$[P_b]_{u.b.} \le \frac{2(1+2Z)^{-1}[(1+1.59Z)^{-1}+(1+2.152Z)^{-1}]}{\{2-2(1+0.152Z)^{-1}-(1+2Z)^{-1}[(1+1.59Z)^{-1}+(1+2.152Z)^{-1}]\}^2} \qquad (5.78)$$

where $Z=\frac{E_b}{4N_0}$ denotes the average bit energy to noise spectral density ratio.

Again, the bound is only valid over the range of E_b/N_0 values for which the denominator in Eq. (5.78) is not equal to zero.

Using the expressions given in Equations (5.74), (5.75) and (5.78), the bounds of the bit error probability for the trellis coded GMSK schemes combined with code [3,1] over AWGN and amplitude-fading channels, are plotted as shown in Fig. 5.5. It can be observed from Fig 5.5, the bounds obtained for the AWGN channel are tight to within 2.5dB.

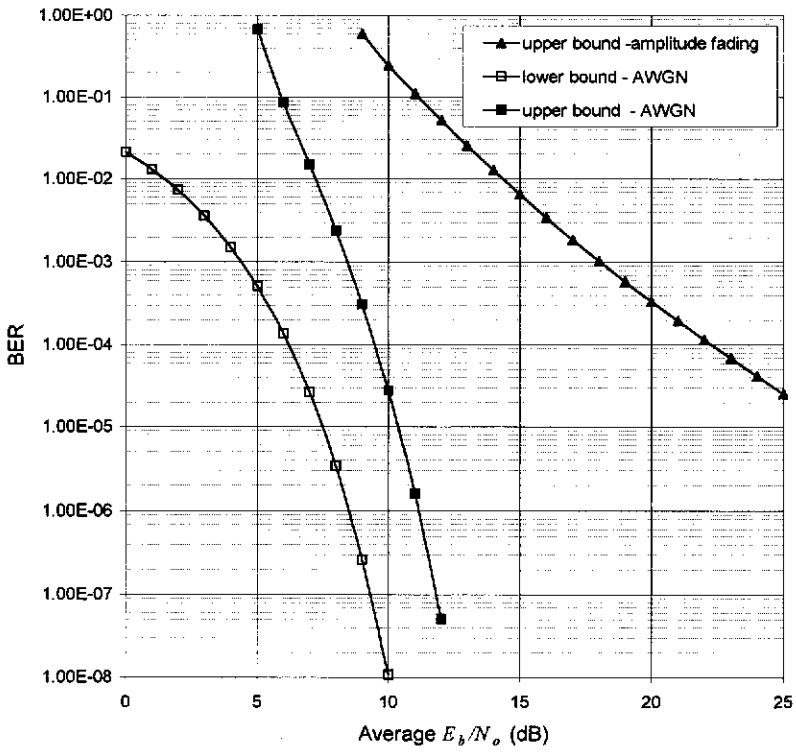

Figure 5.5 The bounds of the bit error probabilities for the trellis coded GMSK scheme in conjunction with the code [3,1] having constraint length 2 for AWGN and amplitude-fading channels.

5.3.4 The transfer function of the error state diagram of the trellis coded scheme having constraint length 3 over AWGN channels

As shown in Table 4.6, code [7,3] has been selected as the appropriate code having constraint length 3. The trellis of the code [7,3] alone, and the trellis of the code [7,3] combined with differentially encoded GMSK have been reproduced from Section 4.8 and shown in Fig. 5.6a and 5.6b, respectively. Assuming that an all zero coded sequence has been transmitted, the error state diagram of this trellis coded scheme can be represented as shown in Fig. 5.7.

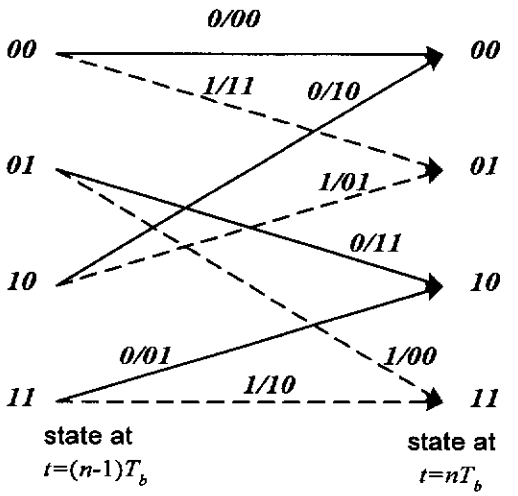

(a)

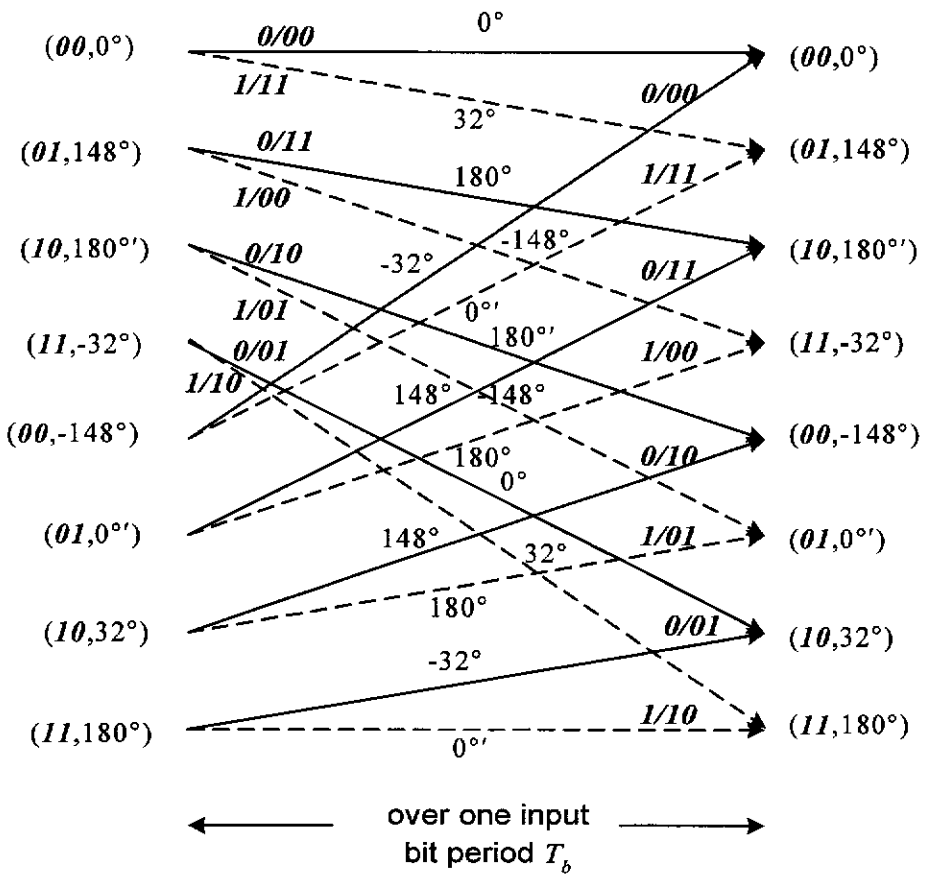

(b)

Figure 5.6 (a) The trellis diagram of the code [7,3] (b) Trellis diagram of the code [7,3] combined with differentially encoded GMSK.

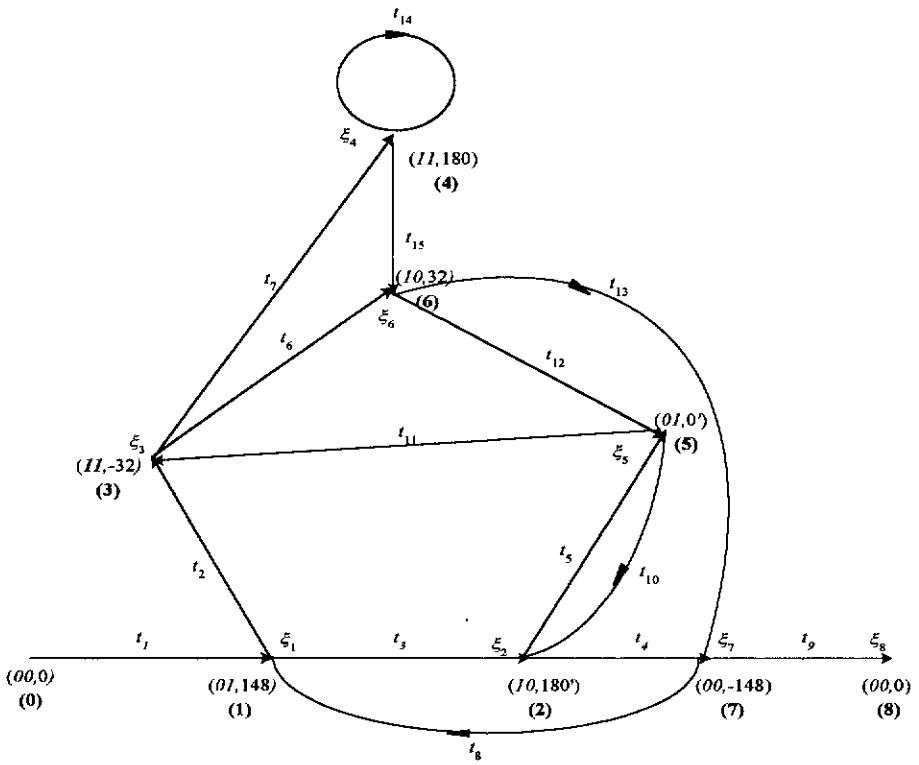

Note : Here the phase states are in degrees

Figure 5.7 Error state diagram of the code [7,3] in combination with differentially encoded GMSK.

Let ξ_i denotes the matrix transfer function of node (i), and the branch matrix labels as $t_1, t_2, t_3, ..., t_{15}$ as presented in Section 5.3.1. Accordingly, the matrix transfer function **G** of the error state diagram shown in Fig. 5.7 may be expressed as ξ_8. It may be seen from Fig. 5.7, that node (8) can only be reached from node (7) through the branch having the matrix label t_9. Thus, the matrix transfer function **G** of the error state diagram may be expressed as (Biglieri *et al*, 1991)

$$\mathbf{G} = \xi_7 t_9 \tag{5.79a}$$

Furthermore, it may be observed that node (7) can be reached either from node (2) through the branch labelled as t_4, or from node (6) through the branch labelled as t_{13}. Thus, ξ_7 can be written as,

$$\xi_7 = \xi_6 t_{13} + \xi_2 t_4 \tag{5.79b}$$

Similarly,

$$\xi_6 = \xi_3 t_6 + \xi_4 t_{15} \tag{5.79c}$$

$$\xi_5 = \xi_6 t_{12} + \xi_2 t_5 \tag{5.79d}$$

$$\xi_4 = \xi_3 t_7 + \xi_4 t_{14} \tag{5.79e}$$

$$\xi_3 = \xi_1 t_2 + \xi_5 t_{11} \quad (5.79\text{ f})$$

$$\xi_2 = \xi_1 t_3 + \xi_5 t_{10} \quad (5.79\text{g})$$

and $$\xi_1 = t_1 + \xi_7 t_8 \quad (5.79\text{h})$$

As discussed in Section 5.3.1, the corresponding branch matrices labelled t_1, t_2, t_3, ..., t_{15}, over an AWGN channel may be obtained as

$$t_1 = G(\boldsymbol{11})_{(0°)} J^1 = \frac{1}{2} D^2 J \begin{bmatrix} 1 & 1 \\ 1 & 1 \end{bmatrix} \quad (5.80\text{a})$$

$$t_2 = G(\boldsymbol{00})_{(148°)} J^1 = \frac{1}{2} J \begin{bmatrix} 1 & 1 \\ 1 & 1 \end{bmatrix} \quad (5.80\text{b})$$

$$t_3 = G(\boldsymbol{11})_{(148°)} = \frac{1}{2} D^2 \begin{bmatrix} 1 & 1 \\ 1 & 1 \end{bmatrix} \quad (5.80\text{c})$$

$$t_4 = G(\boldsymbol{10})_{(180°)} = \frac{1}{2} \begin{bmatrix} D^{1.59} & D^{1.59} \\ D^{2.152} & D^{2.152} \end{bmatrix} \quad (5.80\text{d})$$

$$t_5 = G(\boldsymbol{01})_{(180°)} J^1 = \frac{1}{2} D^{0.152} J \begin{bmatrix} 1 & 1 \\ 1 & 1 \end{bmatrix} \quad (5.80\text{e})$$

$$t_6 = G(\boldsymbol{01})_{(-32°)} = \frac{1}{2} D^{0.152} \begin{bmatrix} 1 & 1 \\ 1 & 1 \end{bmatrix} \quad (5.80\text{ f})$$

$$t_7 = G(\boldsymbol{10})_{(-32°)} J^1 = \frac{1}{2} J \begin{bmatrix} D^{2.152} & D^{2.152} \\ D^{1.59} & D^{1.59} \end{bmatrix} \quad (5.80\text{g})$$

$$t_8 = G(\boldsymbol{11})_{(-148°)} J^1 = \frac{1}{2} D^2 J \begin{bmatrix} 1 & 1 \\ 1 & 1 \end{bmatrix} \quad (5.80\text{h})$$

$$t_9 = G(\boldsymbol{00})_{(-148°)} = \frac{1}{2} \begin{bmatrix} 1 & 1 \\ 1 & 1 \end{bmatrix} \quad (5.80\text{i})$$

$$t_{10} = G(\boldsymbol{11})_{(0°)} = \frac{1}{2} D^2 \begin{bmatrix} 1 & 1 \\ 1 & 1 \end{bmatrix} \quad (5.80\text{j})$$

$$t_{11} = G(\boldsymbol{00})_{(0°)} J^1 = \frac{1}{2} J \begin{bmatrix} 1 & 1 \\ 1 & 1 \end{bmatrix} \quad (5.80\text{k})$$

$$t_{12} = G(\boldsymbol{01})_{(32°)} J^1 = \frac{1}{2} D^{0.152} J \begin{bmatrix} 1 & 1 \\ 1 & 1 \end{bmatrix} \quad (5.80\text{l})$$

$$t_{13} = G(\boldsymbol{10})_{(32°)} = \frac{1}{2}\begin{bmatrix} D^{1.59} & D^{1.59} \\ D^{2.152} & D^{2.152} \end{bmatrix} \quad (5.80m)$$

$$t_{14} = G(\boldsymbol{10})_{(180°)}J^1 = \frac{1}{2}J\begin{bmatrix} D^{2.152} & D^{2.152} \\ D^{1.59} & D^{1.59} \end{bmatrix} \quad (5.80n)$$

and $$t_{15} = G(\boldsymbol{01})_{(180°)} = \frac{1}{2}D^{0.152}\begin{bmatrix} 1 & 1 \\ 1 & 1 \end{bmatrix} \quad (5.80o)$$

Substituting these matrices t_1, t_2, t_3, ..., t_{15}, in Equations (5.79a) to (5.79h), the matrix transfer function **G** of the error state diagram representing the trellis coded scheme having constraint length 3 code over an AWGN channel can be obtained as discussed in Section 5.3.1. However, the solution of these set of equations may not be as simple as the one discussed in Section 5.3.1, due to the increase in the number of equations and the number of matrices involved. Therefore, the set of Equations (5.79a) to (5.79h), to be solved in this case has been first formatted into the form of a set of linear equations by considering the matrices by their elements. Solving these set of linear equations as discussed in Appendix E, the matrix transfer function **G** of the error state diagram has been obtained. Using Eq. (5.70), the transfer function of the error state diagram $T(D,J)$ has been obtained as shown in Eq. (E.21) of Appendix E, such that

$$T(D,J) = \beta_1 J \frac{\left\{\left(\frac{-p_1}{2p_2}\right)\left(\frac{p_4 J}{\beta_1}\right)+\left(\frac{p_1}{2p_2}\right)\right\}}{\left\{\left[-\beta_1 J\left\{\left(\frac{-p_1}{2p_2}\right)\left(\frac{p_4 J}{\beta_1}\right)+\left(\frac{p_1}{2p_2}\right)\right\}\right]-\left[\left(\frac{-p_4 J}{\beta_1}\right)-\left(\frac{1}{\beta_1\beta_6 J}\right)+1\right]\right\}} \quad (5.81)$$

where, $p_1 = \{\beta_3 + \beta_4\}$; $p_2 = \beta_5 J$; and $p_4 = \frac{-\beta_6}{(m_2)}$.

$\beta_1 = D^2$, $\beta_3 = D^{1.59}$, $\beta_4 = D^{2.152}$, $\beta_6 = D^{0.152}$ and $D = \exp\left(-\frac{E_b}{4N_0}\right)$.

5.3.5 The transfer function of the error state diagram of the trellis coded scheme having constraint length 3 over amplitude-fading channel

As discussed in Section 5.3.2, the transfer function of the error state diagram $T(Z,J)$ over an amplitude-fading channel may be obtained as shown in Eq. (E.21) of Appendix E as

$$T(Z,J) = \beta_1 J \frac{\left\{\left(\frac{-p_1}{2p_2}\right)\left(\frac{p_4 J}{\beta_1}\right)+\left(\frac{p_1}{2p_2}\right)\right\}}{\left\{\left[-\beta_1 J\left\{\left(\frac{-p_1}{2p_2}\right)\left(\frac{p_4 J}{\beta_1}\right)+\left(\frac{p_1}{2p_2}\right)\right\}\right]-\left[\left(\frac{-p_4 J}{\beta_1}\right)-\left(\frac{1}{\beta_1\beta_6 J}\right)+1\right]\right\}} \tag{5.82}$$

where, $p_1 = \{\beta_3 + \beta_4\}$; $p_2 = \beta_5 J$; and $p_4 = \frac{-\beta_6}{(m_2)}$.

$\beta_1=\{1+2Z\}^{-1}$, $\beta_3=\{1+1.59Z\}^{-1}$, $\beta_4=\{1+2.152Z\}^{-1}$, $\beta_6=\{1+0.152Z\}^{-1}$ and $Z=\frac{E_b}{4N_0}$.

5.3.6 The bounds on the bit error probability of trellis coded GMSK scheme having constraint length 3

As shown in Eq. (E.26) of Appendix E, the partial derivative of $T(D,J)$ with respect to J over an AWGN channel may be expressed as

$$\frac{\partial}{\partial J}T(D,J)\Big|_{J=1,D=\exp(-E_b/4N_0)} = \frac{A_2}{B_2} \tag{5.83}$$

where,

$$A_2=2(\beta_3+\beta_4)\{2\beta_1\beta_6[2-(\beta_3+\beta_4)]+\beta_1^2[2-(\beta_3+\beta_4)]^2+4\beta_1\beta_6 \tag{5.84a}$$

and

$$B_2 = \{[2-(\beta_3+\beta_4)][2-\beta_1^2(\beta_3+\beta_4)]-4\beta_6^2-4\beta_1\beta_6\}^2 \tag{5.84b}$$

Moreover, $\beta_1 = D^2$, $\beta_3 = D^{1.59}$, $\beta_4 = D^{2.152}$, $\beta_6 = D^{0.152}$ and $D = \exp\left(-\frac{E_b}{4N_0}\right)$.

As shown in Table 4.6, the free distance d^2_{free}, of the selected code [7,3] when combined with differentially encoded GMSK is equal to 8. Using this value of d^2_{free} and the derivative of $T(D,J)$ as given in Eq. (5.83), the upper bound on the bit error probability, $[P_b]_{u.b.}$, of the trellis coded scheme having

constraint length 3 over an AWGN channel may be obtained from Eq. (5.61), such that

$$[P_b]_{u.b.} \leq \frac{1}{2}\operatorname{erfc}\left(\sqrt{\frac{8E_b}{4N_0}}\right)\exp\left(\frac{8E_b}{4N_0}\right).\frac{A_2}{B_2} \tag{5.85}$$

where A_2 and B_2 are as given in Eq. (5.84a) and (5.84b) and $D=\exp\left(-\frac{E_b}{4N_0}\right)$.

However, note that this bound is valid over the range of E_b/N_0 values for which the denominator B_2 in Eq. (5.85) is not equal to zero. Similarly, the lower bound on the bit error probability, $[P_b]_{l.b.}$, of the trellis coded scheme having constraint length 3 over an AWGN channel may be obtained using Eq. (5.62) as

$$[P_b]_{l.b.} \geq \frac{1}{2}\operatorname{erfc}\left(\sqrt{\frac{8E_b}{4N_0}}\right). \tag{5.86}$$

Furthermore, the upperbound on the bit error probability, $[P_b]_{u.b.}$, of the trellis coded scheme over an amplitude-fading channel may be obtained using the transfer function of the error state diagram expressed in Eq. (5.82). As a result, the upperbound on the bit error probability, $[P_b]_{u.b.}$, over an amplitude-fading channel as given in Eq. (5.76) may be expressed as

$$P_b \leq \frac{A_2}{B_2} \tag{5.87}$$

Again A_2 and B_2 are as given in Eq. (5.84a) and (5.84b). However, in this case, $\beta_1=\{1+2Z\}^{-1}$, $\beta_3=\{1+1.59Z\}^{-1}$, $\beta_4=\{1+2.152Z\}^{-1}$, $\beta_6=\{1+0.152Z\}^{-1}$ and $Z=\frac{E_b}{4N_0}$.

Now, using the expressions given in Equations (5.85), (5.86) and (5.87), the bounds of the bit error probability of the trellis coded GMSK schemes combined with code [7,3] over AWGN and amplitude-fading channels, respectively may be obtained as shown in Fig. 5.8.

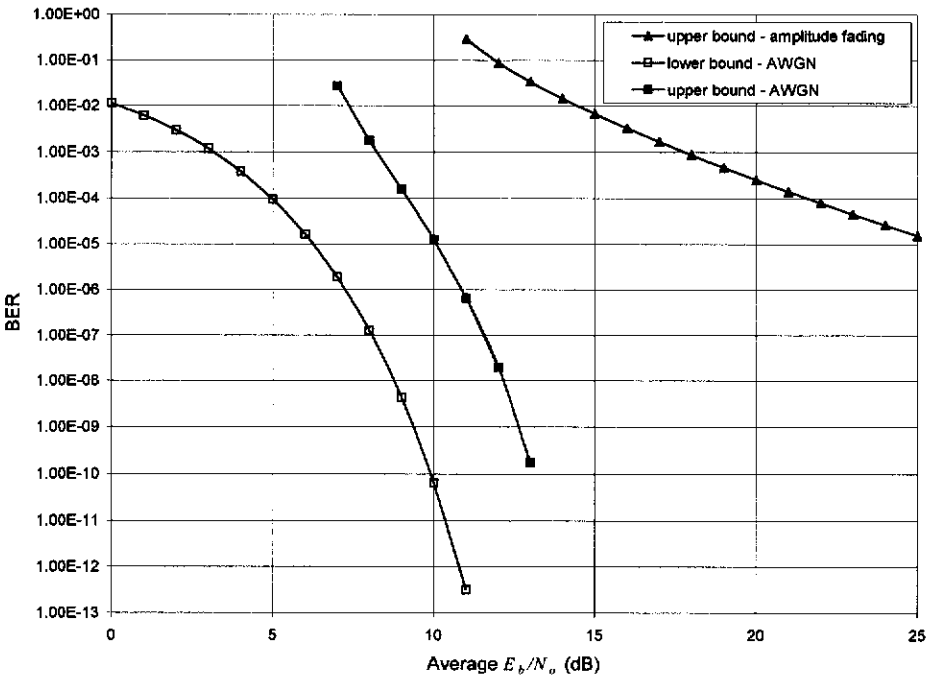

Figure 5.8 The bounds of the bit error probabilities for the trellis coded GMSK scheme in conjunction with the code [7,3] having constraint length 3 for AWGN and amplitude-fading channels.

5.4 Comments on the Analyses

From Sections 5.3.1 and 5.3.4, it has been observed that when the number of states in the trellis diagram increases, the error state diagram becomes complex and determination of the associated transfer function becomes a tedious task. Therefore, the trellis coded schemes selected, which have up to 8 states in the combined trellis have only been considered in the analysis. Moreover, these analyses of the bit error probabilities over an AWGN channel are obtained assuming ideal carrier recovery and timing recovery conditions. Therefore, the effect of possible practical impairments such as phase and timing errors has not been evaluated. The effect of fading has also been simplified by assuming that it only affects the amplitude of the received signal. In practical situations, it may not be possible for the phase variations of the received signal over a fading channel to be fully tracked. In such situations, simulations may be more effective to study the exact system performance, including practical impairments, rather than the bounds on the bit error probabilities assuming ideal practical conditions. Therefore, in the

following chapters the BER performances of the selected trellis coded schemes over AWGN, and fading channels based on both frequency-nonselective and selective conditions, are carried out using simulations.

CHAPTER 6

PERFORMANCE OF SELECTED TRELLIS CODED GMSK SIGNALS IN THE PRESENCE OF AWGN

6.1 Introduction

The BER performances of the selected trellis coded GMSK schemes having constraint lengths 2 and 3, in the presence of AWGN have been analytically evaluated in Chapter 5. In the case of the frequency non-selective fading environment, the theoretical analysis has been simplified to include only amplitude fading.

In this chapter, computer simulation techniques have been used to evaluate the BER performance in the presence of AWGN, when practical system impairments such as sample timing error and carrier phase error are present.

6.2 Computer Simulation Model

The system model which has been adopted in this study, consisting of the transmitter, the channel, and the receiver, is shown in Fig. 6.1.

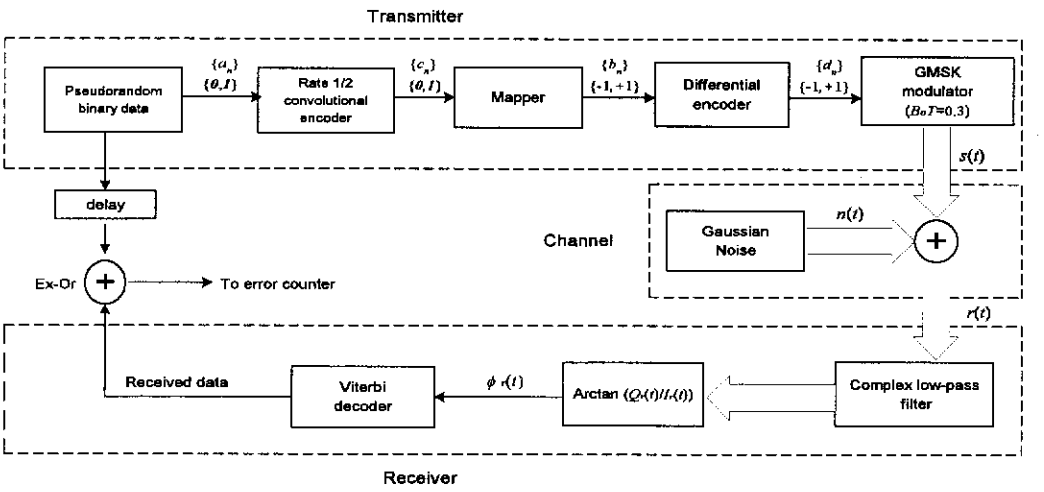

Figure 6.1 Simulation system model.

In this model, the statistically independent random input binary data, $\{a_n\}$, is first derived from a pseudorandom sequence generator. The generated random data $\{a_n\}$, is then encoded using rate-½ convolutional encoders. Here, the encoding is carried out using the codes [3,1], [7,3], and [13,7] and [15,7], having constraint lengths 2, 3, and 4, respectively as selected in Section 4.8. The resulting encoded binary data $\{c_n\}$, is then mapped to another sequence $\{b_n\}$, such that $0 \rightarrow$ -1 and $1 \rightarrow$ +1. The data sequence $\{b_n\}$ is then differentially encoded before applying to the GMSK modulator. As discussed in Section 4.3, differential encoding is applied in order to reduce the number of states required for Viterbi decoding. The output, d_n of the differential encoder is obtained from the modulo-2 addition of b_n and b_{n-1}. i.e., $d_n = b_n \oplus b_{n-1}$ with $\oplus$ denoting modulo-2 addition (or EX-OR logical operation). After modulation, the equivalent complex baseband GMSK signal is given by

$$s(t) = A_1 \cos \phi(t) + jA_1 \sin \phi(t), \tag{6.1}$$

where A_1 is a constant and $\phi(t)$, the information bearing phase of the GMSK signal is given by

$$\phi(t) = \pi h \int_{-\infty}^{t} \sum_{i=-\infty}^{i=\infty} d_i \, g(\tau - iT) \, d\tau. \tag{6.2}$$

Here, $g(t)$ is the Gaussian pulse shape assuming B_0T=0.3. The resulting complex baseband GMSK signal is then transmitted over an AWGN channel. The complex AWGN is simulated according to the Box-Muller's transformation (Dahlquis *et al*, 1974).

The received signal $r(t)$ consisting of the transmitted signal $s(t)$ added to the AWGN $n(t)$, is first filtered using an equivalent complex low-pass filter with Gaussian impulse response. The inphase and quadrature components of the filtered signal are subsequently sampled once every bit period, at the instants where the eye opening is maximum. The phase value $\phi_r(t)$, of the received signal is then calculated according to

$$\phi_r(nT+t_0) = \tan^{-1}\left(\frac{Q_r(nT+t_0)}{I_r(nT+t_0)}\right), \tag{6.3}$$

where, t_0 is the sampling time offset corresponding to the maximum eye opening. $I_r(nT+t_0)$ and $Q_r(nT+t_0)$ are the inphase and quadrature components of the received signal at these sampling instants. They can be expressed as

$$I_r(nT+t_0) = I(nT+t_0) + n_I(nT+t_0) \tag{6.4}$$

and

$$Q_r(nT+t_0) = Q(nT+t_0) + n_Q(nT+t_0), \tag{6.5}$$

where, $I(nT+t_0)$ and $n_I(nT+t_0)$ are the inphase components of the transmitted signal and the AWGN component at the sampling instants, respectively. Similarly, $Q(nT+t_0)$ and $n_Q(nT+t_0)$ are the corresponding quadrature components.

The computer simulations in this study are carried out using 8 samples per bit period of the signal. With this choice, the sampling rate becomes significantly larger than the signal bandwidth causing no appreciable aliasing. Moreover, the number of samples per bit period in this case is large enough to give a good approximation of the continuous signal that is simulated.

Therefore in the simulation, t_0 has been replaced by $k_0T/8$ where, k_0 is the number of samples giving an offset corresponding to the maximum eye opening of the simulated signal. Then Eq. (6.3) becomes

$$\phi_r(nT+k_0T/8) = \tan^{-1}\left(\frac{Q_r(nT+k_0T/8)}{I_r(nT+k_0T/8)}\right). \tag{6.6}$$

These phase values of the received signal are used in the trellis decoder, employing the Viterbi algorithm, for determining the most likely transmitted sequence as discussed in Section 2.6.1. The trellis diagrams used for Viterbi decoding corresponding to the selected codes with constraint length 2, 3 and 4, combined with differentially encoded GMSK are given in Section 4.8. Finally, by comparing the transmitted and the received data, the BERs are then obtained.

6.3 Simulated BERs under Ideal Timing and Carrier Phase

As the detection of the received signal is affected by the signal-to-noise-ratio (SNR) at the output of the receive filter, the influence of the filter bandwidth on the BER performance of the system has first been studied assuming exact recovery of the reference carrier and the timing clock. That is, the exact frequency and phase of the carrier at the receiver are assumed to be known. Also, the sampling time instant is assumed to be exactly at the place where the eye opening is maximum. Under these conditions, the filter bandwidth, which provides the best BER performance is selected. This filter bandwidth is then adopted for the rest of the simulations.

The effect of filter bandwidth on the BER performance has been obtained for input SNR values of 3, 4 and 5 dB. Comparison of the results showed that the optimum bandwidth does not depend on the value of input SNR, providing it is kept constant. Therefore only the BER curves obtained assuming the input SNR equivalent to 4 dB are shown in Fig. 6.2. From the BER curves shown in Fig. 6.2, the best bandwidth, normalised to bit period, of the equivalent low pass filter is found to be 0.3. Moreover, it may also be observed that, the BER performances are not very sensitive to the bandwidth of the receive filter over the range of $\pm$ 33% of the best bandwidth selected. Consequently, for the simulations carried out in this study, the normalised bandwidth of the equivalent low pass filter is set at 0.3. Also, it may be observed from Fig. 6.2, that the coded schemes using the selected codes [13,7] and [15,7] with constraint length 4 show very similar BER performances. Therefore, only one of these two codes, represented by [15,7], will be considered in this study.

As shown in Fig. 6.3, the simulated BER results of the uncoded and the coded GMSK signals have been obtained by setting the normalised bandwidth of the equivalent low-pass filter to the selected value of 0.3. The simulations have been carried out assuming ideal carrier recovery and timing synchronisation. In the simulations, the data rate of the coded schemes using rate-½ codes is reduced by ½ compared to the uncoded scheme in

order to maintain the same transmission bandwidth. In this case, the E_b/N_0 of the coded scheme corresponding to a given SNR becomes twice as much as the uncoded scheme. Note that in Fig. 6.3, the E_b/N_0 of the uncoded scheme is taken as the reference. The E_b/N_0 of the coded schemes are adjusted by 3 dB (equivalent to half power) with respect to the uncoded scheme to account for the reduced data rate. Therefore it may be observed from Fig. 6.3, that at a BER of 10^{-3}, using codes of constraint lengths 2, 3 and 4, coding gains of approximately 1.7 dB, 2.2 dB and 3.1 dB can be achieved compared with the uncoded scheme. Moreover, it has been shown in Section 4.7, that the complexity of the receiver, based on the number of states required for Viterbi decoding, is half that of the uncoded scheme compared to the coded scheme using constraint length 2. It has also been shown in Section 4.7 that the receiver complexity of the coded scheme with constraint length 3 is the same as that of the uncoded scheme. Therefore, it may be concluded from the above results that in the presence of AWGN, assuming exact carrier recovery and timing synchronisation, a coding gain of up to 2.2 dB can be achieved with coded schemes without increasing the receiver complexity. It may also be noted that a larger coding gain can be achieved using a code with a larger constraint length but at the expense of an increase in the receiver complexity.

The theoretical lower bounds obtained in Sections 5.3.3 and 5.3.6 are also included in Fig. 6.3. A comparison of the simulated BERs with the analytical results for the coded schemes having constraint lengths 2 and 3, shows that the simulated BERs fall within 1 dB of the theoretical lower bounds.

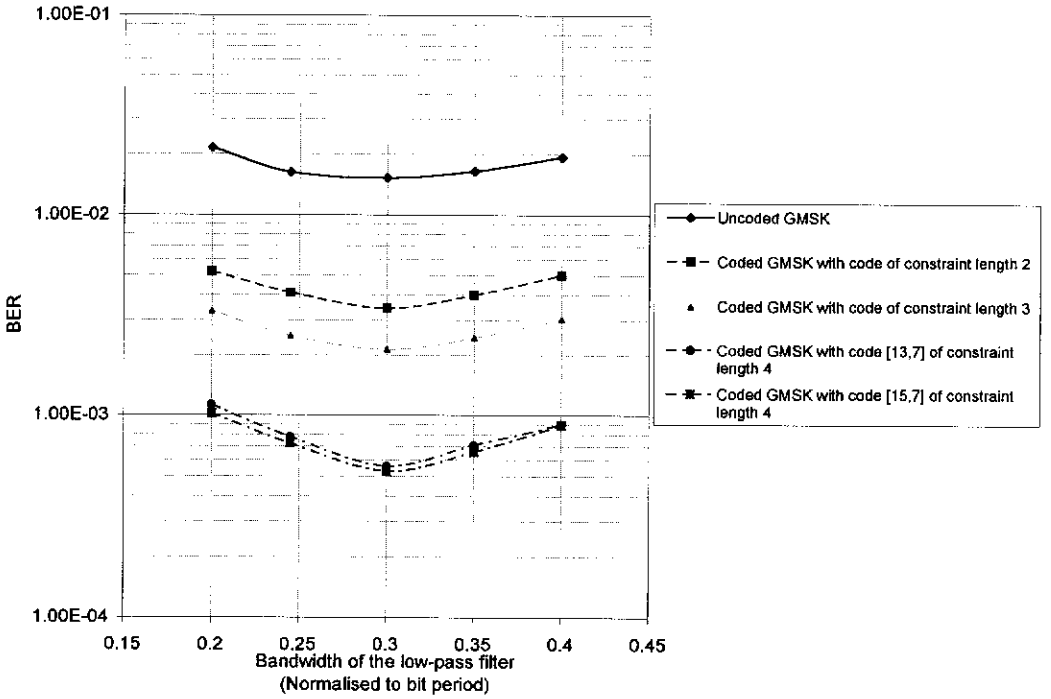

Figure 6.2 Influence of the bandwidth of the receive filter on the BERs of uncoded and trellis coded GMSK signals.

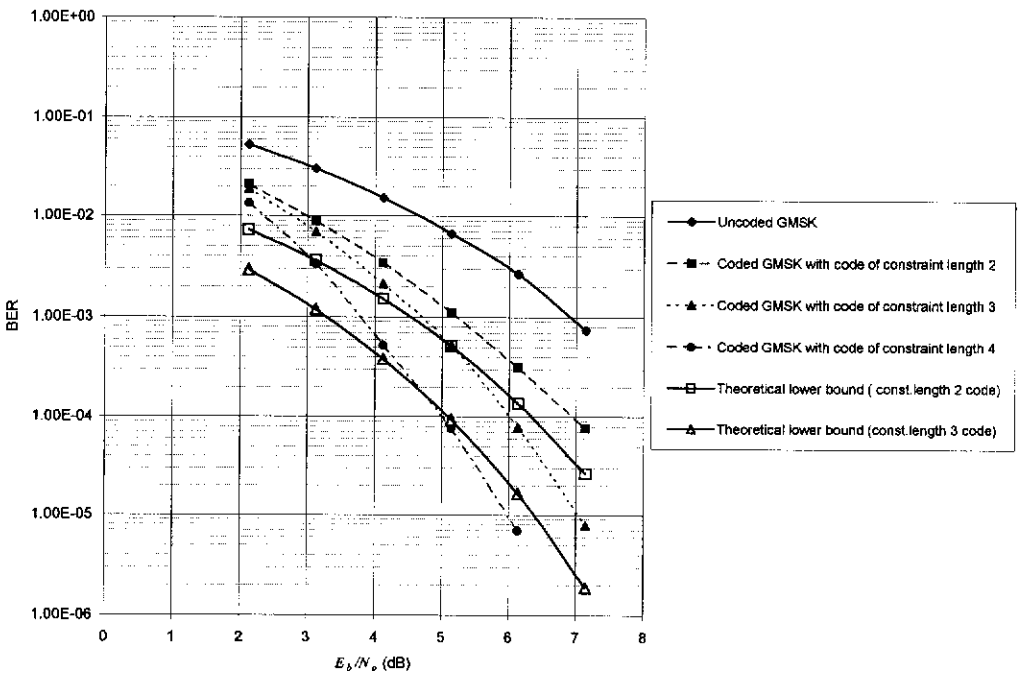

Figure 6.3 BERs of the uncoded and trellis coded GMSK signals.

6.4 The Effect of Timing Clock and Carrier Phase Errors

In practical applications, a clock signal at the receiver in synchronism with the clock signal at the transmitter is used to sample the received signal at precise instants (Proakis, 1989). In such situations, small random deviations of the sampling instant Δt, known as timing error, may occur for such reasons as noise, interference, and clock errors. This results in an increase in the BER.

Furthermore, with coherent detection, the precise recovery of the carrier frequency and phase at the receiver is essential. However, frequency and phase errors may arise in practical systems due to the carrier recovery loop not being able to follow the phase changes of the received signal caused by noise and multipath propagation.

In this section, the sensitivity of the proposed coherent detection scheme to such timing and carrier phase errors is investigated. In the presence of timing and carrier phase errors, the probability of error of the received signal P_{Error} can be approximated as

$$P_{Error} \approx \int_{-T/2}^{T/2} \int_{-\pi/2}^{\pi/2} P_e(\Delta\phi, \Delta t) p(\Delta\phi) p(\Delta t) d(\Delta\phi) d(\Delta t) \tag{6.7}$$

assuming $\Delta\phi$ and Δt are independent. Here, $\Delta\phi$ and Δt are the carrier phase error and the timing error, respectively. Then, the error probability corresponding to the joint effect of phase and timing errors is represented by $P_e(\Delta\phi, \Delta t)$. The probability distributions corresponding to the effects of carrier phase error and timing error are represented by $p(\Delta\phi)$ and $p(\Delta t)$, respectively. The probability of error given in Eq. (6.7) may be theoretically evaluated if the distributions of carrier phase error and timing error are known. However, these distributions which depend on the noise and distortions in the system, as well as the loop dynamics of the timing and carrier recovery loops, are generally not available. Therefore, the effect of

such errors on the BER performances of the uncoded and coded schemes is best estimated using computer simulations.

In the computer simulations carried out in this study, the individual effects of timing and carrier phase errors on the BER performances are first obtained. In this case, the effect of timing errors on the BER performances has been studied assuming no carrier phase error is present. After that, the effect of carrier phase errors is studied assuming that no timing error is present.

In the presence of timing error alone, i.e., with $\Delta\phi = 0$, Eq. (6.7) reduces to

$$P_{Error} \approx \int_{-T/2}^{T/2} P_e(0, \Delta t)p(\Delta t)d(\Delta t). \tag{6.8a}$$

Similarly, in the presence of phase error alone with $\Delta t = 0$, the probability of error of the received signal can be expressed as

$$P_{Error} \approx \int_{-\pi/2}^{\pi/2} P_e(\Delta\phi, 0)\, p(\Delta\phi)d(\Delta\phi). \tag{6.8b}$$

Although the timing and phase errors are more realistically random variations, deterministic values are first used in the simulations to examine the effect of these errors on the BER performances. In this case, the effect of a fixed sampling time error is studied by introducing a fixed sampling time offset Δt to the nominal sampling instant corresponding to the maximum eye opening. Accordingly, the phase values of the received signal at the sampling instants are obtained as

$$\phi_r(nT+k_0T/8) = \tan^{-1}\left(\frac{Q_r(nT + k_0T/8 + \Delta t)}{I_r(nT + k_0T/8 + \Delta t)}\right). \tag{6.9}$$

As the number of samples per transmitted bit period used in the simulations is 8, the minimum variation of the timing error Δt becomes $\pm 12.5\%$ of the transmitted bit period T.

For a more realistic effect of timing error on the BER performance, random variations of Δt have been considered. These variations are obtained in the simulations by filtering a set of Gaussian distributed random numbers. As the timing error in practice tends to be correlated, this correlation between the Gaussian distributed random errors is achieved through the use of averaging filters. In addition, the variations of the timing error depend on the bandwidth of the timing recovery circuit. The effect of the bandwidth of the averaging filters used on the BER performance is also studied.

Next, the effect of fixed carrier phase errors on the BER performance has been studied, by adding a fixed phase error $\Delta\phi$ to the phase value of the received signal sampled at the instants of maximum eye opening. Accordingly, the phase values of the received signal at the sampling instants are obtained, such that

$$\phi_r(nT+k_0T/8) = \tan^{-1}\left(\frac{Q_r(nT+k_0T/8)}{I_r(nT+k_0T/8)}\right) \pm \Delta\phi\,. \qquad (6.10)$$

Gaussian distributed random phase errors have also been used to model variations in carrier phase offsets.

Finally, the joint effect of symbol timing errors and carrier phase errors has been studied using fixed error values. In these simulations, the phase values of the received signal at the sampling instants are obtained according to

$$\phi_r(nT+k_0T/8) = \tan^{-1}\left(\frac{Q_r(nT+k_0T/8+\Delta t)}{I_r(nT+k_0T/8+\Delta t)}\right) \pm \Delta\phi\,. \qquad (6.11)$$

6.4.1 Simulation results in the presence of timing errors

In this section, the simulated BER results in the presence of timing errors alone for the uncoded and the trellis coded GMSK signals are presented. As the number of samples per transmitted bit period used in the simulations is 8,

the fixed timing error Δt can only be varied in steps of ±12.5% of the transmitted bit period T. i.e., in steps of $\pm T/8$. Therefore, the simulations have been carried out for timing errors of ±12.5%, ±25% and ±37.5% of the transmitted bit period T. First, the required E_b/N_0 in dB to achieve a BER of 10^{-3} has been obtained when the timing error is ±12.5% of T i.e., $=\pm T/8$. This is shown in Table 6.1. With this timing error, the uncoded scheme has shown a performance degradation of 0.26dB and the coded schemes with constraint lengths 2, 3, and 4 have shown degradations of 0.15 dB, 0.1 dB and 0.15 dB, respectively. The BER performances for an increased timing error of ±25% of T are shown in Fig. 6.4. The BER curves shown in Fig. 6.5 have been obtained by introducing a fixed timing offset of ±37.5% of the transmitted bit period T.

The effect of random timing error on the BER performance has been studied by introducing a random error of Δt generated as discussed in Section 6.4. In practice, random timing variations with an approximate rms value of ±25% of T present very severe timing errors. In this case, depending on the bandwidth of the timing recovery circuit, the maximum timing errors may extend up to ±75% of T. Therefore, the worst-case effect of random timing error on the BER performance is studied using random variations with an rms value approximately ±25% of T. In the simulations, the effect of the bandwidth of the averaging filter, which in practice represents the timing recovery circuit, has also been studied. This bandwidth is set at 0.1% or 0.5% of the input bit rate. In this study, the random timing errors are simulated by passing the Gaussian distributed random numbers through a low-pass averaging filter with a bandwidth of 0.1% or 0.5% of the input bit rate. In the simulations, the above bandwidths of the averaging filters are set by selecting the number of samples required in the running average. The required rms value of the timing error is obtained by setting the variance for the random number generator. For the above two bandwidths, it is observed that the timing variations of the random errors generated are extended over ±75% of T. However, it has also been observed that, when the bandwidth of the filter is smaller, the random timing variations are slowly varying and the

correlation between the adjacent variations is high. The converse is also true for the higher bandwidth, in that the variations are fast and the correlation is smaller. The simulated BER results in the presence of random timing error with a rms value of approximately ±25% of T, and the filter bandwidth set to 0.1% and 0.5% of the input bit rate are shown in Fig. 6.6 and Fig. 6.7, respectively.

Signal GMSK	E_b/N_0 in dB required to achieve a BER of 10^{-3}								
	Ideal carrier recovery					Ideal timing recovery			Timing error of ±T/4 and carrier phase error of ±18°
	Ideal timing	Timing error of ±T/8	Timing error of ±T/4	Random error of ±T/4 rms. Bandwidth = 0.1%f_b	Random error of ±T/4 rms. bandwidth =0.5%f_b	Carrier phase error of ±10°	Carrier phase error of ±15°	Carrier phase error of ±18°	
Uncoded	6.90	7.16	7.80	8.50	10.20	8.50	10.16	12.00	13.41
Constraint length 2 code	5.20	5.35	5.50	5.73	6.24	5.38	5.64	5.80	6.42
Constraint length 3 code	4.70	4.80	5.00	5.36	5.68	4.80	5.34	5.50	6.60
Constraint length 4 code	3.80	3.95	4.10	4.60	4.81	3.90	4.20	4.75	4.95

Note : T is the transmitted bit period and f_b is the input bit rate

Table 6.1 The required E_b/N_0 in dB to achieve a BER of 10^{-3}

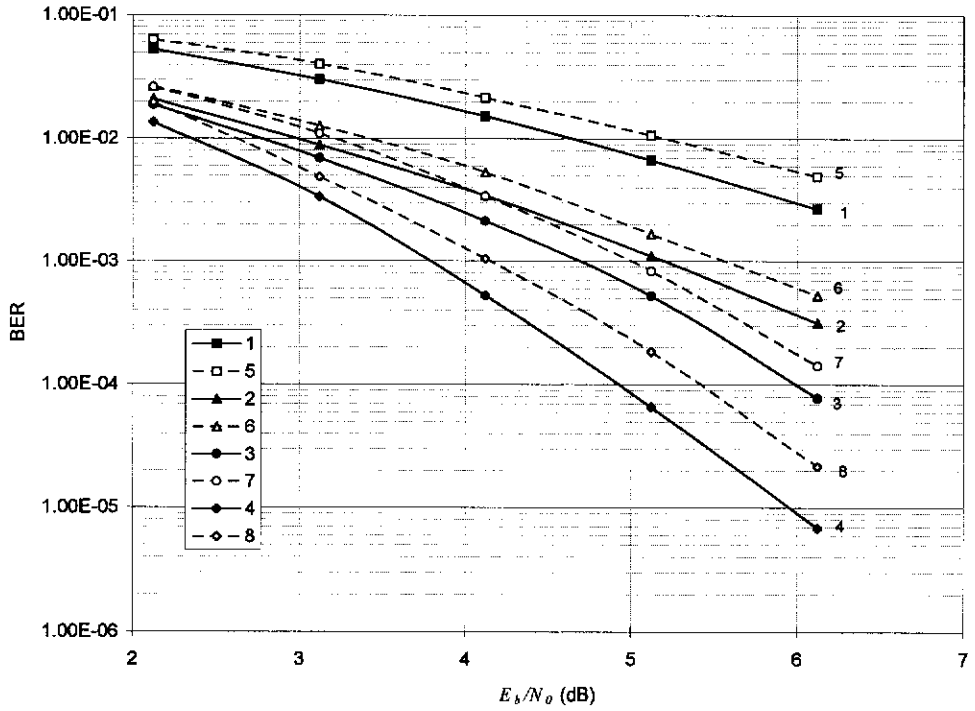

Note : BER curves with ideal carrier recovery and ideal timing recovery of

1 - uncoded GMSK
2 - coded GMSK with code of constraint length 2
3 - coded GMSK with code of constraint length 3
4 - coded GMSK with code of constraint length 4

BER curves with ideal carrier recovery and fixed timing error of ±25% of T of

5 - uncoded GMSK
6 - coded GMSK with code of constraint length 2
7 - coded GMSK with code of constraint length 3
8 - coded GMSK with code of constraint length 4

Figure 6.4 BER curves of uncoded and coded GMSK schemes, (1-4) with ideal carrier and timing recoveries, and (5-8) with ideal carrier recovery and fixed sampling time error of ±25% of T.

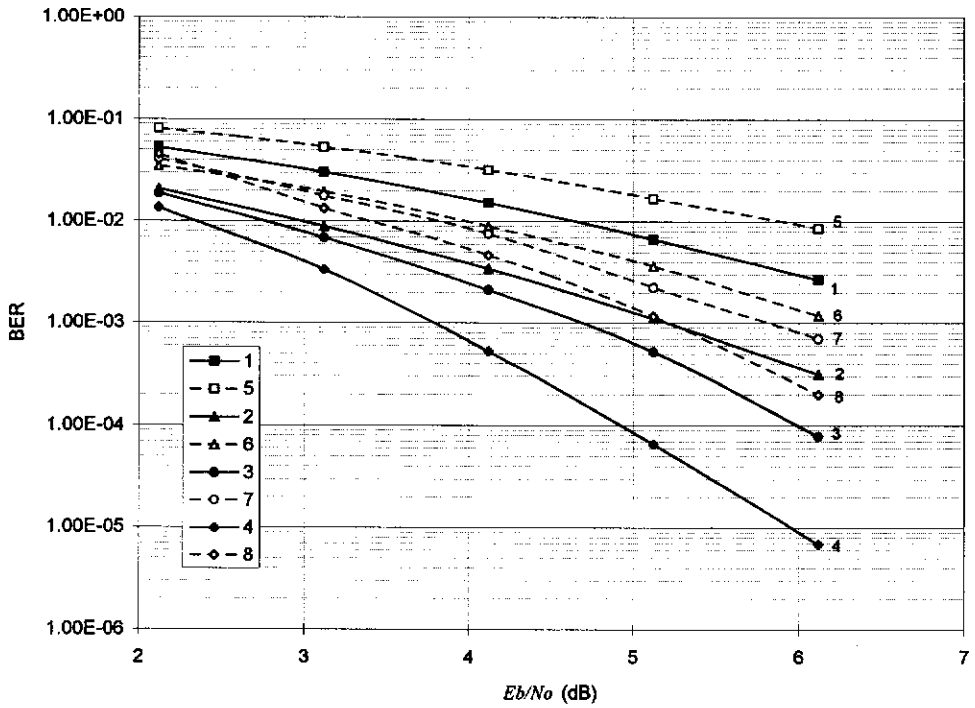

Note : BER curves with ideal carrier recovery and ideal timing recovery of
1 - uncoded GMSK
2 - coded GMSK with code of constraint length 2
3 - coded GMSK with code of constraint length 3
4 - coded GMSK with code of constraint length 4
BER curves with ideal carrier recovery and fixed timing error of ±37.5% of T of
5 - uncoded GMSK
6 - coded GMSK with code of constraint length 2
7 - coded GMSK with code of constraint length 3
8 - coded GMSK with code of constraint length 4

Figure 6.5 BER curves of uncoded and coded GMSK schemes, (1-4) with ideal carrier and timing recoveries, and (5-8) with ideal carrier recovery and fixed sampling time error of ±37.5% of T.

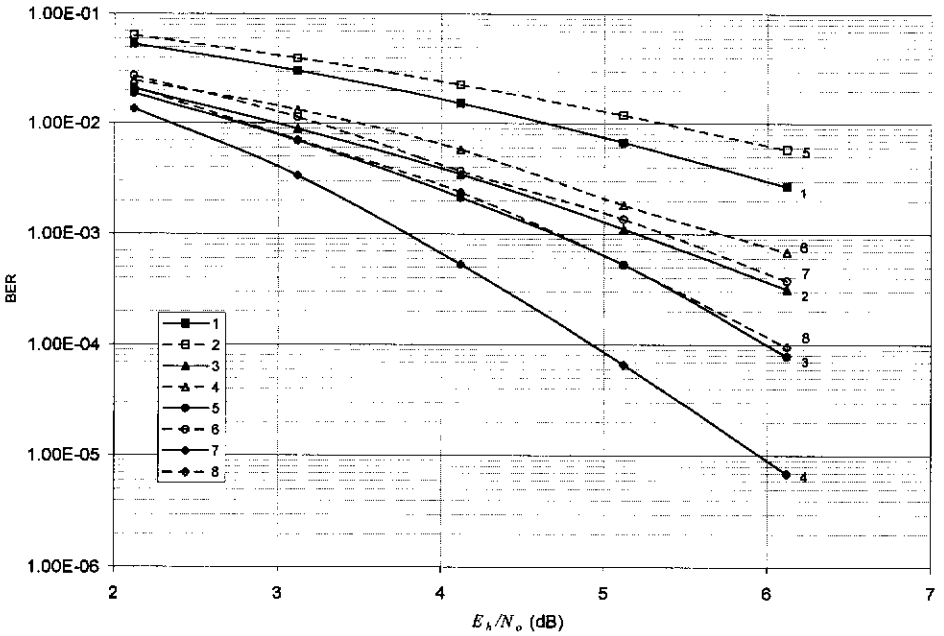

Note : BER curves with ideal carrier recovery and ideal timing recovery of

1 - uncoded GMSK

2 - coded GMSK with code of constraint length 2

3 - coded GMSK with code of constraint length 3

4 - coded GMSK with code of constraint length 4

BER curves with ideal carrier recovery and random timing error of ±25% of T rms (bandwidth is 0.1% of the input bit rate) of

5 - uncoded GMSK

6 - coded GMSK with code of constraint length 2

7 - coded GMSK with code of constraint length 3

8 - coded GMSK with code of constraint length 4

Figure 6.6 BER curves of uncoded and coded GMSK schemes, (1-4) with ideal carrier and timing recoveries, and (5-8) with ideal carrier recovery and random timing error of ±25% of T rms (bandwidth is 0.1% of the input bit rate).

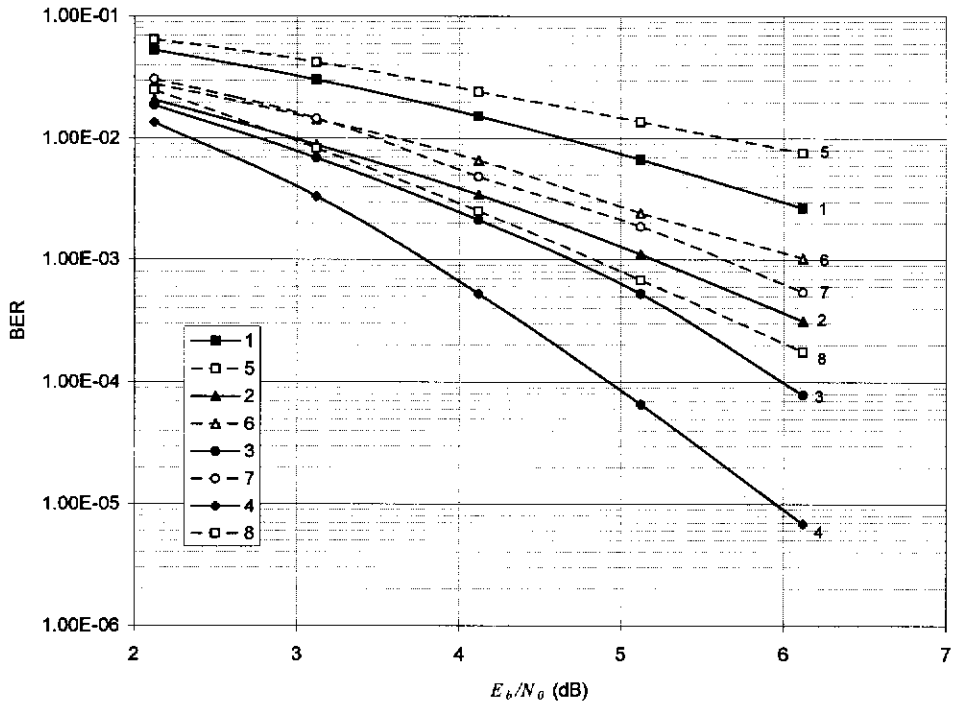

Note : BER curves with ideal carrier recovery and ideal timing recovery of
1 - uncoded GMSK
2 - coded GMSK with code of constraint length 2
3 - coded GMSK with code of constraint length 3
4 - coded GMSK with code of constraint length 4
BER curves with ideal carrier recovery and random timing error of ±25% of T rms (bandwidth is 0.5% of the input bit rate) of
5 - uncoded GMSK
6 - coded GMSK with code of constraint length 2
7 - coded GMSK with code of constraint length 3
8 - coded GMSK with code of constraint length 4

Figure 6.7 BER curves of uncoded and coded GMSK schemes, (1-4) with ideal carrier and timing recoveries, and (5-8) with ideal carrier recovery and random timing error of ±25% of T rms (bandwidth is 0.5% of the input bit rate).

6.4.2 Simulation results in the presence of carrier phase errors

In this section, the effect of carrier phase errors alone on the BER performance of the proposed schemes has been studied assuming no symbol timing errors. In the simulations, the phase errors $\Delta\phi$ are introduced as given in Eq. (6.12). First, the effect of fixed phase errors on the BER performance has been obtained. The study started with the introduction of a fixed offset of ±10°. The required values of E_b/N_0 in dB to achieve a BER of

10^{-3}, for the various schemes have been obtained in the presence of this fixed phase error, as tabulated in Table 6.1. It may be observed from Table 6.1 that the performance degradation of the uncoded scheme in the presence of the fixed phase error of $\pm 10°$ is about 1.6 dB, whereas the maximum degradation associated with a trellis coded scheme is only 0.18 dB. BER performances of the coded schemes, for larger phase errors of $\pm 15°$ and $\pm 18°$, are shown in Fig. 6.8 and 6.9, respectively.

The effect of random phase errors on the BER performances is also studied. The random phase offset $\Delta\phi$ is generated as discussed in Section 6.4. In practice, the bandwidth of the carrier recovery circuits is set to about 1% of the input bit rate. Therefore, the random phase errors in this study are simulated by passing a set of Gaussian distributed random numbers through a low-pass averaging filter with a bandwidth equivalent to 1% of the input bit rate, as discussed in Section 6.4.1. To observe severe effect of random phase errors on the BER performances, the approximate rms value of the phase errors generated is set at $\pm 18^{\circ}$. It has been observed that the variations of these phase errors generated in the simulation are extended over $\pm 60^{\circ}$. Fig. 6.10 presents the simulated BER curves of the uncoded and coded schemes in the presence of random phase errors.

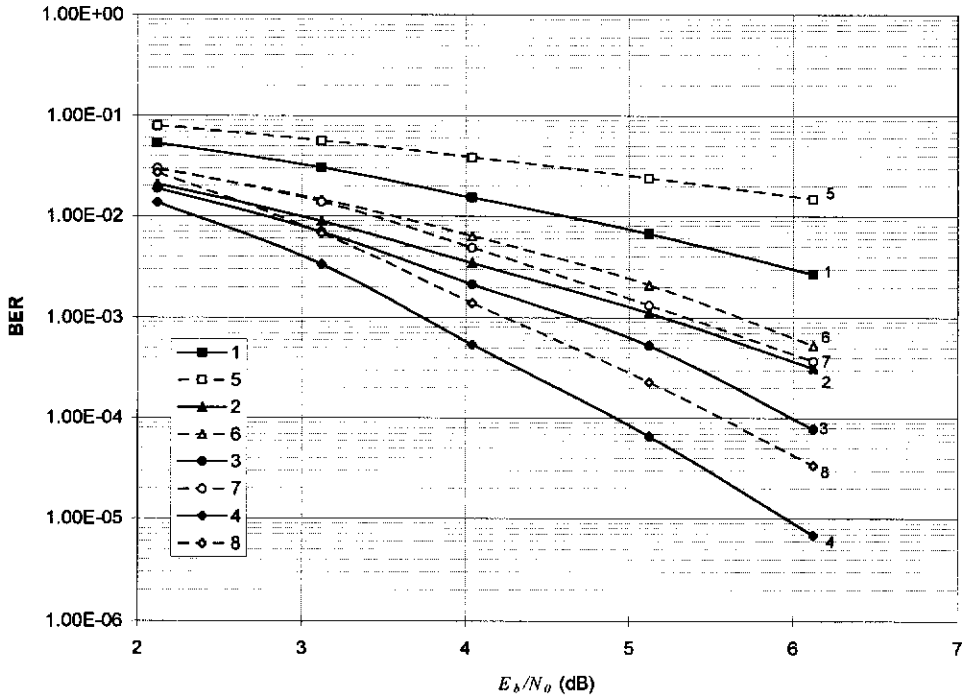

Note : BER curves with ideal carrier recovery and ideal timing recovery of
1 - uncoded GMSK
2 - coded GMSK with code of constraint length 2
3 - coded GMSK with code of constraint length 3
4 - coded GMSK with code of constraint length 4
BER curves with ideal timing recovery and fixed carrier phase error of $\pm 15^{\circ}$ of.
5 - uncoded GMSK
6 - coded GMSK with code of constraint length 2
7 - coded GMSK with code of constraint length 3
8 - coded GMSK with code of constraint length 4

Figure 6.8 BER curves of uncoded and coded GMSK schemes, (1-4) with ideal timing and carrier recoveries, and (5-8) with ideal timing recovery and fixed carrier phase error of $\pm 15^{\circ}$.

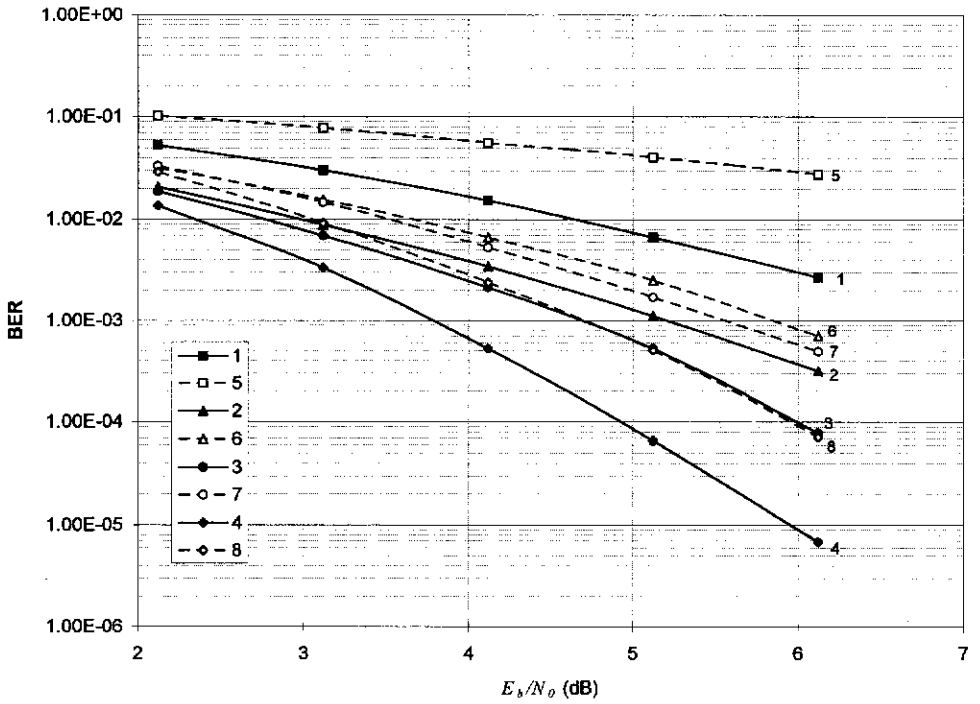

Note : BER curves with ideal carrier recovery and ideal timing recovery of
1 - uncoded GMSK
2 - coded GMSK with code of constraint length 2
3 - coded GMSK with code of constraint length 3
4 - coded GMSK with code of constraint length 4
BER curves with ideal timing recovery and fixed carrier phase error of $\pm 18^{\circ}$ of.
5 - uncoded GMSK
6 - coded GMSK with code of constraint length 2
7 - coded GMSK with code of constraint length 3
8 - coded GMSK with code of constraint length 4

Figure 6.9 BER curves of uncoded and coded GMSK schemes, (1-4) with ideal timing and carrier recoveries, and (5-8) with ideal timing recovery and fixed carrier phase error of $\pm 18^{\circ}$.

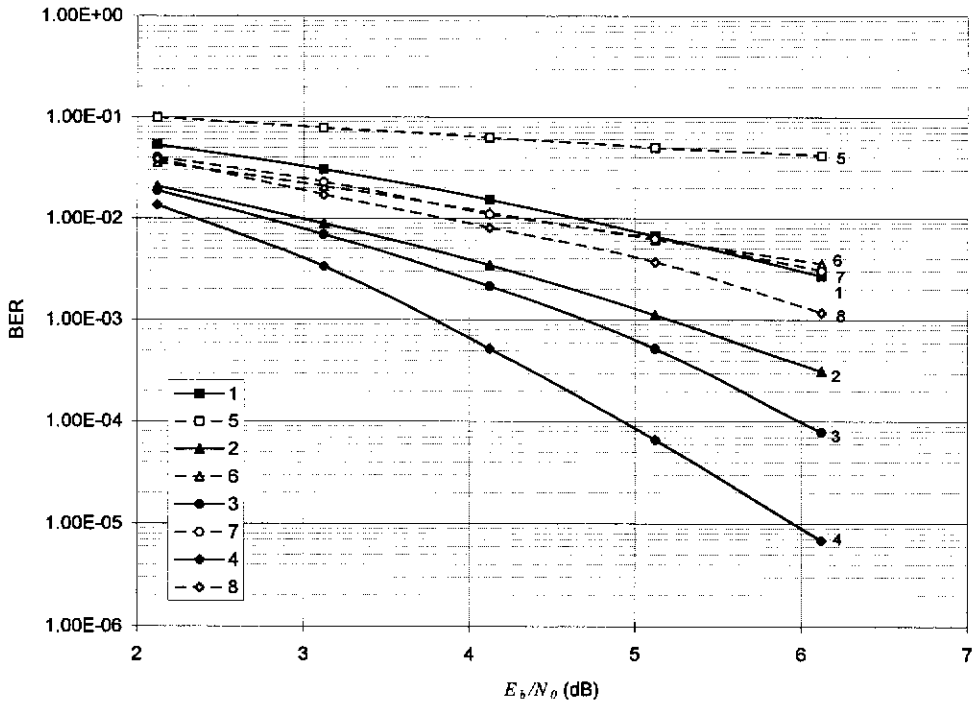

Note : BER curves with ideal carrier recovery and ideal timing recovery of
1 - uncoded GMSK
2 - coded GMSK with code of constraint length 2
3 - coded GMSK with code of constraint length 3
4 - coded GMSK with code of constraint length 4
BER curves with ideal timing recovery and random carrier phase error of $\pm 18^{\circ}$rms (bandwidth is 1% of the input bit rate) of
5 - coded GMSK
6 - coded GMSK with code of constraint length 2
7 - coded GMSK with code of constraint length 3
8 - coded GMSK with code of constraint length 4

Figure 6.10 BER curves of uncoded and coded GMSK schemes, (1-4) with ideal timing and carrier recoveries, and (5-8) with ideal timing recovery and random carrier phase error of $\pm 18^{\circ}$rms (bandwidth is 1% of the input bit rate).

6.4.3 Simulated BER performance in the presence of both timing and carrier phase errors

The joint effect of timing and carrier phase errors on the BER performance has been studied in this section by introducing a fixed sampling error and a fixed phase error. In the simulations, the phase values of the received signal at the sampling instants are obtained using Eq. (6.13). Here, the timing errors and the phase errors are set at ±25% of T and ±18°, as has been used in the previous investigations in this study. The BER curves under these conditions are presented in Fig. 6.11.

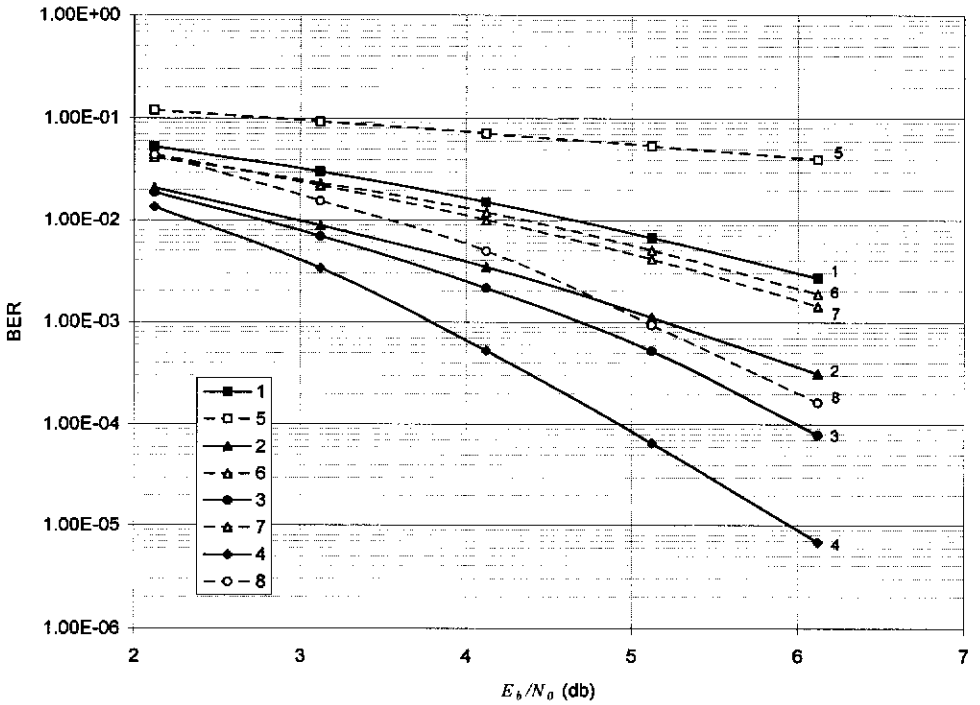

Note : BER curves with ideal carrier recovery and ideal timing recovery of
1 - uncoded GMSK
2 - coded GMSK with code of constraint length 2
3 - coded GMSK with code of constraint length 3
4 - coded GMSK with code of constraint length 4
BER curves with fixed timing error of ±25% of T and fixed carrier phase error of ±18° of
5 - uncoded GMSK
6 - coded GMSK with code of constraint length 2
7 - coded GMSK with code of constraint length 3
8 - coded GMSK with code of constraint length 4

Figure 6.11 BER curves of uncoded and coded GMSK schemes, (1-4) with ideal timing and carrier recoveries, and (5-8) with fixed timing error of ±25% of T and fixed carrier phase error of ±18°.

6.5 Summary

The values of E_b/N_0 in dB, required to achieve a bit error rate of 10^{-3} for uncoded and trellis coded GMSK, in the presence of various carrier and timing impairments, are tabulated in Table 6.1. Using the uncoded GMSK scheme with ideal carrier and timing recovery as the reference, the performance gains at a BER of 10^{-3} for coded and uncoded schemes, in the presence of these timing and carrier phase errors, are tabulated in Table 6.2.

Signal GMSK	Performance gain/loss in dB at a BER of 10^{-3}								
	Ideal carrier recovery					Ideal timing recovery			Timing error of $\pm T/4$ and carrier phase error of $\pm 18°$
	Ideal timing	Timing error of $\pm T/8$	Timing error of $\pm T/4$	Random error of $\pm T/4$ rms. bandwidth = $0.1\%f_b$	Random error of $\pm T/4$ rms. bandwidth = $0.5\%f_b$	Carrier phase error of $\pm 10°$	Carrier phase error of $\pm 15°$	Carrier phase error of $\pm 18°$	
Uncoded	0.00*	-0.26	-0.90	-1.60	-3.30	-1.60	-3.26	-5.10	-6.51
Constraint length 2 code	+1.70	+1.55	+1.40	+1.17	+0.66	+1.52	+1.26	+1.10	+0.48
Constraint length 3 code	+2.20	+2.10	+1.90	+1.54	+1.22	+2.10	+1.56	+1.40	+0.30
Constraint length 4 code	+3.10	+2.95	+2.80	+2.30	+2.09	+3.00	+2.70	+2.15	+1.95

Note : * uncoded GMSK with ideal carrier recovery and timing recovery used as the reference

Table 6.2 The performance gain/loss in dB at a BER of 10^{-3}

From Table 6.2, it is observed that in the presence of sampling timing error of ±25% of T i.e., $\pm T/4$ alone, the BER performance of uncoded GMSK is degraded by 0.90dB, whereas trellis coded GMSK signals with codes of

constraint lengths 2, 3, and 4, achieved respective coding gains of 1.4 dB, 1.90 dB, and 2.80 dB. When the sampling time instants suffer from random timing error with an rms offset of ±25% of T, the BER performance degradation of both uncoded and trellis coded schemes considered is increased, compared to that having a fixed error. However, the results with both fixed and random timing errors show that the uncoded GMSK signal is much more sensitive to sampling timing errors than the coded GMSK signals considered, when no carrier phase error is present.

Even when the fixed carrier phase offset considered is as high as $\pm 18^{\circ}$, the coded schemes with codes of constraint lengths 2, 3, and 4, have shown respective coding gains of 1.10 dB, 1.40 dB, and 2.15 dB while the uncoded scheme has shown a degradation of more than 5 dB. Furthermore, it may be observed in Fig. 6.10 that the effect of random carrier phase error is more severe than the fixed phase error on the performance of both the coded and uncoded schemes considered. This may be due to the extension of the phase errors over a larger range of up to $\pm 60^{\circ}$, when the random errors having a rms of $\pm 18^{\circ}$ is introduced. From these results, it may be concluded that the coded signals are more tolerant to carrier phase errors than the uncoded signal.

In addition, the results in Tables 6.1 and 6.2 show that the coded schemes may be more tolerant to the joint effect of phase errors and timing errors compared to the uncoded scheme. Finally, it may be concluded that the BER performances of the selected trellis coded schemes in the presence of AWGN are better than the uncoded scheme in both ideal situations and in the presence of practical impairments.

CHAPTER 7

PERFORMANCE OF SELECTED TRELLIS CODED GMSK SIGNALS OVER FADING CHANNELS

7.1 Introduction

In this chapter, the BER performances of the selected trellis coded GMSK schemes over flat fading and frequency-selective fading channels are evaluated using computer simulations. The received signal is detected using quadrature demodulation followed by Viterbi decoding. A differential phase detection scheme based on the signal phase difference over one bit period is studied first. An improved receiver using adaptive Viterbi detection, which takes into account the intersymbol interference (ISI) introduced by frequency-selective fading is then introduced.

7.2 Simulation Model

The model used for computer simulations in determining the BERs of the proposed trellis coded schemes is based on three main functional blocks, namely the transmitter, the channel, and the receiver.

7.2.1 Transmitter

The transmitter, consisting of a pseudorandom sequence generator, an encoder, a mapper, a differential encoder and the GMSK modulator, is shown in Fig. 6.1. The equivalent complex baseband GMSK signal is generated using the same method as discussed in Section 6.1.

7.2.2 Fading channel

Two types of fading channels have been considered in the simulations, namely (i) frequency non-selective (flat), and

(ii) frequency-selective fading.

7.2.2.1 Frequency non-selective (flat) fading

As explained in Section 2.2, multipath fading in land mobile radio causes Rayleigh distributed envelope fluctuations and uniformly distributed random phase changes. These effects have been modelled in the simulations using two independent Gaussian low-pass noise sources, $x_c(t)$ and $x_s(t)$, added in quadrature as illustrated in Fig. 7.1 (Jakes, 1974). The independent Gaussian noise sources $x_c(t)$ and $x_s(t)$ have been generated using the Jakes algorithm (Jakes, 1974), such that

$$x_c(t) = 2\sum_{n=1}^{N_0} \cos\beta_n \cos\omega_n t + \sqrt{2}\cos\alpha\cos\omega_m t\,, \tag{7.1a}$$

and

$$x_s(t) = 2\sum_{n=1}^{N_0} \sin\beta_n \cos\omega_n t + \sqrt{2}\sin\alpha\cos\omega_m t\,, \tag{7.1b}$$

where, ω_m is the maximum Doppler frequency, and

$$\omega_n = \omega_m \cos(2\pi n/N),$$

with $N = 2(2N_0+1)$ and $N_0 \geq 8$.

It has been shown in Jakes (1974), when α and β_n are selected such that, $\alpha = \pi/4$ and $\beta_n = \pi n/N_0$, the envelope of the resulting signal output, $s_{flat}(t)$, for an unmodulated carrier signal, $s_i(t)$, follows the Rayleigh distribution, and the phase is uniformly distributed between 0 and 2π.

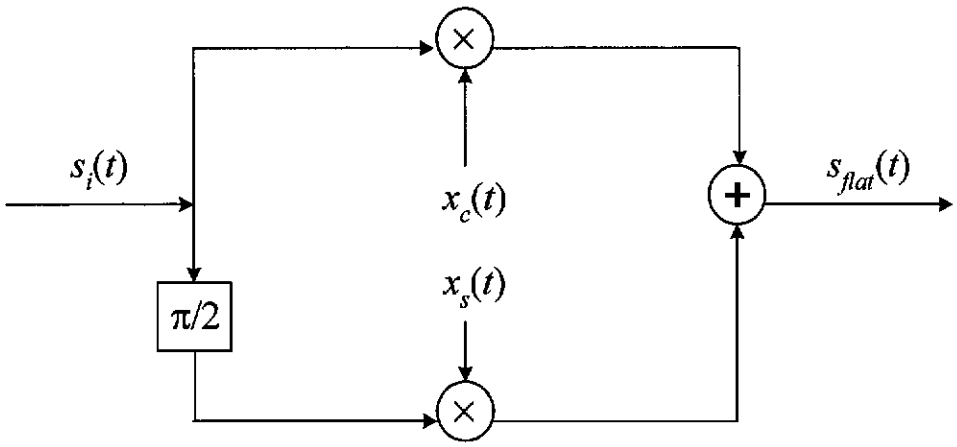

Figure 7.1 Block diagram of a frequency non-selective Rayleigh fading simulator.

7.2.2.2 Frequency-selective fading

The effect of frequency-selective fading has been examined using a two-ray fading model, as shown in Fig. 7.2. This two-ray fading model consists of two independent Rayleigh fading signal paths with a relative delay of τ. Here, $x_{c1}(t)$, $x_{s1}(t)$, $x_{c2}(t)$, and $x_{s2}(t)$ represent independent uncorrelated Gaussian noise sources. Such a model has been extensively used in analytical and simulation studies on the effects of frequency-selective fading (Svensson, 1987; Korn, 1992; Tellambura and Bhargava, 1995). Furthermore, this model is more flexible compared to the empirical models, since the average power and the relative delay between the two paths can be readily controlled. Even though the relative path delay, τ, between the two rays in this model is a random variable, it is common practice to consider it as a constant in computer simulations (Varshney and Kumar, 1991; Korn, 1992). Therefore, in this study, τ will be treated as a constant. Furthermore, in this study, the average signal powers for the main and the delayed paths are considered to be equal. This condition corresponds to the worst case frequency-selective fading scenario for a given delay τ.

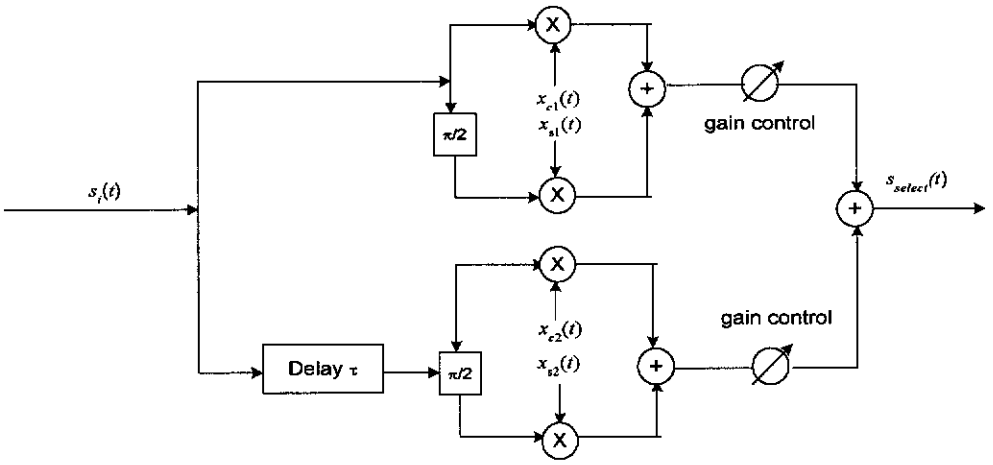

Figure 7.2 Block diagram of a frequency-selective two-ray model.

Besides simulating the frequency-selective fading channel as a two-ray model, other channel models have also been considered. For example, the empirical models adopted in the GSM standard define propagation models in the form of six- and twelve- ray typical impulse responses (ETSI, 1993). These models are specified based on extensive field measurements carried out in typical propagation environments, such as rural area (RA), hilly terrain (HT) and typical urban area (TU). In this study, computer simulations have also been carried out assuming frequency-selective fading represented by the six-ray propagation models as defined by the GSM standard (ETSI, 1993). The typical six-ray GSM channel models used in this study are given in Appendix F.

7.2.3 Receiver

The received signal is first filtered using an equivalent complex low-pass filter with Gaussian impulse response, as discussed in Section 6.2. The filter bandwidth of the equivalent low-pass filter, normalised to the bit period, is set at 0.3, as explained in Section 6.3. The phase values of the received signal have been estimated from the sampled values of the inphase and quadrature components of the filtered signal, as explained in Section 6.2. Exact timing synchronisation has been assumed. However in practical situations, phase errors are present due to the Doppler effect and the local oscillator frequency offset. Usually, the rate of change of the phase error

introduced by the local oscillator is slow compared to the bit rate. If the Doppler rate is also small relative to the bit rate, then the phase error may be assumed to remain constant during one bit period. In this case, the error in the phase difference $\Delta\phi(nT)=\phi(nT)-\phi((n-1)T)$ over one bit period, may be negligible.

In view of this, a distance measure in Viterbi decoding, based on the signal phase difference $\Delta\phi(nT)$, over one bit period may be a more attractive alternative to the one which requires the absolute phase, $\phi(nT)$, as given in Eq. (4.12). Such a differential phase detection method will be explained in the following section.

7.3 Differential Phase Detection over Fading Channels

With the differential phase detection scheme, the signal space distances between the received signal and all the possible transmitted signals required in Viterbi decoding, are obtained using the squared Euclidean distance based on the phase difference over one bit period. In this case, the squared Euclidean distance between any two signals $s_i(t)$ and $s_j(t)$ having one sample per bit period over an interval $nT \leq t < (n+1)T$ as given in Eq. (4.9) can be re-written as

$$\int_{nT}^{(n+1)T} [s_i(t)-s_j(t)]^2 \, dt \approx 2E \{1- \cos [\Delta\Phi_i((n+1)T) - \Delta\Phi_j ((n+1)T)]\} \qquad (7.2)$$

where

$$\Delta\Phi_i((n+1)T) = \phi_i((n+1)T) - \phi_i(nT)$$

and $$\Delta\Phi_j((n+1)T) = \phi_j((n+1)T) - \phi_j(nT).$$

$\phi_i(nT)$ and $\phi_j(nT)$ are the phase values of the signals $s_i(t)$ and $s_j(t)$, respectively, at the sampling instant $t=nT$. The computer simulations of the BER performances for the proposed Viterbi decoder are then carried out based on the distance measure given in Eq. (7.2). The corresponding trellis diagrams of the selected codes combined with differentially encoded GMSK, have been presented in Section 4.8.

7.3.1 Simulation results over flat fading channels

First, computer simulations have been carried out to determine the BER performance, under flat fading conditions, using this differential phase detection scheme. In the simulations, the Doppler frequency is calculated assuming a carrier frequency of 900 MHz and a transmission bit rate of 270.8 kb/s. These values have been chosen for their practical applications such as in the GSM systems (Gibson, 1996). The simulated BER results obtained for different vehicular speeds of the uncoded and the trellis coded GMSK schemes are presented in Fig. 7.3. In the simulations, only the trellis coded scheme with the constraint length 2 code is considered, due to the reduced number of states required for Viterbi decoding (refer to Section 4.8). As differential encoding is often introduced before GMSK modulation in practical systems, such as in the GSM, the differentially encoded GMSK signal is considered here to be the uncoded scheme. For the BER curves shown in Fig. 7.3, the values of E_b/N_0 for the trellis coded scheme take into account the reduced data rate, as discussed in Section 6.3. From these results, it may be observed that at a vehicular speed of 50 km/h i.e., f_DT=1.5x10^{-4}, the trellis coded scheme achieves a coding gain of approximately 6.5 dB at a BER of 10^{-3} compared to the uncoded scheme. It is to be noted that this BER improvement of the trellis coded scheme is achieved with a less complex decoder, based on the differential phase detection and Viterbi decoding.

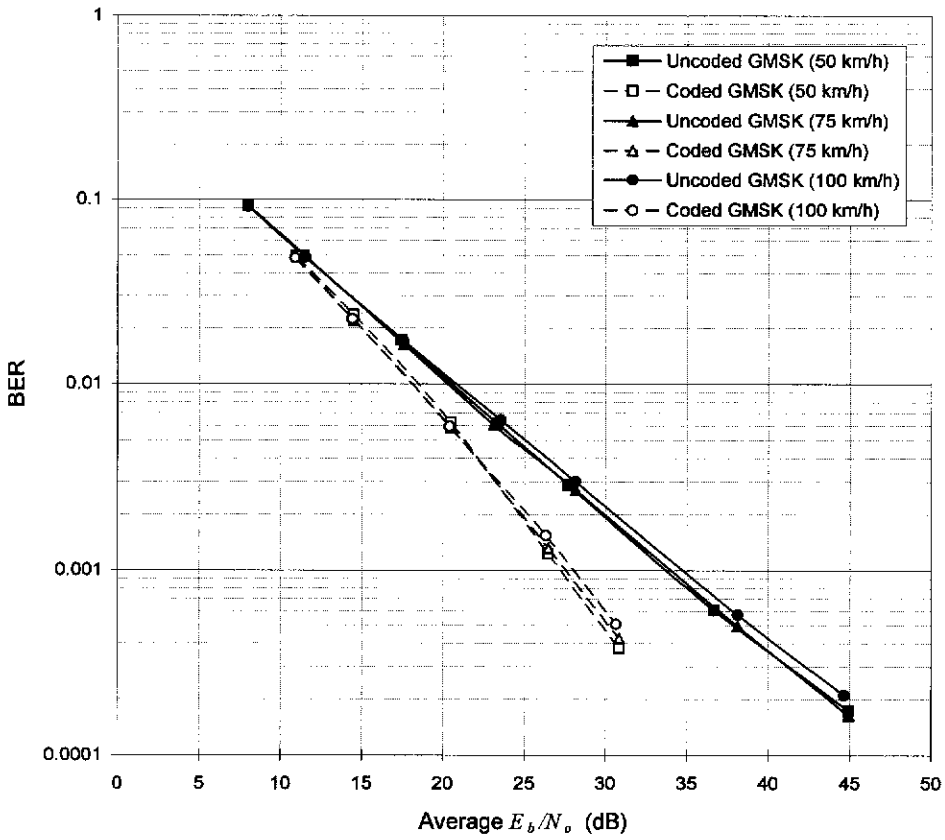

Figure 7.3 The BERs of the uncoded and trellis coded GMSK, using differential phase detection over flat fading channel.

7.3.2 Simulated BER results over two-ray fading channels

In this section, the effect of frequency-selective fading on the differential phase detection scheme is studied using the two-ray fading model, as shown in Fig. 7.2. In frequency-selective fading, the received signal not only experiences fading, but also suffers from waveform distortion due to the intersymbol interference (ISI) introduced by multipath components. The amount of ISI introduced in such situations by the relatively long delay between the multipath signal components, may be so significant as to cause serious degradation of the BER performances (Proakis, 1989). As a result, an irreducible BER exists even when E_b/N_0 is increased arbitrarily large. Therefore, the irreducible BER performance, which reflects the limit of the receiver performance, may become an important measure.

Thus the irreducible BERs of the uncoded and the trellis coded (constraint length 2) GMSK signals are obtained over two-ray fading conditions. The vehicular speed is assumed to be 50 km/h. An average BER of 10^{-2}, which is often considered as a reference for voice communication (D'Avella *et al*, 1989), is used as the target BER value throughout this study. The irreducible BER curves obtained for uncoded and trellis coded schemes for various relative delays between the two paths are shown in Fig. 7.4. It may be observed from the obtained results that the trellis coded scheme performs better than the uncoded scheme. Nevertheless, the coded scheme also fails to reach the threshold BER of 10^{-2}, for relative delays larger than $0.75T$. The performance of the receiver in this situation may be improved through the use of adaptive equalisation or an adaptive MLSE scheme which takes into account the ISI caused by frequency-selective fading (Proakis, 1989).

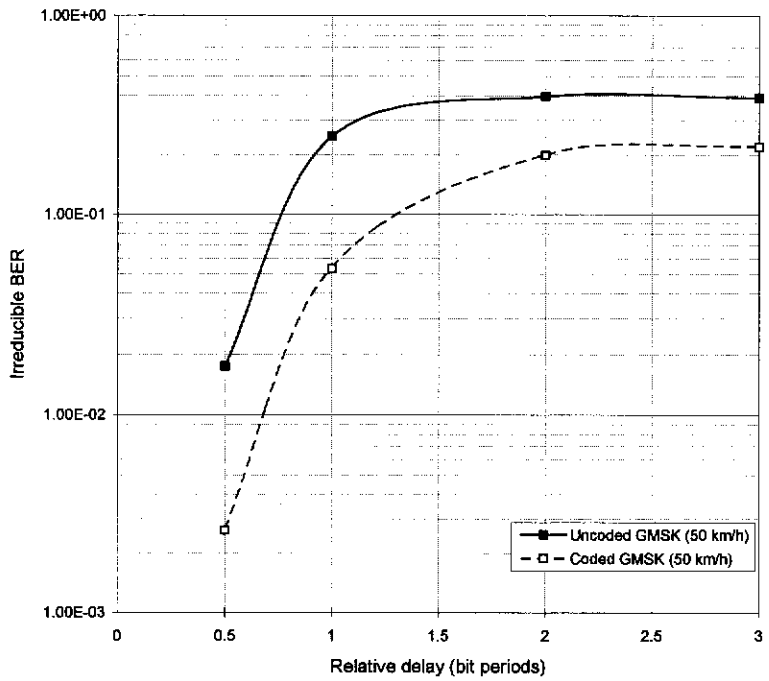

Figure 7.4 The irreducible BERs of the uncoded and trellis coded GMSK using differential phase detection over a two-ray fading channel.

7.4 An Improved Receiver with Adaptive Viterbi Detection Scheme

The ISI introduced by frequency-selective fading may be estimated from the channel impulse response and included in the Viterbi detection scheme. In an adaptive MLSE scheme, the estimated impulse response of the channel is used to update the MLSE states. Although in practice an adaptive channel impulse response estimator is necessary for MLSE state calculations, in this study it is assumed that the channel impulse response is known for this purpose. In this case, assuming that the channel impulse variations are slow, the reference phases at the Viterbi decoder are implicitly acquired during channel estimations. That is, the simulations are initially carried out assuming no phase errors are present. The distance between the transmitted and the received signals required for Viterbi decoding is obtained based on the absolute phase, as discussed in Section 4.5. Since the major concern of this study is not the adaptive equalisation schemes, the details of the channel impulse response estimation are not discussed. However, it is assumed that the impulse response of the channel can be estimated within the duration of a short training sequence, which is comparable in length with what is used in the GSM system (ETSI, 1993).

The adaptive Viterbi decoder proposed in the simulations has been designed to accommodate a channel delay spread, τ, of up to 4 bit periods. This range of delay spread corresponds to the maximum delay spread considered in the GSM systems (ETSI, 1993). In this case, the overall length of the impulse response, associated with the channel and the GMSK modulator, extends over 7 bit periods. Thus, the number of states in the Viterbi decoder representing the uncoded GMSK trellis consists of 2^7 or 128 states. The phase values representing these 128 states can be obtained based on the estimated channel impulse response. In the present study, this has been achieved by transmitting a known sequence of bits containing all the 7-bit long bit patterns. Moreover, as shown in Section 4.3, the introduction of differential encoding before GMSK has the potential to reduce the complexity of the combined trellis diagrams of the coded schemes. Instead

of the 128 states for the uncoded GMSK scheme, it has been observed that the resulting trellis diagrams for the coded schemes with constraint lengths 2, 3, and 4 can be represented by 16, 32 and 64 states, respectively. To keep the complexity of the Viterbi decoding low, only the trellis coded scheme with constraint length 2 code is considered for the study over fading channels.

In the simulation, a training sequence of m bits is added to each block of n data bits, in order to facilitate channel impulse response estimation at the receiver. In this case, the throughput efficiency of an uncoded scheme is reduced to $n/(m+n)$. An update of the channel impulse response in this case may be obtained after every $(m+n)$ transmitted bit periods. Due to the time varying nature of the channel, a more accurate estimation of the channel impulse response may be achieved by updating the channel estimate more often using smaller signal block sizes. i.e., small values of n. However, a smaller n will lead to a reduced throughput efficiency. Therefore, a compromise is called for between the throughput efficiency and the accuracy of the channel impulse response estimation. The tradeoff between the throughput efficiency and the BER performance of the receiver has also been investigated by considering different training sequence lengths and signal block sizes.

7.4.1 Simulation results over two-ray fading channels

In this section, the effect of frequency-selective fading on the BER performance of the proposed adaptive receiver is studied based on the two-ray fading channel. The irreducible BER curves for the uncoded and the trellis coded GMSK signals with constraint length 2 code have been obtained. In accordance with the GSM standard, a training sequence of 26 bits is used for adaptive estimation of the channel impulse response (Luise and Reggiannini, 1992; ETSI, 1993). The data may be transmitted using signal block sizes of 256 or 128 bits, in addition to the training sequence. In this case, with a block size of 256 signal bits, the throughput efficiency of the uncoded scheme is 90.7%. On the other hand, the number of information bits

in a block of 256 coded bits using a rate-½ code is 128. Thus, the overall throughput efficiency of the trellis coded scheme in this case becomes 45.4%. Consequently, the throughput efficiencies of the uncoded and the trellis coded schemes with different signal block sizes are as shown in Table 7.1.

No. of bits in the training sequence	No. of bits in the signal block	Throughput efficiency	
		Uncoded	Coded
26	256	90.7%	45.4%
26	128	83.1%	41.6%

Table 7.1 Throughput efficiencies of the uncoded and trellis coded schemes for signal block sizes of 128 bits and 256 bits.

7.4.1.1 Irreducible BERs over two-ray fading channel

The irreducible BERs obtained for a range of different values of relative delay between the two propagation paths of equal average power, are presented in Fig. 7.5. The vehicle speed is again assumed to be 50 km/h. From the irreducible BER curves of Fig. 7.5, it is observed that the target BER of 10^{-2} for voice traffic may be obtained with both the trellis coded and the uncoded schemes for relative delays of up to $4T$. It may also be observed that the largest improvement in BER performance of the trellis coded scheme is obtained when the relative delay is $4T$. This may be due to the fact that the proposed Viterbi decoder has been designed to accommodate a maximum relative delay of 4 bit periods. However, it may be observed that the BER performances of both the uncoded and trellis coded schemes degrade, when the relative delay exceeds $4T$. Furthermore, better BER performances have been obtained with both the uncoded and trellis coded schemes using the shorter block size of 128 bits, as this provides a more frequent estimation of the channel impulse response, compared to the one with the block size of 256 bits.

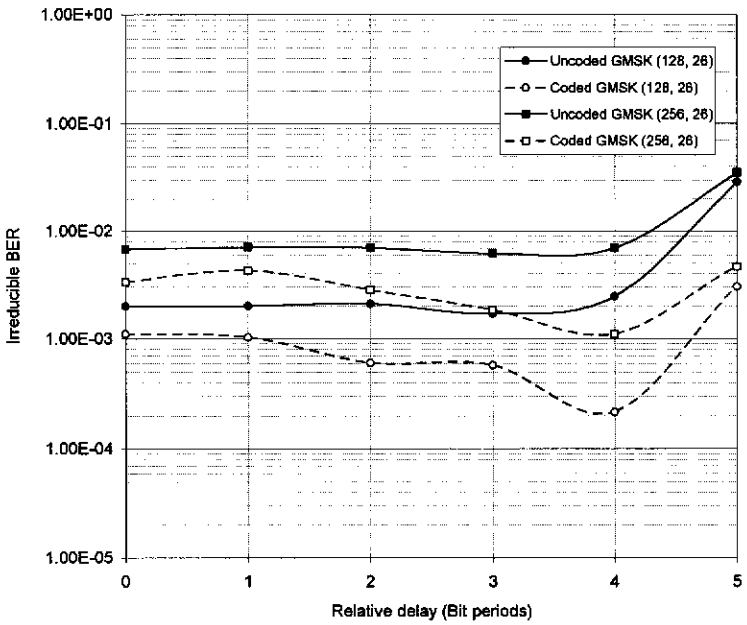

Figure 7.5 The irreducible BERs of the uncoded and trellis coded GMSK, for different relative delays. Signal blocks of 128 bits and 256 bits are assumed.

Also, from Fig. 7.5, it is observed that the target BER of 10^{-2} for voice traffic could be achieved with the trellis coded scheme, even when the relative delay is $5T$.

Based on this observation, an investigation has been made to see whether a less complex receiver designed to accommodate relative delay of up to 3 bit periods is able to achieve the required BER of 10^{-2} for channel delays up to $4T$, under two-ray conditions. The resultant simulated irreducible BER curves of the uncoded and the trellis coded GMSK schemes for different relative delays are presented in Fig. 7.6. In these simulations, the number of bits in a signal block and the number of bits in the training sequence, have been selected as 128 and 26, respectively. It can be observed from the results in Fig. 7.6, that the trellis coded scheme may just achieve the target BER of 10^{-2} for voice quality, when the relative delay is $4T$, whereas the uncoded scheme fails to reach this target value after $3.5T$. Because of its better

performance, the receiver designed to accommodate delay spreads of up to 4 bit periods has been retained for further study.

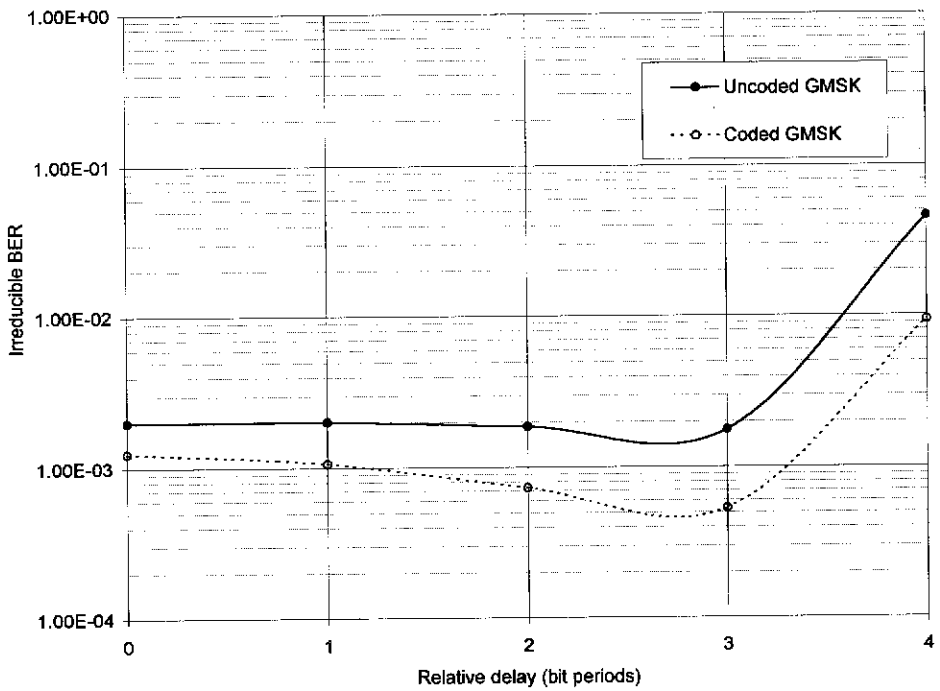

Figure 7.6 The irreducible BERs of the uncoded and trellis coded GMSK achieved using the decoder which is designed to accommodate relative delay of $3T$.

The influence of the length of the training sequence on the BER performance has also been investigated by increasing the original training sequence of 26 bits to 40 bits. The irreducible BERs of the trellis coded and the uncoded schemes, obtained assuming that the data is transmitted using a signal block size of 128 bits, are shown in Fig. 7.7. The results indicate that the effect of the length of the training sequence on the receiver performance is negligible[1]. However, the throughput efficiency of the uncoded scheme using a longer training sequence is reduced from 83.1% to 76.2%. Hence, the length of the training sequence for channel impulse response estimation for the remaining study is assumed to be 26 bits.

[1] The performance obtained with 40 training bits is slightly worse as the channel response may be changed somewhat during the longer period (14 bit periods more than for the case involving 26 training bits) taken for updating the channel impulse response.

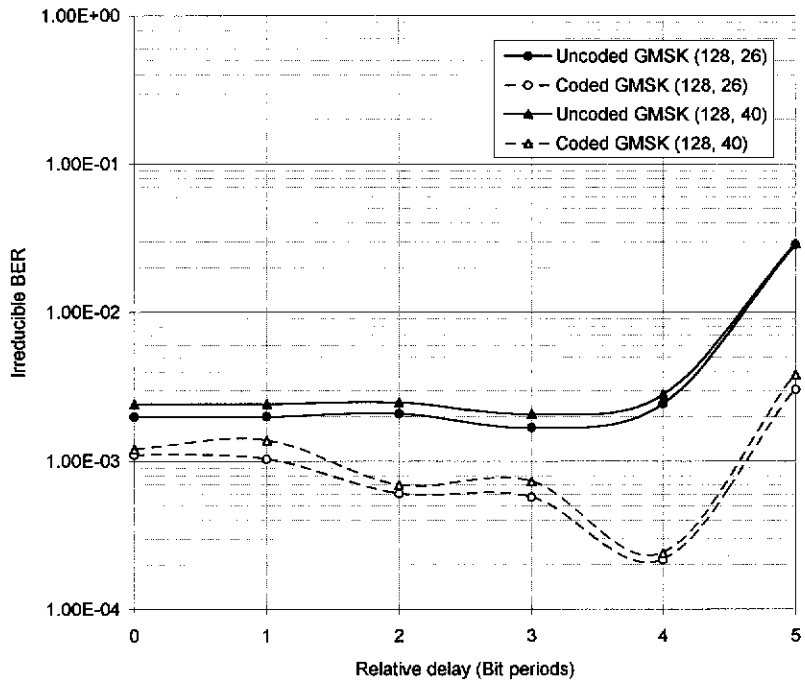

Figure 7.7 The irreducible BERs of the uncoded and trellis coded GMSK for two different lengths of training sequence.

7.4.1.2 BER performances for different relative delays

The BER performances of the uncoded and trellis coded GMSK schemes over frequency-selective fading conditions have been obtained for different values of relative delay, as shown in Figures 7.8 to 7.11. Again, the values of E_b/N_0 are obtained by changing the AWGN levels, while keeping the transmitted signal level constant.

It is noted from Figures 7.8 to 7.11, that for a signal block size of 256 bits, coding gains of about 4.0 dB, 6.0 dB, 6.5 dB and 8.0 dB at a BER of 10^{-2}, may be achieved with the trellis coded GMSK for the relative delays of $1T$, $2T$, $3T$ and $4T$, respectively. Furthermore, it is observed that only negligible improvement in coding gains could be achieved using a smaller block size of 128 bits. Moreover, as shown in Table 7.1, the throughput efficiency of the coded scheme using the block size of 128 bits is 41.6% compared to 45.4% for the block size of 256 bits. Therefore, it may be concluded that an update

of the channel impulse response after every (256+26) bits is a reasonable compromise between the BER performance and the throughput efficiency.

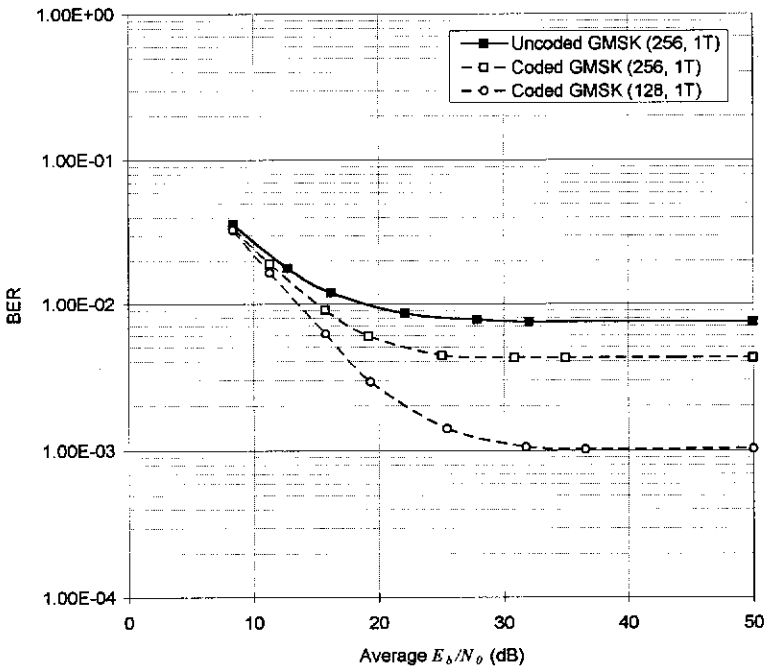

Figure 7.8 The BERs of the uncoded and trellis coded GMSK when the relative delay is $1T$.

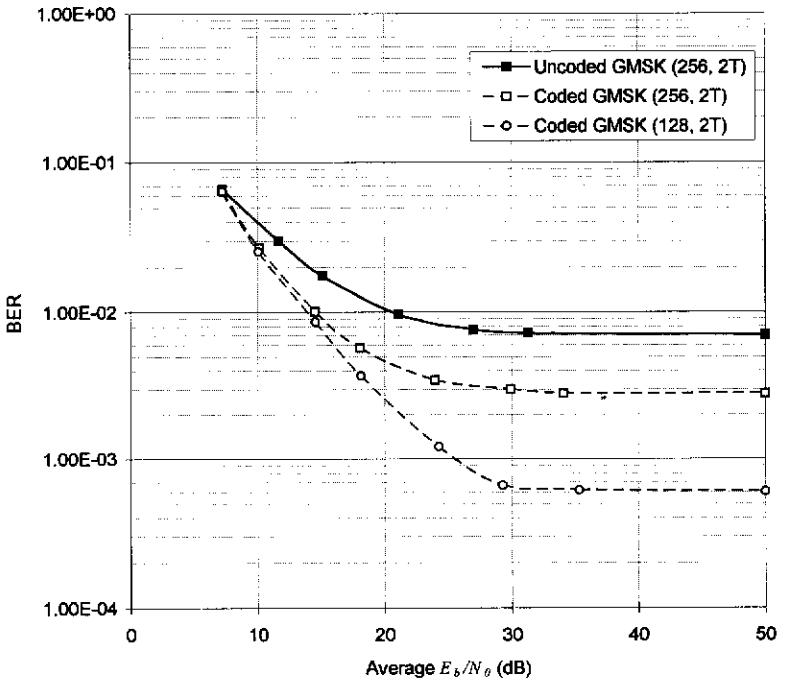

Figure 7.9 The BERs of the uncoded and trellis coded GMSK when the relative delay is $2T$.

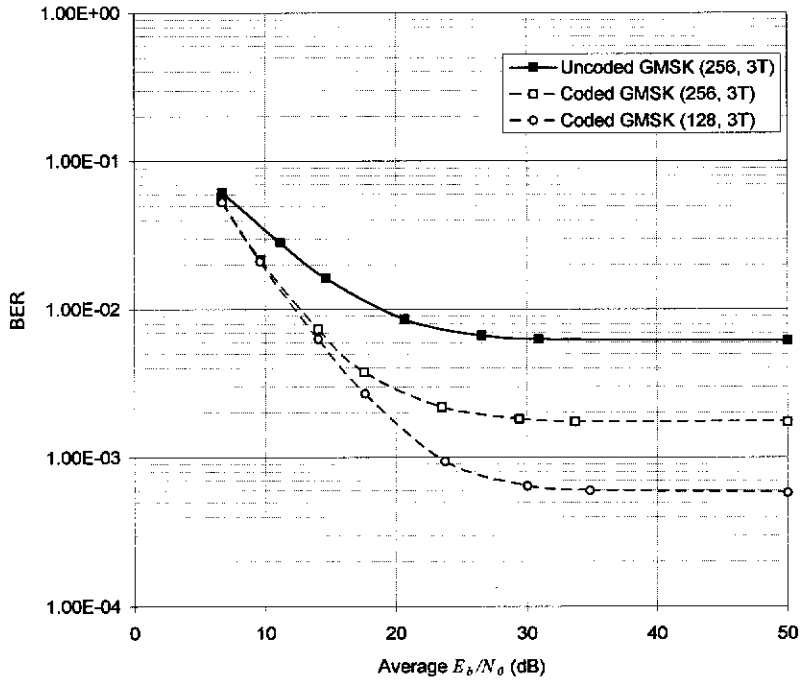

Figure 7.10 The BERs of the uncoded and trellis coded GMSK when the relative delay is $3T$.

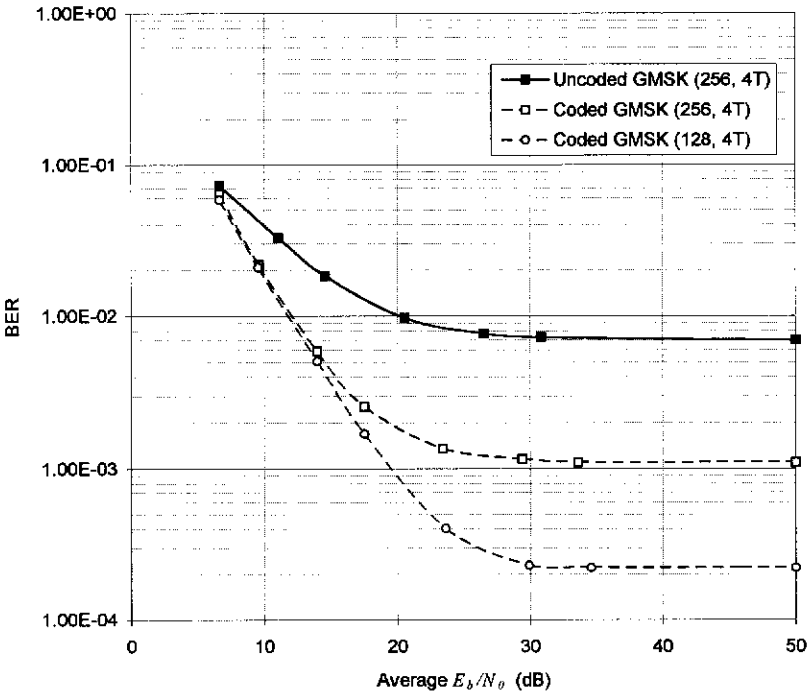

Figure 7.11 The BERs of the uncoded and trellis coded GMSK when the relative delay is $4T$.

7.4.1.3 Influence of Doppler frequency on BER performance

The effect of Doppler frequency on the BERs has been studied for the case involving the maximum delay of $4T$ between the two propagation paths. The corresponding BER curves of the uncoded and the trellis coded GMSK schemes obtained for a range of vehicular speeds are presented in Fig. 7.12. It includes the case involving a typical walking pace of 5 km/h. The faster vehicular speeds of 25 km/h, 50 km/h and 100 km/h have also been considered. From the simulated results, it is observed that with the trellis coded GMSK scheme, coding gains of around 3 dB, 4 dB and 8 dB can be obtained at a BER of 10^{-2} for speeds of 5 km/h, 25 km/h and 50 km/h, respectively. Moreover, the uncoded GMSK scheme fails to meet the required BER of 10^{-2}, at the speed of 100 km/h, whereas the coded scheme achieves this BER value at an E_b/N_0 of approximately 17 dB. Thus, the results show that the trellis coded scheme is more tolerant to the Doppler spread caused by higher vehicular speeds. Also, it may be observed that the irreducible BER of the coded scheme at a speed of 25 km/h, is almost one order of magnitude lower than that of the uncoded scheme, reducing from a BER of $2\text{x}10^{-3}$ to $2\text{x}10^{-4}$.

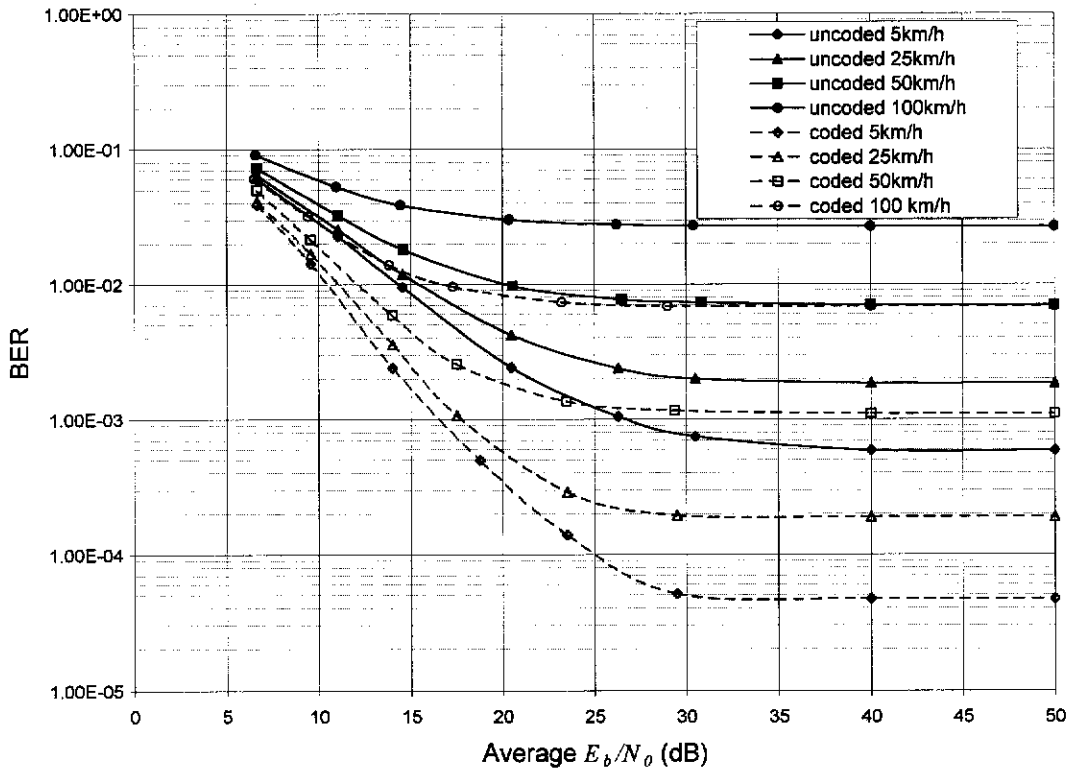

Figure 7.12 The BERs of the uncoded and trellis coded GMSK at different vehicular speeds. A relative delay of $4T$ is assumed.

7.4.2 Simulated BERs over six-ray fading channels

In this section, the BER performances of the proposed trellis coded GMSK scheme operating in frequency-selective fading conditions as specified for the GSM system are studied. Again, ideal estimation of the channel impulse response is assumed and the estimations are assumed to update after every (256+26) transmitted bits. The vehicular speeds are selected to cover a range of values relevant to the particular environments, such as 50 km/h to 150 km/h for the RA; 25 km/h to 100 km/h for the HT; and 5 km/h to 75 km/h for TU.

Fig. 7.13 shows the BER curves of the uncoded and the trellis coded schemes obtained for the rural area (RA) model described in Table F.1 of Appendix F, over a range of vehicular speeds varying from 50 km/h to 150 km/h. From these curves, it is observed that the trellis coded scheme is able

to achieve the required BER of 10^{-2} for voice communication over the RA channel for vehicular speeds of less than 100 km/h.

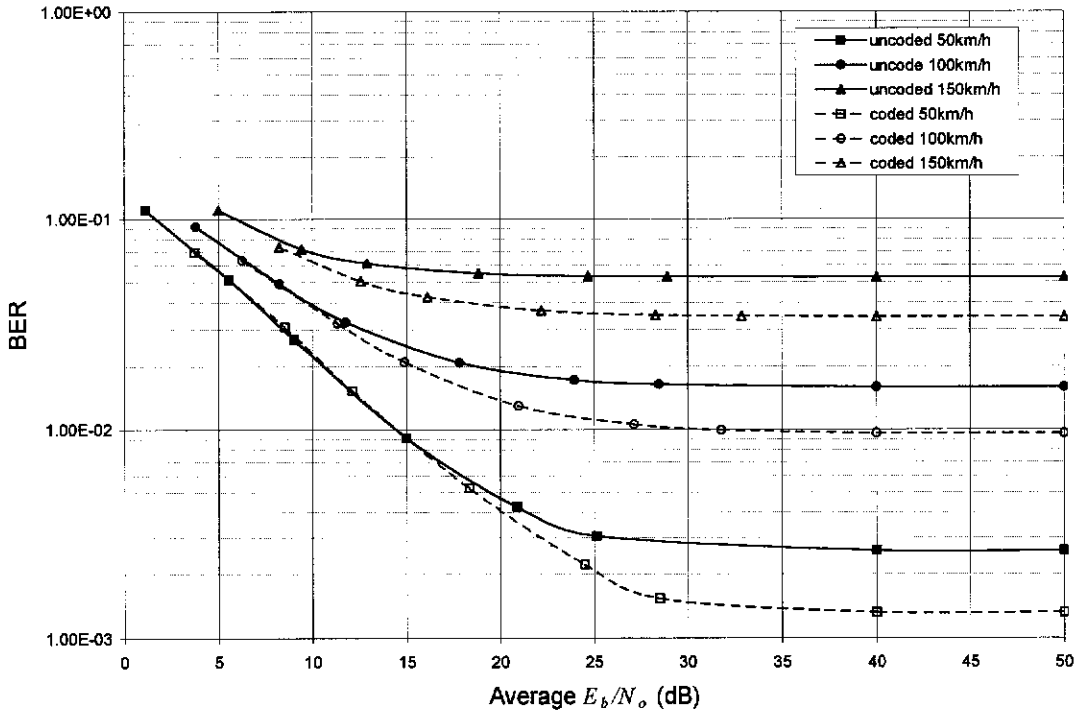

Figure 7.13 The BERs of the uncoded and trellis coded GMSK for different vehicular speeds based on the rural area (RA) model.

The BER curves shown in Fig. 7.14, are obtained assuming the hilly terrain (HT) model described in Table F.2 of Appendix F. From these curves, it is observed that the trellis coded scheme achieves the target BER of 10^{-2} for vehicular speeds of up to 100km/h.

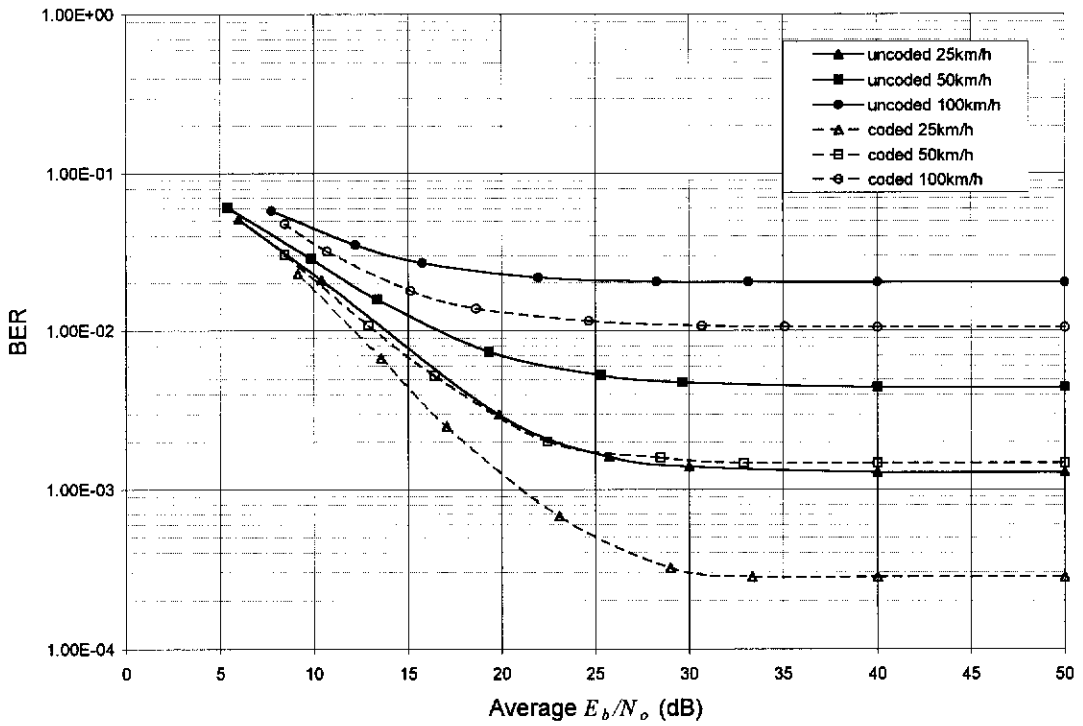

Figure 7.14 The BERs of the uncoded and trellis coded GMSK for different vehicular speeds based on the hilly terrain (HT) model.

Finally, a set of BER curves based on the typical urban area (TU) model described in Table F.3 of Appendix F, has been obtained for speeds of 5 km/h, 50 km/h and 75 km/h. From Fig. 7.15, it is observed that both the trellis coded and the uncoded schemes are able to achieve the required BER of 10^{-2}, for all the three speeds considered. Moreover, lower irreducible BERs have been obtained for these speeds using the trellis coded scheme.

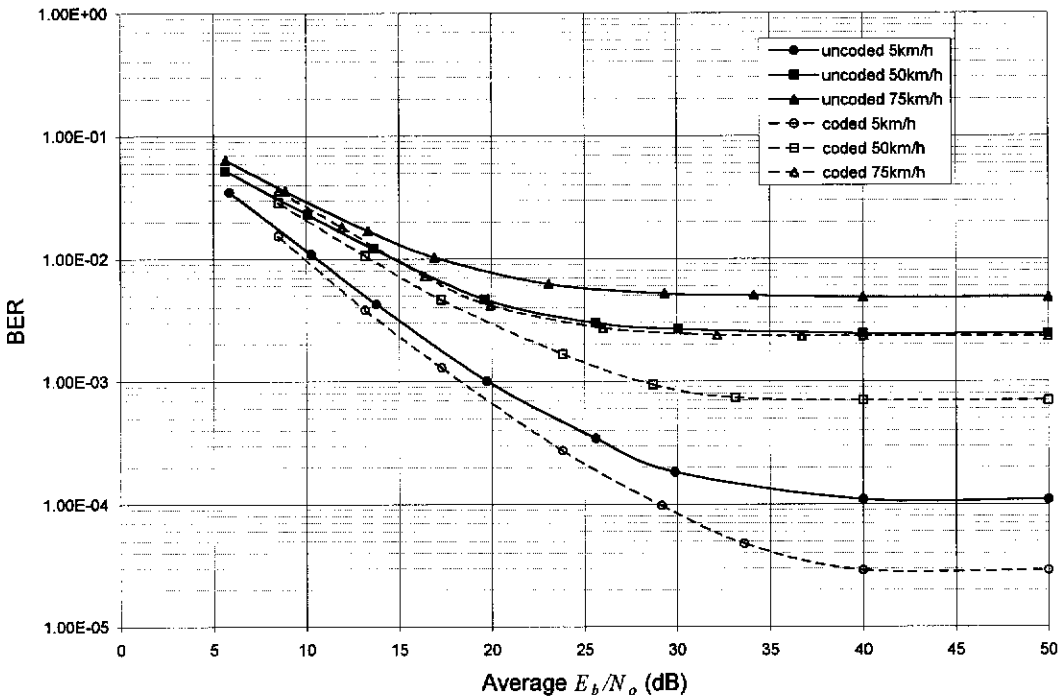

Figure 7.15 The BERs of the uncoded and trellis coded GMSK for different vehicular speeds based on the typical urban area (TU) model.

7.5 Effect of Phase Errors at the Receiver

As discussed in the previous sections, the proposed adaptive receiver performs well under frequency-selective conditions assuming that the reference phases for the Viterbi decoder are correctly acquired during channel estimations. i.e., the phase errors introduced are assumed to be zero. However, in practice, phase errors are present. Therefore in this section, the effect of such phase errors on the receiver performance is investigated. For this study, the two-ray channel model is used. The study assumes the worst case scenario that the two paths have equal power and a maximum relative delay of $4T$. In the simulations, phase error is introduced to the phase of the received signal as discussed in Section 6.4.2. First, the effect of fixed phase errors is studied using a fixed offset of $\pm 10°$. Then, the influence on the BER performance of Gaussian distributed phase errors generated in the way as described in Section 6.4.2, is studied. The bandwidth of the carrier recovery circuit is set at 1% of the input bit rate, as

in the case of AWGN, discussed in Section 6.4.2. The approximate rms values of the random phases generated are set at $\pm 10°$ and $\pm 20°$. The BER performances of the uncoded and the trellis coded schemes, obtained assuming a vehicular speed of 50 km/h, are presented in Fig. 7.16. From Fig. 7.16, it is observed that when the phase error is $\pm 20°$ rms, the uncoded scheme fails to achieve the reference BER of 10^{-2}, and the performance degradation of the trellis coded scheme is about 8 dB. Therefore, this suggests that the adaptive receiver designed for the trellis coded scheme is more tolerant to phase errors compared with the uncoded scheme. This observation has also been verified by using a two-ray frequency-selective fading model with $1T$ delay between the two paths. In this case, the random phase errors with approximate rms values of $\pm 10°$ and $\pm 20°$ have been introduced. From the results presented in Fig. 7.17, it can be confirmed that the proposed trellis coded receiver is less sensitive to carrier phase errors than its uncoded counterparts.

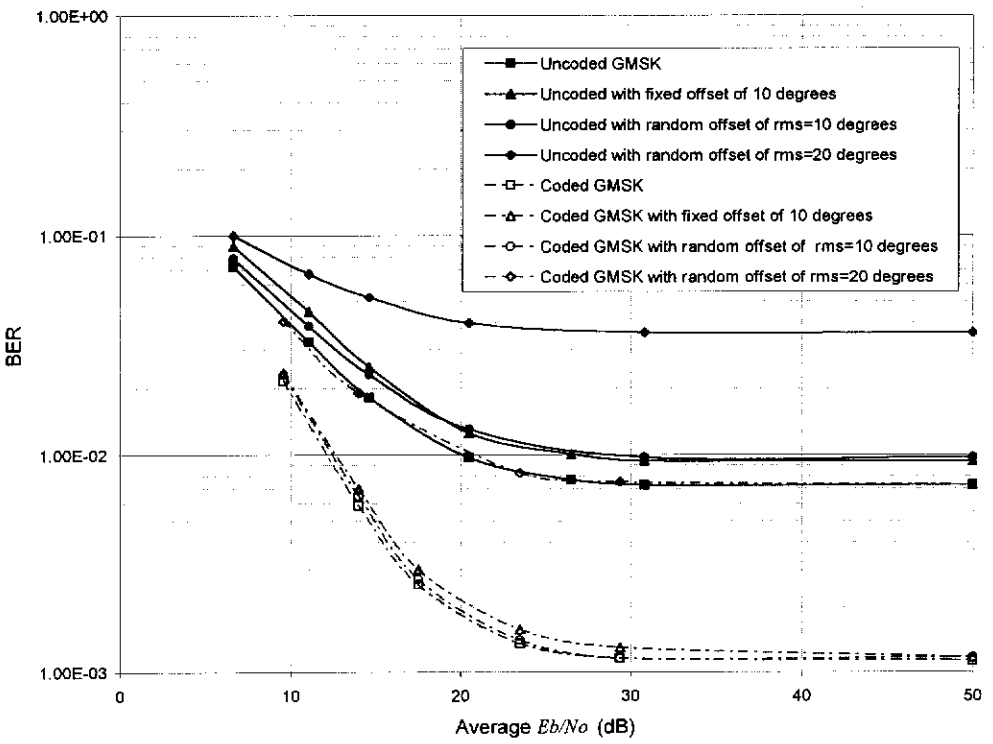

Figure 7.16 The BERs of the uncoded and trellis coded GMSK in the presence of phase errors, when the relative delay between the two paths of the two-ray frequency-selective fading model is $4T$.

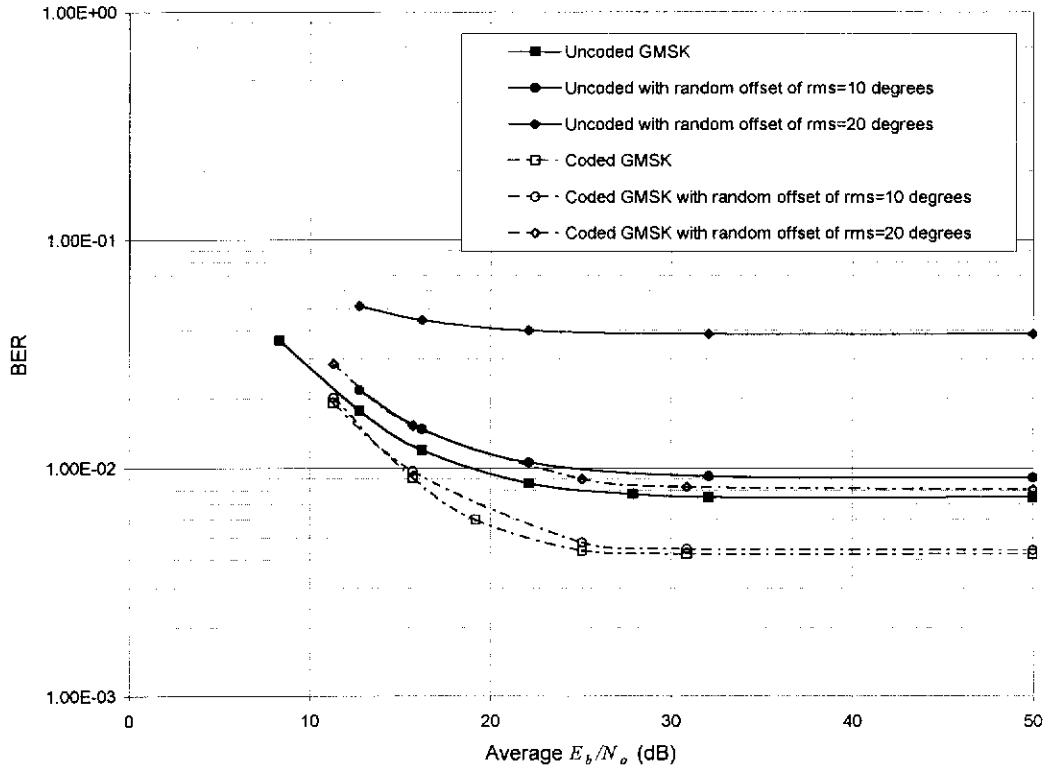

Figure 7.17 The BERs of the uncoded and trellis coded GMSK in the presence of phase errors, when the relative delay between the two paths of the two-ray frequency-selective fading model is $1T$.

7.6 Summary

The BER performances of the uncoded and trellis coded GMSK schemes have been studied using a differential phase detection scheme over frequency non-selective (flat) and frequency-selective fading channels. It is found that using the differential detection scheme, it is not possible to achieve the required threshold BER of 10^{-2} (for voice communication), with the trellis coded GMSK scheme when the relative delay of a two-ray frequency-selective fading channel is larger than $0.75T$. Therefore, an adaptive receiver, which is designed based on the estimation of the channel impulse response to accommodate a channel delay spread of up to 4 bit periods, has been introduced. For this receiver, the Viterbi decoder designed for the uncoded GMSK is represented by 128 phase states. It has been

shown that a large reduction in the number of phase states for the Viterbi decoder could be achieved for the trellis coded GMSK schemes. The BER performances achievable using the adaptive Viterbi decoder have been studied based on the simple two-ray propagation model and the more complicated six-ray GSM empirical models.

It has been observed from the simulated results that the trellis coded GMSK scheme using the adaptive receiver performed well compared to the uncoded scheme over frequency-selective fading conditions. Also, the trellis coded scheme achieved the reference BER of 10^{-2} required for voice communication with an E_b/N_0 of around 15 dB. Also, a significant improvement in the irreducible BERs has been obtained for the trellis coded GMSK scheme as compared to the uncoded scheme for the various fading channel conditions considered. Further, it has been observed that the trellis coded scheme is more tolerant to carrier phase errors than the uncoded signal. Finally it is noted that performance enhancement has been achieved by the trellis coded GMSK scheme with a Viterbi decoder of 16 states as compared with the 128 states required for the uncoded GMSK signal.

CHAPTER 8

CONCLUSIONS AND RECOMMENDATIONS

8.1 Summary of Results and Conclusions

The growing demand for mobile radio services coupled with the limited spectrum available has driven mobile communications toward spectrally efficient digital modulation schemes. CPM signals are good candidates in such applications due to their compact power spectra (Steele, 1992). In a mobile radio environment, signal propagation is not only affected by AWGN but also by envelope fading and random phase variations, giving rise to degradations in the BER performance. In such situations, error control coding techniques are often used in improving the BERs. As discussed in Chapter 2, TCM schemes originally developed for AWGN channels, have received attention for mobile radio. This is because they show improved BER performances without affecting the required bandwidth (Ungerboeck, 1982; Divsalar and Simon, 1987).

A survey of conventional TCM schemes involving high-level modulation, such as multi-level phase and multi-level amplitude schemes, over AWGN and frequency flat fading channels has been given in Chapter 3. This survey has shown that in the presence of AWGN and frequency flat amplitude-fading conditions, the conventional TCM schemes yield good coding gains compared to the uncoded (Ungerboeck, 1982; 1987; Divsalar and Simon, 1987). Moreover these coding gains were achieved without reducing the effective information rate, as would be required by traditional error control coding techniques. A review of the selection of trellis coded CPM schemes, in the presence of AWGN has also been carried out in Chapter 3. A comparison of trellis coded partial response and full response CPM

schemes has shown that the trellis coded partial response CPM schemes provide better energy-bandwidth performances (Pizzi and Wilson, 1985). However, this gain in performance has been achieved at the expense of the MLSD receiver complexity. Also, the review has shown that a reduction in the receiver complexity, based on the number of states in the Viterbi decoder in situations involving partial response CPM, such as TFM, can be obtained by introducing differential encoding prior to modulation (Morales-Moreno et al, 1994). Finally, a review of trellis coded CPM schemes in frequency flat and selective fading channels has been given.

In this thesis, a spectrally efficient communication scheme for mobile applications involving partial response CPM, such as GMSK, in combination with rate-½ trellis coding has been proposed. The selection of the proposed rate-½ trellis codes having constraint lengths 2, 3, and 4 in combination with GMSK, has been carried out in Chapter 4, assuming MLSD based on the Viterbi algorithm, using an extensive computer search method. The code selection has been carried out based on the achievable free Euclidean distance of the coded GMSK scheme, and the complexity of the receiver in terms of the number of phase states involved in the Viterbi decoder. A reduction in the number of phase states in the Viterbi decoder has been achieved using differential encoding before modulation. The codes of generator polynomials [3,1] for constraint length 2, [7,3] and [6,3] for constraint length 3, and [13,7] and [15,7] for constraint length 4, have been identified as the appropriate codes for study in this thesis. However, it has been observed in Section 4.8 that the code [6,3] when combined with differentially encoded GMSK produces an ambiguity in the decoder, producing the same distances corresponding to bits having opposite polarity. Moreover, code [6,3] is a bad code since it is catastrophic. Therefore, the code [6,3] has not been considered for detailed study.

It has been found that an asymptotic coding gain of 2.36 dB could be achieved with code [3,1] in combination with differentially encoded GMSK. Moreover, this gain has been obtained with a decoder having half the

number of states compared to the uncoded GMSK signal. The trellis coded and differentially encoded GMSK scheme involving the code [7,3] has produced a coding gain of 3.61 dB. The number of states in the Viterbi decoder involving the code [7,3] is found to be the same as the uncoded GMSK scheme. As a result, it can be concluded that coding gains of up to 3.61dB could be achieved with the selected trellis coded GMSK schemes involving codes of constraint lengths 2 and 3, with no increase in the receiver complexity. However, a larger coding gain of 5.06 dB could be achieved with the selected codes [13,7] and [15,7] at the expense of doubling the number of states compared to the uncoded scheme.

The upper and lower bounds on the BERs of the selected trellis coded schemes, in the presence of AWGN and frequency flat fading, have been theoretically evaluated in Chapter 5. It has been assumed in the analysis, that the received signal is detected using coherent detection with perfect carrier recovery. Moreover, the only effect of fading considered is on the amplitude of the received signal. In addition, bit interleaving of sufficient depth has been assumed. Consequently, the upper and lower bound values of the BERs have been analytically derived based on a technique designed for memoryless channels, which involves the transfer function of the error state diagram (Proakis, 1989; Biglieri *et al*, 1991). Based on the analysis presented in Chapter 5, it has been observed that when the number of states in the trellis diagram increases, the complexity of the error state diagram increases and hence the theoretical analysis of the BERs becomes extremely complicated. Therefore, the analysis has been restricted to the trellis coded schemes having up to 8 states in the combined trellis. Note that the analyses presented in Chapter 5 of the BER performances over AWGN have been obtained assuming ideal carrier recovery and timing recovery conditions. However, in practical situations, it may not be possible to recover the carrier and sample timing without any errors. Also, it may not be practically possible to track the phase variations of the received signal over a fading channel, as assumed in the analyses. Therefore computer simulations have been used to study the BER performances of the selected

trellis coded schemes in the presence of practical impairments, such as carrier phase errors and sample timing deviations. Moreover, computer simulated BERs assuming ideal carrier recovery and sample timing recovery have been obtained to verify the analytical bounds.

Chapter 6 presents the computer simulations carried out for evaluating the BER performances of the uncoded, and the selected trellis coded GMSK schemes in the presence of AWGN. The received signal has been detected using quadrature demodulation followed by Viterbi decoding. The simulated BER results, assuming ideal carrier recovery and sample timing recovery, have shown that at a BER of 10^{-3}, coding gains of approximately 1.7 dB and 2.2dB can be achieved using codes of constraint lengths 2 and 3, respectively. Moreover, these coding gains of up to 2.2 dB have been obtained using the selected trellis coded schemes without an increase in the receiver complexity, as discussed in Chapter 4. The simulated results also show that a larger coding gain of 3.1 dB can be achieved with the coded scheme using codes of constraint length 4, at the expense of a slight increase in the receiver complexity. A comparison of the simulated BERs with the analytical bounds obtained in Chapter 5 shows that the simulated results typically fall within 1 dB of the lower bound.

The effects of practical impairments, such as timing and phase errors on the BER performances have also been studied in Chapter 6. The individual and the combined effects of timing and phase errors on the BER performances have been simulated. Both fixed and random deviations in the sampling time and carrier phase have been considered. A comparison of performance gain at a BER of 10^{-3} with respect to the uncoded GMSK scheme, under ideal timing and carrier recovery conditions, shows that the BER performances of the uncoded scheme degraded by up to 3.3 dB in the presence of severe random timing error with an rms offset of ±25% of the transmitted bit period T. The peak timing deviations in this case may extend up to ±75% of T. The trellis coded schemes on the other hand, achieved performance gains of up to 2.09dB. In the presence of fixed carrier phase errors of ±18°, the trellis

coded schemes have shown performance gains of up to 2.15 dB, whereas the uncoded scheme has shown a degradation of more than 5 dB. Based on the simulated results of the BER performances in Chapter 6, it can be concluded that the selected trellis coded schemes are more tolerant to practical impairments, such as timing and phase errors, compared to the uncoded scheme. This observation is found to be different from the earlier published results on trellis coded schemes involving high-level modulation schemes discussed in Chapter 3.

In Chapter 7, the BER performances of the uncoded and the selected trellis coded schemes in the presence of frequency-flat and frequency-selective fading conditions have been obtained using computer simulations. A differential phase detection scheme based on the phase difference over one bit period has been proposed. The simulated BER performances of the uncoded and the selected trellis coded schemes over flat fading conditions, using this differential phase detection scheme, have shown a coding gain of approximately 6.5 dB at a BER of 10^{-3} compared to the uncoded scheme. However, over a two-ray frequency-selective fading channel with equal path power, both the uncoded and coded schemes failed to achieve an irreducible BER of 10^{-2}, which is generally assumed to be needed for digital voice communications. Therefore an adaptive Viterbi decoder has been proposed, which takes into account ISI introduced by frequency-selective fading. The proposed receiver has been designed to accommodate a channel delay spread of up to 4 bit periods. This range of delay spread has been considered as it corresponds to the maximum delay spread specified for the GSM systems (ETSI, 1993). The Viterbi decoder designed for the uncoded GMSK signal involves 128 states. On the other hand, the number of states of the Viterbi decoder designed for the trellis coded scheme with a constraint length of 2 is only 16. Consequently, a large reduction in receiver complexity has been obtained.

The BER performances of the uncoded and the trellis coded GMSK schemes employing the proposed adaptive Viterbi decoder have been

obtained assuming the channel impulse response can be accurately estimated using a short training sequence. The proposed trellis coded GMSK scheme has been shown to perform better than the uncoded scheme under the frequency-flat, and severe frequency-selective fading conditions represented by the two-ray channel model as well as the recommended GSM six-ray propagation models, (the TU, the HT and the RA models). Moreover, it has been found that a large improvement in the irreducible BERs could also be obtained using the trellis coded GMSK scheme compared to the uncoded scheme. Furthermore, the simulated BERs, presented in Chapter 7, have shown that the coded scheme is less sensitive to carrier phase errors than the uncoded scheme under frequency-selective fading conditions.

With the above observations, it may be concluded that the selected trellis coded GMSK schemes are good candidates for applications subject to AWGN as well as fading environments, including frequency-flat and frequency-selective conditions. In addition, the proposed trellis coded GMSK schemes are found to be more tolerant to practical impairments, such as carrier phase and sample timing errors. Similar results would be expected with other partial response CPM schemes such as GTFM (Chung, 1984) and 3-RC (Sundberg, 1986), which have similar spectral densities as the GMSK signal.

8.2 Recommendations

The simulated BER performances obtained have shown that the proposed trellis coded GMSK schemes using quadrature demodulation followed by Viterbi decoding are tolerant to the frequency-selective fading conditions often encountered in mobile environments. For this reason, it is recommended that the following topics be considered in an attempt to further improve the performance of the proposed trellis coded GMSK schemes. Practical implementation of the proposed scheme is also suggested.

8.2.1 Adaptive sampling

In the present study, the receiver adopted a fixed sampling instant for the whole transmission. However as suggested in (Molisch *et al*, 1997; 1998), a large reduction in the irreducible BERs can be obtained using an adaptive sampling technique. With this technique, the sampling time for each transmitted frame is differently selected based on a training sequence. The received training sequence, sampled using different sampling instants, is detected and compared with the original training sequence. Assuming that the channel does not change appreciably during one transmitted frame, the sampling instant associated with the sequence with the smallest number of errors is then selected. The influence of such adaptive sampling technique on the BER performances of the proposed trellis coded schemes over frequency-selective fading conditions may be beneficial to study.

8.2.2 Adaptive channel estimation

It has been assumed in the present study that ideal channel impulse response is available for obtaining the phase states of the proposed adaptive Viterbi decoder. In practice adaptive channel estimation techniques based on the cross-correlation of the received signal with a known training sequence, is used to estimate the channel impulse response during the period of that training sequence. Therefore, the effect of imperfect phase estimation of a practical adaptive channel estimator should be investigated.

8.2.3 Practical implementation

Practical implementation of the proposed scheme is suggested, so that the performance in real environments can be studied through field tests.

REFERENCES

(Abrishamkar and Biglieri, 1991)

Abrishamkar, F. and Biglieri, E., "Suboptimum detection of trellis-coded CPM for transmission on bandwidth- and power-limited channels," *IEEE Transaction on Communications*, COM-39(7), pp. 1065-1074, July 1991.

(Ali Adel *et al*, 1989)

Ali Adel A. and Al-Kadi Ibrahim A., "On the Use of Repetition Coding with Binary Digital Modulations on Mobile Channels," *IEEE Transactions on Vehicular Technology*, 38(1), 1989, pp. 14-18, February 1989.

(Anderson *et al*, 1986)

Anderson, J, Aulin, T and Sundberg, C.E., *Digital Phase Modulation*, Plenum Press, New York, NY, USA, 1986.

(Anderson *et al*, 1991)

Anderson, John B. and Sundberg, Carl-Erik W., "Advances in Constant Envelope Coded Modulation," *IEEE Communications Magazine*, pp. 36-45, December 1991.

(Aulin *et al*, 1981)

Aulin, T. and Sundberg, C.-E.W., "Continuous Phase Modulation - Part I : Full Response Signalling," *IEEE Transaction on Communications*, COM-29(3), pp. 196-209, March 1981.

(Aulin *et al*, 1981)

Aulin, T., Rydbeck, Nils and Sundberg, C.-E.W., "Continuous Phase Modulation - Part II : Partial Response Signalling," *IEEE Transaction on Communications*, COM-29(3), pp. 210-225, March 1981.

(Bello 1963)

Bello P. A., "Characterisation of Randomly Time-Variant Linear Channels," *IEEE Trans. Commun. Syst.*, CS-11(4), pp. 360-393, Dec. 1963.

(Bhargava *et al*, 1981)

Bhargava, V. K., Haccoun, D., Matyas, R. and Nuspal, P. P., *Digital Communications by Satellite, Modulation, Multiple Access and Coding*, A Wiley-Interscience Publication, John Wiley & Sons, USA, 1981.

(Biglieri et al, 1991)

Biglieri, Ezio, Divsalar, Dariush, McLane, P.J. and Simon M.K., *Introduction to Trellis-Coded Modulation with Application*, McMillan Publishing Company, New York, NY, USA, 1991.

(Cavers and Ho, 1992)

Cavers, James K. and Ho, Paul, "Analysis of the Error Performance of Trellis Coded Modulations in Rayleigh Fading Channels," *IEEE Transactions on Communications*, COM-40(1), pp. 74-83, January 1992.

Cavers and Liao, 1992)

Cavers, James K. and Liao, M, "A comparison of pilot-tone and pilot-symbol technique for digital mobile communication," *Proc. of IEEE Globecom'92 Conference*, IEEE Globecom'92, Orlando, USA, pp. 915-921, December 1992.

(Chung, 1984)

Chung, Kah-Seng, "Generalized Tamed Frequency Modulation and Its Application for Mobile Radio Communications," *IEEE Journal on Selected Areas in Communications*, SAC-2 (4), pp. 487-497, July 1984.

(Clarke and Cain, 1981)

Clarke, K. and Cain, J.B., *Error-Correction Coding for Digital Communications*, Plenum Press, New York, NY, USA, 1981.

(Dahlquis *et al*, 1974)

Dahlquis, G. and Bjorck, A., Translated by Anderson, N., *Numerical methods*, Prentice Hall Inc., Englewood Cliffs, NJ., 1974.

(Davarian, 1987)

Davarian, F., "Mobile digital communications via tone calibration," *IEEE Trans. On Vehicular Technology*, VT-36(2), pp. 55-62, May1987.

(D'Avella *et al* 1989)

D'Avella R., Moreno L., and Sant'Agostino M., "An Adaptive MLSE Receiver for TDMA Digital Mobile Radio," *IEEE J. Select. Areas Commun*, vol. 7, pp. 122-129, Jan. 1989.

(Diaz *et al*, 1998)

Diaz, P. and Agusti, R., "The use of coding and diversity combining for mitigating fading effects in a DS/CDMA system," *IEEE Trans. On Vehicular Technology*, VT-47(1), pp. 95-102, February 1998.

(Divsalar and Simon, 1987)

Divsalar, D. and Simon, M.K., "Trellis Coded Modulation for 4800/9600 bit/s Transmission Over a Fading Mobile Satellite Channel," *IEEE Journal on Selected Areas in Communications*, SAC-5(2), pp. 162-175, February 1987.

(ETSI 1993)

ETSI-GSM Recommendation GSM 05.05, "Radio Transmission and Reception," Version 3.15.0, Annex 3, European Telecommunications Standard Institute, Valbonne Cedex, France, 1993.

(Fano, 1963)

Fano. R. M., "A heuristic discussion of probabilistic coding," *IEEE Trans. On Information Theory,* IT-9, pp. 64-74, April 1963.

(Fugino *et al*, 1985)

Fugino, T., Umeda, Y. and Yamazaki, E., "Coded Octal PSK System Performance, distributed by Imperfect recovered Phase Reference," *Electron. Commun. Japan*, part 1, 68(7), pp. 114-123, 1985.

(Gibson, 1996)

Gibson, J. D., *The Mobile Communications Handbook*, CRC Press, handbook published in co-operation with IEEE Press, 1996.

(Haykin, 1988)

Haykin, S, *Digital Communications*, John Wiley and Sons, Inc., 1988.

(Hirono *et al*, 1994)

Hirono M., Miki T., and Murota K., "Multilevel Decision Method for Band-Limited Digital FM with Limiter-Discriminator Detection," *IEEE J. Select. Areas in Comms.*, Vol. SAC-2,No. 4, pp. 498-506, July 1984.

(Ho and McLane, 1988)

Ho, P. and McLane, P.J., "Spectrum, Distance and Receiver Complexity of Encoded Continuous Phase Modulation," *IEEE Transactions on Information Theory*, IT-34(5), pp. 1021-1032, September 1988.

(Huang and Campbell, 1991)

Huang, Jei and Campbell, L. Lorne, "Trellis Coded MDPSK in Correlated and Shadowed Rician Fading Channels," *IEEE Transactions on Vehicular Technology*, 40(4), pp. 786-797, November 1991.

(Jakes, 1974)

Jakes Jr., W.C. ed., *Microwave Mobile Communications*, John Wiley, New York, NY, USA, 1974.

(Jamali and Le-Ngoc, 1991)

Jamali, S.H. and Le-Ngoc, Tho, "A New 4-State 8PSK TCM scheme for Fast Fading, Shadowed Mobile Radio Channels," *IEEE Transactions on Vehicular Technology*, 40(1), pp. 216-222, February 1991.

(Kerr and McLane, 1992)

Kerr, Ron W. and McLane, Peter J., "Coherent Detection of Interleaved Trellis Encoded CPFSK on Shadowed Mobile Satellite Channels," *IEEE Transactions on Vehicular Technology*, 41(2), pp. 159-169, May 1992.

(Korn, 1991)

Korn, Israel, "Differential Phase Shift Keying in Two-Path Rayleigh Channel with Adjacent Channel Interference," *IEEE Transactions on Vehicular Technology*, 40(2), pp. 461-47, 1May 1991.

(Lathi, 1995)

Lathi, B.P., *Modern digital and analog communication systems*, Oxford Univ. Press, New York, Oxford, 1995.

(Lee and McLane, 1988)

Lee, A.C.M. and McLane, P.J., "Convolutionally Interleaved PSK and DPSK Trellis Codes for Shadowed, Fast Fading Mobile Satellite Communication Channels," *Proc of Vehicular Technology Conference*, Philadelphia, USA, June 1988.

(Lee and McLane, 1990)

Lee, A.C.M. and McLane, P.J., "Convolutionally Interleaved PSK and DPSK Trellis Codes for Shadowed, Fast Fading Mobile Satellite Communication Channels," *IEEE Transactions on Vehicular Technology*, 39, pp. 37-47, February 1990.

(Leib *et al*, 1986)

Leib, H. and Pasupathy, S., "Effects of Phase Errors on Trellis Coded PSK Schemes," *Proc. of International Conference on Communications*, ICC-86, Toronto, Ontario, Canada, pp. 970-974, 1986.

(Leib *et al*, 1987)

Leib, H. and Pasupathy, S., "Trellis Coded MPSK with Reference Phase Errors," *IEEE Transactions on Communications*, COM-35, pp. 888-900, September 1987.

(Lindell *et al*, 1984)

Lindell, G., Sundberg, C.-E. and Aulin, T., "Minimum Euclidean Distance for Combinations of Short rate-1/2 Convolutional Codes and CPFSK Modulation," *IEEE Transactions on Information Theory*, IT-30(3), pp. 509-519, May 1984.

(Luise and Reggianni, 1992)

Luise, Marco and Reggianni, Ruggero, "An efficient carrier recovery scheme for GSM receivers," *Proc. of Globecom'92*, IEEE Globecom'92 mini-conference, Orlando, USA, pp. 36-40, December 1992.

(Luise and Reggianni, 1993)

Luise, Marco and Reggianni, Ruggero, "Combined modulation and coding for continuous phase FSK with nonuniform alphabet," *IEEE Transactions on Communications*, 41(8), pp. 1201 –1207, August 1993.

(McGeehan and Bateman, 1984)

McGeehan, J. and Bateman, A., "Phase-lock transparent tone-in-band (TTIB): A new spectrum configuration particularly suited to the transmission of data over SSB mobile radio networks," *IEEE Transactions on Communications*, COM-32, pp. 81-87, January 1984.

(McLane *et al*, 1988)

McLane, P.J., Wittke, P.H., Ho, P.K.M. and Loo, C. (1988), "PSK and DPSK Trellis Codes for Fast Fading, Shadowed Mobile Satellite Communication Channels," *IEEE Transactions on Communications*, 36, pp. 1242-1246, November 1988.

(Molisch *et al*, 1997)

Molisch, A.F., Lopes, L.B., Paier, M., Fuhl, J. and Bonek, E., "Error floor of unequalised wireless personal communications systems with MSK modulation and training-sequence-based adaptive sampling," *IEEE Transaction on Communications*, 45(5), pp. 554-562, May 1997.

(Molisch *et al*, 1998)

Molisch, A.F. and Bonek, E., "Reduction of error floor of differential PSK in mobile radio channels by adaptive sampling," *IEEE Transaction on Vehicular Technology*, 47(4), pp. 1276-1280, Nov. 1998.

(Morales-Moreno *et al*, 1988)

Morales-Moreno, F., Holubowicz, W. and Pasupathy, S., "Performance of Trellis Encoded Tamed Frequency Modulation," *Proce. of 38 th IEEE Vehicular Technology Conference*, Philadelphia, Pennsylvania, USA, pp. 12-17, June 15-17 1988.

(Morales-Moreno *et al*, 1994)

Morales-Moreno, F., Holubowicz, W. and Pasupathy, S., "Optimization of Trellis Coded TFM Via Matched Codes," *IEEE Transaction on Communications*, 42(2/3/4), pp. 1886-1594, Feb./March/April 1994.

(Mouly and Pautet, 1995)

Mouly, M. and Pautet, M. *The GSM system for mobile communications*, Paleiseau, France, 1995.

(Mulligan and Wilson, 1984)

Mulligan, Michael G. and Wilson, Stephen G., "An Improved Algorithm for Evaluating Trellis Phase Codes," *IEEE Transactions on Information Theory*, IT-30(6), pp. 846-850, November 1984.

(Murota and Hirade 1981)

Murota K., and Hirade K., "GMSK Modulation for Digital Mobile Radio Telephony," *IEEE Tran. Commun.*, COM-29(7), pp. 1044-1050, July 1981.

(Pasupathy, 1979)

Pasupathy, S., "Minimum Shift Keying: A Spectrally Efficient Modulation," *IEEE Communications Magazine*, pp. 14-22, July 1979.

(Pieper *et al*, 1978)

Pieper, John F., Proakis, J.G., Reed, Roger R., and Wolf, Jack J., "Design of Efficient Coding and Modulation for a Rayleigh Fading Channel," *IEEE Transactions on Information Theory*, IT-24(4), pp. 457-468, July 1978.

(Pizzi and Wilson, 1985)

Pizzi, S.V. and Wilson, S.G. (1985), "Convolutional Coding Combined with Continuous Phase Modulation," *IEEE Transactions on Communications*, COM-33, pp. 20-29, January 1985.

(Proakis, 1989)

Proakis , J.G., *Digital Communications*, McGraw-Hill, New York, NY, USA, 1989.

(Rimoldi, 1989)

Rimoldi, B., "Design of coded CPFSK modulation systems for bandwidth and energy efficiency," *IEEE Trans. on Communications*, COM-37(9), pp. 897-905, September 1989.

(Schlegel *et al*, 1989)

Schlegel, C. and Costello, Jr., D.J., "Bandwidth Efficient Coding for Fading Channels : Code Construction and Performance Analysis," *IEEE Journal on Selected Areas in Communications*, SAC-7, pp. 1356-1368, December 1989.

(Shwartz *et al*, 1974)

Shwartz, M., Bennett, W. R. and Stein, S., *Communication systems and techniques*, New York: Wiley,1974.

(Simon, 1986)

Simon, M. K., "Dual pilot tone calibration technique," *IEEE Transactions on Vehicular Technology*, VT-35, pp. 63-70, May 1986.

(Simon and Divsalar, 1988)

Simon, M.K. and Divsalar, D., "Performance of Trellis-Coded Multilevel DPSK on a Fading Mobile Satellite Channel," *IEEE Transactions on Vehicular Technology*, 37(2), pp. 78-91, May 1988.

(Sklar, 1988)

Sklar, B., *Digital Communications : Fundamentals and Applications*, Prentice-Hall, Englewood Cliffs, NT, 1988.

(Soliman *et al*, 1992)

Soliman, Samir S. and Mokrani, Karim, "Performance of Coded Systems Over Fading Dispersive Channels," *IEEE Transactions on Communications*, 40(1), 1992, pp. 51-59, January 1992.

(Steele 1992)

Steele R., *Mobile Radio Communications*, Pentech Press, London, 1992.

(Sundberg, 1986)

Sundberg, Carl-Erik, "Continuous Phase Modulation," *IEEE Communications Magazine*, 24(4), pp. 25-38, April 1986.

(Svensson, 1987)

Svensson, N. Arne B., "On Optimum and Suboptimum Coherent Detection of Continuous Phase Modulation on a Two-Ray Multipath Fading Channel," *IEEE Transactions on Communications*, COM-35(10), pp. 1041-1049, October 1987.

(Tellambura and Bhargava, 1995)

Tellambura, C. and Bhargava, V. K., "Performance of GMSK in frequency-selective Rayleigh fading and multiple cochannel interferers," *Proc of Vehicular Technology Conference VT'95*, Chicago, Illinois, USA, pp. 211-215, July 1995.

(Ungerboeck, 1982)

Ungerboeck, G., "Channel Coding with Multilevel/Phase Signals," *IEEE Transactions on Information Theory*, IT-28 (1), pp. 55-67, January 1982.

(Ungerboeck, 1987)

Ungerboeck, G., "Trellis Coded Modulation with Redundant Signal Sets Part 1 : Introduction," *IEEE Communications Magazine*, 25, pp. 5-11, February 1987.

(Ungerboeck, 1987)

Ungerboeck, G., "Trellis Coded Modulation with Redundant Signal Sets Part 11 : State of the Art," *IEEE Communications Magazine*, 25, pp. 12-21, February 1987.

(Varshney and Kumar, 1991)

Varshney, Prabodh and Surinder Kumar, "Performance of GMSK in Land Mobile Radio Channel," *IEEE Transactions on Vehicular Technology*, 40(3), pp. 607-614, August 1991.

(Ventura-Travest *et al*, 1997)

Ventura-Travest, J., Caire, G., Biglieri, E. and Taricco, G., "Impact of diversity reception on fading channels with coded modulation-Part I: Coherent detection," *IEEE Transactions on Communications*, COM-45(5), pp. 563-572, May 1997.

(Viterbi, 1967)

Viterbi, A.J., Error Bounds for Convolutional Codes and an Asymptotically Optimum Decoding Algorithm," *IEEE Transactions on Information Theory*, IT-13, pp. 260-269, April 1967.

(Viterbi, 1991)

Viterbi, A.J., "Wireless Digital Communication : A View Based on Three Lessons Learned," *IEEE Communications Magazine*, 29(9), p. 33, September 1991.

(Viterbi and Omura, 1979)

Viterbi, A.J., and Omura, J.K., *Principles of Digital Communication and Coding*, McGraw-Hill, New York, NY, USA, 1979.

(Wozencraft, 1957)

Wozencraft, J. M., "Sequential decoding for reliable communication," *IRE Natl. Conv. rec.*, Vol. 5, pt. 2, pp.11-25, 1957

(Wozencraft and Jacobs, 1965)

Wozencraft, J.M. and Jacobs, I.M., *Principles of Communication Engineering*, John Wiley, New York, NY, USA, 1965.

(Yiin and Stuber, May 1996)

Yiin, L. and Stuber, G. L., "Error Probability of Coherent Detection for Trellis-Coded Partial Response CPM on Rician Fading Channels," *IEEE Transactions on Vehicular Technology*, 45(2), pp. 358-363, May 1996.

(Yiin and Stuber, August 1996)

Yiin, L. and Stuber, G. L., "Non-coherently Detected Trellis-Coded Partial Response CPM on Mobile Radio Channels," *IEEE Transactions on Communications*, Vol 44, pp. 967-975, August 1996.

(Yiin and Stuber, 1997)

Yiin, L. and Stuber, G. L., "MLSE and Soft-output Equalisation for Trellis-Coded CPM on Mobile," *IEEE Transactions on Communications*, 45(6), pp. 651-659, June 1997.

APPENDIX A

THE UPPERBOUND OF P_E IN TERMS OF X_L AND X'_L

Let X_L be the transmitted sequence of length L. Then, the probability of occurrence of an error event X'_L of length L, can be expressed as given in Eq. (5.5) as

$$P_E(L, X'_L, X_L) = P[X_L]\, P(X'_L|\, X_L) \tag{A.1}$$

where $P[X_L]$ is the probability of transmitting X_L.

Now, when the transmitted sequence is X_L, the probability of occurrence of an any error event of length L, i.e., $P_E(L, X_L)$, becomes the sum of $P_E(L, X'_L, X_L)$ over all the possible X'_Ls of length L. That is,

$$P_E(L, X_L) = \sum_{X'_L \neq X_L} P_E(L, X'_L, X_L). \tag{A.2}$$

Similarly, when any sequence of length L is transmitted, the probability of occurrence of an any error event of length L, $P_E(L)$, can be expressed as

$$P_E(L) = \sum_{X'_L \neq X_L} P_E\left(L, X'_L, \left[X_L^{(1)} \cup X_L^{(2)} \cup X_L^{(3)} ..... \cup X_L^{(2^L)}\right]\right) \tag{A.3}$$

where $X_L^{(1)}, X_L^{(2)}$...are the possible transmitted sequences of length L. From the relationship, as given in (Lathi, 1995)

$$P(A \cup B) = P(A) + P(B) - P(A \cap B) \leq P(A) + P(B).$$

Consequently, Eq. (A.3) can be simplified to

$$\begin{aligned} P_E(L) &\leq \sum_{X'_L \neq X_L} \left[P_E\left(L, X'_L, X_L^{(1)}\right) + P_E\left(L, X'_L, X_L^{(2)}\right) + ... + P_E\left(L, X'_L, X_L^{(2^L)}\right)\right] \\ &\leq \sum_{X'_L \neq X_L} \sum_{X_L} P_E(L, X'_L, X_L). \end{aligned} \tag{A.5}$$

Therefore, the upperbound of the probability of occurrence of an error event of any length can be expressed as

$$P_E \leq \sum_{L=1}^{\infty} \sum_{X_L} \sum_{X'_L \neq X_L} P_E(L, X'_L, X_L). \tag{A.6}$$

Substituting Eq. (A.1) in Eq. (A.6), the upperbound of the error probability of an error event of any length can be expressed as

$$P_E \leq \sum_{L=1}^{\infty} \sum_{X_L} \sum_{X'_L \neq X_L} P[X_L]\, P(X'_L | X_L). \qquad \text{(A.7)}$$

APPENDIX B

SIMPLIFICATION OF $\exp[-\Delta_\lambda(x_k, x'_k)]$ FOR AN AWGN CHANNEL

The quantity $\exp[-\Delta_\lambda(x_k, x'_k)]$ is defined in Eq. (5.12) as

$$\exp[-\Delta_\lambda(x_k, x'_k)] = E\left\{\exp\left[\lambda\left(m(y_k, x'_k) - m(y_k, x_k)\right)\right] \middle| X_L\right\} . \tag{B.1}$$

As $x_k \in X_L$, using the decoding metrics corresponding to the correct and the incorrect sequences, $\exp[-\Delta_\lambda(x_k, x'_k)]$ for a given transmitted sequence X_L can be expressed as given in Eq. (5.16), i.e.,

$$\exp[-\Delta_\lambda(x_k, x'_k)] = E\left\{\exp\left[\lambda'\left(-|y_k - x'_k|^2 + |y_k + x_k|^2\right)\right]\right\}. \tag{B.2}$$

The complex random variables x_k, x'_k, and n_k can be represented in the quadrature forms as

$$x_k = \exp(j\phi_k) = (\cos\phi_k + j\sin\phi_k) = x_{rk} + j\,x_{ik} \tag{B.3a}$$

$$x'_k = \exp(j\phi'_k) = (\cos\phi'_k + j\sin\phi'_k) = x'_{rk} + j\,x'_{ik} \tag{B.3b}$$

and $$n_k = \exp(j\phi_{nk}) = (\cos\phi_{nk} + j\sin\phi_{nk}) = n_{rk} + j\,n_{ik} \tag{B.3c}$$

where ϕ_k, ϕ'_k and ϕ_{nk} are the phase angles corresponding to the transmitted signal, the incorrectly detected signal, and the Gaussian noise, at time k, respectively. The real and imaginary parts of the transmitted signal at time k are the x_{rk} and x_{ik}, respectively.

By applying Eq. (B.3a) and Eq. (B.3c), the received signal y_k as given in Eq. (5.13), can be expressed as

$$y_k = (\cos\phi_k + j\sin\phi_k) + (\cos\phi_{nk} + j\sin\phi_{nk}). \tag{B.4}$$

As a result,

$$-|y_k - x_k|^2 = -|\cos\phi_{nk} + j\sin\phi_{nk}|^2 = -[(n_{rk})^2 + (n_{ik})^2]. \tag{B.5a}$$

From Eq. (B.4) and Eq. (B.3b), we obtain

$$-|y_k - x'_k|^2 = -[(\cos\phi_k - \cos\phi'_k) + \cos\phi_{nk}]^2 - [(\sin\phi_k - \sin\phi'_k) + \sin\phi_{nk}]^2$$

$$= -[(x_{rk} - x'_{rk} + n_{rk})^2 + (x_{ik} - x'_{ik} + n_{ik})^2]. \tag{B.5b}$$

Substituting Eq. (B.5a) and Eq. (B.5b), in Eq. (B.2), we obtain

$$\exp[-\Delta_\lambda(x_k,x'_k)] = E\left\{\exp\left[-\lambda'\left[(x_{rk}-x'_{rk}+n_{rk})^2+(x_{ik}-x'_{ik}+n_{ik})^2-(n_{rk})^2-(n_{ik})^2\right]\right]\right\},$$

$$= E\left\{\exp\left[-\lambda'\left[(x_{rk}-x'_{rk})^2+2(n_{rk})(x_{rk}-x'_{rk})+(x_{ik}-x'_{ik})^2+2(n_{ik})(x_{ik}-x'_{ik})\right]\right]\right\}, \quad \text{(B.6a)}$$

From Eq. (B.3a) and Eq. (B.3b), we have

$$(x_{rk}-x'_{rk})^2+(x_{ik}-x'_{ik})^2 = |x_k - x'_k|^2 \quad \text{(B.6b)}$$

As a result, Eq. (B.6a) can be expressed as

$$\exp[-\Delta_\lambda(x_k,x'_k)] = \exp\left(-\lambda'|x_k-x'_k|^2\right)E\left\{\exp\left[-2\lambda'\left[(n_{rk})(x_{rk}-x'_{rk})+(n_{ik})(x_{ik}-x'_{ik})\right]\right]\right\} \quad \text{(B.7)}$$

As the real and imaginary parts, n_{rk} and n_{ik}, of the complex noise n_k are independent Gaussian random variables, the expectation of Eq. (B.7) may then be expanded as

$$E\left\{\exp\left[-2\lambda'\left[(n_{rk})(x_{rk}-x'_{rk})+(n_{ik})(x_{ik}-x'_{ik})\right]\right]\right\} =$$

$$\int_{-\infty}^{+\infty}\int_{-\infty}^{+\infty}\left\{\exp\left[-2\lambda'\left[(n_{rk})(x_{rk}-x'_{rk})+(n_{ik})(x_{ik}-x'_{ik})\right]\right]\right\}p(n_{ik})p(n_{rk})\mathrm{d}n_{ik}\mathrm{d}n_{rk} \quad \text{(B.8)}$$

where,

$$p(n_{ik}) = \frac{1}{\sqrt{2\pi\sigma_K^2}}\exp\left(\frac{-n_{ik}^2}{2\sigma_k^2}\right) \text{ and } p(n_{rk}) = \frac{1}{\sqrt{2\pi\sigma_K^2}}\exp\left(\frac{-n_{rk}^2}{2\sigma_k^2}\right).$$

Consequently, Eq. (B.8) becomes

$$E\left\{\exp\left[-2\lambda'\left[(n_{rk})(x_{rk}-x'_{rk})+(n_{ik})(x_{ik}-x'_{ik})\right]\right]\right\}$$

$$= \frac{1}{\sqrt{2\pi\sigma_K^2}}\int_{-\infty}^{+\infty}\exp\left\{-\left[\frac{n_{rk}}{\sqrt{2\sigma_K^2}}+\sqrt{2\sigma_K^2}\lambda'(x_{rk}-x'_{rk})\right]^2\right\}\exp\left[2\sigma_K^2\lambda'^2(x_{rk}-x'_{rk})^2\right]\mathrm{d}n_{rk}$$

$$\frac{1}{\sqrt{2\pi\sigma_K^2}}\int_{-\infty}^{+\infty}\exp\left\{-\left[\frac{n_{ik}}{\sqrt{2\sigma_K^2}}+\sqrt{2\sigma_K^2}\lambda'(x_{ik}-x'_{ik})\right]^2\right\}\exp\left[2\sigma_K^2\lambda'^2(x_{ik}-x'_{ik})^2\right]\mathrm{d}n_{ik} \quad \text{(B.9)}$$

As

$$\frac{1}{\sqrt{2\pi\sigma_K^2}}\exp\left\{-\left[\frac{n_{rk}}{\sqrt{2\sigma_K^2}}+\sqrt{2\sigma_K^2}\,\lambda'(x_{rk}-x'_{rk})\right]^2\right\}$$

and

$$\frac{1}{\sqrt{2\pi\sigma_K^2}}\exp\left\{-\left[\frac{n_{rk}}{\sqrt{2\sigma_K^2}}+\sqrt{2\sigma_K^2}\,\lambda'(x_{rk}-x'_{rk})\right]^2\right\}$$

have the form of Gaussian pdf, the following integrals can be expressed as

$$\frac{1}{\sqrt{2\pi\sigma_K^2}}\int_{-\infty}^{+\infty}\exp\left\{-\left[\frac{n_{rk}}{\sqrt{2\sigma_K^2}}+\sqrt{2\sigma_K^2}\,\lambda'(x_{rk}-x'_{rk})\right]^2\right\}dn_{rk}=1,$$

and

$$\frac{1}{\sqrt{2\pi\sigma_K^2}}\int_{-\infty}^{+\infty}\exp\left\{-\left[\frac{n_{ik}}{\sqrt{2\sigma_K^2}}+\sqrt{2\sigma_K^2}\,\lambda'(x_{ik}-x'_{ik})\right]^2\right\}dn_{ik}=1.$$

Thus, Eq. (B.9) reduces to

$$E\{\exp[-2\lambda'[(n_{rk})(x_{rk}-x'_{rk})+(n_{ik})(x_{ik}-x'_{ik})]]\}=\exp\left\{2\sigma_K^2\lambda'^2\left[(x_{rk}-x'_{rk})^2+(x_{ik}+x'_{ik})^2\right]\right\} \quad \text{(B.10)}$$

By applying the relationship of Eq. (B.6b), Eq. (B.10) can be expressed as

$$E\{\exp[-2\lambda'[(n_{rk})(x_{rk}-x'_{rk})+(n_{ik})(x_{ik}-x'_{ik})]]\}=\exp\left(2\sigma_K^2\lambda'^2|x_k-x'_k|^2\right) \quad \text{(B.11)}$$

Finally, with Eq. (B.11), Eq. (B.7) becomes

$$\exp[-\Delta_\lambda(x_k, x'_k)]=\exp\left(-\lambda'|x_k-x'_k|^2\right)\exp\left(2\sigma_K^2\lambda'^2|x_k-x'_k|^2\right). \quad \text{(B.12)}$$

APPENDIX C

SIMPLIFICATION OF $\exp[-\Delta_\lambda(x_k, x'_k)]_{fading}$ FOR AN AMPLITUDE FADING CHANNEL

The quantity $\exp[-\Delta_\lambda(x_k, x'_k)]_{fading}$ is defined in Eq. (5.35) as

$$\exp[-\Delta_\lambda(x_k, x'_k)]_{fading} = E\left\{\exp\left[\lambda'\left(-|y_k - \rho_k x'_k|^2 + |y_k - \rho_k x_k|^2\right)\right] \middle| X_L\right\} . \quad \text{(C.1)}$$

Since $x_k \in X_L$, $\exp[-\Delta_\lambda(x_k, x'_k)]_{fading}$ for a given transmitted sequence X_L can be expressed as

$$\exp[-\Delta_\lambda(x_k, x'_k)]_{fading} = E\left\{\exp\left[\lambda'\left(-|y_k - \rho_k x'_k|^2 + |y_k - \rho_k x_k|^2\right)\right]\right\} . \quad \text{(C.2)}$$

As x_k, x'_k, and n_k are complex random variables, they can be represented in the quadrature forms as given in Eq. (B.3a) to (B.3c). Consequently, the received signal y_k over an amplitude fading channel as given in Eq. (5.29b), can be expressed as

$$y_k = \rho_k(\cos\phi_k + j\sin\phi_k) + (\cos\phi_{nk} + j\sin\phi_{nk}). \quad \text{(C.3)}$$

As a result,

$$-|y_k - \rho_k x_k|^2 = -|\cos\phi_{nk} + j\sin\phi_{nk}|^2 = -[(n_{rk})^2 + (n_{ik})^2] \quad \text{(C.4a)}$$

and

$$\begin{aligned} -|y_k - \rho_k x'_k|^2 &= -[\rho_k(\cos\phi_k - \cos\phi'_k) + \cos\phi_{nk}]^2 - [\rho_k(\sin\phi_k - \sin\phi'_k) + \sin\phi_{nk}]^2 \\ &= -\{[\rho_k(x_{rk} - x'_{rk}) + n_{rk}]^2 + [\rho_k(x_{ik} - x'_{ik}) + n_{ik}]^2\}. \end{aligned} \quad \text{(C.4b)}$$

From Eq. (C.4a) and Eq. (C.4b), Eq. (C.2) may be expressed as

$$\exp[-\Delta_\lambda(x_k, x'_k)]_{fading}$$

$$= E\left\{\exp\left[-\lambda'\left[(\rho_k(x_{rk} - x'_{rk}) + n_{rk})^2 + (\rho_k(x_{ik} - x'_{ik}) + n_{ik})^2 - (n_{rk})^2 - (n_{ik})^2\right]\right]\right\}$$

$$=$$

$$E\left\{\exp\left[-\lambda'\left[\rho_k^2(x_{rk} - x'_{rk})^2 + 2(n_{rk})\rho_k(x_{rk} - x'_{rk}) + \rho_k^2(x_{ik} - x'_{ik})^2 + 2(n_{ik})\rho_k(x_{ik} - x'_{ik})\right]\right]\right\}$$

(C.5)

As shown in Eq. (B.6b),

$$(x_{rk} - x'_{rk})^2 + (x_{ik} + x'_{ik})^2 = |x_k - x'_k|^2$$

As a result, Eq. (C.5) can be expressed as

$$\exp[-\Delta_\lambda(x_k, x'_k)]_{fading}$$
$$= \exp\left(-\lambda'\rho_k^2|x_k - x'_k|^2\right) E\{\exp[-2\lambda'\rho_k[(n_{rk})(x_{rk} - x'_{rk}) + (n_{ik})(x_{ik} - x'_{ik})]]\} \quad \text{(C.6)}$$

As shown in Eq. (B.8), the statistical expectation operation in Eq. (C.6) can be obtained using the pdf of Gaussian noise as

$$E\{\exp[-2\lambda'\rho_k[(n_{rk})(x_{rk} - x'_{rk}) + (n_{ik})(x_{ik} - x'_{ik})]]\} = \exp\left(2\sigma_K^2\lambda'^2\rho_k^2|x_k - x'_k|^2\right) \quad \text{(C.7)}$$

Thus, by applying the relationship of Eq. (C.7) in Eq. (C.5), we obtain

$$\exp[-\Delta_\lambda(x_k, x'_k)]_{fading} = \exp\left(-\lambda'\rho_k|x_k - x'_k|^2\right)\exp\left(2\sigma_K^2\lambda'^2\rho_k^2|x_k - x'_k|^2\right). \quad \text{(C.8)}$$

APPENDIX D

MATRIX TRANSFER FUNCTION OF THE ERROR STATE DIAGRAM OF THE TRELLIS CODED SCHEME HAVING CONSTRAINT LENGTH 2

The branch matrix labels t_1, t_2, ..., t_7 of the error state diagram of the combined coded scheme having constraint length 2, may be expressed as shown in Section 5.2.3 and Section 5.3.1 as

$$t_1 = \frac{1}{2}\alpha_1 J\begin{bmatrix}1 & 1\\ 1 & 1\end{bmatrix} = t_5 \qquad \text{(D.1)}$$

where $\alpha_1 = D^2$ for an AWGN channel,

and $\alpha_1 = \{1+2Z\}^{-1}$ for an amplitude-fading channel,

with $D = \exp\left(\frac{-E_b}{4N_0}\right)$, and $Z = \left(\frac{E_b}{4N_0}\right)$.

$$t_2 = \frac{1}{2}\alpha_2 J\begin{bmatrix}1 & 1\\ 1 & 1\end{bmatrix} = t_6 \qquad \text{(D.2)}$$

where $\alpha_2 = D^{0.152}$ for an AWGN channel,

and $\alpha_2 = \{1+0.152Z\}^{-1}$ for an amplitude-fading channel.

$$t_3 = \frac{1}{2}\begin{bmatrix}\alpha_3 & \alpha_3\\ \alpha_4 & \alpha_4\end{bmatrix} = t_4 \qquad \text{(D.3)}$$

where $\alpha_3 = D^{1.59}$ for an AWGN channel,

$\alpha_3 = \{1+1.59Z\}^{-1}$ for an amplitude-fading channel,

$\alpha_4 = D^{2.152}$ for an AWGN channel,

and $\alpha_4 = \{1+2.152Z\}^{-1}$ for an amplitude-fading channel.

$$\text{and } t_7 = \frac{1}{2}\begin{bmatrix}1 & 1\\ 1 & 1\end{bmatrix}. \qquad \text{(D.4)}$$

As a result, the matrix transfer functions ξ_i from node (**0**) to node (**i**), where (i=1,4), may be expressed as given in Eq. (5.63a) to (5.63d) as

$$\xi_1 = t_1 + \xi_3 t_5 \quad \text{(D.5a)}$$

$$\xi_2 = \xi_2 t_6 + \xi_1 t_2 \quad \text{(D.5b)}$$

$$\xi_3 = \xi_2 t_3 + \xi_1 t_4 \quad \text{(D.5c)}$$

and $$\xi_4 = \mathbf{G} = \xi_3 t_7. \quad \text{(D.5d)}$$

Using Eq. (D.1), Eq. (D.5a) may be expressed as

$$\xi_1 = \frac{1}{2}\alpha_1 J[1 + \xi_3]\begin{bmatrix}1 & 1\\ 1 & 1\end{bmatrix}. \quad \text{(D.6a)}$$

Substituting Eq. (D.2) and Eq. (D.6a) in Eq. (D.5b),we obtain

$$\xi_2 = \frac{1}{2}\alpha_1 J[1 + \xi_3]\begin{bmatrix}1 & 1\\ 1 & 1\end{bmatrix}\frac{1}{2}\alpha_2 J\begin{bmatrix}1 & 1\\ 1 & 1\end{bmatrix} + \xi_2 \frac{1}{2}\alpha_2 J\begin{bmatrix}1 & 1\\ 1 & 1\end{bmatrix}. \quad \text{(D.6b)}$$

Eq. (D.6b) may be re-written as

$$\xi_2\left[\begin{bmatrix}1 & 0\\ 0 & 1\end{bmatrix} - \frac{1}{2}\alpha_2 J\begin{bmatrix}1 & 1\\ 1 & 1\end{bmatrix}\right] = \frac{1}{2}\alpha_1\alpha_2 J^2[1+\xi_3]\begin{bmatrix}1 & 1\\ 1 & 1\end{bmatrix}. \quad \text{(D.6c)}$$

Let,

$$\left[\begin{bmatrix}1 & 0\\ 0 & 1\end{bmatrix} - \frac{1}{2}\alpha_2 J\begin{bmatrix}1 & 1\\ 1 & 1\end{bmatrix}\right] = [P].$$

As $[P][P]^{-1} = \begin{bmatrix}1 & 0\\ 0 & 1\end{bmatrix}$, ξ_2 may be obtained by multiplying both sides of Eq. (D.6c) by $[P]^{-1}$, then

$$\xi_2 = \frac{1}{2}\alpha_1\alpha_2 J^2[1+\xi_3]\begin{bmatrix}1 & 1\\ 1 & 1\end{bmatrix}\left[\begin{bmatrix}1 & 0\\ 0 & 1\end{bmatrix} - \frac{1}{2}\alpha_2 J\begin{bmatrix}1 & 1\\ 1 & 1\end{bmatrix}\right]^{-1}. \quad \text{(D.6d)}$$

Now, $[P]^{-1}$ may be expressed as

$$\left[\begin{bmatrix}1 & 0\\ 0 & 1\end{bmatrix} - \frac{1}{2}\alpha_2 J\begin{bmatrix}1 & 1\\ 1 & 1\end{bmatrix}\right]^{-1} = \frac{-1}{\left(1-\frac{1}{2}\alpha_2 J\right)^2 - \left(-\frac{1}{2}\alpha_2 J\right)^2}\begin{bmatrix}-\left(1-\frac{1}{2}\alpha_2 J\right) & \left(-\frac{1}{2}\alpha_2 J\right)\\ \left(-\frac{1}{2}\alpha_2 J\right) & -\left(1-\frac{1}{2}\alpha_2 J\right)\end{bmatrix}$$

$$= \frac{1}{(1-\alpha_2 J)}\begin{bmatrix}\left(1-\frac{1}{2}\alpha_2 J\right) & \left(\frac{1}{2}\alpha_2 J\right)\\ \left(\frac{1}{2}\alpha_2 J\right) & \left(1-\frac{1}{2}\alpha_2 J\right)\end{bmatrix}. \qquad \text{(D.6e)}$$

Substituting Eq. (D.6e) in Eq. (D.6d), ξ_2 may be expressed as

$$\xi_2 = \frac{1}{2}\frac{\alpha_1\alpha_2 J^2}{(1-\alpha_2 J)}[1+\xi_3]\begin{bmatrix}1 & 1\\ 1 & 1\end{bmatrix}\begin{bmatrix}\left(1-\frac{1}{2}\alpha_2 J\right) & \left(\frac{1}{2}\alpha_2 J\right)\\ \left(\frac{1}{2}\alpha_2 J\right) & \left(1-\frac{1}{2}\alpha_2 J\right)\end{bmatrix}$$

$$= \frac{1}{2}\frac{\alpha_1\alpha_2 J^2}{(1-\alpha_2 J)}[1+\xi_3]\begin{bmatrix}1 & 1\\ 1 & 1\end{bmatrix}. \qquad \text{(D.6f)}$$

Using the expressions obtained for ξ_1 and ξ_2, Eq. (D.5c) may now be expressed as

$$\xi_3 = \frac{1}{2}\frac{\alpha_1\alpha_2 J^2}{(1-\alpha_2 J)}[1+\xi_3]\begin{bmatrix}1 & 1\\ 1 & 1\end{bmatrix}\frac{1}{2}\begin{bmatrix}\alpha_3 & \alpha_3\\ \alpha_4 & \alpha_4\end{bmatrix}$$

$$+ \frac{1}{2}\alpha_1 J\,[1+\xi_3]\begin{bmatrix}1 & 1\\ 1 & 1\end{bmatrix}\frac{1}{2}\begin{bmatrix}\alpha_3 & \alpha_3\\ \alpha_4 & \alpha_4\end{bmatrix}. \qquad \text{(D.6g)}$$

Eq. (D.6g) can be re-written as

$$\xi_3\begin{bmatrix}1 & 0\\ 0 & 1\end{bmatrix} = \frac{1}{2}\frac{\alpha_1\alpha_2 J^2}{(1-\alpha_2 J)}[1+\xi_3]\frac{1}{2}(\alpha_3+\alpha_4)\begin{bmatrix}1 & 1\\ 1 & 1\end{bmatrix} + \frac{1}{2}\alpha_1 J[1+\xi_3]\frac{1}{2}(\alpha_3+\alpha_4)\begin{bmatrix}1 & 1\\ 1 & 1\end{bmatrix}$$

$$= \frac{\left(\alpha_1\alpha_2 J^2 + \alpha_1 J - \alpha_1\alpha_2 J^2\right)}{2(1-\alpha_2 J)}\frac{1}{2}(\alpha_3+\alpha_4)[1+\xi_3]\begin{bmatrix}1 & 1\\ 1 & 1\end{bmatrix}$$

$$= \frac{\alpha_1 J}{2(1-\alpha_2 J)}\frac{1}{2}(\alpha_3+\alpha_4)[1+\xi_3]\begin{bmatrix}1 & 1\\ 1 & 1\end{bmatrix}$$

Now, solving for ξ_3

$$\xi_3\left[\begin{bmatrix}1 & 0\\ 0 & 1\end{bmatrix} - \frac{\alpha_1 J}{2(1-\alpha_2 J)}\frac{1}{2}(\alpha_3+\alpha_4)\begin{bmatrix}1 & 1\\ 1 & 1\end{bmatrix}\right] = \frac{\alpha_1 J}{2(1-\alpha_2 J)}\frac{1}{2}(\alpha_3+\alpha_4)\begin{bmatrix}1 & 1\\ 1 & 1\end{bmatrix} \qquad \text{(D.6h)}$$

Let

$$\left[\begin{bmatrix}1 & 0\\ 0 & 1\end{bmatrix} - \frac{\alpha_1 J}{2(1-\alpha_2 J)}\frac{1}{2}(\alpha_3+\alpha_4)\begin{bmatrix}1 & 1\\ 1 & 1\end{bmatrix}\right] = [Q]$$

As $[Q][Q]^{-1}=\begin{bmatrix}1 & 0\\ 0 & 1\end{bmatrix}$, ξ_3 may be obtained by multiplying both sides of Eq. (D.6h) by $[Q]^{-1}$, then

$$\xi_3 = \frac{\alpha_1 J}{2(1-\alpha_2 J)}\frac{1}{2}(\alpha_3+\alpha_4)\begin{bmatrix}1 & 1\\ 1 & 1\end{bmatrix}\left[\begin{bmatrix}1 & 0\\ 0 & 1\end{bmatrix}-\frac{\alpha_1 J}{2(1-\alpha_2 J)}\frac{1}{2}(\alpha_3+\alpha_4)\begin{bmatrix}1 & 1\\ 1 & 1\end{bmatrix}\right]^{-1} \qquad \text{(D.6i)}$$

Now, $[Q]^{-1}$ may be expressed as

$$[Q]^{-1} = \left[\begin{bmatrix}1 & 0\\ 0 & 1\end{bmatrix}-\frac{\alpha_1 J}{2(1-\alpha_2 J)}\frac{1}{2}(\alpha_3+\alpha_4)\begin{bmatrix}1 & 1\\ 1 & 1\end{bmatrix}\right]^{-1} = \frac{-1}{(1-Y)^2-(-Y)^2}\begin{bmatrix}-(1-Y) & (-Y)\\ (-Y) & -(1-Y)\end{bmatrix}$$

where, $Y = \left[\frac{\alpha_1 J}{2(1-\alpha_2 J)}\frac{1}{2}(\alpha_3+\alpha_4)\right]$.

Eq. (D.6i) now simplifies to

$$\xi_3 = \frac{Y}{(1-2Y)}\begin{bmatrix}1 & 1\\ 1 & 1\end{bmatrix}\begin{bmatrix}(1-Y) & Y\\ Y & (1-Y)\end{bmatrix} = \frac{Y}{(1-2Y)}\begin{bmatrix}1 & 1\\ 1 & 1\end{bmatrix} \qquad \text{(D.6j)}$$

Substituting for Y, Eq (D.6j) simplifies to provide ξ_3 as

$$\xi_3 = \frac{1}{2}\frac{\alpha_1 J(\alpha_3+\alpha_4)}{[2-2\alpha_2 J-\alpha_1 J(\alpha_3+\alpha_4)]}\begin{bmatrix}1 & 1\\ 1 & 1\end{bmatrix}. \qquad \text{(D.6k)}$$

Substituting the expression obtained for ξ_3 in Eq. (D.5d), the matrix transfer function $\mathbf{G}$ of the combined coded scheme having constraint length 2 may be expressed as

$$\mathbf{G} = \frac{1}{2}\frac{\alpha_1 J(\alpha_3+\alpha_4)}{[2-2\alpha_2 J-\alpha_1 J(\alpha_3+\alpha_4)]}\begin{bmatrix}1 & 1\\ 1 & 1\end{bmatrix}\frac{1}{2}\begin{bmatrix}1 & 1\\ 1 & 1\end{bmatrix}$$

$$= \frac{1}{2}\frac{\alpha_1 J(\alpha_3+\alpha_4)}{[2-2\alpha_2 J-\alpha_1 J(\alpha_3+\alpha_4)]}\begin{bmatrix}1 & 1\\ 1 & 1\end{bmatrix}.$$

Substituting for α_1, α_2, α_3, and α_4 as given in Eq. (D.1) to (D.3), the matrix transfer function $\mathbf{G}$ of the combined coded scheme having constraint length 2 over an AWGN channel can be expressed as

$$\mathbf{G} = \frac{1}{2}\frac{D^2 J\left(D^{1.59} + D^{2.152}\right)}{\left[2 - 2D^{0.152}J - D^2 J\left(D^{1.59} + D^{2.152}\right)\right]}\begin{bmatrix}1 & 1\\ 1 & 1\end{bmatrix}. \qquad \text{(D.7a)}$$

Similarly, the matrix transfer function **G** of the combined coded scheme having constraint length 2 for an amplitude-fading channel can be expressed as

$$\mathbf{G} = \frac{1}{2}\frac{[1+2Z]^{-1}J([1+1.59Z]^{-1} + [1+2.152Z]^{-1})}{[2 - 2[1+0.152Z]^{-1}J - [1+2Z]^{-1}J([1+1.59Z]^{-1} + [1+2.152Z]^{-1})]}\begin{bmatrix}1 & 1\\ 1 & 1\end{bmatrix}. \qquad \text{(D.7b)}$$

APPENDIX E

MATRIX TRANSFER FUNCTION OF THE ERROR STATE DIAGRAM OF THE TRELLIS CODED SCHEME HAVING CONSTRAINT LENGTH 3

The branch matrix labels t_1, t_2, ..., t_{15} of the error state diagram of the combined coded scheme having constraint length 3, may be expressed as shown in Section 5.2.3 and Section 5.3.4 as

$$t_1 = \frac{1}{2}\beta_1 J\begin{bmatrix}1 & 1\\ 1 & 1\end{bmatrix} = t_8, \qquad \text{(E.1)}$$

where $\beta_1 = D^2$ for an AWGN channel,

and $\beta_1 = \{1+2Z\}^{-1}$ for an amplitude-fading channel,

with $D = \exp\left(\frac{-E_b}{4N_0}\right)$, and $Z = \left(\frac{E_b}{4N_0}\right)$.

$$t_2 = \frac{1}{2}J\begin{bmatrix}1 & 1\\ 1 & 1\end{bmatrix} = t_{11}. \qquad \text{(E.2)}$$

$$t_3 = \frac{1}{2}\beta_2\begin{bmatrix}1 & 1\\ 1 & 1\end{bmatrix} = t_{10}, \qquad \text{(E.3)}$$

where $\beta_2 = D^2$ for an AWGN channel,

and $\beta_2 = \{1+2Z\}^{-1}$ for a channel with amplitude-fading.

$$t_4 = \frac{1}{2}\begin{bmatrix}\beta_3 & \beta_3\\ \beta_4 & \beta_4\end{bmatrix} = t_{13}, \qquad \text{(E.4)}$$

where $\beta_3 = D^{1.59}$ for an AWGN channel,

$\beta_3 = \{1+1.59Z\}^{-1}$ for an amplitude-fading channel,

$\beta_4 = D^{2.152}$ for an AWGN channel,

and $\beta_4 = \{1+2.152Z\}^{-1}$ for an amplitude-fading channel.

Now, the matrices ξ_i, where (i=1,8), may be represented using their elements as

$$\xi_1 = \begin{bmatrix} a_{11} & a_{12} \\ a_{13} & a_{14} \end{bmatrix}; \qquad \xi_2 = \begin{bmatrix} a_{21} & a_{22} \\ a_{23} & a_{24} \end{bmatrix};$$

$$\xi_3 = \begin{bmatrix} a_{31} & a_{32} \\ a_{33} & a_{34} \end{bmatrix}; \qquad \xi_4 = \begin{bmatrix} a_{41} & a_{42} \\ a_{43} & a_{44} \end{bmatrix};$$

$$\xi_5 = \begin{bmatrix} a_{51} & a_{52} \\ a_{53} & a_{54} \end{bmatrix}; \qquad \xi_6 = \begin{bmatrix} a_{61} & a_{62} \\ a_{63} & a_{64} \end{bmatrix};$$

and $\xi_7 = \begin{bmatrix} a_{71} & a_{72} \\ a_{73} & a_{74} \end{bmatrix}$.

Substituting for ξ_1 and ξ_7, Eq. (E.9a) can be expressed as

$$\begin{bmatrix} a_{11} & a_{12} \\ a_{13} & a_{14} \end{bmatrix} - \frac{1}{2}\beta_1 J \begin{bmatrix} a_{71} & a_{72} \\ a_{73} & a_{74} \end{bmatrix} \begin{bmatrix} 1 & 1 \\ 1 & 1 \end{bmatrix} = \frac{1}{2}\beta_1 J \begin{bmatrix} 1 & 1 \\ 1 & 1 \end{bmatrix}. \qquad \text{(E.10)}$$

Expansion of Eq. (E.10) results in

$$\begin{aligned} a_{11} - \frac{1}{2}\beta_1 J\{a_{71} + a_{72}\} &= \frac{1}{2}\beta_1 J, \\ a_{12} - \frac{1}{2}\beta_1 J\{a_{71} + a_{72}\} &= \frac{1}{2}\beta_1 J, \\ a_{13} - \frac{1}{2}\beta_1 J\{a_{73} + a_{74}\} &= \frac{1}{2}\beta_1 J, \\ a_{14} - \frac{1}{2}\beta_1 J\{a_{73} + a_{74}\} &= \frac{1}{2}\beta_1 J. \end{aligned} \qquad \text{(E.10a)}$$

From the set of equations in Eq. (E.10a), it can be seen that, $a_{11} = a_{12}$ and $a_{13} = a_{14}$.

Similarly, Eq. (E.9b) can be expressed using the elements of the matrices ξ_1, ξ_2, and ξ_5 as

$$\begin{bmatrix} a_{21} & a_{22} \\ a_{23} & a_{24} \end{bmatrix} - \frac{1}{2}\beta_2 \begin{bmatrix} a_{11} & a_{12} \\ a_{13} & a_{14} \end{bmatrix} \begin{bmatrix} 1 & 1 \\ 1 & 1 \end{bmatrix} - \frac{1}{2}\beta_2 \begin{bmatrix} a_{51} & a_{52} \\ a_{53} & a_{54} \end{bmatrix} \begin{bmatrix} 1 & 1 \\ 1 & 1 \end{bmatrix} = 0. \qquad \text{(E.11)}$$

Now, Eq. (E.11) may be expanded as

$$a_{21} - \frac{1}{2}\beta_2\{a_{11} + a_{12}\} - \frac{1}{2}\beta_2\{a_{51} + a_{52}\} = 0,$$

$$a_{22} - \frac{1}{2}\beta_2\{a_{11} + a_{12}\} - \frac{1}{2}\beta_2\{a_{51} + a_{52}\} = 0,$$

$$a_{23} - \frac{1}{2}\beta_2\{a_{13} + a_{14}\} - \frac{1}{2}\beta_2\{a_{53} + a_{54}\} = 0,$$

$$a_{24} - \frac{1}{2}\beta_2\{a_{13} + a_{14}\} - \frac{1}{2}\beta_2\{a_{53} + a_{54}\} = 0. \qquad \text{(E.11a)}$$

From the set of equations in Eq. (E.11a), it can be seen that, $a_{21} = a_{22}$ and $a_{23} = a_{24}$.

Similarly, using the elements of the matrices ξ_1, ξ_3, and ξ_5, Eq. (E.9c) may be expressed as

$$\begin{bmatrix} a_{31} & a_{32} \\ a_{33} & a_{34} \end{bmatrix} - \frac{1}{2}J\begin{bmatrix} a_{11} & a_{12} \\ a_{13} & a_{14} \end{bmatrix}\begin{bmatrix} 1 & 1 \\ 1 & 1 \end{bmatrix} - \frac{1}{2}J\begin{bmatrix} a_{51} & a_{52} \\ a_{53} & a_{54} \end{bmatrix}\begin{bmatrix} 1 & 1 \\ 1 & 1 \end{bmatrix} = 0. \qquad \text{(E.12)}$$

The Eq. (E.12) can be expanded as

$$a_{31} - \frac{1}{2}J\{a_{11} + a_{12}\} - \frac{1}{2}J\{a_{51} + a_{52}\} = 0,$$

$$a_{32} - \frac{1}{2}J\{a_{11} + a_{12}\} - \frac{1}{2}J\{a_{51} + a_{52}\} = 0,$$

$$a_{33} - \frac{1}{2}J\{a_{13} + a_{14}\} - \frac{1}{2}J\{a_{53} + a_{54}\} = 0,$$

$$a_{34} - \frac{1}{2}J\{a_{13} + a_{14}\} - \frac{1}{2}J\{a_{53} + a_{54}\} = 0. \qquad \text{(E.12a)}$$

From the set of expressions in Eq. (E.12a), it may be seen that $a_{31} = a_{32}$ and $a_{33} = a_{34}$.

Similarly, using the elements of the matrices ξ_i, where (i=1,8), the following simplifications to the equations (E.9d) to (E.9h), can be obtained. The expansion of Eq. (E.9d) results in

$$a_{41} - \frac{1}{2}J\{a_{41}\beta_7 + a_{42}\beta_8\} - \frac{1}{2}J\{a_{31}\beta_7 + a_{32}\beta_8\} = 0,$$

$$a_{42} - \frac{1}{2}J\{a_{41}\beta_7 + a_{42}\beta_8\} - \frac{1}{2}J\{a_{31}\beta_7 + a_{32}\beta_8\} = 0,$$

$$a_{43} - \frac{1}{2}J\{a_{43}\beta_7 + a_{44}\beta_8\} - \frac{1}{2}J\{a_{33}\beta_7 + a_{34}\beta_8\} = 0,$$

$$a_{44} - \frac{1}{2}J\{a_{43}\beta_7 + a_{44}\beta_8\} - \frac{1}{2}J\{a_{33}\beta_7 + a_{34}\beta_8\} = 0. \qquad \text{(E.13)}$$

It may be seen from the above set of expressions in Eq. (E.13), that $a_{41} = a_{42}$ and $a_{43} = a_{44}$.

Similarly, the expansion of Eq. (E.9e) results in

$$a_{51} - \frac{1}{2}\beta_5 J\{a_{21} + a_{22}\} - \frac{1}{2}\beta_5 J\{a_{61} + a_{62}\} = 0,$$

$$a_{52} - \frac{1}{2}\beta_5 J\{a_{21} + a_{22}\} - \frac{1}{2}\beta_5 J\{a_{61} + a_{62}\} = 0,$$

$$a_{53} - \frac{1}{2}\beta_5 J\{a_{23} + a_{24}\} - \frac{1}{2}\beta_5 J\{a_{63} + a_{64}\} = 0,$$

$$a_{54} - \frac{1}{2}\beta_5 J\{a_{23} + a_{24}\} - \frac{1}{2}\beta_5 J\{a_{63} + a_{64}\} = 0. \qquad \text{(E.14)}$$

From the above set of equations in Eq. (E.14), it may be seen that $a_{51} = a_{52}$ and $a_{53} = a_{54}$.

Similarly, Eq. (E.9f) may be expanded as

$$a_{61} - \frac{1}{2}\beta_6\{a_{31} + a_{32}\} - \frac{1}{2}\beta_6\{a_{41} + a_{42}\} = 0,$$

$$a_{62} - \frac{1}{2}\beta_6\{a_{31} + a_{32}\} - \frac{1}{2}\beta_6\{a_{41} + a_{42}\} = 0,$$

$$a_{63} - \frac{1}{2}\beta_6\{a_{33} + a_{34}\} - \frac{1}{2}\beta_6\{a_{43} + a_{44}\} = 0,$$

$$a_{64} - \frac{1}{2}\beta_6\{a_{33} + a_{34}\} - \frac{1}{2}\beta_6\{a_{43} + a_{44}\} = 0. \qquad \text{(E.15)}$$

This results in $a_{61} = a_{62}$ and $a_{63} = a_{64}$.

Similarly, expanding Eq. (E.9g) as

$$a_{71} - \frac{1}{2}\{a_{21}\beta_3 + a_{22}\beta_4\} - \frac{1}{2}\{a_{61}\beta_3 + a_{62}\beta_4\} = 0,$$

$$a_{72} - \frac{1}{2}\{a_{21}\beta_3 + a_{22}\beta_4\} - \frac{1}{2}\{a_{61}\beta_3 + a_{62}\beta_4\} = 0,$$

$$a_{73} - \frac{1}{2}\{a_{23}\beta_3 + a_{24}\beta_4\} - \frac{1}{2}\{a_{63}\beta_3 + a_{64}\beta_4\} = 0,$$

$$a_{74} - \frac{1}{2}\{a_{23}\beta_3 + a_{24}\beta_4\} - \frac{1}{2}\{a_{63}\beta_3 + a_{64}\beta_4\} = 0. \qquad \text{(E.16)}$$

From the set of expressions in Eq. (E.16), it may be seen that $a_{71} = a_{72}$ and $a_{73} = a_{74}$.

Using the above simplifications, the set of Equations given in Eq. (E.10a), Eq. (E11a), Eq. (E.12a), and Equations (E.13) to (E.16) can be expressed as

$$a_{11} - \beta_1 J\{a_{71}\} = \frac{1}{2}\beta_1 J,$$

$$a_{13} - \beta_1 J\{a_{73}\} = \frac{1}{2}\beta_1 J,$$

$$a_{21} - \beta_2\{a_{11}\} - \beta_2\{a_{51}\} = 0,$$

$$a_{23} - \beta_2\{a_{13}\} - \beta_2\{a_{53}\} = 0,$$

$$a_{31} - J\{a_{11}\} - J\{a_{51}\} = 0,$$

$$a_{33} - J\{a_{13}\} - J\{a_{53}\} = 0,$$

$$a_{41} - \frac{1}{2}J\{a_{41}\}\{\beta_7 + \beta_8\} - \frac{1}{2}J\{a_{31}\}\{\beta_7 + \beta_8\} = 0,$$

$$a_{43} - \frac{1}{2}J\{a_{43}\}\{\beta_7 + \beta_8\} - \frac{1}{2}J\{a_{33}\}\{\beta_7 + \beta_8\} = 0,$$

$$a_{51} - \beta_5 J\{a_{21}\} - \beta_5 J\{a_{61}\} = 0,$$

$$a_{53} - \beta_5 J\{a_{23}\} - \beta_5 J\{a_{63}\} = 0,$$

$$a_{61} - \beta_6\{a_{31}\} - \beta_6\{a_{41}\} = 0,$$

$$a_{63} - \beta_6\{a_{33}\} - \beta_6\{a_{43}\} = 0,$$

$$a_{71} - \frac{1}{2}\{a_{21}\}\{\beta_3 + \beta_4\} - \frac{1}{2}\{a_{61}\}\{\beta_3 + \beta_4\} = 0,$$

$$a_{73} - \frac{1}{2}\{a_{23}\}\{\beta_3 + \beta_4\} - \frac{1}{2}\{a_{63}\}\{\beta_3 + \beta_4\} = 0. \qquad \text{(E.17)}$$

The above set of 14 linear equations in Eq. (E.17) may now be written in the form as [A] $\underline{X}$ = $\underline{B}$ where [A] is a 14×14 square matrix of known coefficients. $\underline{B}$ and $\underline{X}$ are column vectors having known and unknown coefficients, respectively.

The matrix [A] and the vectors $\underline{B}$ and $\underline{X}$ have the form,

[A] =

$$\begin{bmatrix}
1 & 0 & 0 & 0 & 0 & 0 & 0 & 0 & 0 & 0 & 0 & 0 & -\beta_1 J & 0 \\
0 & 1 & 0 & 0 & 0 & 0 & 0 & 0 & 0 & 0 & 0 & 0 & 0 & -\beta_1 J \\
-\beta_2 & 0 & 1 & 0 & 0 & 0 & 0 & 0 & -\beta_2 & 0 & 0 & 0 & 0 & 0 \\
0 & -\beta_2 & 0 & 1 & 0 & 0 & 0 & 0 & 0 & -\beta_2 & 0 & 0 & 0 & 0 \\
-J & 0 & 0 & 0 & 1 & 0 & 0 & 0 & -J & 0 & 0 & 0 & 0 & 0 \\
0 & -J & 0 & 0 & 0 & 1 & 0 & 0 & 0 & -J & 0 & 0 & 0 & 0 \\
0 & 0 & 0 & 0 & m_1 & 0 & m_2 & 0 & 0 & 0 & 0 & 0 & 0 & 0 \\
0 & 0 & 0 & 0 & 0 & m_1 & 0 & m_2 & 0 & 0 & 0 & 0 & 0 & 0 \\
0 & 0 & -\beta_5 J & 0 & 0 & 0 & 0 & 0 & 1 & 0 & -\beta_5 J & 0 & 0 & 0 \\
0 & 0 & 0 & -\beta_5 J & 0 & 0 & 0 & 0 & 0 & 1 & 0 & -\beta_5 J & 0 & 0 \\
0 & 0 & 0 & 0 & -\beta_6 & 0 & -\beta_6 & 0 & 0 & 0 & 1 & 0 & 0 & 0 \\
0 & 0 & 0 & 0 & 0 & -\beta_6 & 0 & -\beta_6 & 0 & 0 & 0 & 1 & 0 & 0 \\
0 & 0 & m_3 & 0 & 0 & 0 & 0 & 0 & 0 & 0 & m_3 & 0 & 1 & 0 \\
0 & 0 & 0 & m_3 & 0 & 0 & 0 & 0 & 0 & 0 & 0 & m_3 & 0 & 1
\end{bmatrix}$$

where m_1=-$\frac{1}{2}J\{\beta_7 + \beta_8\}$; m_2=1-$\frac{1}{2}J\{\beta_7 + \beta_8\}$ and m_3= -$\frac{1}{2}\{\beta_3 + \beta_4\}$.

and $\underline{X}$ = $\begin{bmatrix} a_{11} \\ a_{13} \\ a_{21} \\ a_{23} \\ a_{31} \\ a_{33} \\ a_{41} \\ a_{43} \\ a_{51} \\ a_{53} \\ a_{61} \\ a_{63} \\ a_{71} \\ a_{73} \end{bmatrix}$ and $\underline{B}$ = $\begin{bmatrix} 0.5\beta_1 J \\ 0.5\beta_1 J \\ 0 \\ 0 \\ 0 \\ 0 \\ 0 \\ 0 \\ 0 \\ 0 \\ 0 \\ 0 \\ 0 \\ 0 \end{bmatrix}$

From the matrix [A], and the vectors $\underline{X}$ and $\underline{B}$, it may be seen that, the set of 14 linear equations in Eq. (E.17) may be written in the form as,

$$[A1]\ \underline{X1} = \underline{B1} \qquad \text{(E.18a)}$$

and

$$[A1]\ \underline{X2} = \underline{B1} \qquad \text{(E.18b)}$$

$$\text{where [A1]} = \begin{bmatrix} 1 & 0 & 0 & 0 & 0 & 0 & -\beta_1 J \\ -\beta_2 & 1 & 0 & 0 & -\beta_2 & 0 & 0 \\ -J & 0 & 1 & 0 & -J & 0 & 0 \\ 0 & 0 & m_1 & m_2 & 0 & 0 & 0 \\ 0 & -\beta_5 J & 0 & 0 & 1 & -\beta_5 J & 0 \\ 0 & 0 & -\beta_6 & -\beta_6 & 0 & 1 & 0 \\ 0 & m_3 & 0 & 0 & 0 & m_3 & 1 \end{bmatrix}$$

$$\text{and } \underline{X1} = \begin{bmatrix} a_{11} \\ a_{21} \\ a_{31} \\ a_{41} \\ a_{51} \\ a_{61} \\ a_{71} \end{bmatrix} \quad \underline{X2} = \begin{bmatrix} a_{13} \\ a_{23} \\ a_{33} \\ a_{43} \\ a_{53} \\ a_{63} \\ a_{73} \end{bmatrix} \quad \text{and} \quad \underline{B1} = \begin{bmatrix} 0.5\beta_1 J \\ 0 \\ 0 \\ 0 \\ 0 \\ 0 \\ 0 \end{bmatrix}$$

From Eq. (E.18a) and Eq. (E.18b), it may also be seen that $\underline{X1} = \underline{X2}$. As a result, $a_{11} = a_{13}$, $a_{21} = a_{23}$, $a_{31} = a_{33}$, $a_{41} = a_{43}$, $a_{51} = a_{53}$, $a_{61} = a_{63}$ and $a_{71} = a_{73}$. Accordingly, the number of linear equations in Eq. (E.17) reduces to 7 from 14.

Substituting Eq. (E.8) in Eq. (E.9h), the matrix transfer function **G** of the error state diagram of the combined coded scheme having constraint length 3, may be expressed as

$$\mathbf{G} = \begin{bmatrix} a_{71} & a_{72} \\ a_{73} & a_{74} \end{bmatrix} \frac{1}{2} \begin{bmatrix} 1 & 1 \\ 1 & 1 \end{bmatrix}$$

As shown above, $a_{71} = a_{72} = a_{73} = a_{74}$ resulting in

$$\mathbf{G} = a_{71} \begin{bmatrix} 1 & 1 \\ 1 & 1 \end{bmatrix} \frac{1}{2} \begin{bmatrix} 1 & 1 \\ 1 & 1 \end{bmatrix} = a_{71} \begin{bmatrix} 1 & 1 \\ 1 & 1 \end{bmatrix} \qquad \text{(E.19)}$$

Accordingly, the matrix transfer function **G** of the error state diagram of the combined coded scheme having constraint length 3, can be obtained by solving for a_{71}. The solution for a_{71} has been reached using the elementary row operations to Eq. (E.18a), as shown below.

Eq. (E.18a) can be expressed as

$$\begin{bmatrix} 1 & 0 & 0 & 0 & 0 & 0 & -\beta_1 J \\ -\beta_2 & 1 & 0 & 0 & -\beta_2 & 0 & 0 \\ -J & 0 & 1 & 0 & -J & 0 & 0 \\ 0 & 0 & m_1 & m_2 & 0 & 0 & 0 \\ 0 & -\beta_5 J & 0 & 0 & 1 & -\beta_5 J & 0 \\ 0 & 0 & -\beta_6 & -\beta_6 & 0 & 1 & 0 \\ 0 & m_3 & 0 & 0 & 0 & m_3 & 1 \end{bmatrix} \begin{bmatrix} a_{11} \\ a_{21} \\ a_{31} \\ a_{41} \\ a_{51} \\ a_{61} \\ a_{71} \end{bmatrix} = \begin{bmatrix} 0.5\beta_1 J \\ 0 \\ 0 \\ 0 \\ 0 \\ 0 \\ 0 \end{bmatrix}.$$

In applying the elementary row operations, the above can be expressed as

$$\left[\begin{array}{ccccccc|c} 1 & 0 & 0 & 0 & 0 & 0 & -\beta_1 J & 0.5\beta_1 J \\ -\beta_2 & 1 & 0 & 0 & -\beta_2 & 0 & 0 & 0 \\ -J & 0 & 1 & 0 & -J & 0 & 0 & 0 \\ 0 & 0 & m_1 & m_2 & 0 & 0 & 0 & 0 \\ 0 & -\beta_5 J & 0 & 0 & 1 & -\beta_5 J & 0 & 0 \\ 0 & 0 & -\beta_6 & -\beta_6 & 0 & 1 & 0 & 0 \\ 0 & m_3 & 0 & 0 & 0 & m_3 & 1 & 0 \end{array}\right]$$

Now, applying the elementary row operations to row 5 as

$$\text{row } 5 \Rightarrow \frac{\text{row } 2}{\beta_2} + \text{row } 5$$

$$\left[\begin{array}{ccccccc|c} 1 & 0 & 0 & 0 & 0 & 0 & -\beta_1 J & 0.5\beta_1 J \\ -\beta_2 & 1 & 0 & 0 & -\beta_2 & 0 & 0 & 0 \\ -J & 0 & 1 & 0 & -J & 0 & 0 & 0 \\ 0 & 0 & m_1 & m_2 & 0 & 0 & 0 & 0 \\ -1 & \left(\frac{1}{\beta_2} - \beta_5 J\right) & 0 & 0 & 0 & -\beta_5 J & 0 & 0 \\ 0 & 0 & -\beta_6 & -\beta_6 & 0 & 1 & 0 & 0 \\ 0 & m_3 & 0 & 0 & 0 & m_3 & 1 & 0 \end{array}\right]$$

Now, row $5 \Rightarrow \left(\frac{\text{row } 5}{-\beta_5 J}\right) m_3 -$ row 7 results in

$$\left[\begin{array}{cccccccc|c}
1 & 0 & 0 & 0 & 0 & 0 & -\beta_1 J & 0.5\beta_1 J \\
-\beta_2 & 1 & 0 & 0 & -\beta_2 & 0 & 0 & 0 \\
-J & 0 & 1 & 0 & -J & 0 & 0 & 0 \\
0 & 0 & m_1 & m_2 & 0 & 0 & 0 & 0 \\
\left(\frac{m_3}{\beta_5 J}\right) & \left[\frac{-m_3}{\beta_5 J}\left(\frac{1}{\beta_2}-\beta_5 J\right)-m_3\right] & 0 & 0 & 0 & 0 & -1 & 0 \\
0 & 0 & -\beta_6 & -\beta_6 & 0 & 1 & 0 & 0 \\
0 & m_3 & 0 & 0 & 0 & m_3 & 1 & 0
\end{array}\right]$$

Let, $\left[-\frac{m_3}{\beta_5 J}\left(\frac{1}{\beta_2}-\beta_5 J\right)-m_3\right] = s_3$. Applying row $2 \Rightarrow \left(\frac{\text{row } 2}{-\beta_2}\right) J +$ row 3 gives

$$\left[\begin{array}{cccccccc|c}
1 & 0 & 0 & 0 & 0 & 0 & -\beta_1 J & 0.5\beta_1 J \\
0 & \left(\frac{-J}{\beta_2}\right) & 1 & 0 & 0 & 0 & 0 & 0 \\
-J & 0 & 1 & 0 & -J & 0 & 0 & 0 \\
0 & 0 & m_1 & m_2 & 0 & 0 & 0 & 0 \\
\left(\frac{m_3}{\beta_5 J}\right) & s_3 & 0 & 0 & 0 & 0 & -1 & 0 \\
0 & 0 & -\beta_6 & -\beta_6 & 0 & 1 & 0 & 0 \\
0 & m_3 & 0 & 0 & 0 & m_3 & 1 & 0
\end{array}\right]$$

Using the operation, $\text{row } 4 \Rightarrow \left(\frac{\text{row } 4}{m_2}\right)\beta_6 + \text{row } 6$ results in

$$\left[\begin{array}{ccccccc|c} 1 & 0 & 0 & 0 & 0 & 0 & -\beta_1 J & 0.5\beta_1 J \\ 0 & \left(\frac{-J}{\beta_2}\right) & 1 & 0 & 0 & 0 & 0 & 0 \\ -J & 0 & 1 & 0 & -J & 0 & 0 & 0 \\ 0 & 0 & \left(\frac{m_1}{m_2}\beta_6 - \beta_6\right) & 0 & 0 & 1 & 0 & 0 \\ \left(\frac{m_3}{\beta_5 J}\right) & s_3 & 0 & 0 & 0 & 0 & -1 & 0 \\ 0 & 0 & -\beta_6 & -\beta_6 & 0 & 1 & 0 & 0 \\ 0 & m_3 & 0 & 0 & 0 & m_3 & 1 & 0 \end{array}\right]$$

Now, applying, $\text{row } 7 \Rightarrow \text{row } 7 - m_3 \times (\text{row } 4)$ yields

$$\left[\begin{array}{ccccccc|c} 1 & 0 & 0 & 0 & 0 & 0 & -\beta_1 J & 0.5\beta_1 J \\ 0 & \left(\frac{-J}{\beta_2}\right) & 1 & 0 & 0 & 0 & 0 & 0 \\ -J & 0 & 1 & 0 & -J & 0 & 0 & 0 \\ 0 & 0 & \left(\frac{m_1}{m_2}\beta_6 - \beta_6\right) & 0 & 0 & 1 & 0 & 0 \\ \left(\frac{m_3}{\beta_5 J}\right) & s_3 & 0 & 0 & 0 & 0 & -1 & 0 \\ 0 & 0 & -\beta_6 & -\beta_6 & 0 & 1 & 0 & 0 \\ 0 & m_3 & -m_3\left(\frac{m_1}{m_2}\beta_6 - \beta_6\right) & 0 & 0 & 0 & 1 & 0 \end{array}\right]$$

Applying the operation row 7 $\Rightarrow$ row $5 - \left(\frac{\text{row 7}}{m_3}\right) s_3$ results in

$$\left[\begin{array}{cccccccc|c}
1 & 0 & 0 & 0 & 0 & 0 & -\beta_1 J & 0.5\beta_1 J \\
0 & \left(\frac{-J}{\beta_2}\right) & 1 & 0 & 0 & 0 & 0 & 0 \\
-J & 0 & 1 & 0 & -J & 0 & 0 & 0 \\
0 & 0 & \left(\frac{m_1}{m_2}\beta_6 - \beta_6\right) & 0 & 0 & 1 & 0 & 0 \\
\left(\frac{m_3}{\beta_5 J}\right) & s_3 & 0 & 0 & 0 & 0 & -1 & 0 \\
0 & 0 & -\beta_6 & -\beta_6 & 0 & 1 & 0 & 0 \\
\left(\frac{m_3}{\beta_5 J}\right) & 0 & s_3\left(\frac{m_1}{m_2}\beta_6 - \beta_6\right) & 0 & 0 & 0 & \left(-1 - \frac{s_3}{m_3}\right) & 0
\end{array}\right]$$

and row 2 $\Rightarrow$ row $5 + \left(\frac{\text{row 2}}{J}\right)\beta_2 s_3$ results in

$$\left[\begin{array}{cccccccc|c}
1 & 0 & 0 & 0 & 0 & 0 & -\beta_1 J & 0.5\beta_1 J \\
\left(\frac{m_3}{\beta_5 J}\right) & 0 & \left(\frac{\beta_2 s_3}{J}\right) & 0 & 0 & 0 & -1 & 0 \\
-J & 0 & 1 & 0 & -J & 0 & 0 & 0 \\
0 & 0 & \left(\frac{m_1}{m_2}\beta_6 - \beta_6\right) & 0 & 0 & 1 & 0 & 0 \\
\left(\frac{m_3}{\beta_5 J}\right) & s_3 & 0 & 0 & 0 & 0 & -1 & 0 \\
0 & 0 & -\beta_6 & -\beta_6 & 0 & 1 & 0 & 0 \\
\left(\frac{m_3}{\beta_5 J}\right) & 0 & s_3\left(\frac{m_1}{m_2}\beta_6 - \beta_6\right) & 0 & 0 & 0 & \left(-1 - \frac{s_3}{m_3}\right) & 0
\end{array}\right]$$

Now, applying, row $2 \Rightarrow \left(\frac{\text{row } 2}{\beta_2}\right) J\left(\frac{m_1}{m_2}\beta_6 - \beta_6\right) - \text{row } 7$ provides

$$\left[\begin{array}{cccccccc|c}
1 & 0 & 0 & 0 & 0 & 0 & -\beta_1 J & 0.5\beta_1 J \\
s_4 & 0 & 0 & 0 & 0 & 0 & s_5 & 0 \\
-J & 0 & 1 & 0 & -J & 0 & 0 & 0 \\
0 & 0 & \left(\frac{m_1}{m_2}\beta_6 - \beta_6\right) & 0 & 0 & 1 & 0 & 0 \\
\left(\frac{m_3}{\beta_5 J}\right) & s_3 & 0 & 0 & 0 & 0 & -1 & 0 \\
0 & 0 & -\beta_6 & -\beta_6 & 0 & 1 & 0 & 0 \\
\left(\frac{m_3}{\beta_5 J}\right) & 0 & s_3\left(\frac{m_1}{m_2}\beta_6 - \beta_6\right) & 0 & 0 & 0 & \left(-1 - \frac{s_3}{m_3}\right) & 0
\end{array}\right]$$

where

$$s_4 = \left\{\left(\frac{m_3}{\beta_5 J}\right)\left(\frac{J}{\beta_2}\right)\left(\frac{m_1}{m_2}\beta_6 - \beta_6\right) - \left(\frac{m_3}{\beta_5 J}\right)\right\},$$

and

$$s_5 = \left\{-\left(\frac{J}{\beta_2}\right)\left(\frac{m_1}{m_2}\beta_6 - \beta_6\right) - \left(-1 - \frac{s_3}{m_3}\right)\right\}.$$

Using the operation, row $1 \Rightarrow (\text{row } 1) \times s_4 - \text{row } 2$ results in

$$\left[\begin{array}{cccccccc|c}
0 & 0 & 0 & 0 & 0 & 0 & \left(-\beta_1 J s_4 - s_5\right) & \left(0.5\beta_1 J s_4\right) \\
s_4 & 0 & 0 & 0 & 0 & 0 & s_5 & 0 \\
-J & 0 & 1 & 0 & -J & 0 & 0 & 0 \\
0 & 0 & \left(\frac{m_1}{m_2}\beta_6 - \beta_6\right) & 0 & 0 & 1 & 0 & 0 \\
\left(\frac{m_3}{\beta_5 J}\right) & s_3 & 0 & 0 & 0 & 0 & -1 & 0 \\
0 & 0 & -\beta_6 & -\beta_6 & 0 & 1 & 0 & 0 \\
\left(\frac{m_3}{\beta_5 J}\right) & 0 & s_3\left(\frac{m_1}{m_2}\beta_6 - \beta_6\right) & 0 & 0 & 0 & \left(-1 - \frac{s_3}{m_3}\right) & 0
\end{array}\right]$$

Now, we have

$$\begin{bmatrix} 0 & 0 & 0 & 0 & 0 & 0 & (-\beta_1 J s_4 - s_5) \\ s_4 & 0 & 0 & 0 & 0 & 0 & s_5 \\ -J & 0 & 1 & 0 & -J & 0 & 0 \\ 0 & 0 & \left(\frac{m_1}{m_2}\beta_6 - \beta_6\right) & 0 & 0 & 1 & 0 \\ \left(\frac{m_3}{\beta_5 J}\right) & s_3 & 0 & 0 & 0 & 0 & -1 \\ 0 & 0 & -\beta_6 & -\beta_6 & 0 & 1 & 0 \\ \left(\frac{m_3}{\beta_5 J}\right) & 0 & s_3\left(\frac{m_1}{m_2}\beta_6 - \beta_6\right) & 0 & 0 & 0 & \left(-1 - \frac{s_3}{m_3}\right) \end{bmatrix} \begin{bmatrix} a_{11} \\ a_{21} \\ a_{31} \\ a_{41} \\ a_{51} \\ a_{61} \\ a_{71} \end{bmatrix} = \begin{bmatrix} (0.5\beta_1 J s_4) \\ 0 \\ 0 \\ 0 \\ 0 \\ 0 \\ 0 \end{bmatrix}.$$

This results in

$$(-\beta_1 J s_4 - s_5) a_{71} = 0.5\beta_1 J s_4 .$$

Now, substituting for s_4 and s_5, a_{71} can be expressed as

$$a_{71} = \frac{1}{2}\beta_1 J \frac{\left\{\left(\frac{-p_1}{2p_2}\right)\left(\frac{p_4 J}{\beta_1}\right) + \left(\frac{p_1}{2p_2}\right)\right\}}{\left\{\left[-\beta_1 J\left\{\left(\frac{-p_1}{2p_2}\right)\left(\frac{p_4 J}{\beta_1}\right) + \left(\frac{p_1}{2p_2}\right)\right\}\right] - \left[\left(\frac{-p_4 J}{\beta_1}\right) - \left(\frac{1}{\beta_1\beta_6 J}\right) + 1\right]\right\}}$$

where, $p_1 = \{\beta_3 + \beta_4\}$; $p_2 = \beta_5 J$; and $p_4 = \frac{-\beta_6}{(m_2)}$.

It may also be seen from Eq. (E.1) to Eq. (E.7), that, $\beta_1 = \beta_2$, $\beta_3 = \beta_8$, $\beta_4 = \beta_7$ and $\beta_5 = \beta_6$. Substituting Eq. (E.19) in Eq. (5.70), the transfer function of the error state diagram $T(D,J)$, can be obtained as

$$T(D,J) = \frac{1}{N} 1^T \mathbf{G}\, \mathbf{1} = 2a_{71}. \qquad \text{(E.20)}$$

Thus, the transfer function $T(D,J)$ of the error state diagram of the combined coded scheme having constraint length 3 becomes

$$T(D,J) = \beta_1 J \frac{\left\{\left(\frac{-p_1}{2p_2}\right)\left(\frac{p_4 J}{\beta_1}\right) + \left(\frac{p_1}{2p_2}\right)\right\}}{\left\{\left[-\beta_1 J\left\{\left(\frac{-p_1}{2p_2}\right)\left(\frac{p_4 J}{\beta_1}\right) + \left(\frac{p_1}{2p_2}\right)\right\}\right] - \left[\left(\frac{-p_4 J}{\beta_1}\right) - \left(\frac{1}{\beta_1\beta_6 J}\right) + 1\right]\right\}} \qquad \text{(E.21)}$$

Now, substituting for p_1, p_2 and p_4 in terms of β_i (i=1,8) Eq. (E.21) can be expressed as

$$T(D,J) = \frac{A_3}{B_3}$$

where

$$A_3 = \frac{(\beta_3+\beta_4)[2\beta_6 J + 2\beta_1 - \beta_1 J(\beta_3+\beta_4)]}{2\beta_6[2-J(\beta_3+\beta_4)]}, \qquad \text{(E.22a)}$$

and

$$B_3 = \left\{-\frac{(\beta_3+\beta_4)[2\beta_6 J + 2\beta_1 - \beta_1 J(\beta_3+\beta_4)]}{2\beta_6[2-J(\beta_3+\beta_4)]} - \frac{2\beta_6 J}{\beta_1[2-J(\beta_3+\beta_4)]} + \frac{1}{\beta_1\beta_6 J} - 1\right\} \qquad \text{(E.22b)}$$

Substituting for the corresponding values of β_i (i=1,8) in Eq. (E.22a) and (E.22b), the transfer functions of the error state diagram representing the trellis coded scheme having constraint length 3 for an AWGN channel and an amplitude fading channel have been obtained.

Now, the partial derivative of $T(D,J)$ with respect to J can be expressed as

$$\frac{\partial}{\partial J}T(D,J)\Big|_{J=1, D=\exp(-E_b/4N_0)} = \frac{B_3\frac{\partial}{\partial J}(A_3) - A_3\frac{\partial}{\partial J}(B_3)}{(B_3)^2}$$

Differentiating Eq. (E.22a) with respect to J, we obtain

$$\frac{\partial}{\partial J}(A_3) = \frac{2(\beta_3+\beta_4)}{[2-J(\beta_3+\beta_4)]^2} \qquad \text{(E.23)}$$

From Eq. (E.22a) and Eq. (E.22b), it can be seen that

$$B_3 = \left\{-A_3 - \frac{2\beta_6 J}{\beta_1[2-J(\beta_3+\beta_4)]} + \frac{1}{\beta_1\beta_6 J} - 1\right\} \qquad \text{(E.24)}$$

By differentiating Eq. (E.22c) with respect to J, we obtain

$$\frac{\partial}{\partial J}(B_3) = -\frac{\partial}{\partial J}(A_3) + \frac{\partial}{\partial J}\left[-\frac{2\beta_6 J}{\beta_1[2-J(\beta_3+\beta_4)]} + \frac{1}{\beta_1\beta_6 J} - 1\right]$$

$$= -\frac{2(\beta_3+\beta_4)}{[2-J(\beta_3+\beta_4)]^2} - \frac{4\beta_1\beta_6}{\beta_1^2[2-J(\beta_3+\beta_4)]^2} - \frac{1}{\beta_1\beta_6 J^2} \qquad \text{(E.25)}$$

Now, substituting for A_3, B_3, and the partial derivatives of A_3 and B_3 with respect to J, obtained as shown in Eq. (E.22a), Eq.(E.22b), Eq.(E.23) and Eq. (E.25), the partial derivative of $T(D,J)$ with respect to J can be obtained as

$$\frac{\partial}{\partial J}T(D,J)\Big|_{J=1,D=\exp(-E_b/4N_0)} = \frac{A_2}{B_2} \qquad \text{(E.26)}$$

where,

$$A_2 = 2(\beta_3+\beta_4)\{2\beta_1\beta_6[2-(\beta_3+\beta_4)] + \beta_1^2[2-(\beta_3+\beta_4)]^2 + 4\beta_1\beta_6 \qquad \text{(E.27a)}$$

and

$$B_2 = \{[2-(\beta_3+\beta_4)][2-\beta_1^2(\beta_3+\beta_4)] - 4\beta_6^2 - 4\beta_1\beta_6\}^2 \qquad \text{(E.27b)}$$

APPENDIX F

THE GSM PROPAGATION MODELS

(All the information presented here is based on the ETSI Rec. 0.5. 0.5)

The different GSM propagation models for hardware and software simulations are presented in terms of a discrete number of taps having pre-specified individual time delays and average powers. The amplitude of each individual tap is Rayleigh distributed and varies according to a Doppler spectrum $S(\nu)$. Two types of Doppler spectra, namely classical (CLASS) and Rician (Rice), are used in the definition of the GSM models. The CLASS spectrum is given by,

$$S(\nu) = \frac{S(0)}{\sqrt{1-(\nu / f_D)^2}} \quad \text{for } |\nu| < f_D \tag{F.1}$$

where ν is the frequency and f_D represents the maximum Doppler shift.

On the other hand, the RICE spectrum is given by,

$$S(\nu) = \frac{0.41}{2\pi f_D \sqrt{1-(\nu / f_D)^2}} + 0.91\,\delta(\nu - 0.7 f_D) \quad \text{for } |\nu| < f_D \tag{F.2}$$

In addition, there are two equivalent alternative tap settings for each model. These are indicated by (1) and (2), respectively, in the appropriate columns in the tables.

The six-ray propagation channel models, showing the relative path power and the relative time delay corresponding to the tap setting (1), are shown in Fig. F.1.

Tap Number	Relative Time Delay (μs)		Average Relative Power (dB)		Doppler Spectrum
	(1)	(2)	(1)	(2)	
1	0.0	0.0	0.0	0.0	RICE
2	0.1	0.2	-4.0	-2.0	CLASS
3	0.2	0.4	-8.0	-10.0	CLASS
4	0.3	0.6	-12.0	-20.0	CLASS
5	0.4	-	-16.0	-	CLASS
6	0.5	-	-20.0	-	CLASS

Table F.1 Tap settings for the 6-tap rural area (RA) model.

Tap Number	Relative Time Delay (μs)		Average Relative Power (dB)		Doppler Spectrum
	(1)	(2)	(1)	(2)	
1	0.0	0.0	0.0	0.0	CLASS
2	0.1	0.2	-1.5	-2.0	CLASS
3	0.3	0.4	-4.5	-4.0	CLASS
4	0.5	0.6	-7.5	-7.0	CLASS
5	15.0	15.0	-8.0	-6.0	CLASS
6	17.2	17.2	-17.7	-12.0	CLASS

Table F.2 Tap settings for the 6-tap hilly terrain (HT) model.

Tap Number	Relative Time Delay (μs)		Average Relative Power (dB)		Doppler Spectrum
	(1)	(2)	(1)	(2)	
1	0.0	0.0	-3.0	-3.0	CLASS
2	0.2	0.2	0.0	0.0	CLASS
3	0.5	0.6	-2.0	-2.0	CLASS
4	1.6	1.6	-6.0	-6.0	CLASS
5	2.3	2.4	-8.0	-8.0	CLASS
6	5.0	5.0	-10.0	-10.0	CLASS

Table F.3 Tap settings for the 6-tap typical urban area (TU) model.

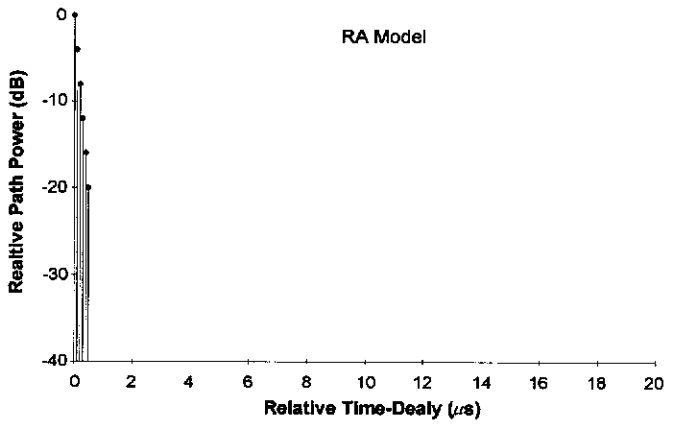

(a)

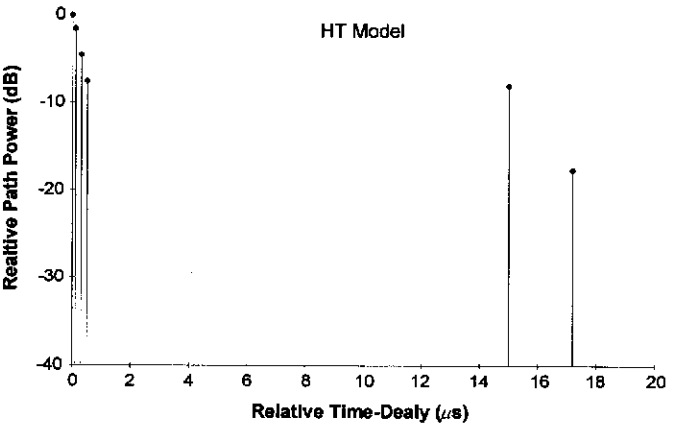

(b)

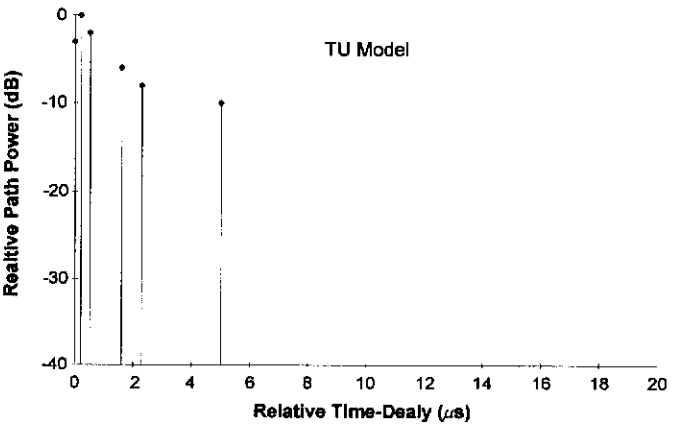

(c)

Figure F.1 The six-ray propagation channel models defined by the GSM for (a) the rural area, (b) the hilly terrain, and (c) the typical urban environment.

APPENDIX G

PUBLICATIONS

The following conference papers have been published on the topics related to this study.

- Caldera, M.K. and Chung, K. S., "Trellis coded GMSK in frequency-selective fading channels," *5th International Symposium on DSP for communication systems, DSPCS'99*, Perth, Scarborough, pp. 5-9, February 1999.

- Caldera, M.K. and Chung, K. S., "Sensitivity to timing and phase errors on trellis coded CPM," *Proc. the 3rd Asia-Pacific Conference on Communications, APCC'97*, Sydney, pp. 518-522, December 1997.

- Caldera, M.K., Chung, K. S. and Razavi, S.H., "Trellis coded CPM using coherent detection," Presented at the *4th International Symposium on communication theory and applications*, Charlotte Mason College, U.K., July 1997.

TRELLIS CODED GMSK IN FREQUENCY SELECTIVE FADING

M. K. Caldera and K. S. Chung
Curtin University of Technology
P O Box U1987 Perth, Western Australia.

ABSTRACT

The bit error rate (BER) performance of trellis coded Gaussian minimum shift keying (GMSK) over two-ray frequency-selective fading channel is investigated. The received signal is detected by coherent demodulation based on adaptive Viterbi decoding. Coding gains of approximately 4.0 dB, 6.0 dB, 6.5 dB and 8.0 dB, at a BER of $1x10^{-2}$, are achieved with trellis coded GMSK for relative delays of 1, 2, 3, and 4 bit periods, respectively, assuming a bit rate of $270.8x10^{3}$ bits/s and a vehicle speed of 50 km/h. Moreover, these coding gains have been obtained with a significant decrease in receiver complexity for the coded scheme.

1. Introduction

The partial response Continuous Phase Modulation (CPM) signals such as GMSK [1], having smooth phase transitions between the successive signalling intervals, produce a narrower spectrum than the full response CPM signals [2]. Moreover, the inherent constant envelope property of CPM signals permits the use of efficient non-linear power amplifiers. In view of the constraints on spectrum availability and transmitter power, CPM signals are good candidates for mobile radio communications.

In general, Trellis Coded Modulation (TCM) schemes are power efficient as a result of improvement in the detection reliability for a given signal-to-noise ratio [3]. The partial response CPM signals, on the other hand, have low spectral occupancy and constant envelope. Thus, the combination of TCM, and partial response CPM, is expected to provide good coding and modulation over channels, which are limited in both bandwidth and transmitter power, such as those encountered in mobile radio communications.

This paper examines the bit-error-rate (BER) performance of GMSK signal, when it is combined with convolutional codes of rate 1/2 and constraint length 2, operating in a two-ray frequency-selective fading channel. The received signal has been detected by coherent demodulation based on adaptive Viterbi decoding. The BER results obtained by extensive computer simulations are presented in Section 4.

2. Trellis Coded GMSK

Fig. 1 shows the block diagram of the trellis coded GMSK model considered in this paper. Here, the input data is encoded using a rate 1/2 convolutional code having a constraint length 2. It has been shown in [4], that the combination of such code with GMSK will produce the largest free Euclidean distance. The connection vectors G_1 and G_2 of this encoder have the form *[1 1]* and *[0 1]*. The octal representation of the generator polynomial of this code is (3,1). The coded sequences of the input data are serially fed to the GMSK modulator, which generates the transmitted signal, $s(t, \alpha)$. The resulting GMSK signal corresponds to a normalised bandwidth (B_0T) of 0.3. The trellis coded GMSK signal is then transmitted through a two-ray frequency-selective fading channel. The received signal, $r(t)$, with Additive White Gaussian Noise (AWGN) is then detected by coherent demodulation based on adaptive Viterbi decoding.

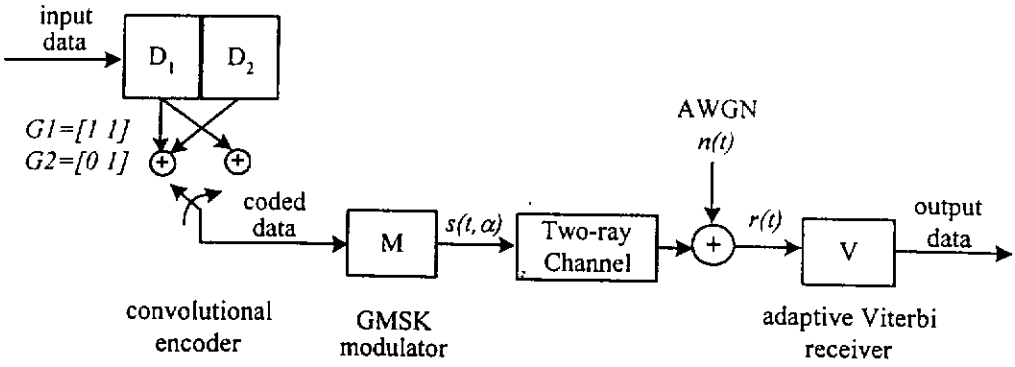

Figure 1 A model of the trellis coded GMSK (B_0T=0.3) scheme

The receiver complexity of the combined coded GMSK signals can be expressed by the number of decoder states in the Viterbi decoder. The number of states representing the combined signal, which corresponds to the number of states in the optimum Viterbi decoder, is the product of the number of states in the convolutional code and the number of states in the GMSK signal. However, the complexity of the receiver can be minimised by precoding the input to the GMSK modulator as shown in Fig. 2 [5]. The transfer function of the binary precoder can be represented by $T(D)=1+D$, i.e. $a_n = b_n \oplus b_{n-1}$, where $\oplus$ denotes modulo-2 addition (or EX-OR operation), b_n is the input to the precoder and a_n is the output of the precoder. D represents a one bit delay.

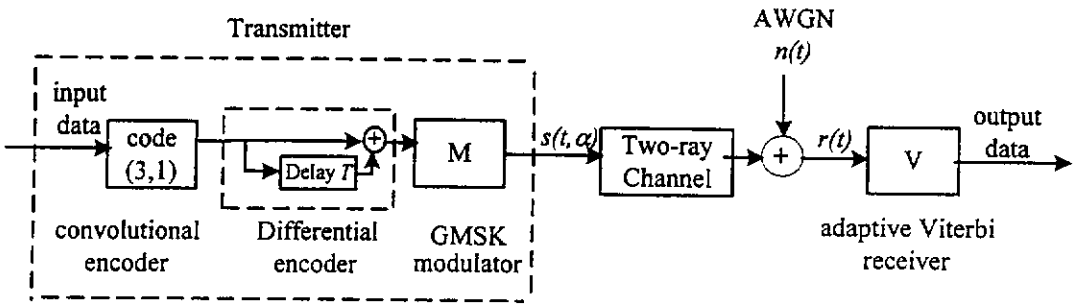

Figure 2 A model of the trellis coded and differentially encoded GMSK (B_0T=0.3) scheme

3. Computer Simulation Model

The model used for computer simulation in this study is based on three functional blocks, namely, the transmitter, the channel and the receiver. The transmitter consists of the convolutional encoder, the differential encoder, and the GMSK modulator as shown in Fig. 2. The transmitted binary data is derived from a pseudorandom sequence generator of length 256 bits, having equiprobable "1"s and "0"s. This binary source digit stream is then encoded by the rate 1/2 convolutional encoder having a constraint length 2, and represented by its generator polynomial as (3,1). This coded data is differentially encoded before applying it to the GMSK (B_0T=0.3) modulator. The resulting trellis coded, and differentially encoded GMSK signal, is transmitted through a two-ray frequency-selective fading channel, having equal path power. The received signal, expressed in the equivalent low-pass in-phase and quadrature components, is first filtered using a low-pass equivalent of a Gaussian band-pass filter having a band-pass bandwidth of BT=0.6. It has been shown in [4], that this bandwidth provides the optimum BER in AWGN. The phase values obtained from the I and Q components of the demodulated signal are used to determine the most likely transmitted sequence using the adaptive Viterbi decoder.

In this paper, the impulse response of the channel, $h(t)$, is assumed to be available, so that the decoder states at the receiver can be modified to account for the Inter-symbol Interference (ISI) introduced by frequency-selective fading. Furthermore, it is assumed that the impulse response of the channel can be estimated within a short training sequence. A training sequence of 26 bits is used in GSM for estimating the adaptive channel impulse response.

The Viterbi decoder has been designed to accommodate a channel delay spread τ of up to 4 bit periods. This range of delay spread is encountered in the GSM systems. In this case, the overall length of the impulse response, associated with the channel and the GMSK modulator, extends over 7 bit periods. Thus, the number of states in the Viterbi decoder representing the uncoded GMSK trellis, consists of 2^7 or 128 states. The phase values representing these 128 states in the Viterbi decoder, corresponding to each of the 7-bit long bit sequences, can be obtained based on the estimated channel impulse response. Furthermore, it has been observed that when the trellis of the rate 1/2 convolutional code (3,1) is combined with the trellis of the differentially encoded GMSK having 128 states, the resultant trellis of the coded scheme can be represented by only 16 states. Consequently, this leads to a large reduction in the receiver complexity of the coded scheme, as compared with the uncoded GMSK.

In the simulation, a training sequence of m bits have been inserted into blocks of n data bits, to account for the need of channel impulse response estimation. This results in a throughput efficiency of $(n/(m+n))\%$. Hence, an update of the channel impulse response is obtained after every $(m+n)$ bit periods. Due to the time varying nature of the channel, a more accurate estimation of the channel impulse response can be provided to the receiver by updating the estimate more often, using a smaller block size. i.e. small values of n. However, a smaller n, will lead to a reduced throughput efficiency. Therefore, a compromise is called for between the throughput efficiency and the accuracy of the channel impulse response estimation. Thus, the effect of throughput efficiency on the BER performance has also been investigated by changing the block size of the data. The average BER of 10^{-2} has been used as a reference for performance comparison in this study. This value is often considered to be adequate for yielding acceptable voice quality in mobile telephony [6].

4. Simulation Results

The simulated irreducible BER curves for the uncoded and the trellis-coded GMSK signals are shown in Fig. 3, for a range of different values of relative delay between the two propagation paths of equal power. It is assumed that the data has been transmitted using two different block sizes, i.e. 256 and 128 data bits, respectively, and a training sequence of 26 bits for channel impulse response estimation. The vehicle speed is assumed to be 50 km/h. The Doppler frequency has been calculated assuming a carrier frequency of 900 MHz and a bit rate of 270.8×10^3 bit/s. In this case, with a block size of 256 bits, the throughput efficiency of the uncoded scheme becomes 90.7%. The number of information bits in a block of 256 coded bits using a rate 1/2 code is 128. Thus, the throughput efficiency of the coded scheme becomes 128/(256+26)%. i.e. 45.4%. Also, when the block size is reduced to 128, the throughput efficiency of the uncoded and coded schemes become 83.1%, and 41.6%, respectively. From the BER curves of Fig. 3, it is observed that the target BER of 10^{-2} for voice traffic can be obtained with both the coded and the uncoded schemes for relative delays up to $4T$. Moreover, the BER curves follow the same pattern for both the block sizes considered. Also, it has been observed, that the improvement in BER performance of the coded scheme is greater when the relative delay between the two rays is increased.

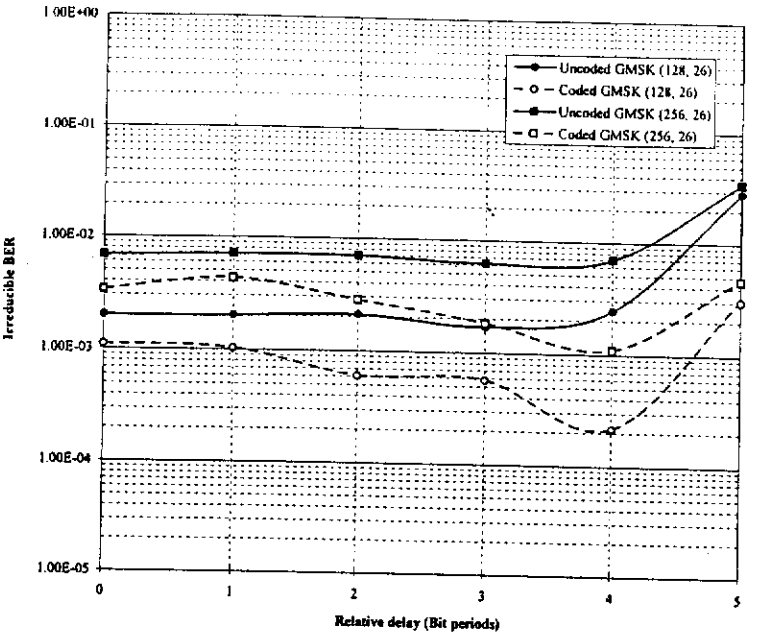

Figure 3 The irreducible BER of uncoded and trellis coded GMSK (B_0T=0.3) for two different lengths of data blocks

The BER curves of the uncoded and the coded schemes obtained are shown in Figures 4 to 7 for different relative delays. For the coded scheme, two different block sizes have been considered. It is observed from these results that the gain achieved at a BER of 10^{-2} is negligible for the shorter of the two block sizes. Moreover, the throughput efficiency is reduced from 45.4% to 41.6% for the shorter block size. From these figures, it has also been observed that, coding gains of approximately 4.0 dB, 6.0 dB, 6.5 dB and 8.0 dB at a BER of 10^{-2}, can be achieved with trellis coded GMSK for relative delays of 1, 2, 3 and 4 bit periods, respectively. Furthermore, these coding gains are obtained, while reducing the receiver complexity from 128 states to 16 states. The maximum coding gain has been obtained when the relative delay between the two rays is 4 bit periods. Also, it has been observed in Fig. 7, that the irreducible BER of the coded scheme in this case is almost 2 orders lower than that of the uncoded scheme.

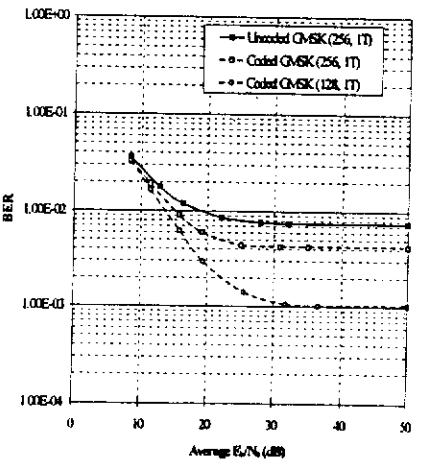

Figure 4 The BER of uncoded and trellis coded GMSK (B_0T=0.3) when the relative delay=1T

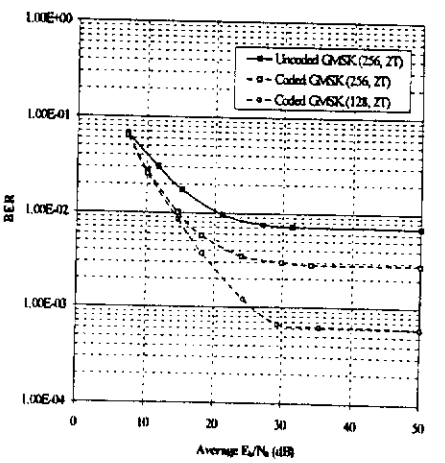

Figure 5 The BER of uncoded and trellis coded GMSK (B_0T=0.3) when the relative delay=2T

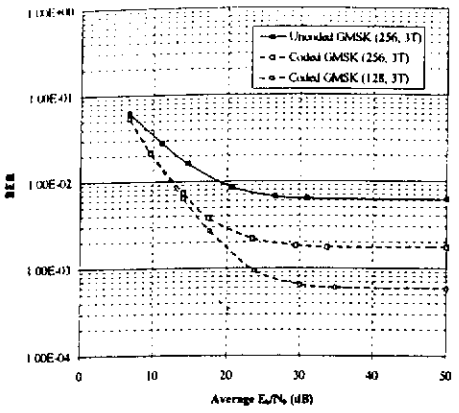

Figure 6 The BER of uncoded and trellis coded GMSK (B_0T=0.3) when the relative delay=$3T$

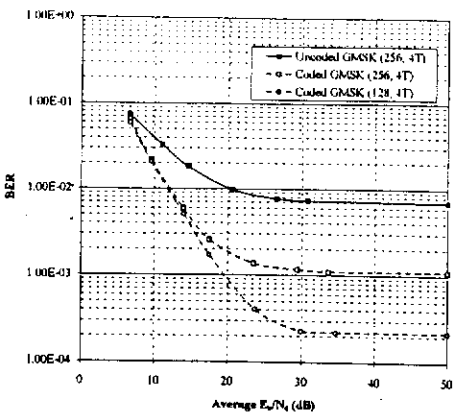

Figure 7 The BER of uncoded and trellis coded GMSK (B_0T=0.3) when the relative delay=$4T$

5. Conclusions

The BER performance of constant envelope partial response CPM, such as GMSK, combined with trellis coding over two-ray frequency-selective fading channel, has been investigated using computer simulations. The received signal is detected using coherent demodulation based on adaptive Viterbi decoding. A training sequence is used to account for the need of channel impulse response estimation, which is required for the operation of the Viterbi algorithm. The Viterbi decoder is designed to accommodate channel delay spreads of up to 4 bit periods. It has been observed that coding gains of approximately 4.0dB, 6.0dB, 6.5dB and 8.0dB, are achieved with trellis coded GMSK at a BER of $1x10^{-2}$, for relative delays of 1, 2, 3, and 4 bit periods, respectively. The Doppler shift has been obtained assuming a bit rate of $270.8x10^3$ bits/s and a vehicle speed of 50 km/h. Furthermore, the coded scheme has shown lower irreducible BERs compared to the uncoded scheme. Moreover, a significant decrease in receiver complexity can be obtained using the coded scheme.

6. References

1. Murota, K. and Hirade, K., "GMSK Modulation for Digital Mobile Telephony," IEEE Trans. on Communications, COM-29, pp. 1044-1050, July 1981.
2. Sundberg, Carl-Erik, "Continuous Phase Modulation," IEEE Communications Magazine, 24(4), pp. 25-38, April 1986.
3. Ungerboeck, G., "Channel Coding with Multilevel/Phase Signals," IEEE Trans. on Information Theory, IT-28(1), pp. 56-57, January 1982.
4. Caldera, M.K., and Chung, K.S., "Sensitivity to Timing and Phase Errors on Trellis Coded CPM," Proc. APCC'97, Sydney, Australia, pp. 518-522, 7-10 Dec. 1997.
5. Morales-Moreno, F., Holubowicz, W. and Pasupathy, S., "Optimisation of Trellis Coded Via Matched Codes," IEEE Trans. on Communications, 42(2/3/4), pp. 1586-1594, Feb./March/April, 1994.
6. D'Avella R., Moreno L., and Sant'Agostino M., "An adaptive MLSE Receiver for TDMA Digital Mobile Radio," IEEE J. Select. Areas Commun, Vol. 7, pp. 122-129, Jan. 1989.

SENSITIVITY TO TIMING AND PHASE ERRORS ON TRELLIS CODED CPM

M. K. Caldera and K. S. Chung
Curtin University of Technology
P O Box U1987 Perth Western Australia

ABSTRACT The bit error rate (BER) performance of constant envelope partial response continuous phase modulation (CPM) such as Gaussian minimum shift keying (GMSK) combined with trellis coded modulation (TCM) over additive white Gaussian noise is investigated. Trellis coded GMSK signal is detected by coherent demodulation based on Viterbi decoding. Coherent detection requires the knowledge of the exact phase of the transmitted carrier at the receiver. However, in practice exact carrier recovery and clock recovery cannot be achieved due to the presence of timing and phase jitters in the system. The proposed study examines the sensitivity of the coherent receiver to timing and phase impairments. The required E_b/N_0 in dB to achieve a BER of $1\text{x}10^{-3}$ of the trellis coded GMSK signal and the uncoded GMSK signal have been obtained under various timing jitters and carrier phase offsets. The results obtained are compared with the uncoded GMSK assuming ideal carrier and clock recoveries at the receiver.

1. INTRODUCTION

Due to constraints on spectrum availability and transmitter power, both bandwidth and power efficient digital modulation techniques are desirable in mobile radio communications. CPM signals have gained attention because of their attractive power spectra. Moreover, the partial response CPM signals such as Gaussian minimum shift keying (GMSK) having smooth phase transitions between the successive signalling intervals produce a narrower spectrum than the full response CPM signals [1,2]. Also, the inherent constant envelope property of CPM signals permits the utilisation of efficient non-linear power amplifiers without causing undesired spectral splashing. On the other hand, TCM schemes could provide better bit error rate performances compared to the uncoded schemes [3]. Therefore, the combination of TCM which improves error probability and partial response CPM signals which yield constant envelope and low spectral occupancy is expected to provide good coding and modulation over bandwidth and power limited channels such as the one encountered in mobile radio communications.

This paper examines the improvement in BER performance of GMSK signal when combined with rate 1/2 trellis coding in an additive Gaussian noise environment. Coherent detection based on Viterbi decoding has been adopted. However, with coherent detection, the carrier recovery becomes essential. Previous studies on coherent detection of GMSK over Gaussian noise channel often assumed exact recovery of the reference carrier and the timing clock [2]. This study examines the effect of timing jitters and the carrier phase offsets on the BER performances.

2. CONTINUOUS PHASE MODULATION (CPM)

In continuous phase modulation, the information carrying phase of the carrier is a continuous function of time. This signal phase continuity is given rise by the correlation between symbols in adjacent signalling intervals. The mathematical representation of a CPM signal has the form [4],

$$s(t,\alpha)=\sqrt{2E/T}\cos(2\pi f_c t+\phi(t,\alpha)+\phi_0) \qquad (1)$$

where E is the symbol energy of the signal, T is the symbol duration, f_c is the carrier frequency, ϕ_0 is an arbitrary constant which represents the initial phase, and it can be set to zero with no loss of generality. $\phi(t,\alpha)$ is the information carrying phase given by,

$$\phi(t,\alpha)=2\pi h\sum_{i=-\infty}^{t=\infty}\alpha_i q(t-iT)$$

$$\text{and}\quad q(t)=\int_{-\infty}^{t} g(\tau)\,d\,\tau \qquad (2)$$

where $\alpha_i = \pm1, \pm3, \pm5, \ldots, \pm(M\text{-}1)$ for M-ary data. This paper considers only binary modulation, so that $\alpha_i = \pm1$. The pulse waveform $q(t)$ determines the phase changes in the signal modulation in response to each data symbol. Normally, the frequency pulse, $g(t)$ is a smooth pulse shape over a finite duration LT, where L is an integer. The shape of $g(t)$ determines the smoothness of the transmitted information carrying phase. The rate of change of the phase or the instantaneous frequency is proportional to the parameter h, which is normally referred to as the modulation index.

By choosing different frequency pulses $g(t)$ and varying the parameters h and M, a variety of CPM schemes can be realised. CPM schemes derived using a frequency pulse $g(t)$ occupying a duration of L symbol intervals greater than one have overlapping pulse shaping. If $L > 1$, then the resulting schemes are referred to as partial response CPM [5,6].

In GMSK, which belongs to the class of partial response CPM scheme, the binary data are filtered by a Gaussian low-pass filter before applying to an FM modulator. The pre-modulation Gaussian filter shapes the data signal to provide a smooth phase variation. This smoothness in phase variation produces a compact spectrum compared to its full response counterparts like Minimum shift keying (MSK) signal. The modulation index of GMSK equals to 0.5. The impulse response of the Gaussian low-pass filter is given by,

$$h(t)=A\sqrt{\frac{2\pi}{\ln 2}}B_0\exp\left\{\frac{-2\pi^2B_0^2t^2}{\ln 2}\right\} \qquad (3)$$

where B_0 is the 3 dB bandwidth and A is a constant. By varying the 3-dB bandwidth of the impulse response of the Gaussian filter, a set of different GMSK signals having different power spectra can be obtained. The frequency pulse $g(t)$ of the GMSK signal has the form,

$$g(t)=\frac{1}{2T}\left[Q\left(2\pi B_0\frac{t-\frac{T}{2}}{\sqrt{\ln 2}}\right)-Q\left(2\pi B_0\frac{t+\frac{T}{2}}{\sqrt{\ln 2}}\right)\right] \quad (4)$$

$$\text{for} \quad 0\le B_0T<\infty$$

$$\text{where} \quad Q(t)=\int_t^{\infty}\frac{1}{\sqrt{2\pi}}e^{-r^2/2}\,dr$$

For GMSK, the duration of the Gaussian phase shaping pulse $g(t)$ is infinite. However, for practical reasons, it can be truncated over several bit periods. When B_0T is equal to 0.25, the GMSK pulse can be truncated symmetrically over 4 bit periods.

3. TRELLIS CODED GMSK

Fig. 1 shows the block diagram of the trellis coded GMSK model considered in this paper. G is a binary convolutional encoder. A convolutional encoder is usually denoted by (n,k,ν). Here the encoder accepting k serial input bits at a given time interval yields n output bits using a ν-stage shift register. For the same code (n,k,ν), there are a large number of equivalent encoders having different structures. A convolutional code can be described by a row vector called the connection vector,

$$G_j=(g_{j1},g_{j2},\ldots,g_{j\nu}), \qquad j=1,2,\ldots,n \quad (5)$$

specifying the connection between the j - th output and each stage of the shift register. The component g_{ji} is equal to 1 if the j th output is connected to stage i: otherwise it is equal to zero. The length of the shift register in the encoder is called the constraint length of the code. Code rate is $R_c=k/n$. In this paper, rate 1/2 convolutional encoders having constraint lengths 2, 3, and 4 have been studied in conjunction with GMSK modulation. The connection vectors G_1 and G_2 of the rate 1/2 convolutional encoders considered in this study having constraint lengths 2, 3, and 4 and their generator polynomials are given in Figs. (2.a), (2.b) and (2.c) respectively.

For the code with constraint length 2, the connection vectors G_1 and G_2 have the form *[1 1]* and *[0 1]*. The octal representation of the generator polynomial of this code is (3,1). Similarly, for the code having constraint length 3, G_1 = *[1 1 1]* and G_2 = *[0 1 1]*; the octal representation of the corresponding generator polynomial is (7,3). The code having a constraint length of 4 considered in the study, has the connection vectors G_1 = *[1 1 0 1]* and G_2 = *[0 1 1 1]*. This can be represented as (15,7) in octal form.

The coded sequences of the input data are then serially fed to the GMSK modulator M, which generates the transmitted signal $s(t,\alpha)$. The signal at the input to the coherent receiver is $r(t)=s(t,\alpha)+n(t)$, where $n(t)$ is additive white Gaussian noise with zero mean and double sided power spectral density $N_0/2$. The coherent receiver consists of quadrature demodulation followed by soft decision Viterbi decoding. The phase values of the received signal obtained from quadrature demodulation are used in the trellis decoder to estimate the most likely transmitted sequence using the Viterbi algorithm.

The receiver complexity of the combined coded CPM signals can be expressed by the number of decoder states in the Viterbi decoder. The number of states representing the combined signal, which is the number of states in the optimum Viterbi decoder, is the product of the number of states in the convolutional code and the number of states in the CPM signal. However, the complexity of the receiver can be minimised by precoding the input to the GMSK modulator as shown in Fig. 3 [7]. The transfer function of the binary precoder can be represented by $T(D)=1+D$, i.e. $\alpha_n=b_n\oplus b_{n-1}$, where $\oplus$ denotes modulo-2 addition (or EX-OR operation), b_n is the input to the precoder and α_n is the output of the precoder. D represents the delay by one bit period.

For example, the GMSK trellis is represented by 8 states. Now, consider the code of constraint length 2 represented in octal form as (3,1), its trellis has 2 states. Thus, when this code is combined with GMSK, the resultant trellis will have 16 states. However, when this constraint length 2 code combines with the differentially encoded GMSK, there is symmetry in the resultant trellis, and the combined trellis can be represented by 4 states. This leads to a reduction in receiver complexity as compared with the case of uncoded GMSK. Similarly, for codes of constraint lengths 3 and 4, their trellises have 4 and 8 states respectively. When these codes are combined with differentially encoded GMSK, the resultant trellises have 8 and 16 states respectively instead of 32 and 64 states in the case of combining with GMSK without differential encoding.

4. SIMULATION MODEL

Computer simulations based on the functional block diagram of Fig. 4 have been used in determining the bit error rate (BER) in the presence of additive white Gaussian noise. The transmitted data, $\{a_n\}$, is derived from a pseudorandom sequence generator of length 256 bits and with equiprobable bits of logical *1* and *0*. This data is encoded by a rate 1/2 convolutional encoder. Here, the rate 1/2 convolutional codes having constraint length 2, 3, and 4 represented by their generator polynomials in octal form as (3,1), (7,3), and (15,7) respectively are used. The coded binary data $\{c_n\}$ is then mapped to the real number inputs $\{b_n\}$ to the differential encoder as *0* $\rightarrow$ *-1* and *1* $\rightarrow$ *+1*. This data $\{b_n\}$ is then differentially encoded before applying to the GMSK modulator. The 3-dB bandwidth of the premodulation Gaussian filter normalised to the bit period is set at 0.25. The GMSK frequency pulse is truncated symmetrically over 4 bit periods and considered zero outside. The additive white Gaussian noise has been simulated according to the Box Muller's transformation. The received signal is filtered using a low pass equivalent of a Gaussian band pass filter. The band pass bandwidth cf this filter normalised to

the bit period is set at 0.6. The filtered signal is then demodulated into its inphase (I) and quadrature (Q) components $\cos(\phi(t))$ and $\sin(\phi(t))$ using a quadrature demodulator with the reference carrier in quadrature. The sampling instants of the I and Q components of the received signal are set at the instants where the eye opening is maximum. The samples of the I and Q components obtained at these sampling instants are then used to compute the phase values. The trellis decoder uses these phase values to determine the most likely transmitted sequence employing the Viterbi algorithm. The BER curves are obtained by comparing the transmitted and the received signals. To ensure the reliability of the simulation results, at least 100 errors have been used to compute the BER for each E_b/N_0 value.

5. SIMULATION RESULTS

Fig. 5 presents the simulated BER results for the uncoded and the trellis coded GMSK signals in the presence of additive white Gaussian noise assuming ideal carrier recovery and timing synchronisation. When compared with the uncoded GMSK schemes at a BER of 10^{-3}, coding gains of 1.7, 2.2, and 3.1 dB have been achieved using codes of constraint lengths 2, 3, and 4 respectively in conjunction with differentially encoded GMSK. Moreover, the number of states in the trellis of the uncoded GMSK scheme is 2, 1, and 1/2 times that of coded scheme for constraint lengths 2, 3, and 4 respectively. Thus, a decrease in receiver complexity has been obtained with the constraint length 2 code while obtaining a coding gain of 1.7 dB.

The sensitivity of the proposed coherent detection scheme to timing and carrier phase offsets has also been investigated. First, the sampling instant has been offset assuming the carrier phase recovery is ideal. Then, the carrier phase errors have been combined assuming no symbol timing error. Finally, the effect of both symbol timing offset and carrier phase errors has been studied. Table 1 tabulates the values of E_b/N_0 required to achieve an error rate of 10^{-3} for uncoded and trellis coded GMSK in the presence of various carrier and timing impairments, including fixed and random variations.

The random timing jitter and the random carrier phase error have been simulated by low pass filtering a set of Gaussian distributed random numbers. Averaging filters have been used to simulate the filtering effect of the carrier and clock recovery loops. The filter bandwidth is varied by changing the number of samples used in the running average. For the bandwidths considered, the peak-to-peak variation of the sampling instant offset of the random jitter is set at $\pm 6T/8$. However, when the bandwidth of the filter is small, the random timing and carrier phase variations are slowly varying and the correlation between the adjacent variations is high.

Using the uncoded GMSK scheme with ideal carrier recovery and timing recovery as the reference, the performance gain at a BER of 10^{-3} for coded and uncoded schemes in the presence of various timing and carrier phase offsets are tabulated in Table 2. When the sampling instant offset is $\pm T/4$, the BER performance of uncoded GMSK is degraded by 0.90 dB, whereas trellis coded GMSK signals with codes of constraint lengths 2, 3, and 4 achieved respective gains of 1.4 dB, 1.90 dB and 2.80 dB in performance under the same conditions. When the sampling instant suffers from random jitter with an rms offset of $\pm T/4$, the performance degradation of all the signals considered is increased. The results under timing offsets show that the uncoded GMSK signal is much more sensitive to sampling instant offsets than the coded GMSK signals considered, provided that the carrier recovery is ideal having no phase errors. Also, both uncoded and trellis coded GMSK signals studied are more sensitive to random errors than the fixed errors due to the large peak-to-peak variations that could be encountered in the case of random errors.

Even at the worst fixed carrier phase offset considered ($\pm 18^0$), the coded schemes with codes of constraint lengths 2, 3, and 4 have shown respective gains of 1.10 dB, 1.40 dB and 2.15 dB in performance while the uncoded scheme has shown a degradation of more than 5 dB. The effect of random phase error has shown a severe reduction of the performance (more than 10 dB) of the uncoded GMSK signal. Also, the coded schemes have shown a degradation in performance under these conditions. It has been observed from these results that the coded signals are more tolerant to carrier phase offset than the uncoded signal. Moreover, the effect of random carrier phase error is more severe on the performance of both coded and uncoded schemes considered than the fixed phase error. This is due to the much higher peak-to-peak variation of the random phase error ($\pm 60^0$) having a rms of $\pm 18^0$ introduced compared to a fixed error of $\pm 18^0$.

Also, the results in Tables 1 and 2 show that the coded schemes are more tolerant to both phase errors and timing errors together compared to the uncoded scheme.

6. CONCLUSIONS

The bit error rate (BER) performance of constant envelope partial response continuous phase modulation (CPM) such as Gaussian minimum shift keying (GMSK) combined with trellis coded modulation (TCM) over additive white Gaussian noise is investigated using computer simulations. The sensitivity to timing and phase errors of the proposed scheme has been studied. It has been observed that a gain of 1.7 dB, 2.2 dB and 3.1 dB can be obtained by introducing coding and differential encoding before GMSK modulation using constraint length 2, 3, and 4 codes respectively under ideal timing and carrier recovery conditions. Also, the performance degradation of the proposed coded schemes is much less than that of the uncoded scheme under the various timing and phase errors considered. The receiver complexity of the coded GMSK schemes considered having constraint length 2 and 3 codes have smaller or the same complexity as the uncoded GMSK scheme.

7. REFERENCES

1. Sundberg, Carl-Erik, "Continuous Phase Modulation," *IEEE Communications Magazine*, 24(4), April, 1986, pp. 25-38.
2. Murota, K. and Hirade, K., "GMSK Modulation for Digital Mobile Telephony," *IEEE Transactions on Communications*, COM-29, July, 1981, pp. 1044-1050.
3. Ungerboeck, G., "Channel Coding with Multilevel/Phase Signals," *IEEE Transactions on Information Theory*, IT-28 (1), January, 1982. pp. 55-67.
4. Anderson, J, Aulin, T and Sundberg, C.E., *Digital Phase Modulation*, Plenum Press, New York, NY, USA, 1986.
5. Aulin, T. and Sundberg, C.-E. W., "Continuous Phase Modulation - Part I : Full Response Signalling," *IEEE Transaction on Communications*, COM-29(3), March, 1981, pp. 196-209.
6. Aulin, T., Rydbeck, Nils and Sundberg, C.-E.W., "Continuous Phase Modulation - Part II : Partial Response Signalling," *IEEE Transaction on Communications*, COM-29(3), March, 1981, pp. 210-225.
7. Morales-Moreno, F., Holubowicz, W. and Pasupathy, S., " Optimization of Trellis Coded Via Matched Codes," *IEEE Transaction on Communications*, 42(2/3/4), Feb./March/April, 1994,pp.1586-1594.

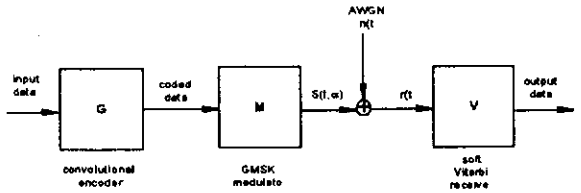

Fig.1 A model of the trellis coded GMSK scheme.

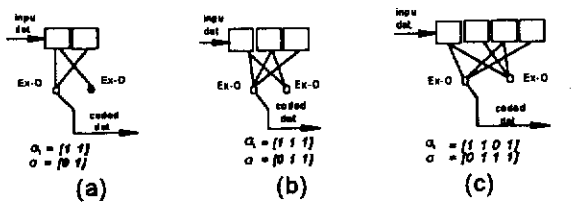

Fig.2 Encoder of the code represented in (a). (3,1) (b). (7,3) and (c). in octal form as (15,7).

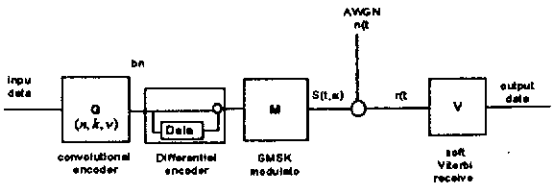

Fig.3 A trellis coded and differentially encoded GMSK scheme.

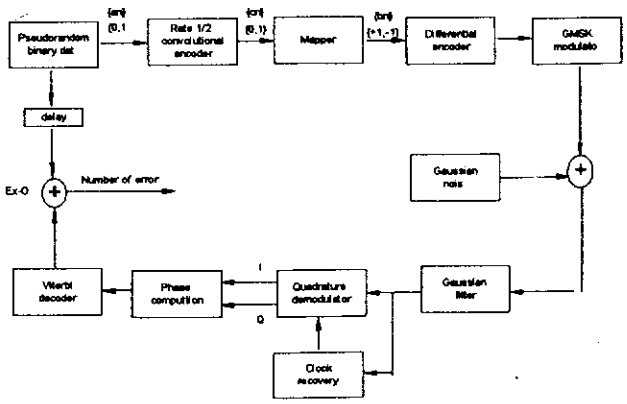

Fig.4 Simulation model.

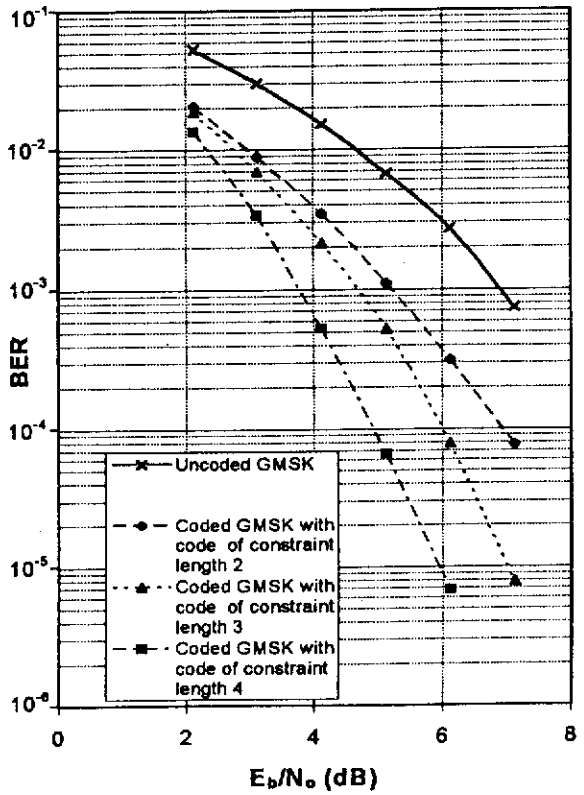

Fig.5 BER of uncoded and trellis coded GMSK schemes.

Signal GMSK	E_b/N_0 in dB required to achieve a BER of $1x10^{-3}$										
	Ideal carrier recovery						Ideal timing recovery				Timing offset of ±T/4 and carrier phase offset of ±18°
	Ideal timing	Timing offset of ±T/8	Timing offset of ±T/4	Timing offset of ±5T/8	Random offset of ±T/4 rms. BW = 0.1%fb	Random offset of ±T/4 rms. BW =0.5%fb	Carrier phase offset of $\pm10^0$	Carrier phase offset of $\pm15^0$	Carrier phase offset of $\pm18^0$	Random phase offset of $\pm18^0$ rms. BW=1%fb	
Uncoded	6.90	7.16	7.80	12.60	8.50	10.20	8.50	10.16	12.00	-	13.41
Constraint length 2 code	5.20	5.35	5.50	8.23	5.73	6.24	5.38	5.64	5.80	8.10	6.42
Constraint length 3 code	4.70	4.80	5.00	7.70	5.36	5.68	4.80	5.34	5.50	8.30	6.60
Constraint length 4 code	3.80	3.95	4.10	6.80	4.60	4.81	3.90	4.20	4.75	7.15	4.95

Note : T is the bit period
f_b is the bit rate

Table 1 The required E_b/N_0 in dB to achieve a BER of $1x10^{-3}$

Signal GMSK	Performance gain in dB at a BER of $1x10^{-3}$										
	Ideal carrier recovery						Ideal timing recovery				Timing offset of ±T/4 and carrier phase offset of ±18°
	Ideal timing	Timing offset of ±T/8	Timing offset of ±T/4	Timing offset of ±5T/8	Random offset of ±T/4 rms. BW = 0.1%fb	Random offset of ±T/4 rms. BW =0.5%fb	Carrier phase offset of $\pm10^0$	Carrier phase offset of $\pm15^0$	Carrier phase offset of $\pm18^0$	Random phase offset of $\pm18^0$ rms. BW=1%fb	
Uncoded	0.00*	-0.26	-0.90	-5.70	-1.60	-3.30	-1.60	-3.26	-5.10	-	-6.51
Constraint length 2 code	+1.70	+1.55	+1.40	-1.33	+1.17	+0.66	+1.52	+1.26	+1.10	-1.20	+0.48
Constraint length 3 code	+2.20	+2.10	+1.90	-0.80	+1.54	+1.22	+2.10	+1.56	+1.40	-1.40	+0.30
Constraint length 4 code	+3.10	+2.95	+2.80	+0.10	+2.30	+2.09	+3.00	+2.70	+2.15	-0.25	+1.95

Note : * The uncoded GMSK with ideal carrier recovery and timing recovery as the reference

Table 2 The performance gain in dB at a BER of $1x10^{-3}$

TRELLIS CODED CPM USING COHERENT DETECTION

M. K. Caldera, K. S. Chung and S. H. Razavi
Curtin University of Technology
P O Box U1987 Perth Western Australia

ABSTRACT The bit error rate (BER) performance of constant envelope partial response continuous phase modulation (CPM) such as Gaussian minimum shift keying (GMSK) combined with trellis coded modulation (TCM) over additive white Gaussian noise is investigated. The received signal is demodulated by coherent detection based on Viterbi decoding. Coherent detection requires the knowledge of the exact phase of the transmitted carrier at the receiver. However, in practice the exact carrier recovery and clock recovery cannot be achieved due to the presence of timing and phase jitters in the system. The proposed study examines the sensitivity of the coherent receiver to timing and phase impairments. The BER curves of the coded GMSK signal and the uncoded GMSK signal are obtained using computer simulations under various timing jitters and carrier phase offsets. The results obtained are compared with those having exact carrier recovery and clock recovery at the receiver. The effect of the bandwidth of the clock recovery system on the BER is also observed.

The trellis coded GMSK schemes show better bit error rate performances than the uncoded GMSK schemes under ideal conditions as well as under timing and phase errors. Coding gains of 1.7 dB, 2.2 dB and 3.1 dB at a BER of $1x10^{-3}$ are respectively achieved with coded GMSK with constraint lengths of 2, 3, and 4 under ideal timing and carrier recovery conditions. Furthermore, the coded schemes are shown to be more tolerant to timing jitters and carrier phase offsets. For example, for a timing offset of ±T/4, the degradation suffered by the coded and uncoded cases at a BER of $1x10^{-3}$ are 0.3 dB and 0.9 dB respectively. As for the carrier phase offsets of $\pm 18^0$, the uncoded scheme suffers more than 5 dB degradation while that of the coded system is less than 1 dB.

1. INTRODUCTION

Due to constraints on spectrum availability and transmitter power, both bandwidth and power efficient digital modulation techniques are desirable in mobile radio communications. CPM signals have gained attention because of their attractive power spectra. Moreover, the partial response CPM signals such as Gaussian minimum shift keying (GMSK) having smooth phase transitions between the successive signalling intervals produce a narrower spectrum than the full response CPM signals [1,2]. Also, the inherent constant envelope property of CPM signals permits the utilisation of efficient non-linear power amplifiers without causing undesired spectral splashing. On the other hand, TCM schemes could provide better bit error rate performances compared to the uncoded schemes [3]. Therefore, the combination of TCM which improves error probability and partial response CPM signals which yield constant envelope and low spectral occupancy is expected to provide good coding and modulation over bandwidth and power limited channels such as the one encountered in mobile radio communications.

This paper examines the improvement in BER performance of GMSK signal when combined with rate 1/2 trellis coding in an additive Gaussian noise environment. Coherent detection based on Viterbi decoding has been adopted. However, with coherent detection, the carrier recovery becomes essential. Previous studies on coherent detection of GMSK over Gaussian noise channel often assumed exact recovery of the reference carrier and the timing clock [3]. This study examines the effect of timing jitters and the carrier phase offsets on the BER performances.

2. CONTINUOUS PHASE MODULATION (CPM)

In continuous phase modulation, the information carrying phase of the carrier is a continuous function of time. This signal phase continuity is given rise by the correlation between symbols in adjacent signalling intervals. The mathematical representation of a CPM signal has the form [4],

$$s(t,\alpha) = \sqrt{2E/T}\cos(2\pi f_c t + \phi(t,\alpha) + \phi_0) \qquad (1)$$

where E is the symbol energy of the signal, T is the symbol duration, f_c is the carrier frequency, ϕ_0 is an arbitrary constant which represents the initial phase, and it can be set to zero with no loss of generality. $\phi(t,\alpha)$ is the information carrying phase given by,

$$\phi(t,\alpha) = 2\pi h \sum_{i=-\infty}^{i=n} \alpha_i q(t-iT)$$

$$\text{and} \quad q(t) = \int_{-\infty}^{t} g(\tau)\, d\,\tau \qquad (2)$$

where $\alpha_i = \pm 1, \pm 3, \pm 5, \ldots, \pm (M\text{-}1)$ for M-ary data. This paper considers only binary modulation, so that $\alpha_i = \pm 1$. The pulse waveform $q(t)$ determines the phase changes in the signal modulation in response to each data symbol. Normally, the frequency pulse, $g(t)$ is a smooth pulse shape over a finite duration LT, where L is an integer. The shape of $g(t)$ determines the smoothness of the transmitted information carrying phase. The rate of change of the phase or the instantaneous frequency is proportional to the parameter h, which is normally referred to as the modulation index.

By choosing different frequency pulses $g(t)$ and varying the parameters h and M, a variety of CPM schemes can be realised. CPM schemes derived using a frequency pulse $g(t)$ occupying a duration of L symbol intervals greater than one have overlapping pulse shaping. If $L > 1$, then the resulting schemes are referred to as partial response CPM [5, 6].

In GMSK, which belongs to the class of partial response CPM scheme, the binary data are filtered by a Gaussian low-pass filter before applying to an FM modulator. The pre-modulation Gaussian filter shapes

the data signal to provide a smooth phase variation. This smoothness in phase variation produces a compact spectrum compared to its full response counterparts like Minimum shift keying (MSK) signal. The modulation index of GMSK equals to 0.5. The impulse response of the Gaussian low-pass filter is given by,

$$h(t) = A\sqrt{\frac{2\pi}{\ln 2}}B_0 \exp\left\{\frac{-2\pi^2 B_0^2 t^2}{\ln 2}\right\} \quad (3)$$

where B_0 is the 3 dB bandwidth and A is a constant. By varying the 3-dB bandwidth of the impulse response of the Gaussian filter, a set of different GMSK signals having different power spectra can be obtained. The frequency pulse $g(t)$ of the GMSK signal has the form,

$$g(t) = \frac{1}{2T}\left[Q\left(2\pi B_0 \frac{t-\frac{T}{2}}{\sqrt{\ln 2}}\right) - Q\left(2\pi B_0 \frac{t+\frac{T}{2}}{\sqrt{\ln 2}}\right)\right] \quad (4)$$

$$\text{for} \quad 0 \le B_0 T < \infty$$

$$\text{where} \quad Q(t) = \int_t^\infty \frac{1}{\sqrt{2\pi}} e^{-r^2/2}\, dr$$

For GMSK, the duration of the Gaussian phase shaping pulse $g(t)$ is infinite. However, for practical reasons, it can be truncated over several bit periods. When $B_0 T$ is equal to 0.25, the GMSK pulse can be truncated symmetrically over 4 bit periods.

3. TRELLIS CODED GMSK

Fig. 1 shows the block diagram of the trellis coded GMSK model considered in this paper. G is a binary convolutional encoder. A convolutional encoder is usually denoted by (n,k,ν). Here the encoder accepting k serial input bits at a given time interval yields n output bits using a ν-stage shift register. For the same code (n,k,ν), there are a large number of equivalent encoders having different structures. A convolutional code can be described by a row vector called the connection vector,

$$G_j = (g_{j1}, g_{j2}, \ldots, g_{j\nu}), \qquad j = 1,2,\ldots,n \quad (5)$$

specifying the connection between the j - th output and each stage of the shift register. The component g_{ji} is equal to 1 if the j th output is connected to stage i: otherwise it is equal to zero. The length of the shift register in the encoder is called the constraint length of the code. Code rate is $R_c = k/n$. In this paper, rate 1/2 convolutional encoders having constraint lengths 2, 3, and 4 have been studied in conjunction with GMSK modulation.

The coded sequences of the input data are then serially fed to the GMSK modulator M, which generates the transmitted signal $s(t,\alpha)$. The signal at the input to the coherent receiver is $r(t) = s(t,\alpha) + n(t)$, where $n(t)$ is additive white Gaussian noise with zero mean and double sided power spectral density $N_0/2$. The coherent receiver consists of quadrature demodulation followed by soft decision Viterbi decoding. The phase values of the received signal obtained from quadrature demodulation are used in the trellis decoder to estimate the most likely transmitted sequence using the Viterbi algorithm.

In general, a binary convolutional code having $k=1$ and constraint length ν has $2^{\nu-1}$ states in the trellis diagram. When such code is decoded by means of the Viterbi algorithm, there are $2^{\nu-1}$ surviving paths at each stage and $2^{\nu-1}$ metrics, one for each surviving path. Thus, the receiver complexity of the Viterbi decoder is proportional to the number of states in the trellis. The receiver complexity of the combined coded CPM signals can be expressed by the number of decoder states in the Viterbi decoder. The number of states representing the combined signal, which is the number of states in the optimum Viterbi decoder, is the product of the number of states in the convolutional code and the number of states in the CPM signal. However, the complexity of the receiver can be minimised by precoding the input to the GMSK modulator as shown in Fig. 2 [7]. The transfer function of the binary precoder can be represented by $T(D)=1+D$, i.e. $\alpha_n = b_n \oplus b_{n-1}$, where $\oplus$ denotes modulo-2 addition (or EX-OR operation), b_n is the input to the precoder and α_n is the output of the precoder. D represents the delay by one bit period.

In designing a trellis coded CPM signal, the convolutional encoder, the mapper and the CPM scheme must all be optimised jointly to create a good power and spectrally efficient code. The optimisation criterion used in this study is based on the largest minimum Euclidean distance (the largest free distance) between signals leaving a common state in the combined trellis of the convolutional code of a given constraint length with the trellis of the CPM signal, and merging into another common state after a certain time interval. An exhaustive search on selecting the optimum combination of rate 1/2 convoultional codes having constraint lengths 2, 3, and 4 with differentially encoded GMSK has been carried out in this study. The codes having all the possible combinations of generator polynomials have been considered in the search.

The connection vectors G_1 and G_2 of the selected optimum rate 1/2 convolutional encoder having constraint lengths 2 producing the largest free distance have the form *[1 1]* and *[0 1]*. The octal representation of the generator polynomial of this code is (3,1). The selected optimum codes having constraint lengths 3 and 4 producing the largest free distances have the connection vectors G_1 = *[1 1 1]* and G_2 = *[0 1 1]*, and G_1 = *[1 1 0 1]* and G_2 = *[0 1 1 1]* respectively. The octal representations of the corresponding generator polynomials of these selected optimum codes having constraint lengths 3 and 4 are (7,3), and (15,7) respectively. When these selected codes having constraint lengths 2, 3, and 4 are combined with differentially encoded GMSK, the resultant trellises have 4, 8 and 16 states respectively whereas the GMSK trellis has 8 states.

4. SIMULATION MODEL

Computer simulations based on the functional block diagram of Fig. 3 have been used in determining the bit error rate (BER) in the presence of additive white Gaussian noise. The transmitted data, $\{a_n\}$, is derived from a pseudorandom sequence generator of length 256 bits and with equiprobable bits of logical *1* and *0*.

This data is encoded by a rate 1/2 convolutional encoder. Here, the rate 1/2 convolutional codes having constraint length 2, 3, and 4 represented by their generator polynomials in octal form as (3,1), (7,3), and (15,7) respectively are used. The coded binary data $\{c_n\}$ is then mapped to the real number inputs $\{b_n\}$ to the differential encoder as $0 \rightarrow -1$ and $1 \rightarrow +1$. This data $\{b_n\}$ is then differentially encoded before applying to the GMSK modulator. The 3-dB bandwidth of the premodulation Gaussian filter normalised to the bit period is set at 0.25. The GMSK frequency pulse is truncated symmetrically over 4 bit periods and considered zero outside. The additive white Gaussian noise has been simulated according to the Box Muller's transformation. The received signal is filtered using a low pass equivalent of a Gaussian band pass filter. The performance of the system changes with the bandwidth of this low pass filter. Therefore, the optimum bandwidth of this low pass filter, which produces the best performance at a given SNR has also been considered and obtained in the simulation. The filtered signal is then demodulated into its inphase (I) and quadrature (Q) components $\cos(\phi(t))$ and $\sin(\phi(t))$ using a quadrature demodulator with the reference carrier in quadrature. The sampling instants of the I and Q components of the received signal are set at the instants where the eye opening is maximum. The samples of the I and Q components obtained at these sampling instants are then used to compute the phase values. The trellis decoder uses these phase values to determine the most likely transmitted sequence employing the Viterbi algorithm. The BER curves are obtained by comparing the transmitted and the received signals. To ensure the reliability of the simulation results, at least 100 errors have been used to compute the BER for each E_b/N_0 value.

5. SIMULATION RESULTS

In selecting the optimum BW of the low pass filter, the BER behaviour of uncoded and trellis coded GMSK with the selected convolutional codes having constraint lengths 2, 3, and 4 had been first obtained with different bandwidths in the simulation at an arbitrarily selected E_b/N_0 (= 4dB) value. From Fig 4, the optimum band pass bandwidth of the low pass equivalent of the band pass filter normalised to the bit period can be approximated to 0.6 for both uncoded and trellis coded GMSK signals. This optimum bandwidth has then been selected as the filter bandwidth of the low pass equivalent of the Gaussian band pass filter, in the rest of the simulations carried out in this study. Fig. 5 presents the simulated BER results for the uncoded and the trellis coded GMSK signals in the presence of additive white Gaussian noise assuming ideal carrier recovery and timing synchronisation. When compared with the uncoded GMSK schemes at a BER of 10^{-3}, coding gains of 1.7, 2.2, and 3.1 dB have been achieved using codes of constraint lengths 2, 3, and 4 respectively in conjunction with differentially encoded GMSK. Moreover, the number of states in the trellis of the uncoded GMSK scheme is 2, 1, and 1/2 times that of coded scheme for constraint lengths 2, 3, and 4 respectively. Thus, a decrease in receiver complexity has been obtained with the constraint length 2 code while obtaining a coding gain of 1.7 dB.

The sensitivity of the proposed coherent detection scheme to timing and carrier phase offsets has also been investigated in the presence of various carrier and timing impairments, including fixed and random variations. First, the sampling instant has been offset assuming the carrier phase recovery is ideal. Then, the carrier phase errors have been combined assuming no symbol timing error. Finally, the effect of both symbol timing offset and carrier phase errors has been studied. Fig. 6 presents the BER performance of the coded and uncoded GMSK signals when the sampling instant offset is $\pm T/4$. Similar BER performances are presented in Fig. 7 when the carrier phase offset is $\pm 18^0$. Table 1 tabulates the values of E_b/N_0 required to achieve an error rate of 10^{-3} for uncoded and trellis coded GMSK in the presence of various carrier and timing impairments, including fixed and random variations.

The random timing jitter and the random carrier phase error have been simulated by low pass filtering a set of Gaussian distributed random numbers. Averaging filters have been used to simulate the filtering effect of the carrier and clock recovery loops. The filter bandwidth is varied by changing the number of samples used in the running average. For the bandwidths considered, the peak-to-peak variation of the sampling instant offset of the random jitter is set at $\pm 6T/8$. However, when the bandwidth of the filter is small, the random timing and carrier phase variations are slowly varying and the correlation between the adjacent variations is high.

When the sampling instant offset is $\pm T/4$, the BER performance of uncoded GMSK is degraded by 0.90 dB compared to the ideal carrier recovery and timing recovery, whereas trellis coded GMSK signals achieved 0.3 dB degradation in performance under the same conditions. When the sampling instant suffers from random jitter with rms offset of $\pm T/4$, the performance degradation of all the signals considered is increased. The results under timing offsets show that the uncoded GMSK signal is much more sensitive to sampling instant offsets than the coded GMSK signals considered, provided that the carrier recovery is ideal having no phase errors. Also, both uncoded and trellis coded GMSK signals studied are more sensitive to random errors than the fixed errors due to the large peak-to-peak variations that could be encountered in the case of random errors.

Even at the worst fixed carrier phase offset considered ($\pm 18^0$), the coded schemes have shown a performance degradation of less than 1 dB while the uncoded scheme has shown a degradation of more than 5 dB. The effect of random phase error has shown a severe reduction of the performance (more than 10 dB) of the uncoded GMSK signal. Also, the coded schemes have shown around 3 dB degradation in performance under these conditions. It has been observed from these results that the coded signals are more tolerant to carrier phase offset than the uncoded signal. Moreover, the effect of random carrier phase error is more severe on the performance of both coded and uncoded schemes considered than the fixed phase error. This is due to the much higher peak-to-peak variation of the random phase error ($\pm 60^0$) having a rms of $\pm 18^0$ introduced compared to a fixed error of $\pm 18^0$.

Also, the results in Table 1 show that the coded schemes are more tolerant to both phase errors and timing errors together compared to the uncoded scheme.

6. CONCLUSIONS

The optimum combinations of rate 1/2 convolutional codes having constraint lengths 2, 3, and 4 combined with differentially encoded GMSK has been obtained based on the largest free distances. The BER performance of differentially encoded GMSK combined with trellis coded modulation (TCM) over additive white Gaussian noise is investigated using computer simulations. The sensitivity to timing and phase errors of the proposed scheme has been studied. It has been observed that a gain of 1.7 dB, 2.2 dB and 3.1 dB can be obtained by introducing coding and differential encoding before GMSK modulation using constraint length 2, 3, and 4 codes respectively under ideal timing and carrier recovery conditions. Also, the performance degradation of the proposed coded schemes is much less than that of the uncoded scheme under the various timing and phase errors considered. Also, the receiver complexity of the coded GMSK schemes considered having constraint length 2 and 3 codes have smaller or the same complexity as the uncoded GMSK scheme.

7. REFERENCES

1. Sundberg, Carl-Erik, "Continuous Phase Modulation," *IEEE Communications Magazine*, 24(4), April, 1986, pp. 25-38.
2. Murota, K. and Hirade, K., "GMSK Modulation for Digital Mobile Telephony," *IEEE Transactions on Communications*, COM-29, July, 1981, pp. 1044-1050.
3. Ungerboeck, G., "Channel Coding with Multilevel/Phase Signals," *IEEE Transactions on Information Theory*, IT-28 (1), January, 1982, pp. 55-67.
4. Anderson, J, Aulin, T and Sundberg, C.E., *Digital Phase Modulation*, Plenum Press, New York, NY, USA, 1986.
5. Aulin, T. and Sundberg, C.-E. W., "Continuous Phase Modulation - Part I : Full Response Signalling," *IEEE Transaction on Communications*, COM-29(3), March, 1981, pp. 196-209.
6. Aulin, T., Rydbeck, Nils and Sundberg, C.-E.W., "Continuous Phase Modulation - Part II : Partial Response Signalling," *IEEE Transaction on Communications*, COM-29(3), March, 1981, pp. 210-225.
7. Morales-Moreno, F., Holubowicz, W. and Pasupathy, S., " Optimization of Trellis Coded Via Matched Codes," *IEEE Transaction on Communications*, 42(2/3/4), Feb./March/April, 1994, pp. 1586-1594.

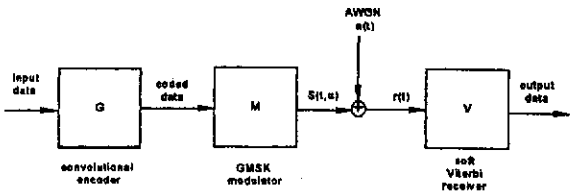

Fig. 1 A model of the trellis coded GMSK scheme.

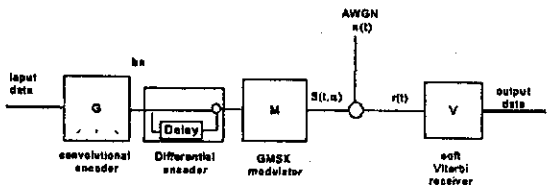

Fig. 2 A trellis coded and differentially encoded GMSK scheme.

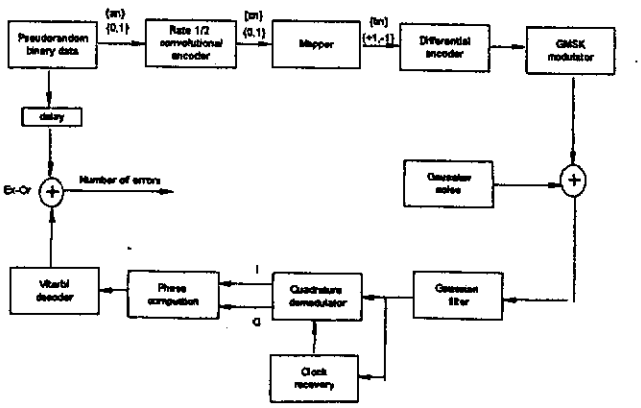

Fig. 3 Simulation model.

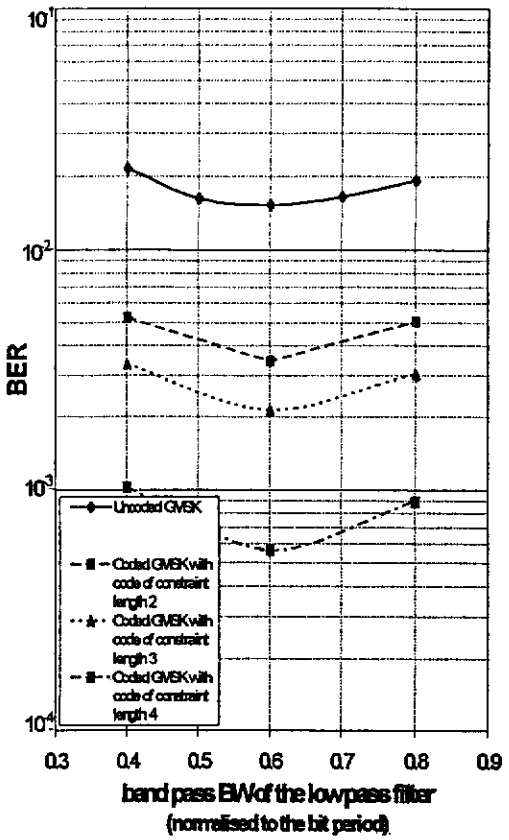

Fig. 4 Influence of the bandwidth of the low pass filter on the BER of coded and uncoded GMSK schemes.

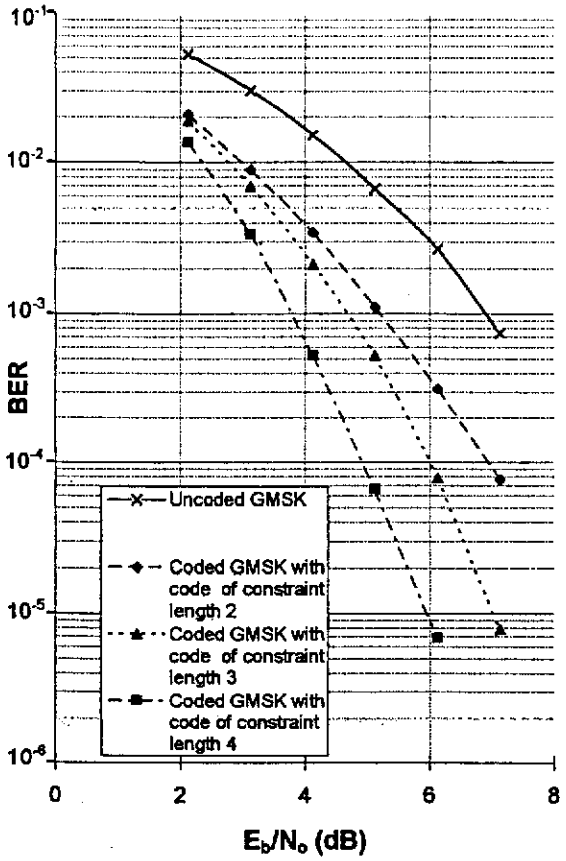

Fig. 5 BER of uncoded and trellis coded GMSK schemes

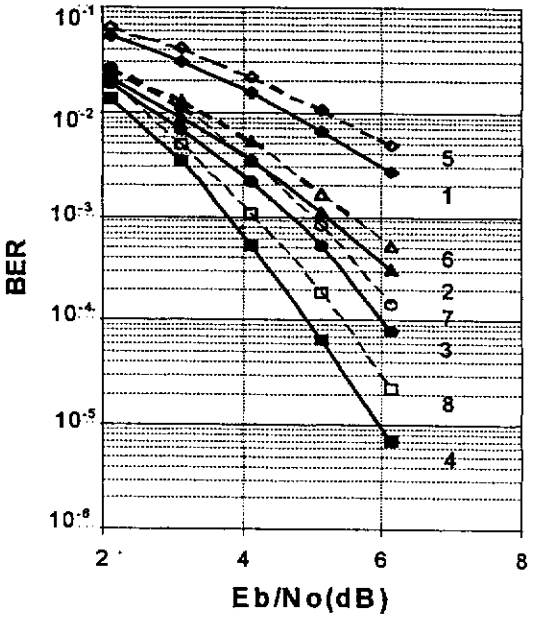

Fig. 6 BER curves of (1) uncoded GMSK, coded GMSK with (2) code of constraint length 2, (3). code of constraint length 3 , (4). code of constraint length 4 with ideal carrier and timing recoveries and (5). uncoded GMSK, coded GMSK with (6). code of constraint length 2, (7). code of constraint length 3 , (8). code of constraint length 4 with sampling instant offset of $\pm T/4$.

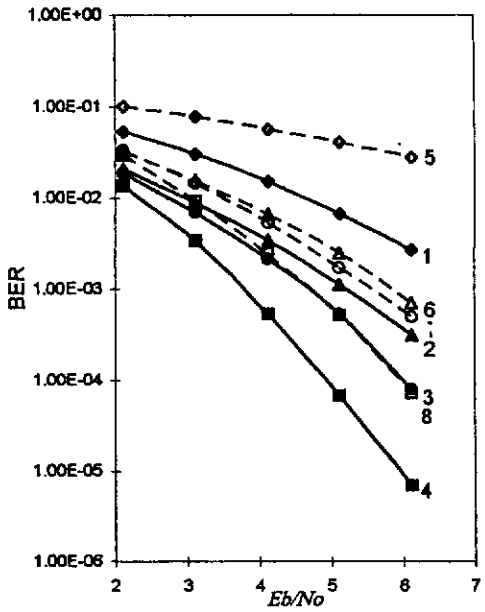

Fig. 7 BER curves of (1) uncoded GMSK, coded GMSK with (2) code of constraint length 2, (3). code of constraint length 3 , (4). code of constraint length 4 with ideal carrier and timing recoveries and (5). uncoded GMSK, coded GMSK with (6). code of constraint length 2, (7). code of constraint length 3 , (8). code of constraint length 4 with sampling instant offset of $\pm 18^0$.

Signal GMSK	E_b/N_0 in dB required to achieve a BER of $1x10^{-3}$										
	Ideal carrier recovery						Ideal timing recovery				Timing offset of ±T/4 and carrier phase offset of ±18°
	Ideal timing	Timing offset of ±T/8	Timing offset of ±T/4	Timing offset of ±5T/8	Random offset of ±T/4 rms. BW = 0.1%fb	Random offset of ±T/4 rms. BW =0.5%fb	Carrier phase offset of $\pm 10^0$	Carrier phase offset of $\pm 15^0$	Carrier phase offset of $\pm 18^0$	Random phase offset of $\pm 18^0$ rms. BW=1%fb	
Uncoded	6.90	7.16	7.80	12.60	8.50	10.20	8.50	10.16	12.00	-	13.41
Constraint length 2 code	5.20	5.35	5.50	8.23	5.73	6.24	5.38	5.64	5.80	8.10	6.42
Constraint length 3 code	4.70	4.80	5.00	7.70	5.36	5.68	4.80	5.34	5.50	8.30	6.60
Constraint length 4 code	3.80	3.95	4.10	6.80	4.60	4.81	3.90	4.20	4.75	7.15	4.95

Note : T is the bit period
f_b is the bit rate

Table 1 The required E_b/N_0 in dB to achieve a BER of $1x10^{-3}$

APPENDIX H

COMPUTER PROGRAMS

The computer search program for the selection of appropriate trellis codes has been carried out using the VAX-VMS system based on a software developed with Pascal. The program **Mindist.pas** calculates the free distance of trellis coded GMSK schemes. The phase values required for the calculation are provided in the **Mindist.com** file. The values provided in the **Mindist.com** file correspond to the phase states and the intermediate phase states of the code [13,7] in combination with differentially encoded GMSK. These phase values corresponding to a particular trellis coded scheme are obtained by combining the trellis of the code with that of the differentially encoded GMSK signal, as discussed in Section 4.4.

The computer simulations in Chapters 6 and 7 have been carried out on IBM PC using custom software developed with Fortran. A list of the major programs, which provide the BERs of uncoded and coded GMSK schemes under various conditions are given below.

Uncod.bat
Uncoded GMSK in the presence of AWGN, assuming ideal timing and carrier phase.

Uncodj.bat
Uncoded GMSK in the presence of AWGN, with random timing error.

Uncodp.bat
Uncoded GMSK in the presence of AWGN, with random phase error.

Cod31.bat
Coded GMSK using code [3,1], in the presence of AWGN, assuming ideal timing and carrier phase.

Cod73.bat
Coded GMSK using code [7,3], in the presence of AWGN, assuming ideal timing and carrier phase.

Cod137.bat
Coded GMSK using code [15,7], in the presence of AWGN, assuming ideal timing and carrier phase.

Codj31.bat
Coded GMSK using code [3,1], in the presence of AWGN, with random timing error.

Codj73.bat
Coded GMSK using code [7,3], in the presence of AWGN, with random timing error.

Codj137.bat
Coded GMSK using code [15,7], in the presence of AWGN, with random timing error.

Codp31.bat
Coded GMSK using code [3,1], in the presence of AWGN, with random phase error.

Codp73.bat
Coded GMSK using code [7,3], in the presence of AWGN, with random phase error.

Codp137.bat
Coded GMSK using code [15,7], in the presence of AWGN, with random phase error.

The simulated BERs using differential phase detection of uncoded GMSK over flat fading channels are obtained using the files **unff1.bat** and **unff2.bat**. Initiating with the file **unff1.bat**, **unff2.bat** is then repeated (128 times) until the required BERs are reached. Similarly the BERs on the coded GMSK involving the code [3,1] are obtained using the files **coff1.bat** and **coff2.bat**.

The irreducible BERs of the uncoded and coded schemes over two-ray frequency-selective fading channels using differential phase detection are obtained using the files **unsf2.bat** (again initiated with the file **unsf1.bat**) and **cosf2.bat** (initiating with **cosf1.bat**), respectively.

The irreducible BERs of the uncoded and the coded schemes using the adaptive Viterbi decoder over two-ray frequency-selective fading channels using different lengths of training sequences, signal blocks and with different complexities of Viterbi receivers are obtained using the following files. Here, the first **.bat** file is run once and the second **.bat** file is repeated until the required BERs are obtained (until the number of transmitted bits considered approximates to ½ million).

un128_21.bat and then **un128_22.bat**
uncoded GMSK using training sequence of 26 bits, signal block of 128 bits and decoder designed to accommodate up to 4 bit periods.

un128_31.bat and then **un128_32.bat**
uncoded GMSK using training sequence of 26 bits, signal block of 128 bits and decoder designed to accommodate up to 3 bit periods.

un128_41.bat and then **un128_42.bat**
uncoded GMSK using training sequence of 40 bits, signal block of 128 bits and decoder designed to accommodate up to 4 bit periods.

un256_21.bat and then **un256_22.bat**
uncoded GMSK using training sequence of 26 bits, signal block of 256 bits and decoder designed to accommodate up to 4 bit periods.

Co128_21.bat and **co128_2.bat** (Here **co128_2.bat** consists of **co128_22.bat, co128_23.bat, co128_24.bat,** and **co128_25.bat)**
coded GMSK with code [3,1] using training sequence of 26 bits, signal block of 128 bits and decoder designed to accommodate up to 4 bit periods.

Co128_31.bat and **co128_3.bat** (Here **co128_3.bat** consists of **co128_32.bat, co128_33.bat, co128_34.bat,** and **co128_35.bat)**
coded GMSK with code [3,1] using training sequence of 26 bits, signal block of 128 bits and decoder designed to accommodate up to 3 bit periods.

Co128_41.bat and **co128_4.bat** (Here **co128_4.bat** consists of **co128_42.bat, co128_43.bat, co128_44.bat,** and **co128_45.bat)**
coded GMSK with code [3,1] using training sequence of 40 bits, signal block of 128 bits and decoder designed to accommodate up to 3 bit periods.

Co256_21.bat and **co256_2.bat** (Here **co256_2.bat** consists of **co256_22.bat** and **co256_23.bat)**
coded GMSK using training sequence of 26 bits, signal block of 256 bits and decoder designed to accommodate up to 4 bit periods.

The irreducible BERs of the uncoded and the coded schemes using the adaptive Viterbi decoder, designed to accommodate up to 4 bit periods, over six-ray GSM fading channel models are obtained using the following files. The length of the training sequence is 26 bits and the signal block size is 256 bits.

un_gsmh1.bat and then **un_gsmh2.bat**
uncoded GMSK over six-ray hilly terrain model

un_gsmr1.bat and then **un_gsmr2.bat**
uncoded GMSK over six-ray rural area model

un_gsmu1.bat and then **un_gsmu2.bat**
uncoded GMSK over six-ray urban area model

Co_gsmh1.bat and **co_gsmh.bat** (Here **co_gsmh.bat** consists of **co_gsmh2.bat,** and **co_gsmh3.bat)**
coded GMSK over six-ray hilly terrain model

Co_gsmr1.bat and **co_gsmr.bat** (Here **co_gsmr.bat** consists of **co_gsmr2.bat,** and **co_gsmr3.bat)**
coded GMSK over six-ray rural area model

Co_gsmu1.bat and **co_gsmu.bat** (Here **co_gsmu.bat** consists of **co_gsmu2.bat,** and **co_gsmu3.bat)**
coded GMSK over six-ray urban area model

A software copy of these subroutines is provided on the floppy disk attached to this thesis. In order to run the subroutines provided on the disk, Pascal and Fortran compilers are required. The variable/s of interest must be specified in each program. The final output is redirected to a text file.